UNIVERSITAT POLITÈCNICA DE VALÈNCIA

Departament of Mechanical and Materials Engineering

PhD Thesis

Comprehensive dynamic models of railway wheelsets and tracks for the prediction of rolling noise

---

Author: Víctor T. Andrés Ruiz

Supervisors: Dr. José Martínez Casas
Prof. Dr. Francisco David Denia Guzmán

Valencia, May 2024

PhD Thesis

Comprehensive dynamic models of railway wheelsets and tracks for the prediction of rolling noise

---

for the degree of

Doctor in Industrial Engineering and Production

presented by

Víctor T. Andrés Ruiz

at the

Departament of Mechanical and Materials Engineering

of Universitat Politècnica de València

Supervised by

Dr. José Martínez Casas

Prof. Dr. Francisco David Denia Guzmán

Valencia, May 2024

PhD Thesis

Comprehensive dynamic models of railway wheelsets and tracks for the prediction of rolling noise

Author: Víctor T. Andrés Ruiz

Supervisors: Dr. José Martínez Casas
Prof. Dr. Francisco David Denia Guzmán

QUALIFYING COMMITTEE

PRESIDENT: Prof. Dr. Francisco Javier Fuenmayor Fernández

VOCAL: Prof. Dr. Jorge Patricio Arenas Bermúdez

SECRETARY: Prof. Dr. Publio Pintado Sanjuán

Valencia, May 2024

This Thesis has been supported by Ministerio de Ciencia, Innovación y Universidades in the framework of the FPU grant program.

Grants FPU18/03999, EST21/00213, and EST22/00353 as well as projects TRA2017-84701-R, PID2020-112886RA-I00, and PID2023-148483OB-I00 funded by MCIN/AEI/10.13039/501100011033, "ESF Investing in your future", and "ERDF A way of making Europe" are acknowledged. The author also expresses his gratitude for the support provided by Programa PROMETEO/2021/046 of Generalitat Valenciana.

UNIÓN EUROPEA
Fondo Social Europeo
El FSE invierte en tu futuro

UNIÓN EUROPEA

FONDO EUROPEO DE
DESARROLLO REGIONAL
"Una manera de hacer Europa"

Abstract

Rolling noise emission in railway systems presents significant challenges in urban and suburban environments, requiring a comprehensive understanding of its underlying mechanisms for effective mitigation. This Thesis offers a thorough investigation into rolling noise generation, considering both tangent and curved tracks, through the development of advanced high-frequency models and calculation tools to predict noise levels accurately.

Rolling noise arises from the interaction between railway wheels and tracks in the presence of roughness on their contact surfaces. The principal components contributing to the acoustic emission are the sleepers, rails, and wheels. Sleepers and rails are interconnected through rail pads, while wheels and rails are dynamically coupled due to their contact. Consequently, changes in any component might impact the dynamic and acoustic behaviour of all of them, outlining the necessity of a comprehensive model to address rolling noise radiation effectively.

Various models for the track and wheelset are explored and developed in this Thesis. The track, assumed to be infinite, is described using periodic structure theory and it is characterised by its wavenumbers and waveshapes. The wheelset is modelled through the Finite Element Method (FEM) and it is characterised by its natural frequencies and vibration modes. The wheelset and track interaction is described as a linearised relationship between the relative motion of both components and the contact forces. The models examined in this work are formulated in the frequency domain.

Identified track properties influencing rolling noise radiation are quantified using statistical techniques. While the rail geometry is found to have a limited impact on the total radiation, the viscoelastic properties of the track, particularly the rail pad stiffness, play a crucial role in noise generation. Variations up to 7.4 dB(A) were observed for different track designs.

Special attention is devoted to the wheelset modelling in this Thesis. Its rotation is considered using Eulerian coordinates, a convenient approach as the wheel contact point with the rail remains at a constant spatial position. Given the axial symmetry of its geometry, the wheelset dynamic response is expanded around the circumferential direction using Fourier series, which yields a two-dimensional (2D) formulation of the dynamic and acoustic behaviour of this three-dimensional (3D) system, with the circumferential coordinate being solved analytically. This methodology, denoted as axisymmetric approach, offers a significant reduction in the associated computational calculation time while preserving accuracy, making the model well suited for its integration into optimisation algorithms.

Lastly, a novel investigation into rolling noise when the vehicle negotiates a curve is conducted. While curved tracks are generally associated with squeal noise, this Thesis offers valuable insights into the importance of rolling noise as well. To achieve this, the inertial and gyroscopic effects associated with a wheelset running on a curve are modelled. Complex phenomena occurring at the wheel/rail contact, such as the relative motion between these two elements, are incorporated into the interaction model. The results indicate that the wheel/rail contact position serves as a reliable indicator of the impact of a curve on the rolling noise.

Keywords

Railway rolling noise; comprehensive model; dynamics; noise mitigation; wheel; rail; sleeper; wheel/rail interaction; track design; wheelset rotation; axisymmetry; rigid body motion; curved track; curve influence.

Resumen

El ruido de rodadura de vehículos ferroviarios presenta importantes desafíos en entornos urbanos y suburbanos, siendo precisa una comprensión integral de sus mecanismos subyacentes para una mitigación efectiva. Esta Tesis ofrece una investigación exhaustiva sobre la generación de ruido de rodadura, tanto en vías rectas como curvas, a través del desarrollo de modelos avanzados de alta frecuencia y herramientas de cálculo para una rigurosa predicción de niveles de ruido.

El ruido de rodadura surge de la interacción entre las ruedas y los carriles en presencia de imperfecciones en sus superficies de contacto. Los principales componentes ferroviarios que contribuyen a la emisión acústica son las traviesas, los carriles y las ruedas. Las traviesas y los carriles están conectados por medio de las placas de asiento, mientras que las ruedas y los carriles están dinámicamente acoplados a través de su contacto. En consecuencia, cambios en cualquier componente pueden afectar al comportamiento dinámico y acústico del resto, subrayando la necesidad de un modelo integral para abordar eficazmente la radiación por ruido de rodadura.

En esta Tesis se exploran y desarrollan diferentes modelos dinámicos de la vía y del eje montado. La vía, que se asume infinita, se describe utilizando la teoría de estructuras periódicas y se caracteriza por sus números y formas de onda. El eje montado se modeliza mediante el Método de Elementos Finitos y se caracteriza por sus frecuencias naturales y modos de vibración. La interacción rueda/carril se describe como una relación linealizada entre el movimiento relativo de ambos componentes y las fuerzas de contacto. Cabe indicar que los modelos explorados en este trabajo están formulados en el dominio de la frecuencia.

Asimismo, se realiza un estudio de influencia del diseño de la vía en la radiación por ruido de rodadura, cuantificando los parámetros más contribuyentes a la emisión acústica mediante técnicas estadísticas. Los resultados apuntan a que la geometría del carril tiene un impacto limitado en la radiación sonora, mientras que las propiedades viscoelásticas de la vía, en particular la rigidez de la placa de asiento, desempeñan un papel fundamental en la generación de ruido. Es remarcable que, entre los distintos diseños de vía estudiados, se han encontrado variaciones de hasta 7,4 dB(A) en la radiación acústica.

Durante el desarrollo de esta investigación, se ha prestado especial atención al modelizado del eje montado ferroviario. Su rotación se incluye en la formulación usando coordenadas Eulerianas, lo que resulta un enfoque conveniente ya que el punto de contacto de la rueda con el carril permanece en una posición espacial constante. Dada la simetría axial de su geometría, la respuesta dinámica del eje montado se expande a lo largo de la dirección circunferencial mediante series de Fourier, lo que permite formular el comportamiento dinámico y acústico de este cuerpo tridimensional (3D) en un marco bidimensional (2D), resolviendo analíticamente la coordenada circunferencial. Esta metodología, denominada enfoque axisimétrico, ofrece sin pérdida de generalidad una reducción significativa del tiempo de cálculo computacional asociado, lo que hace que el modelo sea idóneo para su integración en algoritmos de optimización.

Por último, se realiza una investigación pionera sobre el ruido de rodadura cuando el vehículo negocia una curva. Si bien la curva está generalmente asociada con el ruido por chirridos, esta Tesis explora y confirma la importancia que también tiene el ruido de rodadura en estas condiciones. Para ello, se modelizan los efectos inerciales y giroscópicos que sufre un eje montado al describir una trayectoria curva. Además, diferentes fenómenos complejos que ocurren en el contacto rueda/carril, como por ejemplo el movimiento relativo entre estos elementos, se incorporan en el modelo de interacción. Los resultados indican que la posición del contacto rueda/carril sirve como un buen indicador del impacto que la negociación de una curva tiene en el ruido de rodadura.

Palabras clave

Ruido de rodadura ferroviario; modelo integral; dinámica; mitigación acústica; rueda; carril; traviesa; interacción rueda/carril; diseño de vía; rotación del eje montado; axisimetría; movimiento de sólido rígido; vía curva; influencia de la curva.

Resum

El soroll de rodament de vehicles ferroviaris presenta importants reptes en entorns urbans i suburbans, requerint una comprensió integral dels seus mecanismes subjacents per a una mitigació efectiva. Aquesta Tesi ofereix una investigació exhaustiva sobre la generació de soroll de rodament, tant en vies rectes com corbes, mitjançant el desenvolupament de models avançats d'alta freqüència i eines de càlcul per a la rigorosa predicció dels nivells de soroll radiat.

El soroll de rodament sorgeix de la interacció entre les rodes i els carrils en presència d'imperfeccions en les seues superfícies de contacte. Els principals components ferroviaris que contribueixen a l'emissió acústica són les travesses, els carrils i les rodes. Les travesses i els carrils estan connectats a través de les plaques d'assentament, mentre que les rodes i els carrils estan dinàmicament acoblats mitjançant la seua interacció. En conseqüència, canvis en qualsevol component poden afectar al comportament dinàmic i acústic de la resta, subratllant la necessitat d'un model integral per abordar eficaçment la radiació per soroll de rodament.

En aquesta Tesi s'exploren i desenvolupen diversos models dinàmics de la via i de l'eix muntat. La via, que es considera infinita, es descriu utilitzant la teoria d'estructures periòdiques i es caracteritza pels seus números i formes d'ona. L'eix muntat es modelitza mitjançant el Mètode d'Elements Finits i es caracteritza per les seues freqüències naturals i modes de vibració. La interacció entre l'eix muntat i la via es descriu com una relació linealitzada entre el moviment relatiu d'ambdós components i les forces de contacte. Cal assenyalar que els models explorats en aquest treball estan formulats en el domini de la freqüència.

Així mateix, es realitza un estudi d'influència del disseny de la via en la radiació per soroll de rodament, quantificant els paràmetres més contribuents a l'emissió acústica mitjançant tècniques estadístiques. Els resultats apunten que la geometria del carril té un impacte limitat en la radiació sonora, mentre que les propietats viscoelàstiques de la via, en particular la rigidesa de la placa d'assentament, tenen un paper fonamental en la generació de soroll. És destacable que, entre els diferents dissenys de via estudiats, s'han trobat variacions de fins a 7,4 dB(A) en la radiació per soroll de rodament.

Durant el desenvolupament d'aquesta investigació, s'ha prestat especial atenció al modelatge de l'eix muntat ferroviari. La seua rotació s'inclou en la formulació utilitzant coordenades Eulerianes, la qual cosa resulta un enfocament convenient ja que el punt de contacte de la roda amb el carril roman en una posició espacial constant. Donada la simetria axial de la seua geometria, la resposta dinàmica de l'eix muntat s'amplia al llarg de la direcció circumferencial mitjançant sèries de Fourier, permetent formular el comportament dinàmic i acústic d'aquest cos tridimensional (3D) en un marc bidimensional (2D), i resolent la coordenada circumferencial analíticament. Aquesta metodologia, anomenada enfocament axisimètric, ofereix sense pèrdua de generalitat una reducció significativa del temps de càlcul computacional associat, la qual cosa fa que el model siga idoni per a la seua integració en algoritmes d'optimització.

Finalment, es realitza una investigació pionera sobre el soroll de rodament quan el vehicle negocia una corba. Si bé la corba està generalment associada amb el soroll per grinyols, aquesta Tesi explora i confirma la importància que també té el soroll de rodament en aquestes condicions. Per a això, es modelitzen els efectes inercials i giroscòpics que pateix un eix muntat al descriure una trajectòria corba. A més, diferents fenòmens complexes que ocorren en el contacte roda/carril, com el moviment relatiu entre aquests elements, s'incorporen en el model d'interacció. Els resultats indiquen que la posició del contacte roda/carril serveix com un bon indicador de l'impacte que la negociació d'una corba té en el soroll de rodament.

Paraules clau

Soroll de rodament ferroviari; model integral; dinàmica; mitigació acústica; roda; carril; travessa; interacció roda/carril; disseny de via; rotació de l'eix muntat; axisimetria; moviment de sòlid rígid; via corba; influència de la corba.

Acknowledgements

I would like to express my deepest gratitude to my supervisors, Paco and Jose, for their invaluable guidance and support throughout this journey.

Paco, your (almost) infinite patience, meticulous attention to detail, and unwavering support have been instrumental in shaping this Thesis.

Jose, *The Special One*, you have been more than a supervisor, you have been a gift. Thanks for your sincere enthusiasm.

To my office colleagues and fellow researchers, your camaraderie has made this journey all the more enjoyable. Thank you for creating such a nice environment.

A special thank you to David Thompson for graciously hosting me at the University of Southampton. My time there was incredibly enriching, and I am immensely grateful for the invaluable lessons and the warm welcome from the ISVR fellows.

Likewise, Stefano Bruni, thank you for kindly hosting me at Politecnico di Milano and for all your indispensable help. Additionally, I'd like to express my heartfelt appreciation to my colleagues in Milan, *che piacere conoscervi!*

To my friend Adrián, for your unique way of supporting me. To my parents and brother, *mis compañeros de vida*, thank you for absolutely everything. And to Milena, *minha pessoa favorita*, you appeared in my life to make it easier and funnier.

Lastly, I am grateful to the Spanish educational system for providing me with the opportunities and resources to pursue my academic aspirations to the fullest.

Contents

List of abbreviations

2D	Two-dimensional
3D	Three-dimensional
BE	Boundary Element
BEM	Boundary Element Method
CLD	Constrained layer damping
DoF	Degrees of freedom
EoM	Equation of motion
FE	Finite Element
FEM	Finite Element Method
FRF	Frequency response function
FSI	Fluid-structure interaction
MEM	Moving Element Method
RBM	Rigid body motion
rms	Root mean square
SWL	Sound power level

Part I

Thesis report

Chapter 1

Introduction

1.1 Motivation

Railways are an efficient, safe, and environmentally friendly mode of transportation. In Europe, the railway industry has played a pivotal role in the movement of people and goods in recent years. Eurostat reports that, in 2021, railways accounted for 5.6% of passenger transport and 11.9% of freight transport within the European Union (EU) [1]. Remarkably, despite their significant contribution to the transport, railways exhibit a notably lower carbon footprint compared with other transportation modes such as cars and airplanes. According to the European Environment Agency, a mere 0.4% of transport-related greenhouse gas emissions in the EU in 2021 were attributed to railway vehicles powered by carbon-based fuel [2].

While railway transport boasts environmental advantages, it has been associated with noise problems that can significantly impact neighbouring communities, railway workers, and passengers. The detrimental impact of noise on human health has been well-documented. The World Health Organization reports the loss of at least one million healthy life years annually in Western Europe due to traffic-related noise [3]. Chronic exposure to elevated noise levels can result in various health issues, including hearing loss, annoyance, sleep disturbance, hypertension, cognitive impairment, physiological stress reactions, endocrine imbalance, and

cardiovascular disorders [4]. Moreover, railway noise is often related to vibrations, which can as well induce adverse effects on health [5, 6].

In response to these issues, the railway industry has made substantial investments to meet stringent noise emission standards aimed at reducing acoustic pollution in urban areas. Given this context, the importance of understanding and modelling the dynamics and noise generation of railway elements cannot be overstated. Accurate modelling enables the prediction and evaluation of noise levels, guiding the development of effective strategies for noise mitigation.

This Thesis contributes to the field by developing and improving comprehensive dynamic models of wheelsets and tracks, as well as their interaction. This allows the proposal of optimal designs in terms of noise emission reduction. The findings of this research aim to provide valuable insights for the design of quieter railway systems, ultimately enhancing the sustainability of railway transport and improving the quality of life for communities near railway tracks.

1.2 Railway noise sources

While the primary focus of this Thesis is rolling noise, it is essential to acknowledge that railway systems generate various types of noise, including impact noise, squeal noise, aerodynamic noise, ground-borne noise, and bridge noise, among others.

Rolling noise is the primary phenomenon under investigation in this Thesis. It is usually the most important noise source for railway operations [7], and it is produced as a consequence of the roughness of the wheel and rail running surfaces, which leads to a vertical relative motion between them. The dynamic forces induced at the wheel/rail contact cause both the wheelset and track to vibrate and radiate noise. The roughness wavelength affecting the wheel/rail interaction is typically between 5 and 500 mm [7]. Rolling noise exhibits a broad-band frequency content, extending up to approximately 6 kHz, after which the excitation falls due to the effect of the contact filter [8,9]. Fig. 1.1 provides a schematic representation of this phenomenon.

Impact noise is caused by discrete irregularities of the wheel and rail running surfaces, including wheel flats, rail joints, dipped welds, or crossings [7]. It can be considered as an extreme form of rolling noise [10].

Squeal noise is characterised by a high-frequency tonal sound, often manifesting in sharp curves. According to Thompson [7], it is unlikely on curves with a radius

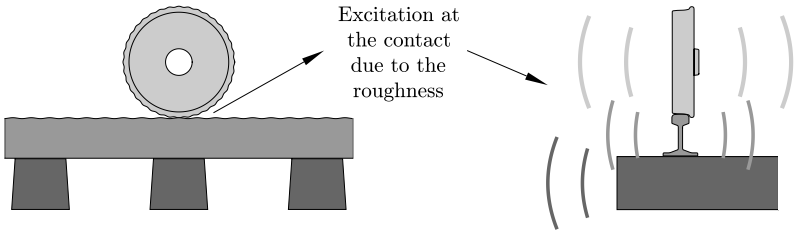

Fig. 1.1: Schematic representation of rolling noise generation.

greater than 500 m, while it is common on curves with a radius smaller than 200 m. Squeal noise is widely attributed to unsteady lateral creepage, leading to self-excited vibration of the wheel [11–14].

In contrast to the preceding sources, aerodynamic noise does not arise from the vibration of railway elements. Instead, it results from the interaction of the train with the surrounding air, particularly at high speeds. The acoustic energy radiated by this source typically concentrates below 500 Hz [7].

Ground-borne noise results from the transmission of vibrations from the track to the ground, which then propagate through the soil to the surrounding structures. This noise becomes a concern in cases where airborne noise cannot be heard, such as for buildings near tunnels. The vibration of these buildings generates low-frequency noise [7], in addition to the discomfort associated with the vibrations themselves.

Bridge noise is specific to trains running over bridges, where the vibration affects the bridge structure, increasing the acoustic radiation levels. It is characterised by a predominantly low-frequency spectrum [15, 16].

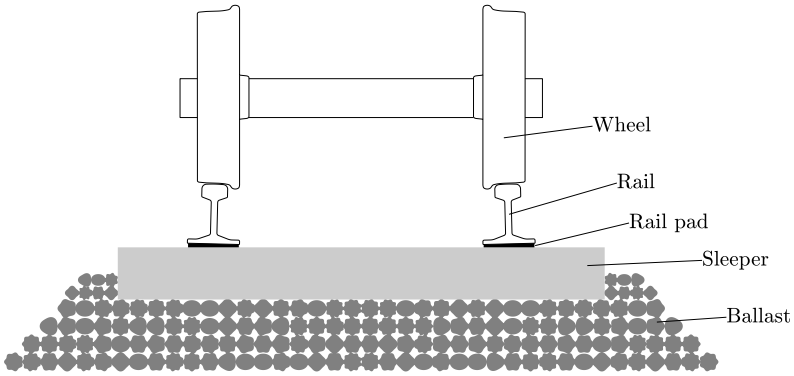

Fig. 1.2: Schematic representation of the railway elements.

1.3 Set of railway elements

In ballasted tracks, the most relevant railway elements contributing to rolling noise are the wheels, rails, and sleepers. The wheelset, comprising both wheels and the axle, is dynamically coupled with the rail through their contact interaction. Additional components such as axleboxes, brakes, and gearboxes may be partially or completely attached to the axle. The rails, made of steel, are connected to the sleepers through the rail pads, made of elastomeric materials, the function of which is to transmit the interaction forces downward. The stiffness of the rail pad plays an important role in rolling noise generation. The sleepers, typically made of concrete, wood, or steel, are discretely positioned along the running direction, providing support for the rails and distributing the dynamic loads to the foundation. The latter usually consists of a bed of stones, known as ballast, typically modelled as a viscoelastic material. Together, the rails, rail pads, sleepers, and ballast constitute the railway track. A schematic representation of a ballasted track and a wheelset is depicted in Fig. 1.2. An alternative configuration involves replacing the sleepers and ballast by a concrete slab [17], denoted as slab or ballastless track, although these are less common than ballasted tracks [7] and beyond the scope of this Thesis.

In the context of rolling noise radiation, each element exhibits a different frequency range of interest. Generally, the sleeper contributes significantly below 750 Hz, the rail between 500 and 2000 Hz, and the wheel above 1500 Hz (further details will be presented in Section 2.1). Although their sound radiation predominates in different frequency ranges, these elements are coupled between them, so that any alteration in one might affect the vibroacoustic behaviour of the others. As

a consequence, the effectiveness of mitigation measures applied to any element must be evaluated based on the total noise, which is the sum of each contribution. Therefore, a comprehensive model that considers all the elements is essential for understanding and mitigating the impact of railway rolling noise.

1.4 Objectives

The aim of the present Thesis is to achieve a better understanding of the generation of railway rolling noise and to propose effective acoustic mitigation measures. The main objectives of this work can be encompassed in the following topics:

- **Comprehensive model.** It is crucial to consider all the elements simultaneously. This objective involves developing, implementing, and validating integral models of the elements and their interaction, which allows rolling noise to be predicted accurately.
- **Influence analysis.** Before proposing mitigation measures, it is essential to understand the impact of any change on rolling noise. This comprehension is fundamental to formulate optimal designs for railway components.
- **Rolling noise in curves.** While curving is generally associated with squeal noise, it can also significantly affect rolling noise. Modelling the complex phenomena of running on a curved track is imperative for studying rolling noise in this context.

1.5 Thesis layout

This Thesis is a collection of articles. It is composed of two parts: Part I is a report that outlines the contributions of the work, while Part II comprises the resulting publications.

In Part I, following this introduction, Chapter 2 reviews the relevant literature on the studied topics. Subsequently, Chapter 3 provides an in-depth overview of the content found in the publications resulting from the Thesis. Then, Chapter 4 summarises the main conclusions and explores potential avenues for future research. Additionally, a computational tool developed in-house to support the objectives outlined in this research is conceptually described in Appendix A.

Part II features the three journal publications associated with this Thesis [18–20], addressing the following topics:

- Paper 1: A comprehensive vibroacoustic model of a wheel, track, and their interaction is implemented and validated against the commercial package TWINS [21]. The model allows the evaluation of the rolling noise emission from the sleeper, rail, and wheel when the vehicle is running on a tangent track. The paper then explores the influence of the track design on the rolling noise radiation by introducing modifications to the rail cross-section geometry and to the viscoelastic properties of the ballast and rail pad.
- Paper 2: The comprehensive model developed in the previous publication is enhanced by introducing an advanced formulation of the railway wheelset, which incorporates the inertial effects associated with its rotation through an Eulerian approach. The dynamic and acoustic behaviour of the wheel is formulated numerically in a 2D frame, while the circumferential direction is described analytically. This significantly reduces the computational demands compared with a 3D methodology, while maintaining accuracy. The proposed procedure is validated against the commercial software Ansys [22].
- Paper 3: The previous comprehensive model is extended to circulation in curved tracks, and rolling noise radiation in such conditions is investigated. The paper first presents a dynamic model of a wheelset running on a curved track, including the inertial and gyroscopic effects associated with both its rotation and curved trajectory. Subsequently, a vehicle/track interaction model during curving is proposed, formulated in the frequency domain. The paper concludes by analysing the influence of the curve characteristics on the rolling noise radiation.

Additionally, a number of Conference papers are also included in Part II, which are generally related to the previous topics.

Chapter 2

State of the art

This Thesis covers the study of rolling noise radiation following a comprehensive approach. In this Chapter, a literature review is presented for the following topics: rolling noise (Section 2.1), vibroacoustic behaviour of the wheelset (Section 2.2) and track (Section 2.3), vehicle/track dynamic interaction (Section 2.4), and acoustic mitigation techniques (Section 2.5).

2.1 Rolling noise

As mentioned earlier, rolling noise occurs during the interaction between the wheel and rail in the presence of roughness. Remington [8] conducted pioneering research on this topic, contributing to a five-part publication [8, 11, 23–25] that covered various aspects of train noise, including squeal noise, impact noise, and experimental work. Later, Remington [26, 27] proposed a comprehensive model for predicting rolling noise. This model characterised the wheel response as a ring and the rail response as a beam. As will be detailed in Section 2.4, the wheel was elastically coupled to the rail in the vertical direction and rigidly in the lateral direction.

Thompson [28–33] later extended Remington's model in various ways. The wheel dynamics was characterised using Finite Element (FE) techniques [29], and its rotation was considered [32]. On the other hand, the track dynamics was charac-

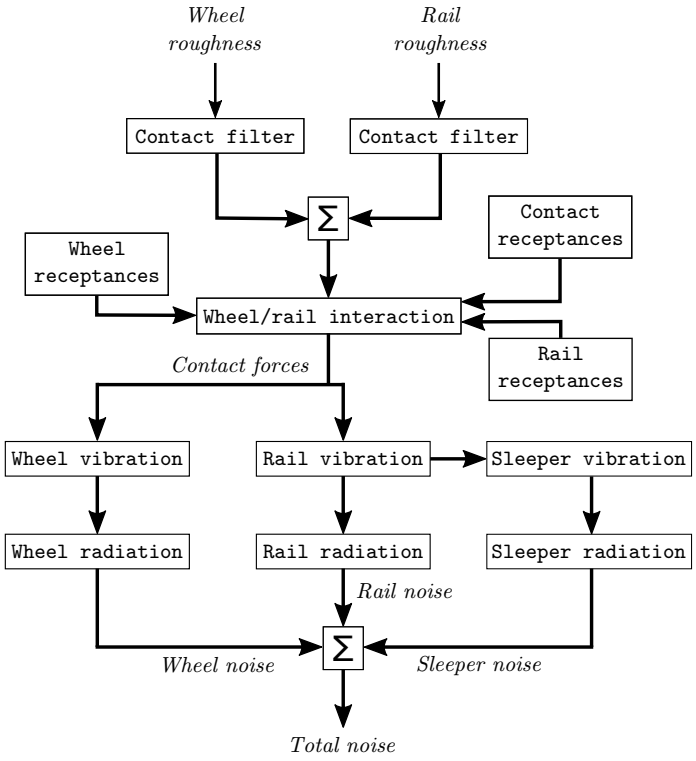

Fig. 2.1: Schematic diagram of rolling noise generation, adapted from [7].

terised using periodic structure theory [30]. The wheel was coupled with the rail in all six coordinates of space (three translations and three rotations), considering local deformations in all coordinates [28, 31]. Similar to Remington's model, the input was the wheel and rail roughness, and the output was the rolling noise radiation. Fig. 2.1 presents a schematic diagram of rolling noise generation adapted from [7]. This thesis focuses on evaluating the total sound power radiated (total noise), which is the sum of the wheel, rail, and sleeper contribution. Consequently, models for the air propagation and sound pressure field, depicted in the original diagram [7], are beyond the scope of the current investigation.

Note that the wheel and rail roughness need to be combined to evaluate the wheel/rail interaction forces. While the wheel roughness is periodic with its circumference, the rail roughness is a random phenomenon due to the passage of multiple wheels [28]. As a result, wheel and rail roughness are uncorrelated, and

their spectra can be combined through an energy sum [26] (square root of the sum of the squares of wheel and rail roughness amplitudes). The wheel, rail, and contact receptances are needed for solving the wheel/rail interaction problem, as will be explained in Section 2.4. In that section, the contact filter effect will also be described. Dynamic and acoustic models of the wheel (or wheelset) and track will be explored in Sections 2.2 and 2.3, respectively.

As highlighted in Section 1.3, the main elements contributing to rolling noise radiation are the wheel, rail, and sleeper. While the perception of this noise is a combination of all three sources, it is crucial to quantify their individual contributions for designing effective mitigation measures. Studies on source separation have identified slightly different frequency ranges of the emission attributed to each element. Bender and Remington [34] investigated the rail contribution to the total train noise, identifying its significance across most of the frequency spectrum, particularly between 500 and 5000 Hz. Later, Thompson [35] explored the influence of other elements, revealing that all sources contributed below 630 Hz, the rail dominated between 800 and 2500 Hz, and the wheel above 2500 Hz. Remington [27, 36] similarly identified the rail as the primary source between 800 and 2500 Hz, with the wheel being influential above 2500 Hz. During the development and validation of TWINS (Track-Wheel Interaction Noise Software) in the 1990s [37, 38], the sleeper was found to contribute only below 250 Hz, the rail in the low and medium frequency range, and the wheel above 1500 Hz (although this actually depends on the vehicle speed), aligning with earlier studies. Similar trends were observed in Japanese railways [39, 40], where the sleeper was observed to contribute up to 400 Hz. In another work, Thompson *et al.* [41] discovered little sleeper contribution, rail predominance between 315 and 1600 Hz, and the wheel as the primary source above 2000 Hz. However, these outcomes correspond to a track with a soft rail pad, where the rail is isolated from the sleeper and thus the vibration of the latter is small.

During the development of this Thesis, particularly in Paper 1, it was observed that the sleeper contribution is not negligible when the stiffness of the rail pads incorporated in the track increases, becoming significant up to approximately 750 Hz. Fig. 2.2 shows the radiated sound power level (SWL) by the three railway elements considering a track with a relatively soft pad (a) and a track with a stiff rail pad (b), having stiffness values of 200 and 800 MN/m in the vertical direction, respectively. The stiffness in the lateral direction for both cases is 13 times smaller than in the vertical direction. In the figure, and henceforth, the following colour scheme is employed: green for the sleeper, blue for the rail, orange for the wheel, and black for the total noise. As depicted in the curves, the sleeper contribution is minimal for the soft rail pad but is substantial for the stiff rail

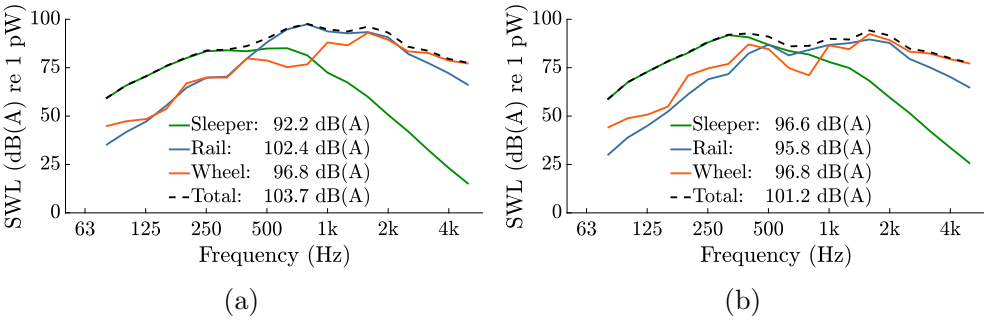

Fig. 2.2: Characteristic example of rolling noise radiation from the railway elements considering a soft (a) and stiff (b) rail pad.

pad, extending up to 750 Hz. The legend displays overall levels, calculated as the sum of the power (in watts) at each one-third frequency band, after applying the A-weighting filter [42], and later converted to the logarithmic scale (decibels). As highlighted in Section 1.3, it can be generalised that the sleeper contributes to the total rolling noise below 750 Hz, the rail between 500 and 2000 Hz, and the wheel above 1500 Hz. However, these ranges might be shortened or modified depending on the wheelset and track properties, as well as the vehicle speed and roughness spectrum.

Previously, the TWINS package [21, 37, 38] was mentioned. Nowadays, this commercial software stands as a widely acknowledged reference for rolling noise prediction. Its calculation methodology is strongly based on the developments and publications of Thompson [7, 28–33]. Further details on the TWINS model are provided in Sections 3.1 and 3.2, where Papers 1 and 2 of this Thesis are described, respectively. Moreover, this software serves as a reference point for comparison and validation of certain developments in this Thesis.

Contribution of this Thesis

This Thesis contributes to the understanding of rolling noise through a multifaceted approach. Paper 1 proposes a comprehensive model for rolling noise prediction and delves into the impact of the track design on the acoustic radiation, thereby offering valuable insights for the development of quieter railway components. Paper 2 presents an enhancement of the previous comprehensive model by developing an efficient dynamic model for the wheelset, enabling a remarkable 1000-fold reduction of the computational expenditure of the rolling noise evaluation compared with a traditional 3D FE model. Lastly, Paper 3 formulates and

analyses the generation of rolling noise in curves, presenting novel insights and revolutionary results.

2.2 Wheelset

Wheelsets are typically arranged in pairs within a structure known as a bogie, a representation of which is depicted in Fig. 2.3. Each wheelset connects to the bogie frame through the primary suspension, while the bogie, in turn, attaches to the vehicle car body through the secondary suspension. Usually, each car has two bogies. The stiffness of the primary suspension effectively isolates the dynamic behaviour of the wheelset from the rest of the vehicle for frequencies above approximately 50 Hz [43]. Thus, for the study of phenomena occurring above this frequency, such as rolling noise, a dynamic model of a single wheelset is generally used [7].

Various approaches exist for modelling a railway wheelset. References [44–46] considered the flexibility of the axle, treating the wheels as rigid bodies. However, Morys [47] argued that the wheel can be considered a rigid body only below 200 Hz. Above this frequency, the flexibility of the wheels must be accounted for. This can be achieved through a number of approaches. For instance, Szolc [48] proposed a methodology based on lumped masses to incorporate the flexibility of the wheelset. Nevertheless, with the increase in computational performance in recent years, the FEM has become the predominant technique to achieve the solution [7, 29].

As mentioned in Section 1.3, the wheel contribution to rolling noise is significant above about 1.5 kHz. In this frequency range, the wheel dynamics is roughly decoupled from the axle. In Reference [49], aiming to evaluate the noise radiation of a railway wheel, the axle is omitted and the wheel, modeled by the FEM, is constrained at the inner edge of the hub. While this provides a good approximation of the wheel contribution to the total noise, it affects the rail and sleeper contributions due to the combination of the incorrect modelling of the wheelset dynamics below 1.5 kHz and the wheel/rail dynamic coupling. To address this, Thompson [7] proposed superimposing the rigid body motion (RBM) of the wheelset on the constrained wheel vibration. This constitutes an alternative approach to a full numerical model of the wheelset, which would provide a more accurate solution but with higher calculation time. The author of this Thesis *et al.* compared both approaches in References [50, 51], and a brief description of the results will be presented in Section 3.2.

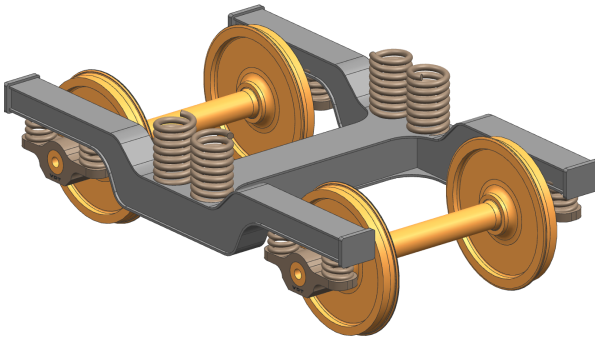

Fig. 2.3: Representation of a railway bogie.

When considering the rotation of the wheelset, resonances associated with vibration modes of multiplicity two split into two peaks [52]. Thompson [32] presented a model of a wheel in which its rotation, along with the wheel/rail interaction, was dealt with as a moving load problem; therefore, the gyroscopic and inertial effects associated with the rotation were neglected. These effects have been widely studied in rotordynamics, generally through models based on Lagrangian coordinates [53, 54]. Regarding a railway wheel, Sheng *et al.* [55] studied the response of a rotating wheel to a vertical harmonic wheel/rail force, using Lagrangian coordinates. When the rotating structure interacts with a fixed body, the use of Eulerian coordinates is more convenient, as the contact generally occurs at a constant spatial position with respect to an inertial frame. Fayos *et al.* [56] presented the equation of motion (EoM) of a wheelset in Eulerian coordinates, although it was initially developed in Lagrangian coordinates and converted afterwards. Later, Martínez-Casas *et al.* [57] developed the EoM of a 3D wheelset using an Eulerian approach, assuming a straight trajectory of the vehicle. When a wheelset describes a generic trajectory (for example, a curve), new inertial and gyroscopic effects influence its dynamics. Martínez-Casas *et al.* [58] extended their previous publication (Reference [57]) by including the effects associated with circulation on a curved track.

The axial symmetry of a railway wheelset leads to a periodicity of the displacements along the circumferential direction. This allows a Fourier expansion to be performed, resulting in an analytical description of the dynamics in such direction [59, 60], technique denoted as axisymmetric approach in this Thesis. This methodology was used, for example, in the aforementioned work by Sheng *et al.* [55]. Regarding the use of Eulerian coordinates, Baeza *et al.* [61] applied an axisymmetric approach to the work in Reference [57] to calculate the modal

properties of the wheelset and showed a significant reduction in the computational calculation time. Again, the previous works implicitly considered the motion of a wheelset on a tangent track. To the author's knowledge, an axisymmetric model of the wheelset including the inertial effects of a non-straight trajectory has not been published before the developments carried out in this Thesis.

In relation to the sound radiation of a railway wheel, two different approaches are distinguished for its calculation. On the one hand, there are methodologies based on the resolution of the fluid-structure interaction (FSI) problem, which solve the pressure field around the wheel. On the other hand, there are formulations based on the use of radiation ratios [62], which do not require solving the pressure field around the radiating object. An example of the first group is Reference [63], where a methodology based on the Boundary Element Method (BEM) was proposed to solve the FSI problem and to evaluate the wheel radiation considering ground reflections. While the methodologies of the first group are more accurate and generally allow the consideration of complex phenomena such as ground effects, the associated calculation time is notably higher. About the second group, the model proposed by Thompson [49] has been established as a reference. In his work, Thompson presented a series of radiation ratios based on the geometry of a railway wheel to evaluate its noise emission.

Contribution of this Thesis

In the present Thesis, different treatments are given to the railway wheelset. In Paper 1, a wheel constrained at the inner edge of the hub is considered, without superimposing the RBM of the wheelset. Although this approach is not convenient for predicting track noise, it does not alter the outcomes of the work. The wheel modal properties are calculated through a 3D model of the body, and its rotation is not included. Sound radiation is evaluated using the model proposed by Thompson based on radiation ratios [49]. Thus, there is no novelty in relation to the wheel treatment.

In Paper 2, a railway wheel constrained at the hub plus the RBM contribution of the wheelset is considered, the latter being described analytically. The effects of the rotation of the wheelset are included using Eulerian coordinates, thus facilitating the numerical solution of its interaction with the track. An axisymmetric approach is applied to the wheel dynamic response, allowing the sound radiation to be formulated in a 2D frame, which is evaluated using the acoustic model of Thompson [49]. Two main novelties are proposed in the paper related to the wheelset model: an analytical model for the rotating wheelset RBM along with its noise contribution and a 2D formulation of the wheel noise.

In Paper 3, a numerical model of a railway wheelset is presented. Its EoM when describing a generic trajectory is developed, including the inertial and gyroscopic effects associated with a non-tangent circulation. Its rotation is also taken into account using Eulerian coordinates. An axisymmetric approach is applied to the body, formulating the dynamic and acoustic behaviour of the wheelset in a 2D frame. As before, the sound power is calculated through the model of Thompson [49]. The main novelty in this work regarding the wheelset is the development of an axisymmetric model of this body when it describes a generic trajectory to study rolling noise in curved tracks.

2.3 Track

Two types of railway track are distinguished: ballasted and slab track. The configuration of the former is described in Section 1.3, and a representation of it is provided in Fig. 1.2. In slab tracks, also known as ballastless tracks, the sleepers and ballast are replaced by a concrete slab [17]. In general, these are less common than conventional ballasted tracks [7].

In the context of modelling, the railway track, due to its extensive length, is often treated as an infinite structure [30, 64, 65]. However, 3D models in the time domain, while being able to account for non-linearities like those at the wheel/rail contact, are inherently finite. This finiteness introduces wave reflections at the ends, a problem that could be mitigated by modelling an extended track length to allow waves to decay before reflection. Due to the high computational effort associated with large models, alternative techniques have been proposed such as the modification of the ends of the rail to recreate non-reflective boundaries [66] or the attachment of two semi-infinite tracks at both sides of a finite track model to provide an infinite boundary condition [67].

On the other hand, frequency domain models offer an advantage by being able to represent the track as infinite. Since the track is an infinite waveguide structure, one can take advantage of the wave propagation theory and describe its vibrational response as a superposition of waves. These are characterised by their waveshape and wavenumber, which are defined in the frequency domain. Using this approach, Thompson [7] introduced a track model considering the rail as a continuously supported beam using Euler-Bernoulli and Timoshenko formulations. When the support structure is continuous, i.e. the track cross-section is assumed to be constant along the longitudinal direction, 2.5D FE models can be used to consider the rail cross-section deformation [64, 65]. In these models, the track cross-section is described numerically through an FE discretisa-

tion, from which the wave properties are evaluated. The longitudinal direction is then solved analytically as a summation of wave contributions through an inverse Fourier transform over the wavenumber. Another approach proposed by Thompson [30] involved evaluating the wave properties from a short 3D slice of the track (an arbitrary length of 10 mm was used). This was based on the developments of Mead [68], where an infinite periodic structure was modelled by analysing a period of it using FE techniques. This concept is based on periodic structure theory and it can be applied to a periodically supported track, assuming a uniform sleeper spacing. A more general approach includes modelling the rail supports as external forces [69, 70], allowing independent descriptions of the rail and its supports.

Concerning the rail, an Euler-Bernoulli beam provides a suitable and accurate representation for modelling its vertical dynamics up to 500 Hz [7]. Beyond this frequency, the influence of shear deformation and rotational inertia becomes significant. While the Timoshenko beam formulation takes into account these effects, it lacks the representation of deformation within the cross-section, thereby limiting the maximum analysable frequency. According to Knothe and Grassie [71], this limitation is around 2.5 kHz when focusing solely on vertical and longitudinal vibrations. However, for lateral motion, the limit is lower due to the greater flexibility of the rail web, being established at approximately 1.5 kHz [7]. Beyond this threshold, it becomes imperative to use a model that considers cross-section deformation. Wu and Thompson [72–74] proposed an approach involving the connection of two infinite Timoshenko beams representing the head and foot of the rail, respectively. A better description of the rail cross-section can be achieved through the use of numerical techniques. A traditional FEM analysis of the rail, while addressing the aforementioned issues, introduces the previously explained problems associated with a finite model. To consider both the infinite nature of the rail and the cross-section deformation, the models explained in the preceding paragraph have been used [30, 64, 65, 68–70].

Since the vehicle is running on the track, the interaction forces move along the length of the rail. Koh *et al.* [75] introduced the Moving Element Method (MEM), a novel approach based on the FEM principles but formulating the governing equations in a coordinate system moving with the vehicle. In their work, the rail was modelled as an Euler-Bernoulli beam supported on a viscoelastic foundation. This method was later extended to a 3D rail by Martínez-Casas *et al.* [76], considering also the cross-section deformation. While the MEM efficiently captures the vehicle motion, Thompson [7] demonstrated that, under normal operating conditions, the influence of the load motion has a limited impact on the noise radiation of a continuously supported rail.

Continuously supported rails are characteristic of slab tracks, which, as mentioned earlier, are generally less common than ballasted tracks. In the latter, rails are discretely supported by sleepers, fact that theoretically introduces differences with respect to the continuously supported case, such as the pinned-pinned resonance. However, Thompson [7] found that, in terms of noise radiation, this resonance is not significantly influential. Additionally, in the practice, sleeper spacing is non-uniform [77]. Wu and Thompson [78] proved that accounting for dispersion of the sleeper spacing results in spatially averaged vibrations (strongly correlated with acoustic power) that resemble those from a continuously supported rail. Consequently, for noise prediction, a model of a rail continuously supported on rail pads, sleepers, and ballast is commonly used [37, 38]. In this case, the properties of these three components are distributed per unit length, considering the sleeper span.

The stiffness of the rail pad plays an important role in noise radiation [79]. As outlined in Section 1.3, the rail pad distributes loads from the rail to the sleeper. Although it is not mentioned in that section, rails are held against the sleepers through spring clips [7], with the rail pad being in between. This fastening system introduces a preload on the rail pad, significantly influencing its stiffness [80]. Additionally, due to the rail pad material (elastomers), the dynamic value of the stiffness for high frequencies (dynamic stiffness) differs from its static value [81]. Hence, the rail pad stiffness exhibits a non-linear behaviour. Thompson *et al.* [80] found that the dynamic stiffness of the rail pad has a weak dependence on the frequency but is significantly affected by the fastening preload. The study also suggested that hysteretic (structural) damping is a suitable approximation for the dissipative properties of the rail pad.

Regarding the sleeper modelling, the simplest approach is to treat it as a mass, which is valid up to 1 kHz according to Knothe and Grassie [71]. Instead, a beam model can be used to capture its flexibility. Grassie [82] proposed a Timoshenko beam to describe the dynamic behaviour of an unsupported sleeper. Later, Thompson [7] extended the formulation by considering the support on the ballast. In his work, Thompson found that while a mass model of the supported sleeper tends to underestimate the noise, a beam model significantly overestimates it at the beam resonances when assuming a constant ballast stiffness.

The ballast, consisting of a layer of stones, exhibits non-linear properties due to a number of factors such as the material characteristics and the interactions between the stones. Thompson [7] highlighted its frequency and load-dependent nature. Given the ballast configuration, high dispersion in its properties is expected. Wu and Thompson [78] investigated the influence of variations in the ballast stiffness on the track dynamics, with a dispersion characterised by a standard deviation

of 40% of the mean value. It was observed that the track response was affected only below 300 Hz, with a negligible impact on the track decay rate, which is associated with the noise radiation.

Within the track structure, both rails and sleepers contribute to rolling noise. Similar to the wheel, Boundary Element (BE) techniques serve as an approach to solve the problem and to assess the acoustic emissions from these elements. Taking advantage of the infinite length of the rail, Nilsson *et al.* [83] combined a wave FE approach for the dynamics with a BE formulation for the acoustics. This BE based-technique was initially proposed by Duhamel [84] and it involves a numerical description of the structure cross-section and a expansion in the wavenumber domain for the longitudinal direction. An alternative approach for the calculation of the rail sound emission considers 2D transversal radiation of the rail cross-section, expanding the solution along the longitudinal direction by accounting for the decay rate of the structural waves. However, since the vibration is not uniform along the longitudinal direction, corrections on the acoustic results are needed to consider the 3D nature of the sound radiation [85]. Commonly, radiation ratios are used to predict this 2D radiation of the rail cross-section [7]. The TWINS package [21] also offers an alternative model based on equivalent acoustic sources. These (imaginary) sources are designed to generate an air velocity around the rail contour as similar as possible to that produced by the structural vibration.

The BEM has found application in assessing the sleeper noise as well. Zhang *et al.* [86] used a 3D BEM to calculate the radiation from multiple sleepers simultaneously. Their findings indicated that above 300 Hz the distance between sleepers is sufficiently large compared with the acoustic wavelength, allowing the radiation from each sleeper to be treated independently. According to Thompson [7], the sound radiation of a vibrating sleeper resembles that of a flat rectangular surface in a plane baffle. Consequently, the acoustic emission from such a sleeper can be predicted using simple radiation ratios. The model based on equivalent sources mentioned earlier can also be applied in TWINS to evaluate sleeper noise radiation.

Contribution of this Thesis

Regarding the treatment of the track in this Thesis, a similar approach is considered in all three papers. The rail is modelled in the frequency domain as an infinite 3D structure, incorporating the flexibility of the cross-section through FE techniques and periodic structure theory [30]. Despite considering a ballasted track, properties of the rail pad, sleeper, and ballast are distributed per unit length,

resulting in a continuous support, although wave propagation through the foundation is not permitted. The motion of the interaction forces due to the vehicle speed is neglected. The sleeper is modelled as a mass and the frequency-dependent behaviour of the rail pad and ballast stiffness is not considered; instead, constant values are employed. Hysteretic damping is assumed to model the dissipative properties of both elements. The acoustic power of both the rail and sleepers is evaluated using the aforementioned model based on equivalent sources.

In Papers 1 and 2, one rail and half a sleeper are modelled. In Paper 3, in contrast, both rails and the full length of the sleeper are considered, given the asymmetric nature of the interaction forces resulting from the curving behaviour. The notable contribution of this Thesis to the track modelling lies in the integration of the acoustic formulation based on equivalent sources with a complete track model. This is done in Paper 3 and briefly described in Section 3.3, where further details are provided.

2.4 Vehicle/track interaction and contact problem

In this section, models of the vehicle/track interaction are explored, with a specific focus on the phenomenon of rolling noise radiation. The main excitation mechanism leading to this type of noise is the roughness present on the wheel and rail running surfaces [7], which introduces a relative displacement between these elements.

As discussed in Section 2.2, the primary suspension isolates the dynamic behaviour of the wheelset from the rest of the vehicle within the frequency range relevant to rolling noise radiation. Both wheels of a wheelset and both rails of the track exhibit small-scale undulations (roughness) on their rolling surfaces. According to Thompson [7], it is reasonable to assume that the roughness on both sides is uncorrelated for wavelengths shorter than about the sleeper spacing (typically 0.6 m). Since wavelengths of interest for rolling noise are generally shorter than this limit [87], the interaction of each wheel/rail pair in the presence of roughness can be independently solved (two load cases). In the context of rolling noise, the corresponding sound powers associated with each load case can then be combined.

Railway vehicles are equipped with multiple wheels that interact with the rails. In contrast to a single wheel/rail pair, two main differences are emphasized [7]: (1) interaction forces on the rail from several wheels may interfere between them and (2) the rail vibration may be influenced by having multiple wheels supported on it. Wu and Thompson [88, 89] investigated both effects and proved that multiple

wheels exciting the rail can be treated as incoherent sources above 20 Hz when the vibration or noise is analysed in one-third octave bands [88]. Additionally, their research indicated that the average rail vibration and noise are not significantly affected by having a series of wheels on it [89]. With these insights, the vehicle/track interaction problem, specifically concerning rolling noise radiation, can be simplified to a series of single wheel/rail interactions.

A pioneering wheel/rail interaction model for comprehensive rolling noise evaluation was introduced by Remington [26, 27]. In his work, Remington treated the wheel and rail as two dynamic systems, each connected vertically to a roughness through a spring. The springs represented the local or Hertzian deformation in the wheel and rail when pressed together. The lateral coupling between the wheel and rail was modelled as rigid. Instead of describing the motion of the wheel, Remington assumed that the roughness moved in the opposite direction. Taking advantage of continuity in the contact, he established relations among wheel and rail displacements, local deformations, and roughness. Integrating these with the wheel and rail frequency response function (FRF), he derived the relation between the roughness (input) and the resulting interaction force at the contact (output).

Later, Thompson [28, 31] expanded Remington's model by coupling the wheel and rail in all six coordinates of space (three translations and three rotations). A schematic representation of this interaction model in the vertical direction is depicted in Fig. 2.4. Thompson also refined the formulation and presented the interaction model in a general form, enabling the consideration of other excitation mechanisms. Moreover, local deformations occurring at the interaction region in all six coordinates were incorporated. Today, Thompson's model is widely acknowledged as a reference for wheel/rail interaction models, particularly in the context of rolling noise prediction.

In Thompson's formulation [28], the interaction forces are also computed based on a roughness input. The roughness is typically defined in the wavenumber spectrum, representing the corresponding amplitude for a given wavelength, with the frequency spectrum being obtained as a function of the vehicle speed. The wheel/rail contact is assumed to occur at a point, so that, in principle, any wavelength excites the system. Since the contact patch is instead an area, roughness wavelengths significantly shorter than a characteristic length of the contact patch have limited impact on exciting the wheel/rail, this phenomenon being known as the contact filter effect [7]. Remington [8] proposed an equation to model this effect for a circular contact area, resulting in a function that filters the roughness based on the contact patch radius. Later, Thompson [7] presented a simplified expression for the contact filter, only requiring algebraic operations. Achieving more

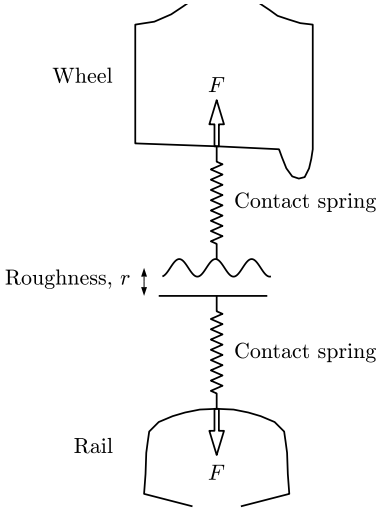

Fig. 2.4: Schematic representation of Thompson's interaction model, adapted from [28].

precise descriptions of the contact filter effect requires numerical methodologies that directly assess the contact forces.

Regarding the local deformations at the contact interface, Thompson [31] related them to the interaction forces (and torques) in the frequency domain using a 6×6 receptance matrix of the contact. In the contact region, the normal direction is assumed to be decoupled from the tangential ones. The normal problem can be solved using Hertz theory [26, 31, 90], where the contact area is considered an ellipse and the normal force is described as a non-linear function of the interpenetration. To formulate the problem in the frequency domain, the normal contact receptance is obtained by linearising the force-interpenetration relation about the steady-state normal load of the vehicle.

Similarly, compliance also exists for the tangential directions [7, 91]. In addition, there is relative motion between the wheel and rail in the contact region, known as creepage [92–94], which generates tangential forces (creep forces). Kalker [95] developed a linear theory for rolling contact, establishing a linear relation between creepages and creep forces through a number of coefficients, denoted as the Kalker's coefficients. However, while the creepages define the overall relative velocity, there are simultaneously regions of adhesion and slip within the contact area [7]. For large slip regions, the creep forces differ from the description given by Kalker's linear theory [95]. In the extreme case of the slip region covering the

entire contact area (saturation of creepage), the creep forces follow Coulomb's Law of Friction as μF_0, with μ being the friction coefficient and F_0 the vehicle normal load. Notably, this expression is independent of the creepages, requiring a non-linear relation to describe the creepages-creep forces relation when the slip region is not small. Kalker [96] developed an exact rolling contact theory and a numerical methodology called CONTACT to solve the creep forces.

While CONTACT is the most accurate solution, it requires a high computational effort. For this reason, simpler approximate models have been proposed as alternatives. Vermeulen and Johnson [97] introduced a heuristic law defining a non-linear relation between creep forces and linear creepages (relative linear velocities) to account for non-small slip regions. Shen *et al.* [98] extended the previous model by including the effect of the spin creepage (relative rotational velocity), although their approach was only valid for small spin values. In these models, the magnitude of the creep force vector is modified based on the creepages values, but the direction always aligns with that of the linear creep forces, even for significant creepage saturation [99]. This last reference proposed a slight modification of the aforementioned Shen, Hedrick, and Elkins' model [98] to consider the correct creep force vector direction in case of saturation of creepage (opposite to the relative sliding velocity). These three models [97–99] are approximate solutions relying on heuristic laws defining the saturation of creepage. In contrast, Kalker [100] proposed an approximate numerical solution of the exact theory denoted as FASTSIM, which is approximately 400 times faster than CONTACT [101].

The approximate models presented in the previous paragraph predict steady creep forces resulting from the relative motion in the contact region. However, these models do not describe the dynamic behaviour of the creep forces due to small oscillations of the creepages. While the CONTACT methodology, based on the exact theory, can capture non-steady behaviour, its high computational cost penalises its use. Knothe and Gross-Thebing [102] proposed a linear relation between creep forces and creepages, where the Kalker's coefficients were complex values dependent on the frequency to take into account the dynamic nature of the forces. Later, Thompson [7, 33] introduced approximate expressions for these coefficients through parameter fitting. Nevertheless, this model considers small oscillations of the creepages about a steady-state condition with zero values of creepages, which, as explained previously, is not valid for non-small slip regions. Subsequently, Gross-Thebing [103] extended the model to obtain the complex coefficients when non-zero steady-state values of the creepages are present.

Contribution of this Thesis

Concerning this Thesis, the wheel/rail interaction model proposed by Thompson [28] is used in all three contributions. However, the description of the tangential local deformations at the contact interface differs slightly in the last contribution. For the normal direction, Hertz theory is always applied. In Papers 1 and 2, where a vehicle running on a tangent track is implicitly considered, the creepages are known to be small. Consequently, Kalker's linear theory is valid in these contributions. To take into account the dynamic nature of the force, Kalker's complex coefficients proposed by Knothe and Gross-Thebing [102], in the simplified form presented by Thompson [7, 33], are considered.

In Paper 3, the curving behaviour of the vehicle is described. In these conditions, the creepages might be large, i.e. the slip region might not be small, and therefore the model proposed by Gross-Thebing [103] is used instead. The methodology to obtain the contact receptances, which are linearized about the steady-state regime, is described in detail in the paper. Additionally, Thompson's interaction model [28] is extended to consider the effect of the contact angle, leading to a coupling of vertical and lateral vibrations of the wheels and rails.

2.5 Mitigation measures

It has been shown that the main elements involved in the rolling noise radiation are the sleeper, rail, and wheel. Additionally, their contribution typically have different frequency ranges of predominance. In the overall noise (sum of energy at each frequency band), the relative importance of the elements depends on complex factors such as their dynamic behaviour, vehicle speed, and roughness spectrum. However, in general terms, the three elements have a non-negligible contribution to the overall noise.

An interesting example is proposed where the three elements have the same contribution to the overall level. If all the resources are allocated towards the mitigation of just one component, and assuming that the measures are effective enough to reduce its contribution to zero, the total overall noise would only decrease by 1.8 dB(A) (the logarithm nature of the decibel scale can be confusing). Instead, the same total mitigation can be achieved by reducing 1.8 dB(A) the radiation of each element, which sounds more realistic, as making an element completely silent might be impractical. To visualize this, the example of Fig. 2.2(b) is established as a reference in Fig. 2.5. If the sleeper sound radiation is completely mitigated, Fig. 2.5(b), the total overall noise is reduced by 1.9 dB(A) (not 1.8 dB(A) as before because the three contributions are not exactly the same in the

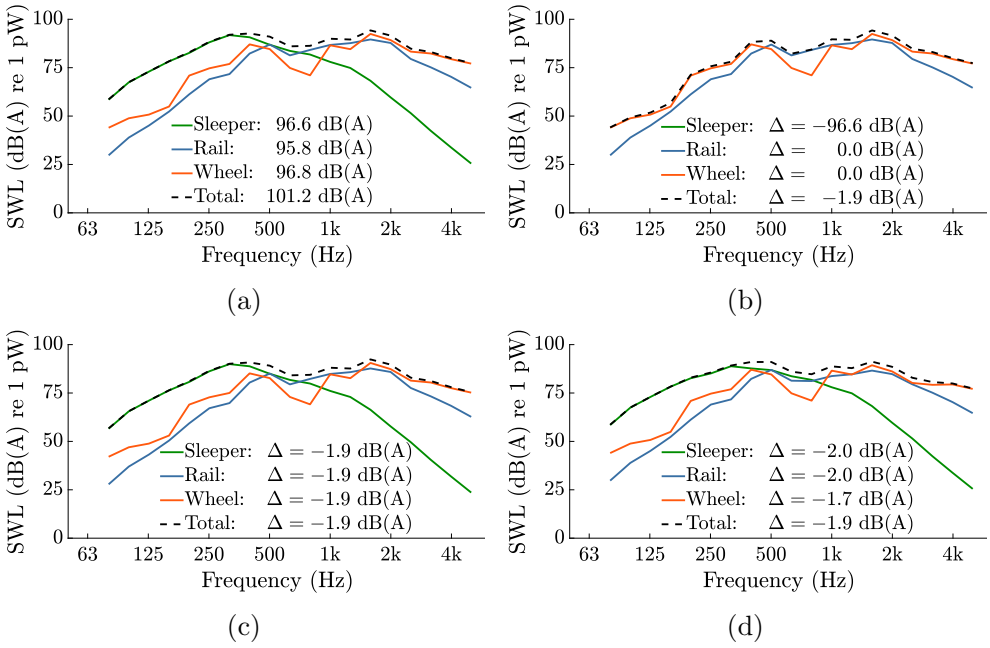

Fig. 2.5: Representative example of different mitigation strategies. (a) Reference case. (b) Complete reduction of the sleeper noise. (c) Even mitigation of the three elements in all the frequency spectrum. (d) Strategic mitigation of the three elements at specific frequency ranges.

reference case). Alternatively, a strategy where the acoustic emission of all three elements is reduced by 1.9 dB(A) is proposed in Fig. 2.5(c), achieving the same total overall noise. This highlights the importance of applying multiple mitigation measures simultaneously when the overall SWL of the three elements is similar.

While targeting the reduction of levels for all three elements simultaneously may be more effective than focusing on just one of them, attempting to do so across the entire frequency spectrum is not the most efficient strategy. In the previous example (Fig 2.5(c)), the three sources were uniformly reduced by 1.9 dB(A) across all frequency bands. A comparable overall mitigation can be achieved by strategically focusing on specific frequency ranges for each element. For instance, in Fig. 2.5(d), the levels were modified by reducing the sound power by 3 dB(A) in the following frequency ranges: 220-450 Hz for the sleeper, 710-2240 Hz for the rail, and 1410-3550 Hz for the wheel. This targeted approach allows for the same mitigation outcomes with potentially less effort. The effectiveness relies on the fact that the elements exhibit distinct frequency ranges of predominance.

Hence, it is more rewarding to reduce their radiation in a specific range where the mitigation is impactful, considering the masking effect of the other elements. Depending on the reference case (without mitigation measures applied), an efficient technique can be designed based on the frequency ranges of predominance for each element.

To ensure the effectiveness of the noise mitigation process, it is crucial to focus on reducing the total level, which is the actually perceived noise. While considering the three railway elements in the mitigation process is important, solely relying on this might mislead the design of an efficient mitigation strategy. A straightforward yet effective guideline is to flatten the peaks of the total noise curve, aiming to create a plane spectrum.

Revisiting Fig. 2.2(b), the flattening strategy is explored in Fig. 2.6. Each row of the figure represents a different mitigation technique, considering only the total noise by now. Notably, the SWL exhibits two broad 'bumps' with high levels, one on the left side of the spectrum (220-560 Hz) and the other on the right side (890-2240 Hz). The first strategy, as shown in Fig. 2.6(a), aims to reduce the left-side bump to varying degrees, revealing that the incremental mitigation diminishes as the curve descends. The interpretation of this trend becomes easier when the sound power is represented in a linear scale, as in Fig. 2.6(b). The second row follows an analogous process, focusing on the right-side bump, and exhibits similar trends. Incremental mitigation diminishes as soon as the targeted bump has lower levels than any other non-modified peak in the spectrum. Therefore, the flattening technique aims at sequentially reducing the highest peaks. The third row illustrates an example of this method, exhibiting more favourable results in terms of overall noise mitigation. Consequently, Fig. 2.6(e) represents the desired spectrum for the total noise after implementing a set of mitigation measures.

While the three railway elements generally have predominance in different frequency ranges, they are dynamically coupled. The rail and sleeper are connected through the rail pad while the wheel and rail are coupled through their interaction, thus indirectly connecting the wheel and sleeper. Consequently, any alteration to one element may impact the others, a crucial consideration when designing techniques to reduce the acoustic radiation from individual elements, as these measures might even yield negative effects on the total overall noise.

To summarise, the following key points should be borne in mind during the design of mitigation measures:

- The primary objective must be to reduce the total acoustic radiation.
- Awareness of the reference (unmitigated) noise spectrum is fundamental.

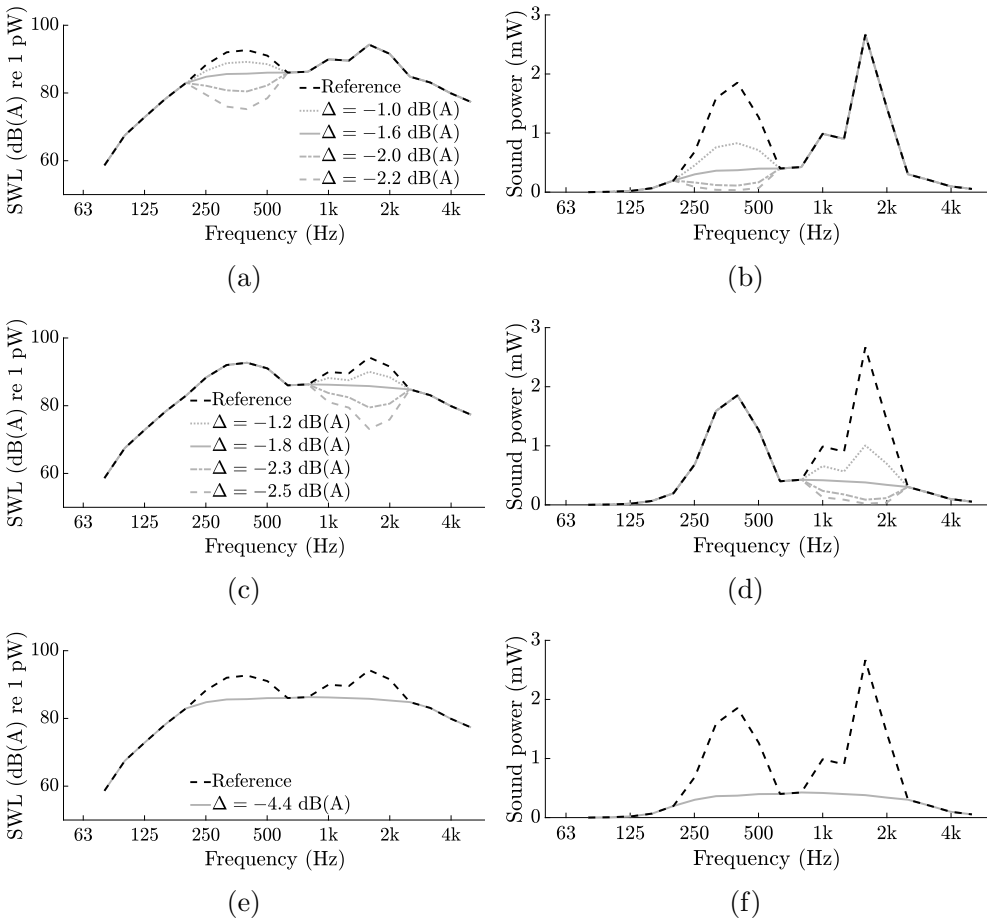

Fig. 2.6: Incremental mitigation when flattening the peaks in the SWL curve. Left column: SWL in decibel scale. Right column: sound power in linear scale. First and second row: individual mitigation. Third row: result of the flattening technique.

- Addressing the noise emission from all three elements simultaneously is generally more effective than focusing on a single element.
- Each element generally contributes within different frequency ranges.
- Efficiency is gained by concentrating resources in the frequency range where an element predominantly contributes.

- The impact of reducing the overall SWL in a specific frequency range is limited, especially if the highest peak occurs elsewhere.
- The dynamic coupling of the three elements requires the evaluation of the mitigation measures on the total noise (sum of the sleeper, rail, and wheel radiation).

The analysis presented above is purely theoretical, offering basic guidelines for effective rolling noise mitigation. The subsequent paragraphs delve into different techniques employed in the literature to reduce the railway noise levels, illustrating the complexity of the mitigation process.

Roughness

By now, it is known that the most effective approach to mitigate rolling noise is to address the radiation from the three railway elements (sleeper, rail, and wheel) simultaneously. A direct method to achieve this is to target roughness, which influences greatly all elements. The SWL is proportional to the square of the combined roughness amplitude, indicating that substantial changes can be accomplished by intervening in this aspect. As mentioned in Section 2.1, the combined roughness is derived as an energy sum of the wheel and rail components. Similarly to the SWL, if a dominant component exists in the combined roughness, alterations to this will have a more pronounced impact. While both components can be dominant, the range of roughness levels is broader for the rail [7]. Hemsworth [104] highlighted in the late 70s the impact of the braking system on the roughness growth and acoustic radiation, reporting substantial noise reductions, up to 10 dB, by transitioning from cast-iron block brakes to disc brakes, attributed to the presence of corrugations on the running surface of wheels equipped with the former [7], as depicted in Fig. 2.7. Alternatively, the use of composite block brakes has also exhibited good performance in terms of noise radiation [105]. Another strategy to reduce the SWL involves periodic rail grinding and wheel reprofiling [7].

Contact

An alternative method to influence the interaction forces, with a direct impact on all three noise contributions, involves modifications in the contact zone. Thompson [7] suggested two measures: reducing the contact stiffness and increasing the contact filter effect (refer to Section 2.4). These adjustments can be achieved by altering the wheel and rail transverse profiles, although practical modifications of these variables are minimal [7, 106, 107]. The use of a rubber tyre for

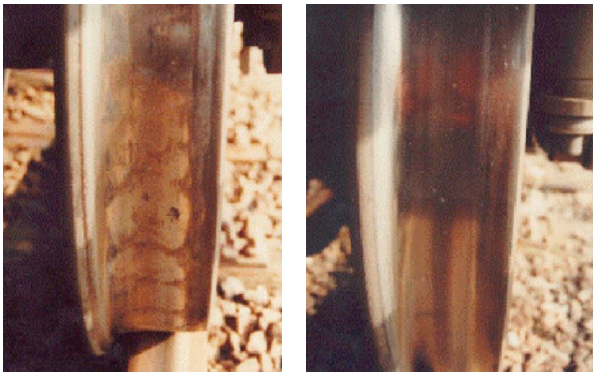

Fig. 2.7: Running surface of wheels equipped with cast-iron block brakes (left) and disc brakes (right), extracted from [7].

the wheel can effectively implement both concepts, but it introduces challenges such as safety concerns and increased rolling resistance (leading to higher energy consumption) [7].

Shape

Optimising the wheel geometry to minimise rolling noise radiation involves three principles [108]: increasing symmetry to reduce radial-axial coupling, minimising radiating surface, and raising natural frequencies above the range of interest (where interaction forces abruptly decay due to the contact filter effect). For increased symmetry, a straight web would be preferable, but it is not compatible with cast-iron block brakes due to thermal loading (curved webs dissipate heat better) [7]. Nevertheless, even a straight web wheel exhibits tread asymmetry due to the flange. One proposed solution to compensate for this is to add extra mass (about 47 kg) to the inner edge of the tyre on the opposite side to the flange, as depicted in Fig. 2.8(a), resulting in a 3 dB reduction in the wheel noise [109,110]. Reducing the wheel diameter achieves the dual purpose of increasing natural frequencies and reducing radiating surface, although diameter changes are limited for practical reasons. Studies by Nielsen and Fredö [111] and Garcia *et al.* [112,113] found geometric optimisation solutions with small diameters, straight and thick webs, and large fillet radii, as represented in Fig. 2.8(b), resulting in increased natural frequencies. Similarly, Jones and Edwards [114] also showed a significant reduction of the wheel noise when considering a small and thick wheel, although in this case the track sound radiation increased by about 2 dB due to the wheel/rail

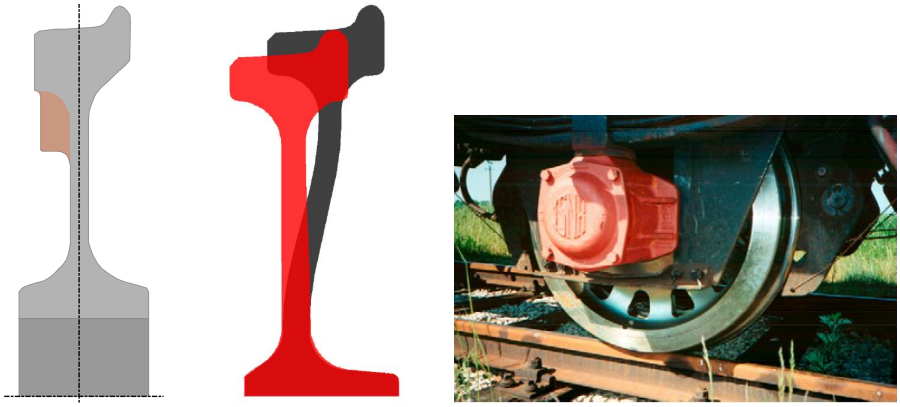

(a) (b) (c)

Fig. 2.8: (a) Wheel with extra mass (coloured in orange) to compensate for the tread asymmetry, adapted from [109]. (b) A reference (black) and optimised (red) wheel geometries, extracted from [112]. (c) Perforated wheel, extracted from [7].

dynamic coupling. Perforations in existing wheels, as shown in Fig. 2.8(c), have also been proposed to reduce the radiated noise [115,116], aiming to create acoustic short-circuiting between both sides of the wheel web. However, the effect of this is only notable in the low frequency range where the wheel contribution is not the dominant source [7, 109].

The impact of the rail cross-section geometry on the rail dynamics is significant only above approximately 1.5 kHz (see Section 2.3). In such range, the total noise is primarily governed by the wheel radiation, the rail contribution being minor. However, changes in the rail cross-section geometry can notably influence the SWL by modifying the radiating surface and, more importantly, the radiation ratio [7]. Vincent [117] suggested that a mitigation up to 4 dB(A) in track noise can be achieved by reducing rail foot width. As will be explored in Section 3.1, results from Paper 1 of this Thesis align with the findings of Vincent [117], observing a mitigation of up to 2.4 dB(A) in the rail noise by reducing the rail foot width.

Studies by Nielsen [118] concluded that sleeper geometry has a minor impact on noise compared with the rail pad and ballast properties.

Material

Wheels are typically made of steel for structural reasons, but alternative materials have been explored for noise reduction. A design featuring an aluminium wheel web reported up to 6 dB noise reduction in the wheel radiation due to a thicker web without weight penalty [109]. Resilient wheels, which feature a rubber element isolating the web from the tread and introducing damping (see Fig. 2.9(a)), can be found in light rail and tramway applications [7, 119]. Bouvet *et al.* [120] found reductions up to 3.6 dB(A) in the total noise with the use of this type of wheel.

Analogously, the rail material is also steel for structural reasons, but modifications can be made to other track components such as the rail pad or the ballast, which have a significant impact on the track dynamics [121, 122]. A stiff ballast reduces the sleeper vibrations but increases the forces transmitted to the ground. Rail pads play a crucial role, with soft ones isolating the rail from the sleeper, thus leading to higher rail vibrations and noise, while stiff ones transmit forces and vibrations to the sleeper (see Fig. 2.2). Vincent *et al.* [79] established the optimal rail pad stiffness as the one that equals the sleeper and rail contribution (the effect on the wheel noise is small). In their work, this value was found to be about 1500-1800 MN/m in the vertical direction, which is often impractical due to mechanical constraints. To reduce track forces and damage to the sleepers and track components, relatively low rail pad dynamic stiffnesses are generally used, in the range 80-400 MN/m [7]. Since the value of the rail pad stiffness influences the relative importance of the sleeper and rail noise, the effectiveness of mitigation techniques might depend on it.

Constrained layer damping

A constrained layer damping (CLD) treatment typically involves a viscoelastic material sandwiched between two stiff plates or between the railway element surface and a stiff plate (constraining plate), as shown in Fig. 2.9(b). The constraint of the viscoelastic layer induces shear deformation of the polymeric material that dissipates energy. Thus, the vibrations transmitted from the element surface to the stiff plate are attenuated. The motion of the latter, which is in contact with the surrounding air, is the source of the noise.

Studies on the CLD treatment for railway wheels indicate promising results. Jones and Thompson [119] predicted wheel noise reductions of up to 3.8 dB(A) using a stiff plate with a 4 mm thickness. Similar research [123] found a 2.7 dB(A) reduction with a 1 mm thickness constraining plate. A recent work by Garcia-

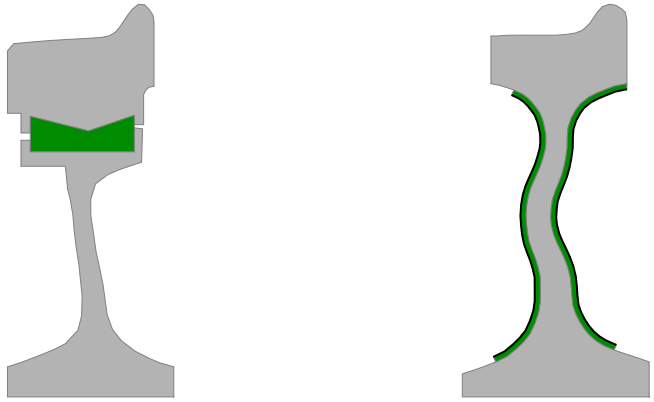

(a) (b)

Fig. 2.9: (a) Resilient wheel (rubber in green). (b) Wheel with a constrained layer damping treatment (viscoelastic material in green and constraining plate in black). Both adapted from [119].

Andrés *et al.* [124] showed about 6 dB(A) reductions in the wheel radiation using a constraining plate with 1 mm in thickness, the frequency-dependent viscoelastic behaviour of polymeric materials being represented through comprehensive models.

The application of a CLD treatment on rails has also been explored [7, 115], showing modest reductions concentrated at high frequencies even for tracks with soft rail pads. Thompson *et al.* [125] suggested that a CLD treatment on the rail would only be effective above 2 kHz, with negligible impact on total noise as this range is dominated by the wheel radiation.

Absorbers and dampers

Absorbers are devices designed to counteract vibrations from the main structure (wheel or track). Typically, absorbers are tuned around resonances to remove energy from the corresponding frequency range [7]. In their more basic form, absorbers consist of spring-mass systems without internal damping. However, they become more effective when damping is added. There are two reasons why absorbers and dampers might be more effective on the wheel than on the track [7]: the wheel is typically less damped than the track and the wheel is a finite structure with several resonances in the frequency range of interest, while the track is an infinite structure, characterised by the decay rate of the propagating waves.

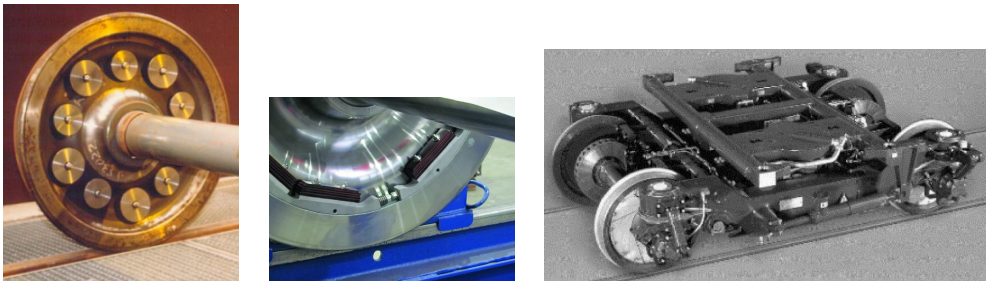

(a) (b) (c)

Fig. 2.10: (a) Tuned absorbers fitted to the web of a wheel, extracted from [7]. (b) Wheel tuned absorbers placed at the inner edge of the tyre, extracted from [126]. (c) Plate dampers mounted on the wheels of a bogie, extracted from [127].

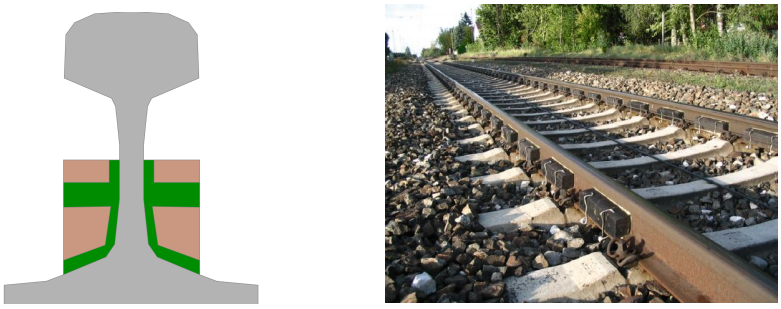

(a) (b)

Fig. 2.11: (a) Rail tuned absorber (elastomers in green and steel masses in orange), adapted from [125]. (b) Dampers attached to the rails, extracted from [128].

Nevertheless, as mentioned before, soft rail pads are commonly used to isolate the rail from the sleeper and to reduce the forces transmitted to the latter, although this decreases the track decay rate (measured at the rail). Therefore, increasing the damping of the rail through the use of absorbers and dampers can be very effective on tracks with soft pads [7].

The use of tuned absorbers on the wheel, such as those shown in Figs. 2.10(a) and 2.10(b), was found to reduce its radiation by 4-8 dB [109, 114, 126, 129]. Dampers located on the web of the wheel, as depicted in Fig. 2.10(c), were reported to mitigate 1-3 dB of the total noise [127, 130].

Similarly, Thompson *et al.* [125] proposed a design for a tuned absorber located on the foot of the rail, resulting in a 6 dB(A) reduction in the rail noise for a track with a soft rail pad. The absorber was made of two steel masses on each side of the rail attached to it through an elastomeric material, as schematised in Fig. 2.11(a). Likewise, Asmussen *et al.* [128] found mitigations up to 4 dB(A) in the total noise above 500 Hz through the use of rail dampers, located as shown in Fig. 2.11(b).

For a more in-depth exploration of the use of absorbers and dampers on the wheel and rail, refer to [7, 109].

Shields

Shielding reduces sound transmission to the receiver. A common example of shielding is the use of trackside barriers, typically located in the surroundings of neighbourhoods as a passive measure of noise control. According to Hemsworth [131], tall absorptive barriers have a maximum noise level reduction of about 20 dB(A), although they can be less effective and more costly than noise reduction at the source.

Shielding can also be located closer to the source. Wheel web screens were found to reduce the wheel radiation by about 6-8 dB [109]. Alternatively, vehicle-mounted bogie shrouds and track-mounted low barriers, when used together (see Fig. 2.12), produced reductions of 8-10 dB in the total noise [132], although a more modest mitigation of about 2 dB was found when considering a larger gap between both shields [7, 109].

Combination of measures

Combining different mitigation measures does not always result in benefits that match the sum of individual applications. If all the measures aim to reduce levels at a specific frequency range, one can end up with low efficiency (see Figs. 2.6(a) and 2.6(c)). Efficient noise reduction requires knowledge of the reference situation. With an optimal strategy, combining different measures can produce higher reductions in noise than the sum of individual ones, as depicted in Fig. 2.6(e).

Jones *et al.* [123] proposed a wheel design with an optimal shape combined with a CLD treatment. Individually, the enhanced shape reduced the wheel noise by 3.4 dB(A) and the CLD treatment by 2.7 dB(A), while the combination produced a mitigation of 5.4 dB(A). The shape changes impacted the wheel SWL almost

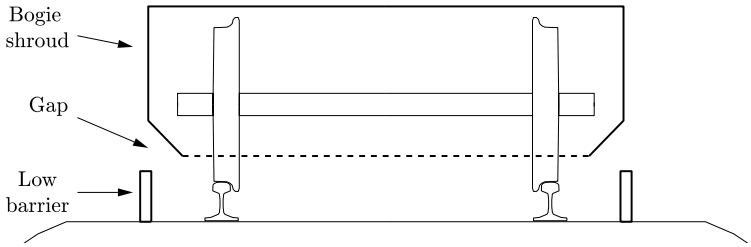

Fig. 2.12: Representation of a vehicle-mounted bogie shroud and track-mounted low barriers, adapted from [7].

in all the frequency spectrum and the CLD treatment above 2 kHz. Given the overlap in the ranges, the combination of measures did not exceed their individual effectiveness. Similarly, Bouvet *et al.* [129] proposed an optimised wheel shape together with absorbers, showing a 4.7 dB(A) reduction due to the shape and 10 dB(A) for the combination, although no information was provided about the individual effect of the absorbers. Regarding the track, Thompson and Gautier [109] summarized the effectiveness of different measures. The use of optimised rail pads and rail absorbers reduced the total noise by 3.7 dB. The individual use of optimised rail pads resulted in mitigations of 2.5 dB, but the rail absorbers were not tested separately.

Different measures acting on the same element are expected to have less effectiveness than the individual sum. On the other hand, acting simultaneously on the wheel and track might have the same or higher impact than the individual measures separately. For example, Létourneaux *et al.* [130] combined wheel ring dampers and rail dampers, finding a cumulative effect on the total noise reduction, with 2.3 dB attributed to the former and 0.9 dB to the latter. More remarkable are the results reported by Thompson and Gautier [109], in which the combination of a wheel with absorbers and a track with optimized rail pads and rail absorbers provided a mitigation of 7.1 dB in the total noise, greater than the sum of the individual measures (1 dB and 3.7 dB, respectively).

Finally, the combination of multiple measures applied on different elements can achieve a huge impact on the perceived levels. According to Oertli [133], a solution that combines composite block brakes, optimised wheels, rail tuned absorbers, rail grinding, and noise barriers would protect 95% of the population exposed to railway noise. However, other relevant factors potentially subjected

to requirements such as weight, ease of maintenance, and cost might jeopardise the implementation of these mitigation measures [7].

Contribution of this Thesis

In Paper 1, the influence of the track design on the rolling noise radiation is studied. Using a Design of Experiments (DoE) approach, parameters defining the rail cross-section geometry and viscoelastic properties of the track are investigated. The objectives include identifying significant design parameters affecting the noise radiation and quantifying their influence. This not only leads to an optimal track design but also enhances understanding of trends that minimise noise. The vibroacoustic behaviour of the elements is evaluated by means of a comprehensive model that takes into account the different couplings. The work reveals that changes in the track design can result in variations up to 7.4 dB(A) in the total sound radiation, with the rail pad stiffness being the most important parameter.

In Paper 2, an efficient wheelset model for noise calculation in tangent tracks is proposed. Although no mitigation techniques are explored, this model is suitable for its integration into optimisation algorithms aimed at designing noise reduction measures, given its minimal computational cost.

In Paper 3, the influence of a generic curve on the rolling noise is modelled and analysed. The study evaluates noise radiation on different curves and compares the associated sound levels to those corresponding to a tangent track, considering curve characteristics such as the radius, non-compensated acceleration, and superelevation. Although no mitigation measures are applied, the impact of the curve on the noise generation is analysed, which might potentially lead to increase the effectiveness of mitigation techniques for curved tracks.

Chapter 3

Description of the papers

This Thesis includes a compendium of three journal papers, presented in Part II. This chapter summarises the three articles, highlights the novelties and contributions to the state of the art, and discusses the main results.

Although the articles are deeply explored in the following sections, a brief description of them is given here, establishing the guiding thread between them.

In Paper 1, a comprehensive model for rolling noise prediction in tangent tracks is implemented and validated by comparison with reference solutions, and then the track design influence on the noise radiation is studied. To achieve this, the track is characterised through periodic structure theory and the wheel is dealt with by using the FEM. Given the low computational cost of the track model, a DoE is proposed that results in multiple calculations with different track designs. For the wheel, a 3D model is considered to evaluate its dynamic response. The high computational cost of the wheel model is significant, although it is not a limitation in this work since no modifications are proposed to this element. However, an enhanced model of the wheel would be convenient to account for changes in its design.

In Paper 2, the comprehensive rolling noise prediction model presented in the previous work is enhanced by developing an efficient vibroacoustic model of a wheel. An axisymmetric approach is performed to model the dynamic and acous-

tic behaviour of the wheel, which ultimately enables the sound radiation to be formulated in a 2D frame. The computational cost of the proposed model is approximately 1000 times lower than a 3D FEM calculation. The rotation of the wheel is considered through an Eulerian approach, which facilitates the resolution of the wheel/rail interaction problem. The model is valid for any design of the wheel (and wheelset) as long as it presents axial symmetry. However, it is implicitly assumed a straight trajectory, so that it is not valid for circulation on a curved track.

In Paper 3, a dynamic model of a wheelset following a generic trajectory is developed, thereby extending the functionality of the comprehensive calculation tool to include circulation on a curved track. The inertial and gyroscopic effects of the generic trajectory are considered in the model. To keep a low calculation time, an axisymmetric approach is perform on the wheelset response. The interaction with the track in the presence of roughness is solved in the frequency domain, considering large creepages and non-negligible contact angles.

In addition, a number of Conference papers are also included in Part II. These are generally related to the previous journal papers and contain some preliminary results.

3.1 Comprehensive model and influence of track design on rolling noise

This section provides a summary of the innovations and findings in Paper 1 of this Thesis, entitled 'Influence study of rail geometry and track properties on railway rolling noise', published in the Journal of Sound and Vibration in May 2022. Alongside the author of this Thesis (V. T. Andrés), J. Martínez-Casas, F. D. Denia, and D. J. Thompson collaborated on the paper.

As implied by the title, the study investigates how track design influences rolling noise emission. While the study considers all three elements contributing to rolling noise (sleeper, rail, and wheel), the proposed modifications focus solely on the track. The analysis incorporates the dynamic interactions between these elements considering a comprehensive modelling of the railway components in an in-house software.

Comprehensive model

The wheel dynamics is characterised by the natural frequencies and vibration modes, serving as the base for the calculation of the wheel response. This is achieved through the FEM, considering a 3D model. Two primary limitations are emphasized regarding the treatment of the wheel. Firstly, the wheel is constrained at the inner edge of the hub, a condition that, as explained in Section 2.2, does not significantly affect its dynamic response (when compared with a wheelset) within its frequency range of predominance. However, this boundary condition may not accurately represent the dynamic behaviour of a wheelset below approximately 1.5 kHz [50, 51], potentially affecting the interaction forces and track response. Secondly, wheel rotation is not considered in the model.

The track is modelled in the frequency domain using periodic structure theory [30, 68]. The rail cross-section is discretised into a number of degrees of freedom (DoF), the sleeper is modelled as a rigid solid, and the rail pad and ballast are described as massless viscoelastic materials with constant stiffness and hysteretic damping. A short segment of the track is considered to derive the waveshapes and wavenumbers, which are employed to evaluate the track dynamic response through an inverse Fourier transform over the wavenumber (a superposition of waves). This allows formulating the dynamic response of the track analytically in the longitudinal (circulation) direction, while it is solved numerically within the track cross-section.

The wheel/rail interaction is solved using Thompson's model [28]. A linearised Hertz contact spring connects the wheel and rail in the vertical direction to a roughness, the spectrum of which is obtained from standard EN 13979-1 [87]. In the lateral direction, the model proposed by Knothe and Gross-Thebing [102] is used to describe the dynamic behaviour of the creep forces. Zero values of the creepages in the steady-state condition are assumed since tangent circulation is implicitly considered. The interaction forces are calculated using the FRF of the wheel, rail, and contact, along with the roughness spectrum.

The wheel sound radiation is assessed through Thompson's acoustic model [49], which relies on the use of radiation ratios. The rail and sleeper radiation is calculated using an acoustic model based on wave propagation and equivalent acoustic sources [21], which is incorporated in TWINS.

This comprehensive model takes as a starting point the developments and publications of Thompson [7, 28–31, 33]. The same formulation is integrated into the commercial package TWINS [37, 38], subsequently used to validate the in-house tool developed in this Thesis.

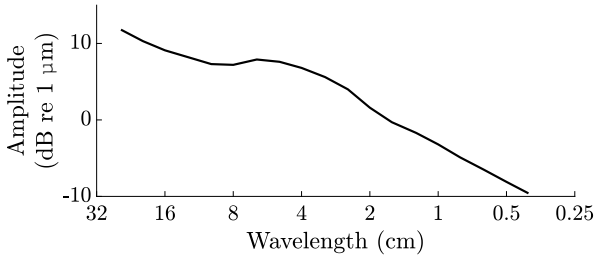

Fig. 3.1: Roughness spectrum.

Validation of the model

The implemented model is validated through comparison with TWINS [21]. The in-house comprehensive tool requires only the wheel and rail roughness as input. In this study, the roughness spectrum is defined, in its combined form, according to the standard EN 13979-1 [87], corresponding to a wheel equipped with cast-iron brake blocks (see Fig. 3.1). The calculation methodology of the implemented tool follows the diagram depicted in Fig. 2.1. The properties of the vehicle, wheel, and track used in the calculations are presented in Table 3.1. A representation of the wheel cross-section geometry is shown in Fig. 3.2. Since the study focuses on the interaction of a single wheel with the track, half of the sleeper is modelled, characterised by a trapezoidal prism geometry.

The SWL evaluated in TWINS is compared with that obtained from the in-house tool in Fig. 3.3. Remarkably, similar noise spectra are observed for all three elements, with maximum discrepancies in the overall noise levels not exceeding 0.2 dB(A).

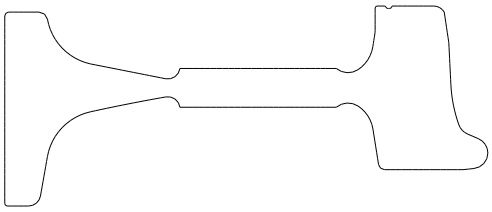

Fig. 3.2: Cross-section geometry of the wheel used in the validation.

Table 3.1: Properties of railway components used in the validation.

Vehicle	
Speed (km/h)	80
Vertical static load per wheel (kN)	50
Wheel: S1002 profile	
Material	Steel*
Mass (kg)	330
Diameter (mm)	900
Web shape	Straight
Rail: UIC60 profile	
Material	Steel*
Damping loss factor (-)	0.02
Rail pad	
Stiffness** (MN/m)	715 | 55
Damping loss factor (-)	0.4
Sleeper	
Mass*** (kg)	122
Spacing (m)	0.6
Semi-length*** (m)	0.84
Bottom width (m)	0.25
Top width (m)	0.25
Height (m)	0.22
Ballast	
Stiffness** (MN/m)	70 | 35
Damping loss factor (-)	1.5

* Young's modulus: 210 GPa. Density: 7850 kg/m^3. Poisson's ratio: 0.3.
** Format: Vertical direction | Lateral direction.
*** Corresponding to half sleeper.

Influence of track design

Once the comprehensive tool has been validated, the research aims to identify and to quantify the influence of the key design parameters of the track on the generation of rolling noise from the sleeper, rail, and wheel. Specifically, ten

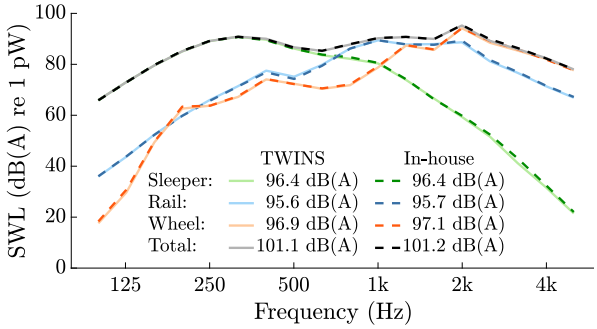

Fig. 3.3: SWL comparison between TWINS (solid line) and the implemented tool (dashed line). Case of a non-rotating wheel.

design parameters are defined: (1) height of the rail, (2) width of the rail web, (3-6) height and width of the rail head and foot, and (7-10) stiffness and damping of the rail pad and ballast. The former six describe the rail cross-section, while the latter four characterise the viscoelastic properties of the rail pad and ballast. A schematic representation of these design parameters is depicted in Fig. 3.4. A factorial design is proposed incorporating these parameters, generating numerous track designs and assessing the overall SWL using the validated calculation tool. The importance of each parameter on the acoustic emission is quantified through ANOVA techniques [134] and the methodology developed by Pratt [135].

To quantify the importance of the design parameters, a polynomial regression is fit to the noise results (dependent variable) derived from the DoE, focusing solely on the design parameters (independent variables) exhibiting statistical significance. The importance of a parameter on the noise radiation is defined as the proportion of variability in the dependent variable explained by that parameter. The cumulative importance of all the significant (contributing) parameters yields the determination coefficient (R-squared) of the regression [134], representing the proportion of variability in the dependent variable explained by the regression model.

The sleeper and rail noise exhibits considerably more variability than the wheel radiation, as the wheel properties remain unaltered. The range of noise variation observed is 11 dB(A) for the sleeper, 16.6 dB(A) for the rail, and 3.3 dB(A) for the wheel. The parameters governing the sleeper noise are the four viscoelastic properties of the rail pad and ballast. For the rail radiation, the influential parameters are the two viscoelastic properties of the rail pad and the rail foot width. As for the wheel, the rail pad stiffness and all geometric parameters defining the

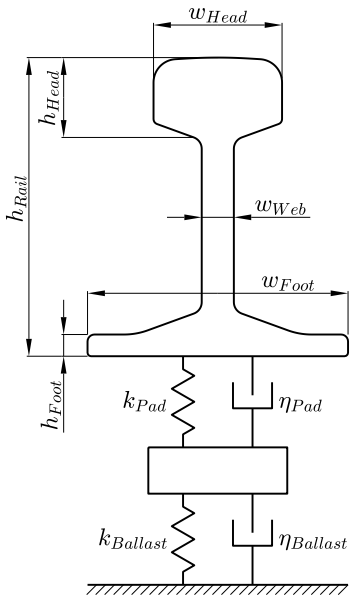

Fig. 3.4: Design parameters of the track.

rail cross-section are relevant. Nonetheless, concerning the total noise, the rail foot width stands as the sole geometric parameter of significance, whereas all four viscoelastic properties of the rail pad and ballast are important.

In summary, the most important parameters in the context of the current investigation are the stiffness and damping of the rail pad and ballast, as well as the rail foot width. Fig. 3.5 depicts the defined importance of each design parameter for the noise radiation from each element, where S, R, W, and T stand for sleeper, rail, wheel, and total, respectively. In the figure, 'Geom.' refers to all geometric parameters (excluding the rail foot width) and 'Inter.' denotes the interaction between parameters. The rail pad stiffness significantly influences the acoustic emission from all elements, explaining about 86% of the variability in the sleeper noise, 94% in the rail noise, 61% in the wheel noise, and 84% in the total noise. Hence, among the parameters studied, the rail pad stiffness stands as the most important one in the context of rolling noise radiation.

Interestingly, only one geometric parameter, the rail foot width, is important on the total radiation. Modifications to the rail cross-section geometry impact the rail bending stiffness and consequently the rail dynamics. However, as explained

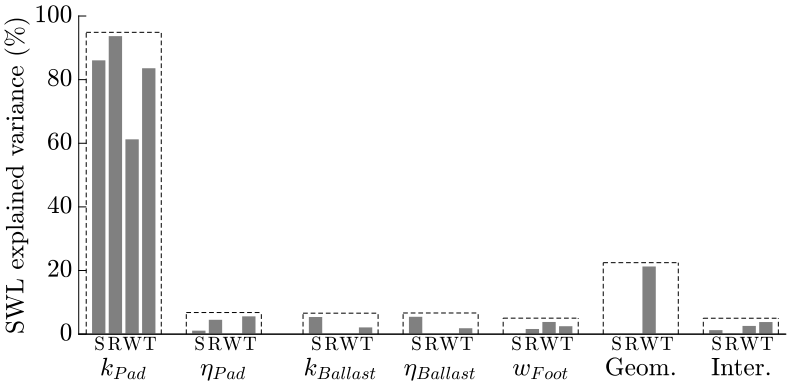

Fig. 3.5: Importance (variance explanation) of the design parameters on the noise radiation.

in Section 2.3, this occurs primarily above about 1.5 kHz, where the rail radiation is masked by the wheel noise (the sleeper contribution is negligible in this range). Hence, modifications to the rail geometry do not induce changes in the sleeper or rail acoustic contributions due to alterations in the track dynamics. Instead, the rail foot width influences the rail radiation through changes in the rail radiating surface and radiation ratio. Similarly, one might anticipate the rail height to have a similar effect; however, this work considers circulation on a tangent track, where the rail vertical vibration (and noise) predominates over lateral vibration.

Given that the rail geometry alters the rail dynamics above 1.5 kHz, and considering the wheel/rail dynamic coupling in the interaction, the geometric parameters are important on the wheel noise (through the interaction forces). Nevertheless, this does not significantly impact the total noise, as (1) the variability in the wheel radiation attributed to the rail geometry is notably smaller than that in the track noise attributed to the other parameters, and (2) the track contribution to the total overall noise is greater than that of the wheel for most of the studied designs.

An alternative, and perhaps more intuitive, measure of the importance based on variations of noise attributed to a parameter is also explored here. Given an arbitrary track design, one parameter is varied within its predefined range, and the difference in the overall SWL between the noisiest and quietest combinations is evaluated. This process is repeated for several arbitrary designs, each time modifying the same parameter. The distribution of the SWL difference for all cases indicates as well the importance of such parameter. This approach is iterated for each design parameter, with the results summarised in Table 3.2. For instance,

Table 3.2: Ranges of maximum changes in the noise from each element in dB(A) due to alterations of the contributing parameters.

	Sleeper noise	Rail noise	Wheel noise	Total noise
k_{Pad}	4.5-8.7	11.5-13.1	0.4-1.8	2.2-6.5
η_{Pad}	0.3-1.7	2.3-3.0	-	0.5-2.0
$k_{Ballast}$	0.3-2.9	-	-	0.0-1.5
$\eta_{Ballast}$	0.7-2.6	-	-	0.0-1.3
w_{Foot}	-	1.1-2.4	-	0.1-1.9

for a given arbitrary track design (within predefined ranges), modifications to the rail pad stiffness can yield a maximum change in the rail noise within the range 11.5-13.1 dB(A), depending on the other design parameters.

While the importance of a parameter indicates the proportion of variability in the noise explained by such parameter, it does not detail how the parameter actually influences the noise. Therefore, an additional investigation into the sign of the coefficients in the polynomial regression model is conducted. This revealed the following trends: an increase in the rail foot width increases the rail and total noise; an increase in the rail pad and ballast damping decreases the sleeper, rail, and total radiation; an increase in the ballast stiffness decreases the sleeper and total noise; and an increase in the rail pad stiffness increases the sleeper noise but decreases the rail and wheel radiation, with a compromise solution on the total noise. Regarding the influence of the rail geometric parameters on the wheel noise, in general terms, an increase in the rail size implies higher section stiffness and thus lower receptance (particularly over 1.5 kHz), hence leading to lower levels of the interaction forces and ultimately a lower wheel sound radiation. However, this effect is not pronounced and the trends may vary depending on the specific wheel geometry considered in the study.

The influence of the rail pad stiffness, being the most important and complex, on the noise radiation is depicted in Fig. 3.6. The optimal rail pad vertical stiffness, in the context of rolling noise radiation, is found to be in the range 700-1000 MN/m, depending on the other design parameters.

Overall, the optimal track design, in terms of rolling noise radiation, is reached with a minimum value of the rail foot width, an intermediate/high value of the rail pad stiffness, a maximum value of the ballast stiffness, and maximum values of the rail pad and ballast damping. In contrast, the least favourable design corresponds to a minimum value of the rail pad stiffness and opposite values compared with the

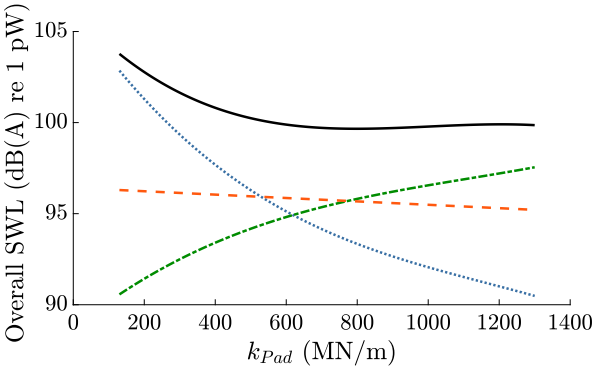

Fig. 3.6: Influence of the rail pad stiffness on the overall noise radiation. -·-·-: Sleeper; ·····: rail; - - -: wheel; ——: total.

optimal design for the other contributing parameters. The total SWL spectrum for both scenarios is depicted in Fig. 3.7. A notable difference of 7.4 dB(A) in the overall total noise is observed between the optimal and worst track designs. The maximum SWL difference between both designs occurs in the frequency range 500-2000 Hz, due to significant reductions in the rail noise resulting from the stiffer rail pad in the optimal case. Interestingly, a side effect of this stiffer rail pad is that the spectrum of the best design surpasses that of the worst design in the range 200-400 Hz, attributed to a poorer isolation of the sleeper. Above 2 kHz, the curves exhibit similarity as the wheel radiation experiences only a slightly reduction.

Contribution to the state of the art

The findings of this study are consistent with previous research. For instance, the influence of the rail pad stiffness on the noise from the elements is coherent with the results of Vincent *et al.* [79]. Additionally, Thompson reported a reduction in the track radiation of 3-4 dB(A) by increasing the rail pad stiffness from 250 MN/m to 560 MN/m, which also aligns with the results of Paper 1. Similarly, modifications to the rail cross-section geometry were found to affect the rail noise not due to changes in the rail stiffness, but rather to alterations in the radiating area and radiation ratios [7]. Also, reducing the rail foot width was suggested to yield mitigations of up to 4 dB(A) in the track noise [117], a finding consistent with the maximum 2.4 dB(A) reduction in the rail noise observed in the present research. Finally, Nielsen [118] highlighted the importance of the rail pad and

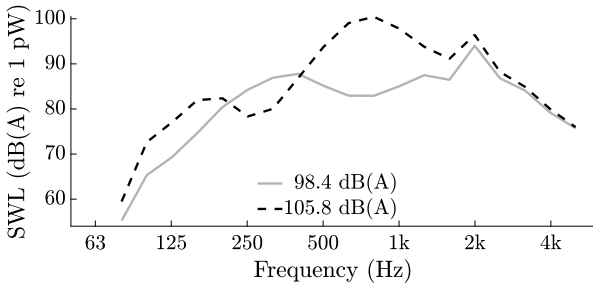

Fig. 3.7: Total SWL for the optimal (solid line) and worst (dashed line) track design.

ballast properties on the sleeper radiation, a correlation observed in the present work.

However, the application of statistical techniques in this investigation enabled the quantification of the influence or importance of specific parameters on the rolling noise radiation. These results contribute to predicting the effectiveness of mitigation measures before their implementation, based on their impact on the defined parameters. Furthermore, the findings of this work serve as a tool for designing efficient measures by identifying the parameters with the most significant influence on the noise for a given track design.

While the development and implementation of the comprehensive rolling noise prediction model do not introduce new concepts to the existing literature, it serves as a foundational aspect of this Thesis. Further innovations based on modifications to the calculation tool are presented in subsequent papers.

Limitations and future work

The absence of wheel rotation in the model represents a limitation. This rotation is known to produce the split of resonances associated with vibration modes of multiplicity two, thus influencing both wheel dynamics and acoustics. Furthermore, the use of 3D FE techniques for modelling the wheel requires a significant computational effort. While this limitation does not impact the current study, as the wheel geometry remains unchanged, it could constrain future research endeavours.

Hence, future work involves (1) the incorporation of the wheel rotation into the model and (2) the development of an efficient approach for modelling the dynamic and acoustic behaviour of the wheel. By addressing these aspects, subsequent

studies can enhance the accuracy and computational efficiency of rolling noise prediction models.

3.2 Enhancement of the comprehensive model: Wheel axisymmetric formulation

This section outlines the innovations and findings of Paper 2 of this Thesis, with title 'A model of a rotating railway wheel for the prediction of sound radiation', published in the Journal of Sound and Vibration in June 2023. Together with the author of this Thesis (V. T. Andrés), J. Martínez-Casas, F. D. Denia, and D. J. Thompson contributed to the paper.

This paper introduces an efficient model of a railway wheel, incorporating the inertial and gyroscopic effects associated with its rotation, and thus enhancing the comprehensive vibroacoustic tool developed in prior research. Taking advantage of the wheel axial symmetry, its response is expanded using Fourier series around the circumferential direction, formulating the dynamic and acoustic behaviour of the wheel in a 2D frame. This axisymmetric approach significantly reduces the computational effort compared with a 3D methodology. Importantly, this model is applicable to any rotating structure with axial symmetry.

The wheel is assumed to be constrained at the inner edge of the hub, and the wheelset RBM is superposed on its response. This approximation, as explained in Section 2.2, effectively models the dynamic behaviour of the wheelset.

Axisymmetric approach

Given the axial symmetry of the wheel geometry, the displacements are periodic in the circumferential direction with a period of 2π radians. Therefore, Fourier series around the angular coordinate θ can be used in order to express the wheel displacement field w, formulated in a cylindrical reference system, as follows [59]:

$$\begin{aligned} w_r =& w_{r,0} + \sum_{n>0} \left(w_{r,n} \cos(n\theta) - \overline{w}_{r,n} \sin(n\theta) \right), \\ w_\theta =& -\overline{w}_{\theta,0} + \sum_{n>0} \left(w_{\theta,n} \sin(n\theta) - \overline{w}_{\theta,n} \cos(n\theta) \right), \\ w_z =& w_{z,0} + \sum_{n>0} \left(w_{z,n} \cos(n\theta) - \overline{w}_{z,n} \sin(n\theta) \right), \end{aligned} \tag{3.1}$$

where subscripts r, θ, and z refer to radial, circumferential, and axial directions, respectively. The second subscript of the Fourier harmonic amplitudes in the right hand of the equations corresponds to the Fourier order, which is denoted by the letter n in the sums. The symmetric and antisymmetric motions about $\theta = 0$ (the origin of this coordinate can be chosen arbitrarily) are represented by variables without and with a bar, respectively.

Utilising the expansion in Eq. (3.1), the kinetic and strain energy of the wheel can be integrated analytically in the circumferential direction, subsequently obtaining the EoM formulated in terms of the harmonic amplitudes, which are functions of the radial and axial coordinates. Thus, this approach enables the EoM to be formulated in a 2D frame. The same methodology can be applied to the external forces, which are also periodic in the circumferential direction.

When the wheel rotation is not incorporated in the model, the different Fourier orders are decoupled in the EoM, and the symmetric motion is also decoupled from the antisymmteric motion. As a result, there are as many equations as twice the number of Fourier terms considered. This methodology was investigated by the author of this Thesis *et al.* in Reference [136] for the case of a stationary wheel. The truncation in the number of Fourier series sets the maximum frequency that can be accurately studied, as it is related to the vibration modes considered in the wheel response.

Incorporating the wheel rotation maintains the decoupling in the Fourier orders, but couples the symmetric and antisymmetric motion, resulting in as many EoM as the number of Fourier terms after truncation. This aspect is further explored in this section and in Paper 2.

Another scenario arises when the wheel is not running on a tangent track but follows a general non-straight trajectory. In this case, the different Fourier terms become coupled, resulting in a unique EoM. This is investigated in the next section and in Paper 3.

Regardless of the scenario, the sound radiation can still be formulated in a 2D frame. The acoustic model developed by Thompson [49] is used, which distinguishes between axial and radial emission. In this model, the wheel sound power W for a given frequency ω is given by

$$W(\omega) = \rho c \sum_{n\geq 0} \left(\sigma_{z,n}(\omega) S_z \langle \widetilde{v}^2_{z,n}(\omega)\rangle\right) + \rho c \sum_{n\geq 0} \left(\sigma_{r,n}(\omega) S_r \langle \widetilde{v}^2_{r,n}(\omega)\rangle\right), \tag{3.2}$$

where ρ and c represent the density of the air and speed of sound in this propagation medium, respectively. The acoustic power in each direction (subscripts z and

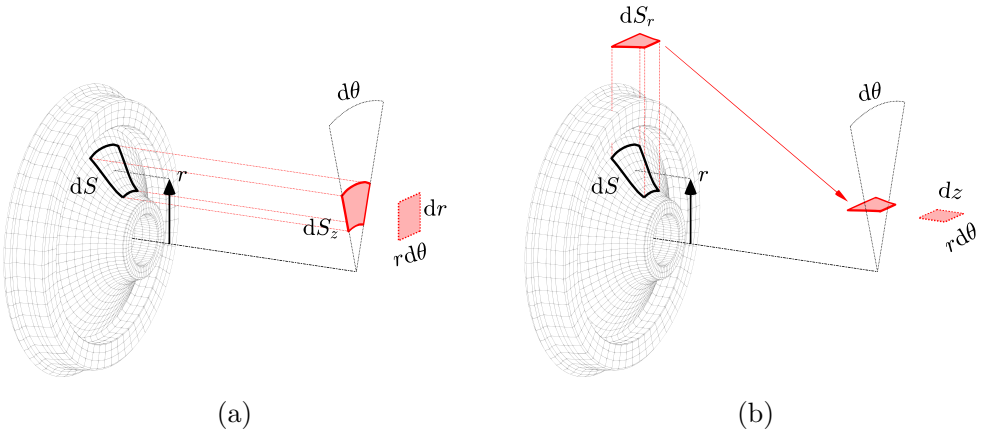

(a) (b)

Fig. 3.8: Schematic representation of the axial (a) and radial (b) surface projections.

r) is evaluated as a sum of contributions from the motion associated with each Fourier term n. Each contribution, in turn, consists of the product of a radiation ratio σ, radiating surface S, and squared mean velocity around the wheel surface v^2, which is averaged over time ($\widetilde{\ }$) and space ($\langle\ \rangle$).

The wheel surface projected in the axial S_z and the radial S_r directions can be expressed as an integral over the boundary of the wheel cross-section, denoted by Γ, as

$$\begin{aligned} S_z &= \int_S \mathrm{d}S_z = \int_\Gamma \int_{\theta=-\pi}^{\pi} r\mathrm{d}\theta\mathrm{d}r = 2\pi \int_\Gamma r\mathrm{d}r, \\ S_r &= \int_S \mathrm{d}S_r = \int_\Gamma \int_{\theta=-\pi}^{\pi} r\mathrm{d}\theta\mathrm{d}z = 2\pi \int_\Gamma r\mathrm{d}z, \end{aligned} \tag{3.3}$$

which is solved numerically in the paper. Note that $\mathrm{d}S_z = r\mathrm{d}\theta\mathrm{d}r$ and $\mathrm{d}S_r = r\mathrm{d}\theta\mathrm{d}z$, as schematised in Fig. 3.8.

Similarly, the mean squared velocity is given by

$$\langle \widetilde{v}_{i,n}^2(\omega) \rangle = \frac{1}{2S_i} \int_S |v_{i,n}(r,\theta,z,\omega)|^2 \mathrm{d}S_i, \qquad i = z,r, \quad n \geq 0, \tag{3.4}$$

where the time average is evaluated in the frequency domain as the root mean square (rms) value of the velocity amplitude $v_{i,n}$, i.e. dividing by $\sqrt{2}$, while the space average is evaluated as an integral over the wheel surface.

The velocities can be expressed as the time derivatives of the displacements in Eq. (3.1), yielding the following expressions:

$$\begin{aligned} v_{i,0}(r,z,\omega) &= \dot{w}_{i,0}(r,z,\omega), && i=z,r,\\ v_{i,n}(r,\theta,z,\omega) &= \dot{w}_{i,n}(r,z,\omega)\cos(n\theta) - \dot{\overline{w}}_{i,n}(r,z,\omega)\sin(n\theta), && i=z,r, \end{aligned} \tag{3.5}$$

with $n \geq 1$. By introducing Eq. (3.5) into Eq. (3.4), and considering the Fourier expansion in Eq. (3.1), the mean squared velocities can be integrated analytically over the circumferential direction, yielding:

$$\begin{aligned} S_z\langle\widetilde{v}^2_{z,0}\rangle &= \pi\int_\Gamma |\dot{w}_{z,0}|^2 r\mathrm{d}r,\\ S_r\langle\widetilde{v}^2_{r,0}\rangle &= \pi\int_\Gamma |\dot{w}_{r,0}|^2 r\mathrm{d}z,\\ S_z\langle\widetilde{v}^2_{z,n}\rangle &= \frac{\pi}{2}\int_\Gamma \left(|\dot{w}_{z,n}|^2 + |\dot{\overline{w}}_{z,n}|^2\right) r\mathrm{d}r, \quad n\geq 1,\\ S_r\langle\widetilde{v}^2_{r,n}\rangle &= \frac{\pi}{2}\int_\Gamma \left(|\dot{w}_{r,n}|^2 + |\dot{\overline{w}}_{r,n}|^2\right) r\mathrm{d}z, \quad n\geq 1. \end{aligned} \tag{3.6}$$

Therefore, by introducing Eq. (3.6) into Eq. (3.2), the wheel acoustic power is evaluated by an integral over the wheel cross-section boundary, i.e. it is formulated in a 2D frame.

Note that the expressions for the velocities and mean squared velocities differ from those in Paper 2 since here the wheelset RBM is still not incorporated. The missing terms in Eqs. (3.5) and (3.6) correspond thus to the wheelset RBM contribution, which will be explored later.

Rotation

An Eulerian approach is adopted in this work to model the wheel rotation. By evaluating the kinetic energy under this approach, the resulting EoM of the system already include the inertial and gyroscopic effects associated with the rotation. Moreover, the use of Eulerian coordinates is advantageous for solving the interaction with the rail, as the contact point of the wheel remains at a constant spatial position.

The position of any particle of the wheel is expressed as the sum of its spatial position before the motion (without deformation nor small RBM) and the displacements due to its flexibility (and small RBM in the case of a non-constrained structure). The time derivatives for obtaining the velocity of any particle, and

subsequently kinetic energy of the body, include the convective term associated with the rotation (material derivative) [137, 138].

An alternative approach involves modelling the rotation of the wheel as a problem of a moving load, where the change in the position of the contact point is taken into account, but the inertial and gyroscopic effects associated with the rotation are not. Thompson [32] developed the formulation to consider this moving load approach, which is currently implemented in TWINS. Recently, Knuth *et al.* [139] investigated the influence of the inertial and gyroscopic effects of the rotation on the wheel noise, finding that the moving load approach provides a suitable approximation even for high-speed trains. While incorporating the inertial and gyroscopic effects may appear more complex than the moving load approach, the associated formulation and solving methodology of the former is, according to the author of this Thesis, simpler and more convenient.

Validation of the model

Although TWINS allows for the incorporation of the wheel rotation, the model proposed in this Thesis overcomes some simplifications of this commercial software, namely:

- Modelling the rotation through a moving load approach, thus neglecting the associated inertial and gyroscopic effects.
- Evaluating the wheel dynamic response at a limited number of points on the wheel surface, rather than considering the entire radiating surface.
- Assuming that radial noise is emitted only by the tyre and axial noise only by the web and lateral faces of the tyre.

While the first simplification is not expected to introduce a significant error in the results, the second may introduce arbitrariness in the methodology and the third may lead to discrepancies, particularly in the case of a wheel with a curved web. For these reasons, in the present work, the proposed model is validated using the commercial FE software ANSYS [22]. Unlike TWINS, ANSYS solves the fluid-structure interaction problem, validating as well the approximation associated with the use of radiation ratios. The rotation in this software is incorporated using a model for flexible rotors developed in 1984 by Geradin and Kill [53]. An overview of this model and its limitations is provided in Paper 2.

The SWL evaluated with the proposed axisymmetric model and ANSYS is compared for a vehicle speed of 80 km/h in Fig. 3.9, showing a discrepancy of only 0.2

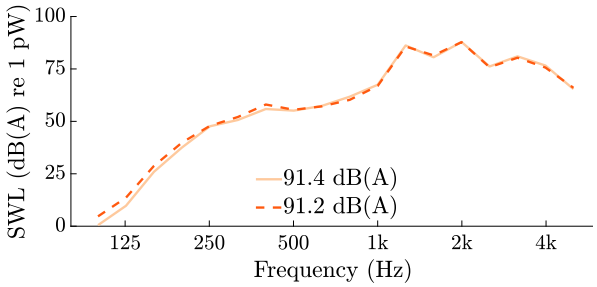

Fig. 3.9: Wheel SWL comparison between ANSYS (solid line) and the proposed axisymmetric model (dashed line). Case of a rotating wheel, with a vehicle speed of 80 km/h.

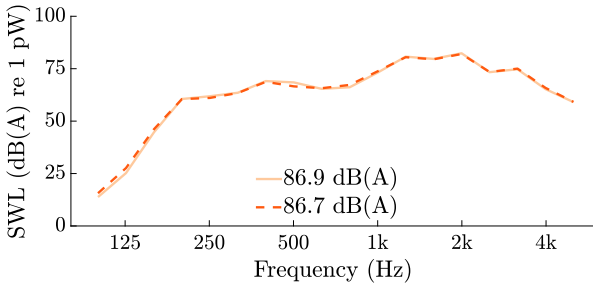

Fig. 3.10: Wheel SWL comparison between ANSYS (solid line) and the proposed axisymmetric model (dashed line). Case of a non-rotating wheel.

dB(A) in the overall wheel noise. A similar comparison for a non-rotating wheel was conducted by the author of this Thesis *et al.* in Reference [136], representing the SWL results in Fig. 3.10. Although different properties of the railway components were used in the rotating and non-rotating cases, similar discrepancies were found when comparing the proposed model with ANSYS. Thus, the influence of the different description of the rotation in the proposed model and ANSYS on the SWL is not significant. In both rotating and non-rotating cases, the main differences are concentrated in the low and medium frequency range, where the approximate radiation ratios used in the proposed model are most influential. Nevertheless, the energy contained in this frequency range is negligible compared with higher frequencies.

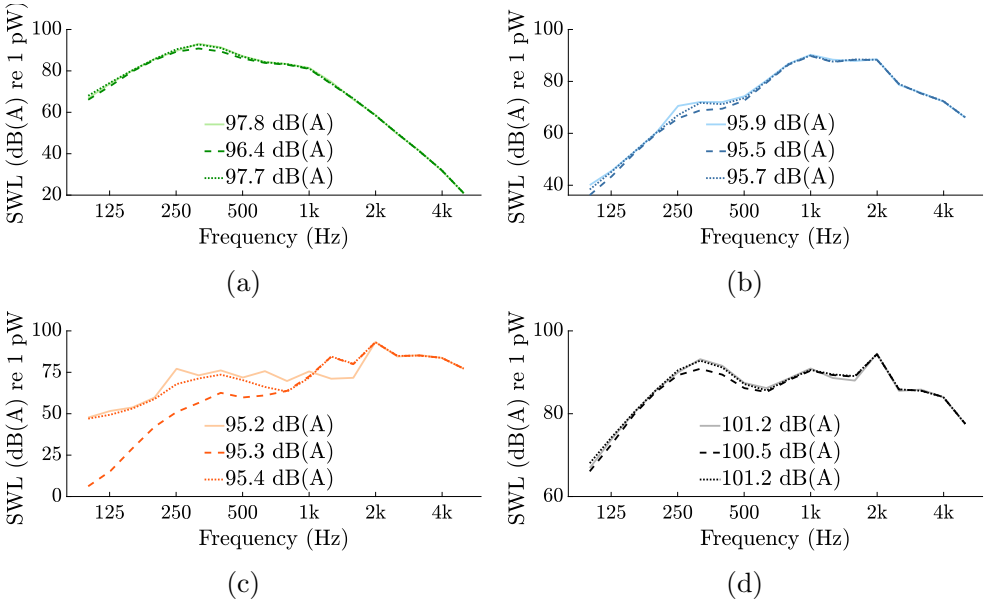

Fig. 3.11: SWL evaluated with different wheelset models. ——: Full numerical model of the wheelset; - - -: only constrained wheel model; ·····: constrained wheel plus wheelset RBM model. (a) Sleeper; (b) rail; (c) wheel; (d) total.

Wheelset RBM

The boundary condition of constraining the inner edge of the wheel hub, when compared with a full wheelset, does not significantly influence the overall wheel noise, but it notably affects the track radiation due to the wheel/rail interaction, as explained in Section 2.2. As an alternative to modelling numerically the full wheelset, Thompson proposed superposing the RBM of the wheelset on the constrained wheel vibration. This approach was explored by the author of this Thesis *et al.* in References [50, 51], comparing the SWL obtained with a model of the constrained wheel, a model of the constrained wheel plus the wheelset RBM, and a full numerical model of the wheelset.

The comparison, depicted in Fig. 3.11, shows that the constrained wheel and the full wheelset exhibit similar overall wheel noise (sum of power at each frequency band). However, for the track and total radiation, especially the sleeper, there are significant differences (a discrepancy of 1.4 dB(A) for the sleeper noise). On the other hand, the constrained wheel with the superposition of the wheelset

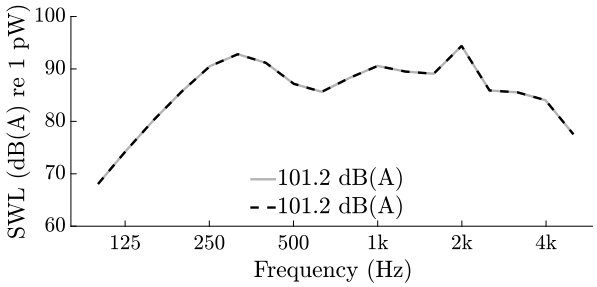

Fig. 3.12: Total SWL for the constrained wheel plus wheelset RBM model, considering a numerical (——) and analytical (- - -) description of the wheelset RBM.

RBM exhibits similar overall noise level than the full numerical wheelset for all elements, with a negligible difference for the total acoustic emission.

The wheelset RBM can be evaluated analytically even in the presence of rotation, assuming small displacements. Similarly to the incorporation of the rotation on the wheel model, an Eulerian approach is also considered in Paper 2 to account for the wheelset rotation. The position of any particle of the rigid wheelset is expressed as the sum of the spatial position of such particle before the RBM and the translational and rotational motion. As before, the velocity of the particle is evaluated through the material derivative to determine the kinetic energy of the wheelset. Using the Lagrange equations, the six EoM of the rotating rigid wheelset are derived, which can be consulted in Eq. (15) of Paper 2.

The contribution of the wheelset RBM to the velocities and mean squared velocities (and therefore SWL) is derived analytically in this work. When the wheelset RBM contribution is considered, the velocities in Eq. (3.5) are expanded, yielding the expressions in Eqs. (65), (67), and (69) of Paper 2, while the mean squared velocities in Eq. (3.6) yield Eqs. (66), (68), and (70) of Paper 2.

The validity of this analytical model was evaluated by the author of this Thesis *et al.* in References [50,51]. To do this, a full numerical model of the wheelset is used to evaluate uniquely the six RB modes (a gross FE discretisation is enough for this). Then, the wheelset RBM is evaluated for both approaches: using the proposed analytical model and using the numerical RB modes. Fig. 3.12 shows the total SWL considering the wheelset RBM contribution through both approaches; as can be seen, they provide the same results.

Contribution to the state of the art

Regarding the wheel model, Martínez-Casas *et al.* [57] initially introduced the approach used in this Thesis to consider the wheelset rotation, employing Cartesian coordinates and a 3D FE model. Later, Baeza *et al.* [61] extended this model by taking advantage of the axial symmetry of the wheelset. However, (1) their approach applied the axisymmetric technique directly to the wheelset EoM after a transformation from a Cartesian to a cylindrical reference system, and (2) their study focused solely on the modal properties of the wheelset.

In contrast, this paper presents two novel contributions to the state of the art regarding the flexible wheel model. Firstly, the energy equation and EoM are developed in a cylindrical reference system, allowing for a more direct application of the axisymmetric approach. Secondly, the investigation extends beyond modal properties to include the wheel noise radiation, formulated in a 2D frame as a result of the wheel axisymmetry. This second contribution is particularly noteworthy as it offers an alternative to the computationally intensive 3D methodologies. It is also worth noting that the proposed model can be used for any rotating structure with axial symmetry.

Regarding the rigid wheelset, to the best of the author's knowledge, no analytical model has previously been presented that describes the dynamic (small displacement) motion of a rotating rigid structure with axial symmetry.

Limitations and future work

The paper presents an accurate approach to describe the dynamic behaviour of a wheelset. However, it is important to note that this investigation assumes that the rotating structure follows a straight trajectory, limiting its applicability to tangent circulation scenarios.

Future work should focus on extending the model to take into account a wheelset circulating on a curved track. This would involve the development of a model capable of accurately capturing the dynamics of a rotating wheelset along a generic trajectory. By doing so, the generation of rolling noise in curved tracks could be studied, which might have significant implications for railway noise mitigation strategies.

3.3 Extension of the comprehensive model: Rolling noise in curved tracks

This section presents the innovations and findings from Paper 3 of this Thesis, entitled 'Railway rolling noise in curved tracks: Dynamic modelling of the wheelset and influence of the curve', submitted to the Journal of Sound and Vibration in December 2023. While the article remains under review, it is available in preprint format. The collaborative effort involves the author of this Thesis (V. T. Andrés), along with J. Martínez-Casas, F. D. Denia, D. J. Thompson, and S. Bruni.

The developments in this Thesis so far have focused on predicting rolling noise in tangent tracks. However, this work also extends to the study of curved tracks. As such, the primary goals of the paper are twofold: first, to develop a comprehensive model for predicting rolling noise in curved tracks, and second, to investigate the influence of the curve on this type of noise. To achieve this, the behaviour of the vehicle is characterised as a superposition of the steady-state condition and the dynamic oscillations around it. The steady-state positioning of the vehicle on a curve is determined using the VI-Rail software [140], with subsequent analysis of wheelset and track dynamics in this configuration. Unlike the previous papers of this Thesis, this work explores the interaction between the two wheels of a wheelset and both rails. The wheelset model accounts for the inertial and gyroscopic effects associated with the curved trajectory and its rotation. Given the radii of the curves studied (greater than 300 m), the dynamic effects associated with the curvature are neglected in the track model, as suggested by Liu *et al.* [141]. The vehicle/track interaction considers changes in the contact position compared with tangent circulation, non-zero mean values of the creepages, and non-negligible contact angles.

Following the development of this comprehensive model, a generic curve is parametrised based on the radius, non-compensated acceleration of the vehicle, and superelevation. The study then examines how these parameters influence rolling noise radiation. While curved tracks are typically associated with squeal noise, this investigation offers valuable insights into the importance of rolling noise radiation.

Vehicle steady-state position

The steady-state position on a curve of a railway vehicle is determined using the commercial software VI-Rail [140]. The calculations employ the Manchester Benchmark vehicle [142], which comprises one car body with two bogies, totalling four wheelsets. The simulation involves inserting the vehicle into a curve with a constant radius. This process includes an initial tangent section followed by a transition and, finally, a curved section of sufficient length to reach a steady-state condition. Various parameters, such as the contact position, contact angle, contact patch size, creepages, and normal load per wheel, are recorded for each wheel/rail pair. Additionally, the dynamic behaviour is linearised around these steady-state variables.

Wheelset model

The vehicle high-frequency dynamics in this study focuses solely on the dynamic behaviour of the wheelset, as the primary suspension effectively isolates the wheelset from the bogie and the rest of the vehicle within the frequency range of interest (see Section 2.2). Moreover, the primary suspension and axlebox are incorporated in the wheelset model.

A similar approach as in the previous paper is presented to consider the wheelset rotation. Also, to include the non-tangent circulation, a trajectory coordinate set is employed, tracking the motion of the wheelset on the track. Initially, this is modelled in a cylindrical 3D frame to derive the energy and EoM of a rotating wheelset. Subsequently, an axisymmetric approach is adopted to analyse the wheelset response. This, as in previous works, involves integrating the energy equation analytically over the circumferential direction. The gyroscopic effects arising from the non-straight trajectory of the rotating wheelset couple the different harmonics, resulting in a unique EoM where the DoF are the Fourier harmonic amplitudes of the expansion (see Eq. (3.1)). However, despite this coupling, the EoM remains formulated in a 2D frame, as these amplitudes are not dependent on the angular coordinate. Furthermore, Thompson's acoustic model [49] is used to assess the wheel radiation, which is also formulated in a 2D frame after considering the developments described in Section 3.2.

The formulation to incorporate the primary suspension is developed for both the 3D cylindrical and axisymmetric models. Given that the primary suspension is defined in Cartesian coordinates, its integration into the proposed models is more complex than in a Cartesian model.

Track model

The same track model as in the previous papers, explained in Section 3.1, is used here, although in this work both rails of the track are simultaneously modelled, with dynamic coupling between them and the sleeper through the rail pads. The acoustic model, which is based on wave propagation and equivalent acoustic sources, requires the assumption that the different waves in the track can be considered to radiate independently [21]. However, this assumption does not hold true for a symmetric track comprising two rails, as there are two independent waves (symmetric and antisymmetric) for each wavenumber. To overcome this limitation, the contribution of these pairs of waves to the track response is combined. This involves merging each pair of waves as if it were a single wave, once the input force is determined.

As previously mentioned, the track model does not account for curvature effects, which according to Liu *et al.* [141] are only influential in the track dynamics for curve radii below 30 m. Given that the curve radii examined in this study are, at least, one order of magnitude larger, the impact of the curvature on the track dynamics is considered negligible.

Vehicle/track interaction

The vehicle/track interaction in the context of rolling noise radiation, as discussed in Section 2.4, can be simplified to a series of single wheelset/track interactions. When considering a wheelset running on a track with roughness present on both rails, the problem can be divided into two load cases: roughness on one side and roughness on the other side. The resulting acoustic radiation can then be computed by summing the corresponding sound power from each load case, enabled by the assumption of incoherent roughness spectra, as also explored in Section 2.4. Despite roughness being present on only one side for each load case, contact on the other side must be ensured.

The curving behaviour of the vehicle causes the contact point to move away from its nominal position. If this displacement is significant, the new contact position may fall within a zone where the plane tangent to the contact surfaces is not parallel to the top-of-rail plane, resulting in a non-negligible contact angle. To address this, Thompson's interaction model [28] is extended by projecting the wheelset and track receptances into the contact reference system, defined by two axes within the contact patch and a third one perpendicular to it.

The vehicle/track interaction problem is formulated in the frequency domain. The normal direction is represented using a linearised Hertzian contact spring,

while the tangential contact dynamics is described by the model proposed by Gross-Thebing [103] (see Section 2.4). This model allows for the consideration of non-zero mean values of the creepages, which, in turn, lead to a coupling between the normal and tangential directions, where a harmonic normal load generates a harmonic tangential vibration.

Curve impact on rolling noise

Curved tracks with radii ranging from 300 to 5500 m are investigated in this study. Circulation on tracks with higher curvatures (smaller radii) than this range might result in squeal noise, which is not within the scope of this work, while lower curvatures resemble tangent circulation. Non-compensated acceleration in the range of 0-1 m/s^2 and super-elevation in the range of 30-120 mm are also considered, with a constant track gauge of 1435 mm. The influence of these three parameters on the difference in radiation between curved and tangent circulation (defined here as the dependent variable) is examined. The overall SWL from the sleeper, rail, and wheel, as well as the total radiation, is considered.

As can be seen in Fig. 3.13, the variability of the dependent variable (in this case, total noise) due to changes in the curve radius is significantly higher than that due to modifications of the other two variables. The influence of the curve radius on the noise difference between a curved and a tangent track is complex, while the influence of the non-compensated acceleration and superelevation can be summarised in the effect of the vehicle speed.

Three key factors are found to be important on the difference between rolling noise radiation in curved and tangent tracks: roughness spectrum, contact filter effect, and wheel/rail contact position. Although the same roughness is considered for both curved and tangent circulation (see Fig. 3.1), its frequency spectrum, which depends on the vehicle speed, is not flat and can thus affect the radiation differently in curved and tangent tracks. The contact filter effect is dependent on the vehicle speed and on the contact patch size, the latter being typically larger in curves, especially for low radii. Therefore, the contact filter effect has generally a greater impact on curved circulation (resulting in larger reductions of the noise levels).

For a given roughness spectrum, the dependent variable (difference in noise between curved and tangent track circulation) is well described by the wheel/rail contact position alone. The noise from the different elements is represented against the displacement of the wheel contact point relative to the nominal position in Fig. 3.14, considering all four wheelsets of the vehicle. A positive lateral

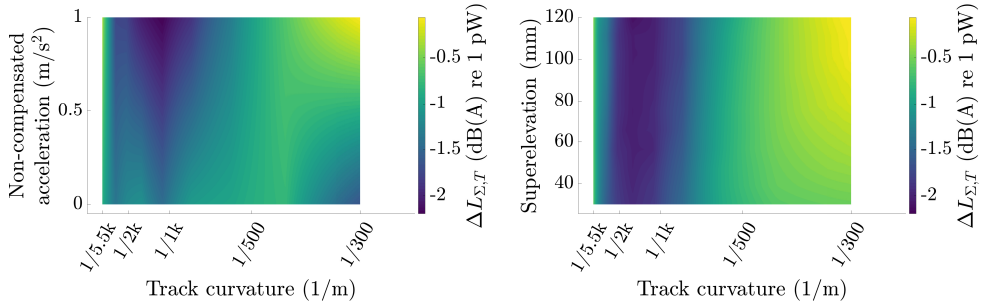

Fig. 3.13: Influence of the three design variables on the total noise difference betweeen curved and tangent track circulation ($\Delta L_{\Sigma,T}$). (a) Variations of track curvature and non-compensated acceleration with 70 mm of superelevation. (b) Variations of track curvature and superelevation with 0.56 m/s^2 of non-compensated acceleration .

displacement is defined as a movement away from the wheel flange. The results are divided into two groups: levels corresponding to the case with roughness applied on the high rail (black markers) and those corresponding to the case with roughness applied on the low rail (grey markers). While the leading wheelsets generally exhibit larger lateral displacements in a curve than the trailing ones, if the contact position is equal in a leading and a trailing wheelset, then there is no significant difference in their sound radiation.

The behaviour of the noise radiation can be attributed to two main factors: differences in the interaction forces between curved and tangent tracks, and an increase in the vertical-lateral coupling as the contact point moves away from the centre of the wheel tread and rail. Generally, even with significant displacements of the contact position (within the study limits), the vertical interaction force levels are higher than the lateral ones.

The sleeper noise predominantly arises from its vertical vibration and it is most notable at low frequencies (<750 Hz). When the wheel/rail contact point moves away from its nominal position, the vertical force in this frequency range decreases in a curved track compared with a tangent one, even before considering the contact filter. Consequently, the sleeper noise is lower in curved tracks, with the difference becoming more pronounced when including the contact filter effect, as observed in Fig. 3.14(a).

The rail noise is influential in the medium to high frequency range (500-2000 Hz). In curved tracks, the lateral vibrations of the rail become important on the

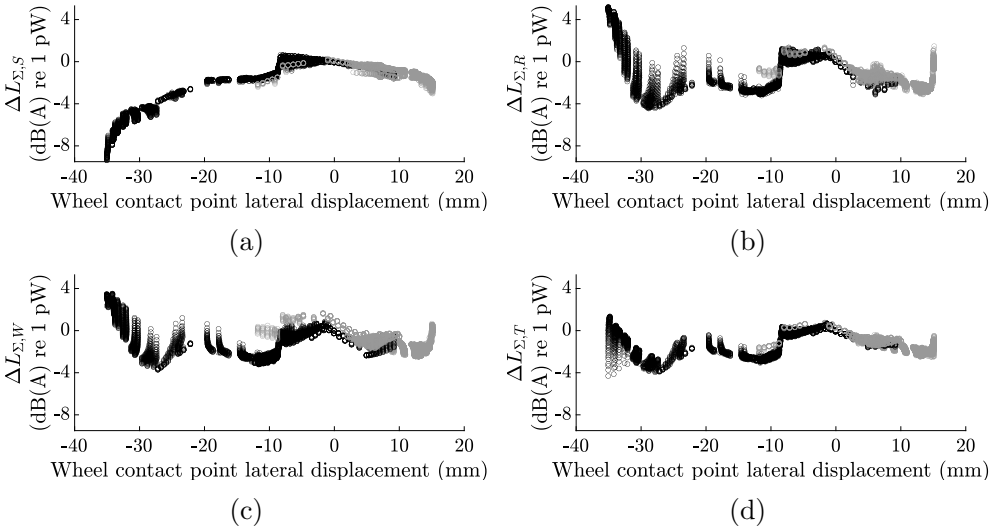

Fig. 3.14: Influence of the lateral displacement of the wheel contact point on the dependent variables (noise difference between curved and tangent track circulation) evaluated for each wheelset in the vehicle and its interaction with the track. Black markers indicate roughness only in the high side and grey markers roughness only in the low side. (a) Sleeper; (b) rail; (c) wheel; (d) total.

overall noise in this frequency range. Additionally, lateral forces are generally higher in curves than in tangent tracks within this range, while vertical forces remain relatively similar. Consequently, a significant displacement of the contact point leads to a notably higher lateral force and vertical-lateral coupling, resulting in increased noise radiation. Although the contact filter effect mitigates this difference to some extent, the rail noise levels remain higher in a curve when the contact point displacement is large. Conversely, a moderate displacement of the contact point reduces the impact of the increasing lateral force and vertical-lateral coupling. In such cases, the opposing influence of the contact filter leads to a negative value of the dependent variable, observing lower noise levels in curved tracks, as depicted in Fig. 3.14(b).

The wheel noise becomes important at higher frequencies (>1500 Hz), with the lateral (axial) radiation being predominant over the vertical (radial) radiation. The differences in the forces when compared with a tangent track follow the same trends as those observed for the rail in the previous paragraph, leading to a similar behaviour in the wheel noise radiation, as can be seen in Fig. 3.14(c).

The total noise, depicted in Fig. 3.14(d), is a combination of all three elements. For moderate displacements of the contact point, where the trends among the three elements align, the overall noise tends to be lower in curved tracks. However, for significant displacements, opposite trends are found between the sleeper and the other two elements (rail and wheel). Large contact position displacements are associated with low radii curves and therefore reduced vehicle speeds. In these scenarios, the roughness frequency spectrum concentrates in the low frequency range, where the sleeper noise is generally dominant. Hence, any variation in the sleeper radiation has a more pronounced impact on the total noise than similar variations in the rail or wheel acoustic emissions. Consequently, under such conditions, the total noise is predominantly influenced by the sleeper, resulting in lower total noise levels in curved tracks than in tangent tracks.

Note that the trend of the total noise ultimately depends on the relative importance of the three elements, which, in turn, are a function of various factors, highlighting the rail pad stiffness. Thus, the observed trend in the total noise may be limited to the specific railway wheelset and track properties considered in this study.

Lastly, given the dependence of the noise radiation on the wheel/rail contact position, the outer wheels of the leading wheelsets, which experience larger contact point displacements, tend to be noisier (by up to 4 dB(A)) than the rest.

Contribution to the state of the art

The wheelset model presented in this paper is an extension of the developments of Martínez-Casas *et al.* [58]. While their study employed Cartesian coordinates and a 3D FEM to analyse the dynamics of a wheelset on a curved track, the paper of this Thesis extends the methodology by adopting cylindrical coordinates and an axisymmetric approach. Additionally, this paper assesses the acoustic behaviour of the wheelset. Notably, this methodology is applicable to model the dynamic behaviour of any rotating structure with axial symmetry following a generic trajectory.

Although an axisymmetric approach is applied to the wheelset, a methodology is proposed to incorporate into the model a primary suspension formulated in Cartesian coordinates.

Additionally, a modification in the wave superposition method of the track model is developed, enabling the use of an acoustic model based on wave propagation. This adaptation becomes necessary when studying a complete track with two symmetric rails.

Moreover, this paper presents a vehicle/track interaction model in the frequency domain for a complete vehicle running on a curved track.

Furthermore, the work pioneers the modelling and investigation of rolling noise generation in curved tracks, quantifying the influence of a generic curve on this type of noise.

Importantly, to the author's knowledge, none of the aforementioned innovations have been previously documented in the published literature.

Limitations and future work

As previously explained, the total noise is, for high curvature tracks, governed by the sleeper contribution, which is attributed to both the roughness spectrum and track properties. While alternative roughness spectra can be explored, they typically exhibit lower amplitudes at higher wavelengths, resulting in similar outcomes. Changes in the track properties, particularly decreasing the rail pad stiffness, may alter the balance between the sleeper and rail contributions, potentially leading to different trends in the total noise. Moreover, modifications to the track or wheelset properties might further influence the impact of curves on the sound radiation from all three elements.

Future work aimed at extending the current study to consider diverse wheel and track properties holds promising avenues for future research in this field.

Chapter 4

Closure

The primary objective of this Thesis was to investigate rolling noise emission in railway systems. The research aimed to develop comprehensive models and computation tools to predict rolling noise accurately and to understand its underlying mechanisms. Circulation on both tangent and curved tracks was studied. The models developed for sound radiation prediction were used to analyse and comprehend the influence of various factors on rolling noise generation.

This chapter outlines the principal conclusions of the present work and proposes promising avenues for future research to expand upon this Thesis.

4.1 Conclusions

The principal conclusions of this Thesis can be summarised as follows:

- A comprehensive model for the prediction of rolling noise has been developed, considering the high-frequency behaviour of a wheelset, a track, and their interaction. The methodology evaluates the sound power radiation from sleepers, rails, and wheels for a given wheel and rail roughness. The wheelset is modelled using FE techniques and the rail is characterised employing periodic structure theory. Although the initial models for the track, wheelset, and their interaction were based on existing literature, subsequent

extensions have been devised. Ultimately, the comprehensive model developed in this Thesis is valid for simulations on both tangent and curved tracks.

- The wheelset modelling has been progressively refined throughout this Thesis. Initially, a single non-rotating wheel constrained at the inner edge of the hub was considered using a 3D approach. Subsequently, the wheel rotation was incorporated into the model, and an axisymmetric approach was proposed to describe the wheel dynamics. Additionally, the RBM of a rotating wheelset, described analytically, was superimposed on the flexible constrained wheel vibration, providing an accurate description of the wheelset dynamics. In this second wheelset model, the sound radiation was formulated in a 2D frame due to the axisymmetric approach, significantly reducing the associated calculation time compared with 3D methodologies. Thirdly, a full model of a wheelset was introduced, enabling the consideration of circulation following a generic trajectory. An axisymmetric approach was again applied to the wheelset response, and the formulation to incorporate quantities formulated in a Cartesian frame into this approach was developed.

- Throughout this Thesis, an infinite continuous track model has been assumed with a ballasted configuration, the properties of the rail pads, sleepers, and ballast being distributed per unit length. The track cross-section deformation is incorporated into the model, and its response is solved analytically in the longitudinal direction as a summation of wave contributions through an inverse Fourier transform over the wavenumber (wave superposition). Initially, half a track was modelled (one rail and half a sleeper), later expanded by including two rails and a full sleeper to study the curving high-frequency behaviour of the vehicle. A modification in the acoustic model of the track has been proposed to take into account multiple propagating waves with the same wavenumber, arising when a full track with two symmetric rails is considered.

- The wheel/rail interaction has been modelled in the frequency domain in the form of a linearised input-output relationship between the relative motion of the wheel and rail surfaces at the contact point and the contact forces. Initially considered for the case of a wheelset running centred over the track, this approach was later extended to the case of a full vehicle running along a curve, considering non-zero mean creepages and non-negligible contact angles.

- With the aforementioned descriptions of the different railway components and their interaction, an in-house software for the comprehensive prediction

of rolling noise has been developed and validated through multiple comparisons with different commercial software. The computational tool requires as a single input the wheel and rail roughness, while providing as an output the noise radiation from sleepers, rails, and wheels. Initially envisaged for rolling noise prediction in tangent circulation, the in-house software has later been expanded to account for curved circulation (see Appendix A).

- The influence of the track design on the rolling noise radiation has been studied. The findings revealed that the rail pad stiffness is the most important parameter, with an opposite effect on the sleeper and rail noise; as the rail pad stiffness increases, the rail noise decreases and the sleeper noise becomes greater. Optimal values of this parameter were observed within the range 700-1000 MN/m, which are at the high end of what would be practical for structural integrity reasons. The rail geometry was observed to not impact notably the sound radiation, with the exception of the rail foot width, significantly modifying the rail radiating surface and radiation ratio. Differences up to 7.4 db(A) in the total noise were found between an optimal and a least favourable track design.

- Rolling noise generation in curves has been modelled and analysed. The difference in the radiation between circulation on a tangent and curved track has been assessed. The results indicated that the track curvature is the most important parameter, being influential even for curves of radius up to 5 km. This was attributed to the track curvature influence on the position of the wheel/rail contact point. Consequently, the noise emission in a curve is mainly dependent on the position of the contact point. In general terms, the sleeper radiation was found to be lower in a curve than in a tangent track, while the rail and wheel noise was observed to be greater for high curvatures and smaller for low curvatures. The total noise, which is a combination of the three previous sources, was found to be typically lower in a curve than in a tangent track, although this may be limited to the considered roughness spectrum and properties of the wheelset and track.

4.2 Open research lines

Throughout the development of this Thesis, a number of limitations have been identified. Post-completion, the following lines are proposed for future research:

- The use of radiation ratios for the wheel sound model has demonstrated good accuracy in the medium and high frequency range, but poor precision for low frequencies. Although the energy concentrated in the low frequency

range does not contribute notably to the overall wheel noise level, a more accurate description of the wheel acoustics could be achieved considering, for example, a BEM based-model. An axisymmetric approach could also be applied to the wheel sound radiation, reducing the computational effort. Moreover, this BEM formulation could be employed in cases where the radiation ratios are not available, as in the case of perforated wheels. Furthermore, complex phenomena such as ground effects could be considered. Once the BEM is developed, it could also be used to compute the sleeper and rail noise.

- The influence of the track design on the total noise radiation is deeply analysed in this Thesis. Previous works studied the influence of the wheel geometry. However, a comprehensive investigation considering the influence of parameters from all the systems is yet to be conducted. Given that changes in any railway component may impact the noise from all the elements, this combined analysis appears promising.

- Although the impact of a curve on the rolling noise radiation has been assessed in the present work, the findings might be confined to the specific track and wheelset properties employed. A combined analysis considering also these properties could yield novel insights into the rolling noise generation in curves. Furthermore, the incorporation of other potentially relevant parameters such as the roughness spectrum and the rail inclination may be interesting.

- It has been justified, based on existing literature, that multiple wheels on the track do not significantly modify the rail vibration nor the interaction forces at each wheel/rail pair in the context of rolling noise emission. However, these findings might be limited to circulation on a tangent track. In a curve, where different wheel/rail pairs exhibit different contact dynamics, this hypothesis needs further investigation.

- The in-house calculation tool developed in this Thesis enables the integration of external acoustic mitigation devices, such as absorbers, dampers, and CDL treatments, which, as explored in the existing literature, can notably influence the noise emissions. The exploration of design strategies for these mitigation measures presents an intriguing avenue for future research.

- Finally, the viscoelastic properties of the rail pad and ballast have been considered frequency-independent in this Thesis. An improvement in this line would involve modelling their frequency-dependence. Additionally, while the sleeper deformation is known to be important only above 1 kHz, its

modelling via beam formulation tends to overestimate the noise when assuming a constant ballast stiffness. Incorporating the frequency-dependent behaviour of the ballast properties would enable the consideration of the sleeper deformation.

Appendix A. In-house software

This Appendix provides a detailed explanation of the in-house calculation tool developed for predicting rolling noise in railway systems. The tool integrates various modules designed to capture the complex dynamics and acoustic behaviour of the wheelset and track. This software is initially grounded in the developments and publications of Thompson [7, 28–31, 33], with its workflow inspired by the commercial package TWINS [37, 38]. Importantly, it incorporates the novel models developed and presented in this Thesis.

The development of this in-house tool has been driven by the need for a flexible and customisable solution tailored to the objectives of this Thesis. It is organised into six distinct modules, each dedicated to specific aspects of the rolling noise generation process, as follows:

- Wheelset dynamic module: Evaluates the wheelset modal properties and FRF.
- Track dynamic module: Calculates the track wave properties and FRF.
- Interaction module: Solves the wheel/rail interaction problem and determines the contact forces (assuming unit roughness input).
- Wheel acoustic module: Determines the wheel sound radiation.
- Track acoustic module: Computes the rail and sleeper sound radiation.
- Roughness module: Adjusts the acoustic radiation of the elements considering a specific spectrum as well as the contact and A-weighting filters.

Following this introduction, a detailed description of each module is provided, outlining its inputs, outputs, methodologies, and computational procedures. Figures illustrating the workflow and interactions between modules are included to enhance clarity and aid understanding.

Fig. A.1 presents the workflow for both the wheelset and track dynamic modules. The former requires as inputs the wheelset geometry and materials, including additional components attached to it such as axleboxes, brakes, gearboxes, and the primary suspension. Regarding the steady-state condition, the vehicle speed (to determine the wheelset rotational velocity) and the contact position with the rail are needed. In the case of circulation on a curve, the two contact positions with both rails are considered. This module incorporates the axisymmetric model proposed in Paper 3, which becomes the one presented in Paper 2 for tangent circulation. The module establishes the calculation frequencies based on the variation of the wheelset FRF and provides the wheelset EoM, modal properties (of the non-rotating structure), and contact point receptance. Colour orange emphasises the variables coming from this module.

The track dynamic module requires as inputs the rail geometry and material, the track configuration (rail inclination and track gauge), and the foundation properties, including the rail pad and ballast viscoelastic behaviour as well as the sleeper geometry, material, and spacing distance (used to distribute the properties

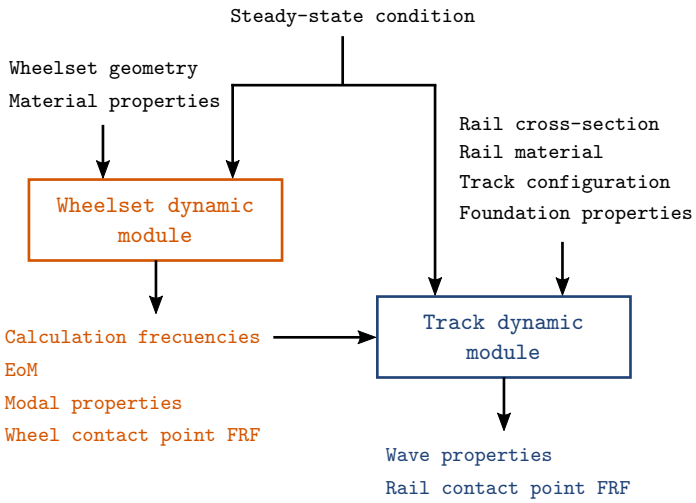

Fig. A.1: Flow diagram of the wheelset and track dynamic modules.

per unit length). Additionally, the steady-state contact position with the wheel (or wheels) and the calculation frequencies (output from the wheelset dynamic module) are necessary. While the wheelset is characterised by multiple vibration modes, resulting in a FRF with numerous resonances, the track FRF exhibits a smoother behaviour. Therefore, it is more convenient to define the calculation frequencies based on the wheelset FRF. A track model based on periodic structure theory, as detailed in Paper 1 and Section 3.1, is implemented in this module. Outputs include the wave properties (waveshapes and wavenumbers) and the rail contact point receptance. Colour blue is employed for the output variables from this module.

The FRF of the wheel and rail contact points, evaluated at the calculation frequencies, serve as inputs for the interaction module to compute the contact forces, as depicted in Fig. A.2. The module also considers the Young's modulus and Poisson's ratio of the wheel and rail materials at their interface, assumed to be identical, along with the friction coefficient. For the steady-state condition, the creepages, size of the contact ellipse, wheel/rail contact position, normal static load of the vehicle per wheel, and vehicle speed are required to determine the contact receptance, while the contact angle is needed to express the wheel, rail, and contact receptances in the same reference system to solve the interaction problem (refer to Paper 3). The interaction model presented in the aforementioned paper is integrated into this module. In the previous contributions, where circulation on a tangent track is considered, zero values of the steady-state creepages and contact angle are assumed; also, the wheel/rail contact is supposed to occur at the nominal position. Additionaly, in this case, the Hertz theory is considered to determine the semi-axis lengths of the contact patch as a function of the normal

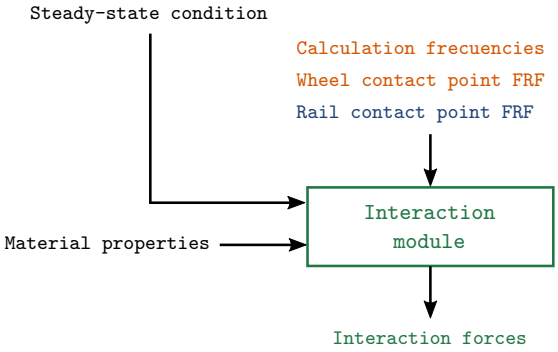

Fig. A.2: Flow diagram of the interaction module.

load [26,31,90], and Thompson's contact model [28,31], explained in Paper 1 and Section 3.1, is employed. Colour green highlights the variable coming from this module.

Note that the roughness is not required in the interaction module as it is assumed to have a flat spectrum of 1 µm for all the calculation frequencies. This will be subsequently adjusted with the actual roughness spectrum.

Once the interaction forces have been computed, these are, along with the air properties (speed of sound and density), common inputs for both the wheel and track acoustic modules, as shown in Fig. A.3. Additionally, the wheel acoustic module requires the wheel geometry, calculation frequencies, wheelset EoM, and the steady-state contact position. While the modal properties are also necessary, they can be derived again from the EoM. For a rotating structure, both the modal properties (of the non-rotating structure) and EoM are needed to solve its vibrational response, as the change to modal coordinates does not decoupled the EoM. The modal transformation is still performed, but the generalised coordinates are obtained by inverting the modal EoM (after the change of coordinates). If rotation is not considered, then the modal properties alone suffice to evaluate the wheel response, and the EoM at this point are unnecessary. As an output, highlighted in red, the module provides the wheel SWL for a unit roughness spectrum, evaluated by the axisymmetric acoustic model proposed in Papers 2 and 3.

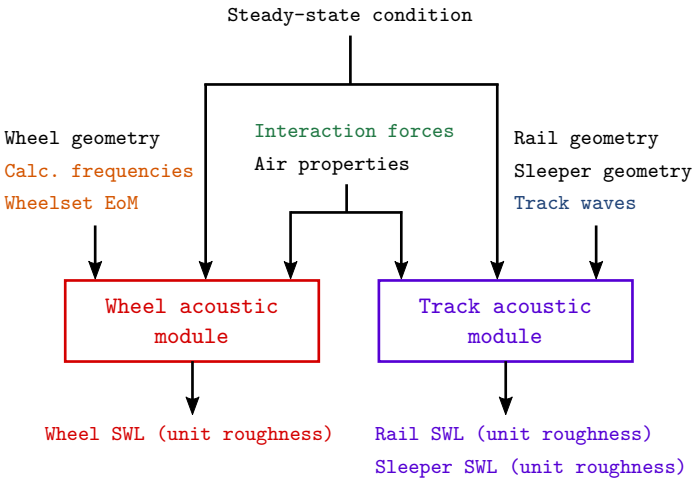

Fig. A.3: Flow diagram of the wheel and track acoustic modules.

For the track acoustic module, in addition to the interaction forces and air properties, the rail and sleeper geometry, track wave properties, and steady-state contact position are inputs. The acoustic models for the rail and sleeper are based on wave propagation and equivalent acoustic sources [21], as detailed in Paper 1 and Section 3.1. Additionally, in the case of curve circulation conditions, the extension proposed in Paper 3 is incorporated to account for a complete track with two rails. This module provides as outputs the rail and sleeper SWL for a unit roughness input (in purple).

In this methodology, the radiated acoustic power is proportional to the squared roughness amplitude, facilitating its correction with an actual roughness spectrum. In the roughness module, depicted in Fig. A.4, the SWL for a unit roughness is adjusted according to the procedure described by the standard EN 13979-1. This considers a wheel/rail combined roughness spectrum, the contact filter effect (in this Thesis, the model proposed by Thompson [7] is employed), and the A-weighting filter to adapt the levels to the human ear perception [42]. As the roughness spectrum is typically expressed in the wavelength domain, the steady-state vehicle speed is required to convert it to the frequency domain. Likewise, the evaluation of the contact filter effect uses this speed and the steady-state contact patch semi-length along the circulation direction. The outputs from this module, highlighted in brown, are the wheel, rail, and sleeper SWL. The total noise is evaluated as an energy sum of the three previous magnitudes.

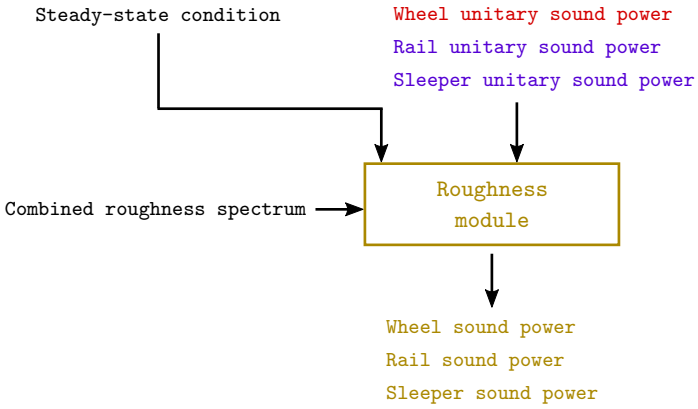

Fig. A.4: Flow diagram of the roughness module.

References

[1] European Comission. *EU Transport, Statistical Pocketbook*. Publications Office of the European Union, 2023.

[2] European Environment Agency. Annual European Union greenhouse gas inventory 1990–2021 and inventory report 2023. Technical report, European Comission, 2023.

[3] World Health Organisation. *Burden of disease from environmental noise - Quantification of healthy life years lost in Europe*. WHO, 2011. ISBN: 9789289002295.

[4] D. Petri, G. Licitra, M. A. Vigotti, and L. Fredianelli. Effects of exposure to road, railway, airport and recreational noise on blood pressure and hypertension. *International Journal of Environmental Research and Public Health*, 18(17), 2021. http://dx.doi.org/10.3390/ijerph18179145.

[5] M. G. Smith, I. Croy, M. Ögren, O. Hammar, E. Lindberg, and K. Persson Waye. Physiological effects of railway vibration and noise on sleep. *The Journal of the Acoustical Society of America*, 141(5):3262–3269, 2017. http://dx.doi.org/10.1121/1.4983302.

[6] A. Seidler, M. Schubert, Y. Mehrjerdian, K. Krapf, C. Popp, I. van Kamp, M. Ögren, and J. Hegewald. Health effects of railway-induced vibration combined with railway noise – a systematic review with exposure-effect curves. *Environmental Research*, 233:116480, 2023. http://dx.doi.org/10.1016/j.envres.2023.116480.

[7] D. J. Thompson. *Railway Noise and Vibration. Mechanisms, Modelling and Means of Control*. Elsevier, 2009. ISBN: 978-0-08-045147-3. http://dx.doi.org/10.1016/B978-0-08-045147-3.X0023-0.

[8] P. J. Remington. Wheel/rail noise—Part IV: Rolling noise. *Journal of Sound and Vibration*, 46(3):419–436, 1976. http://dx.doi.org/10.1016/0022-460X(76)90864-6.

[9] D. J. Thompson and N. Vincent. Track dynamic behaviour at high frequencies. Part 1: Theoretical models and laboratory measurements. *Vehicle System Dynamics*, 24(sup1):86–99, 1995. http://dx.doi.org/10.1080/00423119508969617.

[10] D. J. Thompson and C. J. C. Jones. A review of the modelling of wheel/rail noise generation. *Journal of Sound and Vibration*, 231(3):519–536, 2000. http://dx.doi.org/10.1006/jsvi.1999.2542.

[11] M. J. Rudd. Wheel/rail noise—Part II: Wheel squeal. *Journal of Sound and Vibration*, 46(3):381–394, 1976. http://dx.doi.org/10.1016/0022-460X(76)90862-2.

[12] A. Pieringer. *Time-domain modelling of high-frequency wheel/rail interaction*. PhD Thesis, Chalmers University of Technology, 2011.

[13] J. Giner-Navarro. *Advanced techniques fo the time-domain modelling of high-frequency train/track interaction*. PhD Thesis, Universitat Politècncnica de València, 2017.

[14] J. Giner-Navarro, J. Martínez-Casas, F. D. Denia, and L. Baeza. Study of railway curve squeal in the time domain using a high-frequency vehicle/track interaction model. *Journal of Sound and Vibration*, 431:177–191, 2018. http://dx.doi.org/10.1016/j.jsv.2018.06.004.

[15] X. Li, Q. Liu, S. Pei, L. Song, and X. Zhang. Structure-borne noise of railway composite bridge: Numerical simulation and experimental validation. *Journal of Sound and Vibration*, 353:378–394, 2015. http://dx.doi.org/10.1016/j.jsv.2015.05.030.

[16] Q. Liu, D. J. Thompson, P. Xu, Q. Feng, and X. Li. Investigation of train-induced vibration and noise from a steel-concrete composite railway bridge using a hybrid finite element-statistical energy analysis method. *Journal of Sound and Vibration*, 471:115197, 2020. http://dx.doi.org/10.1016/j.jsv.2020.115197.

[17] C. Esveld. *Modern railway track*. MRT productions, 2nd edition, 2001. ISBN: 9789080032439.

[18] V. T. Andrés, J. Martínez-Casas, F. D. Denia, and D. J. Thompson. Influence study of rail geometry and track properties on railway rolling noise. *Journal of Sound and Vibration*, 525:116701, 2022. http://dx.doi.org/10.1016/j.jsv.2021.116701.

[19] V. T. Andrés, J. Martínez-Casas, F. D. Denia, and D. J. Thompson. A model of a rotating railway wheel for the prediction of sound radiation. *Journal of Sound and Vibration*, 553:117667, 2023. http://dx.doi.org/10.1016/j.jsv.2023.117667.

[20] V. T. Andrés, J. Martínez-Casas, F. D. Denia, D. J. Thompson, and S. Bruni. Railway rolling noise in curved tracks: Dynamic modelling of the wheelset and influence of the curve. *Submitted for publication*. Preprint version available: http://dx.doi.org/10.2139/ssrn.4683502.

[21] D. J. Thompson, M. H. A. Janssens, and F. G. de Beer. *Track Wheel Interaction Noise Software (TWINS) Theoretical Manual (version 3.4)*. TNO report, TNO Institute of Applied Physics, 2019.

[22] Ansys® Academic Research Mechanical. Release 19.2, Help System, ANSYS, Inc.

[23] P. J. Remington. Wheel/rail noise—Part I: Characterization of the wheel/rail dynamic system. *Journal of Sound and Vibration*, 46(3):359–379, 1976. http://dx.doi.org/10.1016/0022-460X(76)90861-0.

[24] I. L. Vér, C. S. Ventres, and M. M. Myles. Wheel/rail noise—Part III: Impact noise generation by wheel and rail discontinuities. *Journal of Sound and Vibration*, 46(3):395–417, 1976. http://dx.doi.org/10.1016/0022-460X(76)90863-4.

[25] I. L. Vér, C. S. Ventres, and M. M. Myles. Wheel/rail noise—Part V: Measurement of wheel and rail roughness. *Journal of Sound and Vibration*, 46(3):437–451, 1976. http://dx.doi.org/10.1016/0022-460X(76)90865-8.

[26] P. J. Remington. Wheel/rail rolling noise, I: Theoretical analysis. *The Journal of the Acoustical Society of America*, 81(6):1805–1823, 1987. http://dx.doi.org/10.1121/1.394746.

[27] P. J. Remington. Wheel/rail rolling noise, II: Validation of the theory. *The Journal of the Acoustical Society of America*, 81(6):1824–1832, 1987. http://dx.doi.org/10.1121/1.394747.

[28] D. J. Thompson. Wheel-rail noise generation, part I: Introduction and interaction model. *Journal of Sound and Vibration*, 161(3):387–400, 1993. http://dx.doi.org/10.1006/jsvi.1993.1082.

[29] D. J. Thompson. Wheel-rail noise generation, part II: Wheel vibration. *Journal of Sound and Vibration*, 161(3):401–419, 1993. http://dx.doi.org/10.1006/jsvi.1993.1083.

[30] D. J. Thompson. Wheel-rail noise generation, part III: Rail vibration. *Journal of Sound and Vibration*, 161(3):421–446, 1993. http://dx.doi.org/10.1006/jsvi.1993.1084.

[31] D. J. Thompson. Wheel-rail noise generation, part IV: Contact zone and results. *Journal of Sound and Vibration*, 161(3):447–466, 1993. http://dx.doi.org/10.1006/jsvi.1993.1085.

[32] D. J. Thompson. Wheel-rail noise generation, part V: Inclusion of wheel rotation. *Journal of Sound and Vibration*, 161(3):467–482, 1993. http://dx.doi.org/10.1006/jsvi.1993.1086.

[33] D. J. Thompson. *Wheel-rail noise: theoretical modelling of the generation of vibrations*. PhD Thesis, University of Southampton, 1990.

[34] E. K. Bender and P. J. Remington. The influence of rails on train noise. *Journal of Sound and Vibration*, 37(3):321–334, 1974. http://dx.doi.org/10.1016/S0022-460X(74)80248-8.

[35] D. J. Thompson. Predictions of acoustic radiation from vibrating wheels and rails. *Journal of Sound and Vibration*, 120(2):275–280, 1988. http://dx.doi.org/10.1016/0022-460X(88)90435-X.

[36] P. J. Remington. Wheel/rail rolling noise: What do we know? What don't we know? Where do we go from here? *Journal of Sound and Vibration*, 120(2):203–226, 1988. http://dx.doi.org/10.1016/0022-460X(88)90430-0.

[37] D. J. Thompson, B. Hemsworth, and N. Vincent. Experimental validation of the TWINS prediction program for rolling noise, part 1: Description of the model and method. *Journal of Sound and Vibration*, 193(1):123–135, 1996. http://dx.doi.org/10.1006/jsvi.1996.0252.

[38] D. J. Thompson, P. Fodiman, and H. Mahé. Experimental validation of the TWINS prediction program for rolling noise, part 2: Results. *Journal of Sound and Vibration*, 193(1):137–147, 1996. http://dx.doi.org/10.1006/jsvi.1996.0253.

[39] T. Kitagawa and D. J. Thompson. Comparison of wheel/rail noise radiation on japanese railways using the TWINS model and microphone array measurements. *Journal of Sound and Vibration*, 293(3):496–509, 2006. http://dx.doi.org/10.1016/j.jsv.2005.08.037.

[40] T. Kitagawa. The influence of wheel and track parameters on rolling noise. *Quarterly Report of RTRI*, 50(1):32–38, 2009. http://dx.doi.org/10.2219/rtriqr.50.32.

[41] D. J. Thompson, G. Squicciarini, J. Zhang, I. Lopez Arteaga, E. Zea, M. Dittrich, E. Jansen, K. Arcas, E. Cierco, F. X. Magrans, A. Malkoun, E. Iturritxa, A. Guiral, M. Stangl, G. Schleinzer, B. Martin Lopez, C. Chaufour, and J. Wändell. Assessment of measurement-based methods for separating wheel and track contributions to railway rolling noise. *Applied Acoustics*, 140:48–62, 2018. http://dx.doi.org/10.1016/j.apacoust.2018.05.012.

[42] Electroacoustics – Sound level meters – Part 1: Specifications. IEC 61672-1:2013. International Electrotechnical Commission, 2013.

[43] H. Kruse K. Popp and I. Kaiser. Vehicle-track dynamics in the mid-frequency range. *Vehicle System Dynamics*, 31(5-6):423–464, 1999. http://dx.doi.org/10.1076/vesd.31.5.423.8363.

[44] T. Szolc. Medium frequency dynamic investigation of the railway wheelset-track system using a discrete-continuous model. *Archive of Applied Mechanics*, 68:30–45, 1998. http://dx.doi.org/10.1007/s004190050144.

[45] J. C. O. Nielsen. Numerical prediction of rail roughness growth on tangent railway tracks. *Journal of Sound and Vibration*, 267(3):537–548, 2003. http://dx.doi.org/10.1016/S0022-460X(03)00713-2.

[46] P. T. Torstensson, A. Pieringer, and J. C. O. Nielsen. Simulation of rail roughness growth on small radius curves using a non-hertzian and non-steady wheel–rail contact model. *Wear*, 314(1):241–253, 2014. http://dx.doi.org/10.1016/j.wear.2013.11.032.

[47] B. Morys. Enlargement of out-of-round wheel profiles on high speed trains. *Journal of Sound and Vibration*, 227(5):965–978, 1999. http://dx.doi.org/10.1006/jsvi.1999.2055.

[48] T. Szolc. Simulation of dynamic interaction between the railway bogie and the track in the medium frequency range. *Multibody System Dynamics*, 6:99–122, 2001. http://dx.doi.org/10.1023/A:1017513021811.

[49] D. J. Thompson and C. J. C. Jones. Sound radiation from a vibrating railway wheel. *Journal of Sound and Vibration*, 253(2):401–419, 2002. http://dx.doi.org/10.1006/jsvi.2001.4061.

[50] V. T. Andrés, J. Martínez-Casas, F. D. Denia, G. Squicciarini, and D. J. Thompson. A model of the rotating rigid wheelset and its influence on the wheel and track rolling noise. In *Proceedings of Internoise*, pages 3959–3965(7), Glasgow, Scotland, 2022. http://dx.doi.org/10.3397/IN_2022_0564.

[51] V. T. Andrés, J. Martínez-Casas, F. D. Denia, G. Squicciarini, and D. J. Thompson. Modelización de la influencia de los modos de sólido rígido del eje ferroviario montado en el ruido de rodadura de rueda y vía. In *Proceedings of Congreso Iberoamericano de Ingeniería Mecánica*, pages 478–483(1), Madrid, Spain, 2022. http://dx.doi.org/10.5944/bicim2022.215.

[52] G. Genta. *Dynamics of Rotating Systems*. Springer New York, NY, 2005. ISBN: 978-0-387-20936-4. http://dx.doi.org/10.1007/0-387-28687-X.

[53] M. Geradin and N. Kill. A new approach to finite element modelling of flexible rotors. *Engineering Computations*, 1(1):52–64, 1984. http://dx.doi.org/10.1108/eb023560.

[54] G. Genta and A. Tonoli. A harmonic finite element for the analysis of flexural, torsional and axial rotordynamic behaviour of discs. *Journal of Sound and Vibration*, 196(1):19–43, 1996. http://dx.doi.org/10.1006/jsvi.1996.0465.

[55] X. Sheng, Y. Liu, and X. Zhou. The response of a high-speed train wheel to a harmonic wheel–rail force. *Journal of Physics: Conference Series*, 744:012145, 2016. http://dx.doi.org/10.1088/1742-6596/744/1/012145.

[56] J. Fayos, L. Baeza, F. D. Denia, and J. E. Tarancón. An Eulerian coordinate-based method for analysing the structural vibrations of a solid of revolution rotating about its main axis. *Journal of Sound and Vibration*, 306(3):618–635, 2007. http://dx.doi.org/10.1016/j.jsv.2007.05.051.

[57] J. Martínez-Casas, L. Mazzola, L. Baeza, and S. Bruni. Numerical estimation of stresses in railway axles using a train–track interaction model. *International Journal of Fatigue*, 47:18–30, 2013. http://dx.doi.org/10.1016/j.ijfatigue.2012.07.006.

[58] J. Martínez-Casas, E. Di Gialleonardo, S. Bruni, and L. Baeza. A comprehensive model of the railway wheelset–track interaction in curves. *Journal of Sound and Vibration*, 333(18):4152–4169, 2014. http://dx.doi.org/10.1016/j.jsv.2014.03.032.

[59] M. Petyt. *Introduction to Finite Element Vibration Analysis*. Cambridge University Press, 2nd edition, 2010. ISBN: 9780521191609. http://dx.doi.org/10.1017/CBO9780511761195.

[60] V. T. Andrés, J. Martínez-Casas, J. Carballeira, and F. D. Denia. Development of a dynamic model of the axisymmetric railway wheel for sound radiation prediction. In *Proceedings of Internoise*, pages 3362–3368(7), Washington, D.C, USA, 2021. http://dx.doi.org/10.3397/IN-2021-2385.

[61] L. Baeza, J. Giner-Navarro, D. J. Thompson, and J. Monterde. Eulerian models of the rotating flexible wheelset for high frequency railway dynamics. *Journal of Sound and Vibration*, 449:300–314, 2019. http://dx.doi.org/10.1016/j.jsv.2019.03.002.

[62] F. J. Fahy and P. Gardonio. *Sound and Structural Vibration: Radiation, Transmission and Response*. Academic Press, 2nd edition, 2007. ISBN: 978-0-12-373633-8. http://dx.doi.org/10.1016/B978-0-12-373633-8.X5000-5.

[63] F. Fabre, J. S. Theyssen, A. Pieringer, and W. Kropp. Sound radiation from railway wheels including ground reflections: A half-space formulation for the fourier boundary element method. *Journal of Sound and Vibration*, 493:115822, 2021. http://dx.doi.org/10.1016/j.jsv.2020.115822.

[64] L. Gavrić. Computation of propagative waves in free rail using a finite element technique. *Journal of Sound and Vibration*, 185(3):531–543, 1995. http://dx.doi.org/10.1006/jsvi.1995.0398.

[65] X. Sheng, C. J. C. Jones, and D. J. Thompson. Responses of infinite periodic structures to moving or stationary harmonic loads. *Journal of Sound and Vibration*, 282(1):125–149, 2005. http://dx.doi.org/10.1016/j.jsv.2004.02.050.

[66] J. Yang and D. J. Thompson. A non-reflecting boundary for use in a finite element beam model of a railway track. *Journal of Sound and Vibration*, 337:199–217, 2015. http://dx.doi.org/10.1016/j.jsv.2014.10.037.

[67] X. Sheng, Y. He, S. Yue, and D. J. Thompson. Receptance of a semi-infinite periodic railway track and an equivalent multi-rigid body system for use

in truncated track models. *Journal of Sound and Vibration*, 559:117783, 2023. http://dx.doi.org/10.1016/j.jsv.2023.117783.

[68] D. J. Mead. A general theory of harmonic wave propagation in linear periodic systems with multiple coupling. *Journal of Sound and Vibration*, 27(2):235–260, 1973. http://dx.doi.org/10.1016/0022-460X(73)90064-3.

[69] M. A. Heckl. Railway noise - can random sleeper spacings help? *Acustica*, 81:559–564, 1995.

[70] M. A. Heckl. Coupled waves on a periodically supported timoshenko beam. *Journal of Sound and Vibration*, 252(5):849–882, 2002. http://dx.doi.org/10.1006/jsvi.2001.3823.

[71] K. Knothe and S. L. Grassie. Modelling of railway track and vehicle/track interaction at high frequencies. *Vehicle System Dynamics*, 22(3-4):209–262, 1993. http://dx.doi.org/10.1080/00423119308969027.

[72] T. X. Wu and D. J. Thompson. A double timoshenko beam model for vertical vibration analysis of railway track at high frequencies. *Journal of Sound and Vibration*, 224(2):329–348, 1999. http://dx.doi.org/10.1006/jsvi.1999.2171.

[73] T. X. Wu and D. J. Thompson. Analysis of lateral vibration behaviour of railway track at high frequencies using a continuously supported multiple beam model. *The Journal of the Acoustical Society of America*, 106(3):1369–1376, 1999. http://dx.doi.org/10.1121/1.427171.

[74] T. X. Wu and D. J. Thompson. Application of a multiple-beam model for lateral vibration analysis of a discretely supported rail at high frequencies. *The Journal of the Acoustical Society of America*, 108(3):1341–1344, 2000. http://dx.doi.org/10.1121/1.1285920.

[75] C. G. Koh, J. S. Y. Ong, D. K. H. Chua, and J. Feng. Moving element method for train-track dynamics. *International Journal for Numerical Methods in Engineering*, 56(11):1549–1567, 2003. http://dx.doi.org/10.1002/nme.624.

[76] J. Martínez-Casas, J. Giner-Navarro, L. Baeza, and F. D. Denia. Improved railway wheelset–track interaction model in the high-frequency domain. *Journal of Computational and Applied Mathematics*, 309:642–653, 2017. http://dx.doi.org/10.1016/j.cam.2016.04.034.

[77] J. Oscarsson. Dynamic train-track interaction: Variability attributable to scatter in the track properties. *Vehicle System Dynamics*, 37(1):59–79, 2002. http://dx.doi.org/10.1076/vesd.37.1.59.3538.

[78] T. X. Wu and D. J. Thompson. The influence of random sleeper spacing and ballast stiffness on the vibration behaviour of railway track. *Acta Acustica united with Acustica*, 86(2):313–321, 2000.

[79] N. Vincent, P. Bouvet, D. J. Thompson, and P-E. Gautier. Theoretical optimization of track components to reduce rolling noise. *Journal of Sound and Vibration*, 193(1):161–171, 1996. http://dx.doi.org/10.1006/jsvi.1996.0255.

[80] D. J. Thompson, W. J. van Vliet, and J. W. Verheij. Developments of the indirect method for measuring the high frequency dynamic stiffness of resilient elements. *Journal of Sound and Vibration*, 213(1):169–188, 1998. http://dx.doi.org/10.1006/jsvi.1998.1492.

[81] D. J. Thompson and J. W. Verheij. The dynamic behaviour of rail fasteners at high frequencies. *Applied Acoustics*, 52(1):1–17, 1997. http://dx.doi.org/10.1016/S0003-682X(97)00016-9.

[82] S. L. Grassie. Dynamic modelling of concrete railway sleepers. *Journal of Sound and Vibration*, 187(5):799–813, 1995. http://dx.doi.org/10.1006/jsvi.1995.0564.

[83] C. M. Nilsson, C. J. C. Jones, D. J. Thompson, and J. Ryue. A waveguide finite element and boundary element approach to calculating the sound radiated by railway and tram rails. *Journal of Sound and Vibration*, 321(3):813–836, 2009. http://dx.doi.org/10.1016/j.jsv.2008.10.027.

[84] D. Duhamel. Efficient calculation of the three-dimensional sound pressure field around a noise barrier. *Journal of Sound and Vibration*, 197(5):547–571, 1996. http://dx.doi.org/10.1006/jsvi.1996.0548.

[85] D. J. Thompson, C. J. C Jones, and N. Turner. Investigation into the validity of two-dimensional models for sound radiation from waves in rails. *The Journal of the Acoustical Society of America*, 113(4):1965–1974, 2003. http://dx.doi.org/10.1121/1.1555612.

[86] X. Zhang, D. J. Thompson, and G. Squicciarini. Sound radiation from railway sleepers. *Journal of Sound and Vibration*, 369:178–194, 2016. http://dx.doi.org/10.1016/j.jsv.2016.01.018.

[87] Railway applications – Wheelsets and bogies – Monobloc wheels – Technical approval procedure – Part 1: Forged and rolled wheels. EN 13979-1:2020. European Committee for Standardization, 2020.

[88] T. X. Wu and D. J. Thompson. Vibration analysis of railway track with multiple wheels on the rail. *Journal of Sound and Vibration*, 239(1):69–97, 2001. http://dx.doi.org/10.1006/jsvi.2000.3157.

[89] T. X. Wu and D. J. Thompson. The effects on railway rolling noise of wave reflections in the rail and support stiffening due to the presence of multiple wheels. *Applied Acoustics*, 62(11):1249–1266, 2001. http://dx.doi.org/10.1016/S0003-682X(01)00003-2.

[90] H. Hertz. Ueber die berührung fester elastischer körper. *Journal für die reine und angewandte Mathematik*, 1882(92):156–171, 1882. http://dx.doi.org/10.1515/crll.1882.92.156.

[91] R. D. Mindlin. Compliance of elastic bodies in contact. *Journal of Applied Mechanics*, 16(3):259–268, 1949. http://dx.doi.org/10.1115/1.4009973.

[92] A. Wickens. *Fundamentals of Rail Vehicle Dynamics*. CRC Press, 2003. ISBN: 9780429224652, http://dx.doi.org/10.1201/9780203970997.

[93] K. Knothe and S. Stichel. *Rail Vehicle Dynamics*. Springer International Publishing, 2017. ISBN: 978-3-319-45376-7, http://dx.doi.org/10.1007/978-3-319-45376-7.

[94] S. Iwnicki, M. Spiryagin, C. Cole, and T. McSweeney, editors. *Handbook of Railway Vehicle Dynamics*. CRC Press, 2nd edition, 2019. ISBN: 9780429469398, http://dx.doi.org/10.1201/9780429469398.

[95] J. J. Kalker. *On the rolling contact of two elastic bodies in the presence of dry friction*. PhD Thesis, Delft University of Technology, 1967. http://resolver.tudelft.nl/uuid:aa44829b-c75c-4abd-9a03-fec17e121132.

[96] J. J. Kalker. *Three-Dimensional Elastic Bodies in Rolling Contact*. Springer Dordrecht, 1990. ISBN: 978-0-7923-0712-9. http://dx.doi.org/10.1007/978-94-015-7889-9.

[97] P. J. Vermeulen and K. L. Johnson. Contact of nonspherical elastic bodies transmitting tangential forces. *Journal of Applied Mechanics*, 31(2):338–340, 1964. http://dx.doi.org/10.1115/1.3629610.

[98] Z. Y. Shen, J. K. Hedrick, and J. A. Elkins. A comparison of alternative creep force models for rail vehicle dynamic analysis. *Vehicle System Dynamics*, 12(1-3):79–83, 1983. http://dx.doi.org/10.1080/00423118308968725.

[99] M. Spiryagin, S. Bruni, C. Bosomworth, P. Wolfs, and C. Cole. *Rail Vehicle Mechatronics*. CRC Press, 1st edition, 2021. http://dx.doi.org/10.1201/9781003028994.

[100] J. J. Kalker. A fast algorithm for the simplified theory of rolling contact. *Vehicle System Dynamics*, 11(1):1–13, 1982. http://dx.doi.org/10.1080/00423118208968684.

[101] J. J. Kalker. Wheel-rail rolling contact theory. *Wear*, 144(1):243–261, 1991. http://dx.doi.org/10.1016/0043-1648(91)90018-P.

[102] K. Knothe and A. Gross-Thebing. Derivation of frequency dependent creep coefficients based on an elastic half-space model. *Vehicle System Dynamics*, 15(3):133–153, 1986. http://dx.doi.org/10.1080/00423118608968848.

[103] A. Gross-Thebing. Frequency-dependent creep coefficients for three-dimensional rolling contact problems. *Vehicle System Dynamics*, 18(6):359–374, 1989. http://dx.doi.org/10.1080/00423118908968927.

[104] B. Hemsworth. Recent developments in wheel/rail noise research. *Journal of Sound and Vibration*, 66(3):297–310, 1979. http://dx.doi.org/10.1016/0022-460X(79)90847-2.

[105] S. Bühler. Methods and results of field testing of a retrofitted freight train with composite brake blocks. *Journal of Sound and Vibration*, 293(3):1041–1050, 2006. http://dx.doi.org/10.1016/j.jsv.2005.08.055.

[106] P. J. Remington and J. Webb. Wheel/rail noise reduction through profile modification. *Journal of Sound and Vibration*, 193(1):335–348, 1996. http://dx.doi.org/10.1006/jsvi.1996.0274.

[107] D. J. Thompson and P. J. Remington. The effects of transverse profile on the excitation of wheel/rail noise. *Journal of Sound and Vibration*, 231(3):537–548, 2000. http://dx.doi.org/10.1006/jsvi.1999.2543.

[108] D. J. Thompson. But are the trains getting any quieter? In *Proceedings of the International Congress on Sound and Vibration*, Cairns, Australia, 2007.

[109] D. J. Thompson and P-E. Gautier. Review of research into wheel/rail rolling noise reduction. *Proceedings of the Institution of Mechanical Engineers, Part F: Journal of Rail and Rapid Transit*, 220(4):385–408, 2006. http://dx.doi.org/10.1243/0954409JRRT79.

[110] P. Fodiman, L. Castel, and G. Gaborit. Validation of a tgv-a trailing-car wheel with an acoustically optimised profile. In *Proceedings of International Wheelset Congress*, Paris, France, 1995.

[111] J. C. O. Nielsen and C. R. Fredö. Multi-disciplinary optimization of railway wheels. *Journal of Sound and Vibration*, 293(3):510–521, 2006. http://dx.doi.org/10.1016/j.jsv.2005.08.063.

[112] X. Garcia-Andrés, J. Gutiérrez-Gil, J. Martínez-Casas, and F. D. Denia. Wheel shape optimization approaches to reduce railway rolling noise. *Structural and Multidisciplinary Optimization*, 62(5):2555–2570, 2020. http://dx.doi.org/10.1007/s00158-020-02700-6.

[113] X. Garcia-Andrés, J. Gutiérrez-Gil, V. T. Andrés, J. Martínez-Casas, J. Carballeira, and F. D. Denia. Rolling noise reduction through ga-based wheel shape optimization techniques. In *Proceedings of ECCOMAS Young Investigators Conference*, pages 304–312, Valencia, Spain, 2021. http://dx.doi.org/10.4995/YIC2021.2021.12577.

[114] C. J. C. Jones and J. W. Edwards. Development of wheels and track components for reduced rolling noise from freight trains. In *Proceedings of Internoise*, pages 403–408(6), Liverpool, England, 1996.

[115] B. Hemsworth, P-E. Gautier, and R. Jones. Silent freight and silent track projects. In *Proceedings of Internoise*, pages 2429–2437(9), Nice, France, 2000.

[116] A. Daneryd, J. C. O. Nielsen, E. Lundberg, and A. Frid. On vibro-acoustic and mechanical properties of a perforated railway wheel. In *Proceedings of the International Workshop on Railway and Tracked Transit System Noise*, page 305–317, Ile des Embiez, France, 1998.

[117] N. Vincent. Rolling noise control at source: State-of-the-art survey. *Journal of Sound and Vibration*, 231(3):865–876, 2000. http://dx.doi.org/10.1006/jsvi.1999.2646.

[118] J. C. O. Nielsen. Acoustic optimization of railway sleepers. *Journal of Sound and Vibration*, 231(3):753–764, 2000. http://dx.doi.org/10.1006/jsvi.1999.2560.

[119] C. J. C. Jones and D. J. Thompson. Rolling noise generated by railway wheels with visco-elastic layers. *Journal of Sound and Vibration*, 231(3):779–790, 2000. http://dx.doi.org/10.1006/jsvi.1999.2562.

[120] P. Bouvet, N. Vincent, A. Coblentz, and F. Demilly. Optimization of resilient wheels for rolling noise control. *Journal of Sound and Vibration*, 231(3):765–777, 2000. http://dx.doi.org/10.1006/jsvi.1999.2561.

[121] V. T. Andrés, J. Martínez-Casas, J. Carballeira, and F. D. Denia. Railway rolling noise mitigation through optimal track design. In *Proceedings of ECCOMAS Young Investigators Conference*, pages 313–319, Valencia, Spain, 2021. http://dx.doi.org/10.4995/YIC2021.2021.12583.

[122] V. T. Andrés, J. Martínez-Casas, J. Carballeira, and F. D. Denia. Desarrollo de un modelo vibroacústico integral rueda-vía para la predicción de ruido de rodadura ferroviario y estudio para su mitigación. In *Proceedings of Congreso Nacional de Ingeniería Mecánica*, Jaén, Spain, 2021.

[123] C. J. C. Jones, D. J. Thompson, A. Frid, and M. Wallentin. Design of a railway wheel with acoustically improved cross-section and constrained layer damping. In *Proceedings of Internoise*, pages 2380–2386(7), Nice, France, 2000.

[124] X. Garcia-Andrés, J. Martínez-Casas, F. D. Denia, A. Pieringer, and W. Kropp. Reducing rolling noise in railway wheels with constrained layer damping treatments considering comprehensive viscoelastic models. In *Proceedings of the International Congress on Sound and Vibration*, Prague, Czech Republic, 2023.

[125] D. J. Thompson, C. J. C. Jones, T. P. Waters, and D. Farrington. A tuned damping device for reducing noise from railway track. *Applied Acoustics*, 68(1):43–57, 2007. http://dx.doi.org/10.1016/j.apacoust.2006.05.001.

[126] C. Gramowski and T. Gerlach. Entering the real operation phase: Design, construction and benefit verification of freight wheel noise absorber. In *Proceedings of International Workshop on Railway Noise*, Ghent, Belgium, 2019.

[127] J. Färm. Evaluation of wheel dampers on an intercity train. *Journal of Sound and Vibration*, 267(3):739–747, 2003. http://dx.doi.org/10.1016/S0022-460X(03)00737-5.

[128] B. Asmussen, D. Stiebel, P. Kitson, D. Farrington, and D. Benton. Reducing the noise emission by increasing the damping of the rail: Results of a field test. In *Proceedings of International Workshop on Railway Noise*, Munich, Germany, 2007.

[129] P. Bouvet, N. Vincent, A. Coblenz, and F. Demilly. Rolling noise from freight railway traffic: Reduction of wheel radiation by means of tuned absorbers. In *Proceedings of Internoise*, pages 2407–2414(8), Nice, France, 2000.

[130] F. Létourneaux, J. F. Cordier, F. Poisson, and N. Douarche. High speed railway noise: Assessment of mitigation measures. In *Proceedings of International Workshop on Railway Noise*, Munich, Germany, 2007.

[131] B. Hemsworth. Rail system environmental noise prediction, assessment, and control. In M. J. Crocker, editor, *Handbook of Noise and Vibration Control*, chapter 121. John Wiley & Sons, 2007. http://dx.doi.org/10.1002/9780470209707.ch121.

[132] R. R. K. Jones. Bogie shrouds and low barriers could significantly reduce wheel/rail noise. *Railway Gazette International*, pages 459–462, 1994.

[133] J. Oertli. The STAIRRS project, work package 1: a cost-effectiveness analysis of railway noise reduction on a european scale. *Journal of Sound and Vibration*, 267(3):431–437, 2003. http://dx.doi.org/10.1016/S0022-460X(03)00705-3.

[134] D. C. Montgomery. *Design and Analysis of Experiments, 10th Edition*. John Wiley & Sons, Inc., 2019. ISBN: 978-1-119-49244-3.

[135] J. W. Pratt. Dividing the indivisible: Using simple symmetry to partition variance explained. pages 245–260. Proceedings of the Second International Conference in Statistics, University of Tampere, Tampere, Finland, 1987.

[136] V. T. Andrés, J. Martínez-Casas, J. Carballeira, and F. D. Denia. A vibroacoustic model of the stationary railway wheel for sound radiation prediction through an axisymmetric approach. In *Proceedings of ECCOMAS Young Investigators Conference*, pages 320–325, Valencia, Spain, 2021. http://dx.doi.org/10.4995/YIC2021.2021.12584.

[137] G. K. Batchelor. *An Introduction to Fluid Dynamics*. Cambridge University Press, 2000. ISBN: 9780511800955, http://dx.doi.org/10.1017/CBO9780511800955.

[138] R. B. Bird, W. E. Stewart, and E. N. Lightfoot. *Transport Phenomena*. John Wiley & Sons, 2nd edition, 2006. ISBN: 978-0-470-11539-8.

[139] C. Knuth, G. Squicciarini, D. Thompson, and L. Baeza. Effects of rotation on the rolling noise radiated by wheelsets in high-speed railways. *Journal of Sound and Vibration*, 572:118180, 2024. http://dx.doi.org/10.1016/j.jsv.2023.118180.

[140] *VI-Grade GmbH, VI-Rail 2022.1 Documentation*. VI-Grade Engineering Software & Services, 2022.

[141] W. Liu, L. Du, W. Liu, and D. J. Thompson. Dynamic response of a curved railway track subjected to harmonic loads based on the periodic structure theory. *Proceedings of the Institution of Mechanical Engineers, Part F: Journal of Rail and Rapid Transit*, 232(7):1932–1950, 2018. http://dx.doi.org/10.1177/0954409718754470.

[142] S. Iwnicki. Manchester benchmarks for rail vehicle simulation. *Vehicle System Dynamics*, 30(3-4):295–313, 1998. http://dx.doi.org/10.1080/00423119808969454.

Part II

Papers

PAPER 1

Influence study of rail geometry and track properties on railway rolling noise

V. T. Andrés[a], J. Martínez-Casas[a], F. D. Denia[a], and D. J. Thompson[b]

[a] Instituto de Ingeniería Mecánica y Biomecánica, Universitat Politècnica de València, Valencia, Spain
[b] Institute of Sound and Vibration Research, University of Southampton, Southampton, UK

Journal of Sound and Vibration
Volume 525, Article number 116701, 2022
DOI: 10.1016/j.jsv.2021.116701

Abstract

Wheel/rail interaction generates an excitation due to the roughness present on the surface of both components that produces vibration and consequently rolling noise. In this work, the railway track properties that most influence rolling noise are identified and this influence is analysed to reduce noise emission. The acoustic calculation methodology consists of characterizing the wheel using finite element techniques and the track using periodic structure theory. The influence of the track properties on the sound radiation is analysed by means of statistical techniques applied to the acoustic power results of different track configurations. To achieve this, the rail cross-section geometry is parameterized and numerous simulations are carried out by modifying these geometric parameters and the viscoelastic properties of the track components. Considering the contribution of the wheel, rail and sleeper, the results obtained indicate that the total radiation can be reduced by up to 7.4 dB(A) through an optimal combination of the track design parameters, compared to the worst combination found. In particular, the rail pad stiffness is shown to be the most influential parameter in the sound radiation.

Keywords

Railway dynamics; track influence; rolling noise; wheel/rail interaction; sound radiation model; design of experiments; noise mitigation.

Contents

1 Introduction

Railway transport is one of the most efficient, safe and environmentally friendly means of transport. However, it has been in the media focus in recent years due to the noise pollution generated. According to the World Health Organization, the noise pollution, in particular due to transport, is the second most damaging environmental factor for humans after air pollution [1]. Rolling noise is considered one of the main sources of railway sound radiation [2] and the most important in most situations [3]. This is produced as a consequence of the roughness of the wheel and rail surfaces which induces relative movement and thereby generates dynamic contact forces. These excite the wheel and the track, causing a vibrational field that results in a radiated sound field. The frequency range of interest for rolling noise generation extends up to about 6 kHz [4]; above that frequency, the sound radiation falls abruptly due to the action of the contact filter [2, 5]. The main railway elements involved in rolling noise radiation are the sleepers, rails and wheels [6]. Furthermore, the frequency ranges of noise emission of each element exhibit some differences: the sleeper radiates at low and medium frequencies, the rail at medium and high frequencies and the wheel mainly at higher frequencies [6, 7].

Due to the great importance of railway noise pollution, especially in urban areas, different measures applied to the wheel and track have been proposed in the literature to mitigate rolling noise [8]. In regard to the wheel, Nielsen and Fredö [9] carried out a design of experiments with geometric parameters of the wheel and set up response surface models to find quieter designs; recently Garcia-Andrés *et al.* [10] proposed the use of optimization techniques on the wheel geometry with the same purpose; Jones and Thompson [11] studied the rolling noise generated by railway wheels with visco-elastic layers; Färm [12] tested the sound radiation for different circulation speeds when wheel dampers were included; Gramowski and Gerlach [13] presented a ready-to-market quiet wheelset design for freight traffic using vibration absorbers and Létourneaux *et al.* [14] proposed the use of wheel damping rings combined with rail dampers to attenuate both wheel and track noise components. In relation to the track, Thompson *et al.* [15] proposed the use of damping devices with viscoelastic materials and spring-mass type systems located both continuously and discretely along the circulation direction; Asmussen *et al.* [16] tested the reduction in the noise radiation of a track equipped with rail dampers for different circulation speeds and train types; Sun *et al.* [17] found large reductions in the radiation above 800 Hz by using this type of device and Gramowski and Suppin [18] assessed the impact of rail dampers on the long-term rail roughness development. The geometry of the rail cross-section has also been under consideration for the reduction of the radiated noise levels [19]. About the

sleeper, Nielsen [7] concluded that the rail pad and ballast are the most important factors for the sleeper radiation, its geometry being of minor relevance. Regarding the rail pad, its design is an important task, since its properties have an opposite influence on the radiation of the rail and sleeper; Vincent *et al.* [20] carried out a parametric study of the influence of the rail pad stiffness and damping on sound radiation and showed that a stiff pad leads to reductions in rail noise and increases in sleeper noise. The optimal pad stiffness was shown to be at the high end of what is practical.

With the purpose of carrying out a detailed study of the influence of different parameters on rolling noise to mitigate sound radiation, a vibroacoustic model of the railway elements has been implemented and compared with the commercial package TWINS [21, 22]. A modal approach is considered for the wheel [23] and the track formulation is based on periodic structure theory [24]. Likewise, the rail cross-section geometry has been parametrized taking into account the European rails specified by the standard EN13674-1 [25] and, along with parameters describing the stiffness and damping of the rail pad and ballast, a design of experiments has been performed. A factorial design is proposed to analyse the influence and importance of these parameters in the sound radiation of the railway elements by means of ANOVA techniques [26] and using the methodology developed by Pratt [27].

The vibroacoustic model of the railway elements is presented in Section 2. Then, in Section 3, the design of experiments carried out and the analysis methodology to investigate the influence of different parameters are described. Section 4 discusses the results and the main conclusions are summarized in Section 5.

2 Railway vibroacoustic model

2.1 Wheel model

A three-dimensional approach is adopted to model the dynamic behaviour of the wheel by the Finite Element Method (FEM), considering the wheel as a flexible solid with N degrees of freedom (dof's). Given the wheel geometry, three directions of motion are defined, namely: axial or out-of-plane, radial and circumferential. These three directions form the cylindrical coordinate system employed for the wheel.

A modal approach is adopted and the motion equation is formulated in the frequency domain. Wheel modeshapes can be characterized in accordance with the

number of nodal lines (i.e. remaining at rest) in different directions [2]. On the one hand, nodal diameters are defined as stationary lines that traverse the wheel in radial direction through its centre; on the other hand, nodal circles are defined as nodal lines with tangential direction, forming a circle the centre of which coincides with the wheel axis. In [2] a relation between the number of nodal diameters n of a modeshape and its modal damping ratio ξ is proposed, so that vibration modes with $n = 0$ have $\xi = 10^{-3}$, modes with $n = 1$ have $\xi = 10^{-2}$ and modes with $n \geq 2$ have $\xi = 10^{-4}$.

The wheel vibrational field in the frequency domain is obtained by means of modal superposition, considering the contribution of each vibration mode to the response. Specifically, it is computed as the product of the interaction force and the frequency response function (FRF) of the wheel. This response can be formulated in terms of velocity (mobility), as follows:

$$Y_{jk}(\omega) = \mathrm{i}\omega \sum_{r=1}^{tr} \frac{\phi_{kr}\phi_{jr}}{\omega_r^2 - \omega^2 + 2\mathrm{i}\xi_r\omega_r\omega}, \tag{1}$$

$$v_j(\omega) = \sum_{i=1}^{nd} Y_{ji}(\omega)F_i(\omega), \tag{2}$$

where ω is the harmonic excitation frequency, $Y_{jk}(\omega)$ is the mobility measured in the jth dof when a unit force is applied in the kth dof, ω_r is the natural frequency of the rth vibration mode, ϕ_{kr} is the modal amplitude of the kth dof for the rth mode normalized to unit mass matrix and tr is the truncation or number of modes considered as basis for the wheel response $v_j(\omega)$, formulated in terms of velocity. The number of directions considered in the wheel/rail interaction problem is given by nd while $F_i(\omega)$ is the value of the contact force applied in the ith direction at the contact point, which is obtained as indicated in Section 2.3.

After solving the railway wheel dynamics, its acoustic radiation is computed by postprocessing the vibrational field on its surface. The radiation model employed in this work was developed by Thompson [28] and it establishes that wheel sound power is obtained as the sum of the power associated with each set of modes with the same number of nodal diameters n. This model is implemented in the commercial software TWINS and the details of the formulation can be found in [29]. The methodology consists of dividing the wheel surface into a number of concentric annular surfaces delimited by two radii assuming that the radiation in axial direction is a consequence of the motion of those annular surfaces, considered of constant amplitude. Likewise, it is assumed that the radiation in radial direc-

tion is due to the wheel tyre motion, also considered of constant amplitude. The wheel acoustic power W^W, considering a finite number p of annular surfaces, is evaluated as follows:

$$W^W(\omega) = \rho c \sum_n \left(\sigma_{a,n}(\omega) \sum_{j=1}^{p} \left(S_{a,j} \overline{\widetilde{v^2}}_{a,j,n}(\omega) \right) + \sigma_{r,n}(\omega) S_r \overline{\widetilde{v^2}}_{r,n}(\omega) \right), \qquad (3)$$

where ρ is the density of air, c is the speed of sound and the subscripts a and r make reference to the axial and radial contribution, respectively. Functions σ are the radiation ratios, that can be obtained numerically, and for which a number of fitting expressions can be found in reference [28]. The subscript j loops over the annular surfaces and $S_{a,j}$ and S_r are the projected axial and radial radiation surfaces, respectively. Finally, the projected squared velocities are averaged over time ($\widetilde{\ }$) and space ($\overline{\ }$) and they are defined for each annular surface in axial direction and for the tyre in radial direction.

2.2 Track model

The railway track considered in this work is formed by the rail, rail pad, sleeper and ballast. The rail is modelled as an infinite structure supported by the sleepers by means of the rail pads and ballast. The latter are modelled as viscoelastic material and the sleeper is considered a rigid solid. In this way, the rail is supported by a spring-mass-spring system so that the railway track is modelled as a continuous viscoelastic two-layer with uniform transverse section as shown in Fig. 1. The properties of the rail pad, sleeper and ballast are distributed per unit length; although this approach omits the effects associated with the pinned-pinned frequency, which are more significant for stiff rail pads, it is commonly used for noise predictions due to its simplicity [21]. In this model, no connection is considered between adjacent sleepers.

The track is modelled as an infinite structure through which, due to the wheel/rail interaction force, structural waves propagate in longitudinal direction (vehicle circulation direction); these waves form the basis for the track response. In order to obtain the variables that define these waves, the methodology proposed by Mead is employed [30]. This methodology consists of analysing a track segment by means of finite element techniques; in this work a segment with a length of 10 mm is considered, as proposed by Thompson [24]. This segment along with its modelling is shown in Fig. 2. The rail section is discretized in a number of dof's, the sleeper section is modelled as a rigid solid and the rail pad and ballast as massless viscoelastic materials.

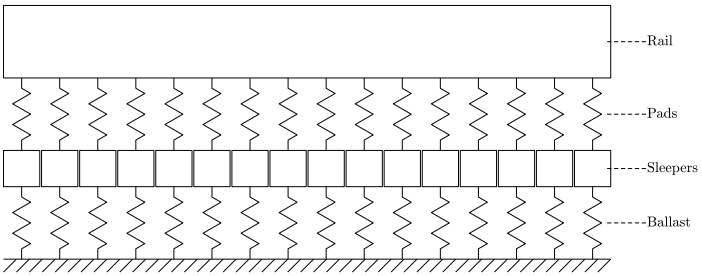

Fig. 1: Railway track model.

The treatment of the motion equation of the segment, in accordance with the methodology presented in [24, 30], allows the information to be known related to structural waves that propagate through the track; specifically, the waveshape ψ_r at any section point and the wavenumber k_r are known for the rth wave. By employing a cartesian reference system with origin in the contact point, where the x and y coordinates are contained in the track section and the z coordinate represents the longitudinal direction, then the displacement of any point on the track u is obtained as wave superposition:

$$u\left(x,y,z\right)=\sum_{r=1}^{m}A_r\psi_r\left(x,y\right)\mathrm{e}^{-\mathrm{i}k_r|z|}, \tag{4}$$

where m is the number of structural waves, which in the FE dynamic model is given by the number of dof's in the track section, and A_r is the generalized coordinate corresponding to the rth wave, that takes into account the contribution of this wave to the system response. By combining Eq. (4) and the motion equation of the segment, and considering continuity in displacements as well as balance of forces, the generalized coordinates are related to the input interaction force, as indicated in [24]. In Eq. (4) the frequency is implicit in the different functions defining the propagation. The FRF of the track is computed through Eq. (4) by applying a unit force and solving the generalized coordinates. After this, the Track Decay Rate (TDR) can be numerically evaluated similarly to the procedure described by the standard EN15461 [31]; the TDR characterizes the attenuation of the vibration on the track and, generally, has an inverse correlation with the track noise.

Regarding the track sound radiation, the contributions from both the rail and sleeper are considered. The acoustic model implemented for the rail is described in

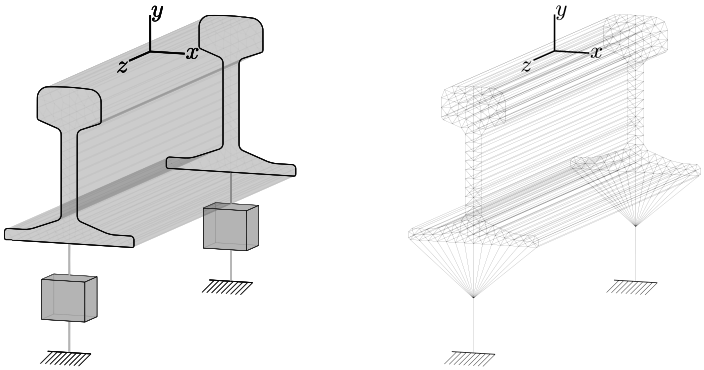

Fig. 2: Track segment (left) and its modelling (right). Figure out of scale in the longitudinal direction (z axis).

[29] and it is assumed a two-dimensional radiation of each rail cross-section, which is subsequently corrected to take into account the three-dimensional nature of the sound radiation. Bearing in mind that the rail acoustic power is proportional to the square velocity of its surface, then the power radiated by a differential of rail δz located at a distance z from the rail contact cross-section (the rail cross-section in which the wheel/rail contact occurs) due to the rth wave is

$$\delta W_r^R(z) = \widehat{W_r'^R}\ \mathrm{e}^{2\mathrm{Im}(k_r)|z|}\delta z, \tag{5}$$

where $\widehat{W_r'^R}$ is the power radiated by the rail contact cross-section per unit length ($\widehat{\ }$ indicates the contact cross-section and $'$ indicates per unit length). By integrating Eq. (5) over the rail (z coordinate from $-\infty$ to $+\infty$), the sound power associated with the rth wave is obtained. Finally, under the assumption that the different waves can be considered to radiate independently [29], the total rail power is the sum of each wave power, that is,

$$W^R = \sum_{r=1}^{m} \frac{\widehat{W_r'^R}}{-\mathrm{Im}(k_r)}. \tag{6}$$

In conclusion, since the response decay law of each wave is known, the rail radiation is obtained by computing the power of the cross-section and solving analytically the longitudinal direction. The sound radiation model of the rail contact cross-section $\widehat{W_r'^R}$ is based on Kirchhoff-Helmholtz integral equation [32], and detailed formulation can be found in appendix D of [29]. It is noted that this

procedure consists of the two-dimensional estimation of the rail sound power and the analytical resolution of the longitudinal direction. This approach supposes a reasonable hypothesis for low decay rate waves; however, for high decay rate waves it is no longer valid. Accordingly, Thompson *et al.* [33] obtained numerically correction terms to consider the three-dimensional nature of the radiation of high decay rate waves, which are used here.

The same radiation model of the rail is employed for the sleeper, the other acoustically relevant element of the track. In this work, the sleeper is modelled as a rigid solid without considering the deformation of its section. Following the same procedure previously indicated for the rail and considering the sleeper motion in the cross-section in which the wheel/rail contact occurs, its sound power per unit length $\widehat{W_r'^S}$ is obtained and, applying Eq. (6), the sleeper acoustic power is calculated. Since the sleeper is in fact located discontinuously along the longitudinal direction, its radiation is adjusted by a factor b/d, where b is the width of the sleeper and d is the distance between sleepers.

2.3 Wheel/rail interaction

The wheel and rail surface roughness implies a source of excitation when the vehicle runs on the track due to the relative movement between both components. This excitation generates a vibrational field in the railway elements, producing rolling noise. Some typical roughness spectra are defined by the standard EN13979-1 [34]; particularly, in this work, the spectrum corresponding to wheels with cast iron brake blocks is considered. Also, the contact model proposed by Thompson is employed and details of the formulation can be found in [2,35]; from the roughness $\mathbf{r}$, which is assumed to have content only in vertical direction, the rail/wheel interaction force $\mathbf{F}$ is obtained solving the system

$$\left(\mathbf{H}^W + \mathbf{H}^C + \mathbf{H}^R\right)\mathbf{F} = \mathbf{r}, \tag{7}$$

where $\mathbf{H}^W$, $\mathbf{H}^C$ and $\mathbf{H}^R$ are the receptances in matrix form defined in the contact point for the wheel, contact and rail, respectively. For the wheel and rail receptance, calculation details have been presented in Section 2.1 and Section 2.2, respectively; contact receptance model is detailed in [2]. In this work, the interaction problem considers vertical and lateral directions and it is assumed that there is no steady state creepage superimposed on the dynamic motion. Likewise, the contact filter model developed by Remington [5] is included using the simplified form presented by Thompson [2]. The implementation of the model described in this Section has been verified by extensive comparisons with TWINS [21, 22].

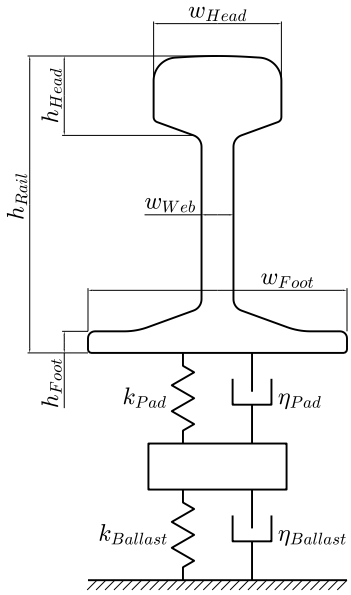

Fig. 3: Design variables of rail cross-section geometry and track properties.

3 Design of experiments

3.1 Design set up

The formulation presented in Section 2 has been implemented in order to analyse the influence of the properties of the railway components on their sound radiation. Regarding the wheel, Nielsen and Fredö [9] parametrized its geometry and they carried out a study of the influence of the geometric parameters on the acoustic radiation. In a recent work, Garcia-Andrés *et al.* [10] performed a geometric optimization of the wheel by using genetic algorithms to reduce rolling noise.

This work focuses on the influence of track properties on rolling noise. Specifically, the influence of the rail geometry and viscoelastic properties of the rail pad and ballast on the rail, sleeper and wheel sound radiation is studied. To this end, firstly, the rail cross-section is parameterized taking into account six main variables and bounds of each one are established; similarly, the viscoelastic properties of the pad and ballast are considered through four variables with their corresponding bounds. These ten design variables are shown in Fig. 3. Subsequently, a design of experiments and an ANOVA [26] on the results are

Table 1: Design variables bounds.

Design variable	Lower bound	Upper bound
h_{Foot} [mm]	8	15
h_{Head} [mm]	39	49
h_{Rail} [mm]	142	172
w_{Foot} [mm]	120	150
w_{Head} [mm]	62	75
w_{Web} [mm]	14	20
k_{Pad} [MN/m]	130	1300
η_{Pad} [-]	0.25	0.5
$k_{Ballast}$ [MN/m]	40	100
$\eta_{Ballast}$ [-]	1	2

performed, looking for a regression model that fits the calculated acoustic power. If the regression model is good enough, the analysis of the regression coefficents makes it possible to know the influence of the different contributing variables on the response variable, that is, on the railway sound radiation.

Regarding the pad and ballast stiffness, for simplicity the ratio between the lateral and vertical components is fixed: 1/13 for pad and 1/2 for ballast [4, 20]. Thus, variables k_{Pad} and $k_{Ballast}$ refer hereinafter to the vertical component of the pad and ballast stiffness, respectively. Likewise, structural damping of pad and ballast is considered through damping loss factors η_{Pad} and $\eta_{Ballast}$, respectively. The ranges of application of each design variable are shown in Table 1. The geometric parameter bounds are established based on the minimum and maximum dimensions that appear on the European rails specified by the standard EN13674-1 [25]. The viscoelastic parameter bounds are set according to the literature: values of k_{Pad} used in the European railway networks are specified in [20], limits of $k_{Ballast}$ are established to determine its influence on the vehicle/track interaction in [36] and the track dynamic behaviour at high frequencies is analysed for, among other parameters, different values of η_{Pad} and $\eta_{Ballast}$ in [37].

3.2 Influence analysis methodology

In order to analyse the influence of the aforementioned ten parameters on the sound radiation of the rail, sleeper and wheel, a factorial design M^{10} without repetitions is proposed, M being the number of levels or values that each variable takes, covering all combinations of those levels in the parameters. An ANOVA is performed on the results of the simulations, modifying the effects to be considered to ensure their statistical significance on the sound power $SWL_{\sum}$, quantified by adding the energy contained in the frequency spectrum and it is expressed in decibels, that is,

$$SWL_{\sum} = 10 \log_{10} \left(\sum_{i=1}^{n_{bands}} 10^{\frac{SWL_i}{10}} \right), \tag{8}$$

where subscript i loops into the frequency one-third octave bands in which radiation is studied, n_{bands} is the number of one-third octave bands and SWL_i is the sound power level of the ith one-third octave band, obtained according to the procedure described by the standard EN13979-1 [34], which includes the effect of the contact filter and the A-weighting filter to consider the human ear perception [38].

This work not only seeks to determine the influence of each parameter on the response variable, but also to define its importance. For this purpose, the technique developed by Pratt [27], widely described by Thomas *et al.* [39, 40], is applied. The methodology allows the importance to be determined of each contributing variable from the set of samples obtained from the calculation of the factorial design. For these samples, a polynomial regression for the sound power of each railway element is performed where the response variable contains the radiation from each combination in the design of experiments after a standarization of the vector to null mean and unit norm, such that

$$\widehat{\mathbf{y}} = \sum_j \beta_j \mathbf{x}_j, \tag{9}$$

where $\widehat{\mathbf{y}}$ contains the response variable adjusted by least squares for each sample, $\mathbf{x}_j$ contains the standarized jth effect for each sample and β_j is the standarized regression coefficient for the jth effect. An effect might be a simple parameter, the interaction between parameters or the exponent of a parameter. In Eq. (9), orthogonal components of $\beta_j \mathbf{x}_j$ to $\widehat{\mathbf{y}}$ sum to zero and their projections onto $\widehat{\mathbf{y}}$ sum to precisely $\|\widehat{\mathbf{y}}\|$, $\| \ \|$ being the Euclidean norm. Therefore, these projections represent the importance of each effect on the response variable. The projection of the jth effect onto the adjusted response variable $\mathbf{P}_{\widehat{\mathbf{y}}}(\beta_j \mathbf{x}_j)$ is calculated as

$$\mathbf{P}_{\widehat{\mathbf{y}}}(\beta_j \mathbf{x}_j) = \frac{\widehat{\mathbf{y}} \cdot \beta_j \mathbf{x}_j}{\|\widehat{\mathbf{y}}\|} \frac{\widehat{\mathbf{y}}}{\|\widehat{\mathbf{y}}\|}. \tag{10}$$

Pratt [27] defined the relative importance of the jth effect as the ratio between the length of this projection and the length of $\widehat{\mathbf{y}}$. Thus, the summation of the relative importances defined by Pratt is unity. In this work, the importance of an effect is redefined as the proportion of variance in the response variable that it explains; in this context, the variance explained by the regression considering all the effects is the coefficient of determination R^2 of the regression model. The importance of an effect d_j is

$$d_j = \widehat{\mathbf{y}} \cdot \beta_j \mathbf{x}_j, \tag{11}$$

so that

$$\sum_j d_j = R^2. \tag{12}$$

4 Results

In this section, the influence of the track on sound radiation is analysed. Initially, a 3^{10} factorial design is proposed, considering three levels of each parameter corresponding to the minimum, medium and maximum values of its range (see Table 1). For each combination, by means of the implemented tool, the vibroacoustic problem is solved; to do this, the rail cross-section geometry is created, the dynamic wheel and track FE models are generated, the interaction between the two is resolved and the sound radiation of each railway element is calculated. An ANOVA with the significant effects is performed on the results and the Pratt methodology, described in Section 3.2, is applied to determine the variance explanation of each effect. By using this technique, the design variables influencing the sound power of each railway element are established. For each element, in order to have a greater spectrum of the noise range with respect to the variation of the most important parameters, this analysis procedure is repeated performing another factorial design with more levels of the contributing variables.

The results are expressed as the sound power due to one wheel and the associated track vibration. The following calculation parameters are considered fixed:

– A wheel with a straight web and a diameter of 900 mm, as well as a mass of 330 kg and a S1002 profile.

– A damping loss factor of 0.02 for the rail.

– A distance between sleepers of 0.6 m and a half sleeper with dimensions of 0.84 m in length (x direction), 0.22 m in height (y direction) and 0.25 m in bottom and top width (z direction), and with a mass of 122 kg.

– A vehicle speed of 80 km/h, a vertical static load of 50 kN per wheel and a roughness spectrum defined by the standard EN13979-1 corresponding to a wheel with cast iron brake blocks.

4.1 Influence on rail radiation

From the initial study, applying the Pratt methodology, the proportion of variance in rail radiation explained by each effect is determined, as well as the cumulative proportion. The variance explained by the more relevant effects is shown in Fig. 4 (colour black); the importance of the remaining effects is summed and represented as 'Rest'. In the context of the current investigation, the most important variables are identified as: w_{Foot}, k_{Pad} and η_{Pad}. Therefore, the sound power variation due to the other variables is considered negligible. In comparison to the three aforementioned variables, rail cross-section geometry barely affects track dynamics in the frequency range of rail radiation (from 500 Hz to 2 kHz), so that the geometric parameters are not important design variables except w_{Foot}; the rail foot width is important since it alters the radiation ratio of the rail [2] and also its surface area has high velocities of vibration at higher frequencies. In this frequency range, the track behaviour is governed by the rail pad, so its stiffness and damping are important parameters in the rail radiation. Regarding the ballast, it is a component that influences the track dynamics below the frequency range in which the rail radiation is important. With these relevant design variables, a design of experiment is carried out considering eight levels of each one, that is, a design with 8^3 combinations. Again, the proportion of variance explained by each effect in the polynomial regression model is determined, which is shown in Fig. 4 (colour blue) along with the cumulative proportion. The regression model has $R^2 = 99.9\%$ and the most important parameter is again the rail pad stiffness, which explains 93.7% of the variance in the rail sound power.

The polynomial regression model is as follows:

$$\begin{aligned} SWL_{\sum,Rail} =& a_0 + a_1 k_{Pad} + a_2 k_{Pad}^2 + a_3 k_{Pad}^3 + a_4 \eta_{Pad} + a_5 w_{Foot} \\ &+ a_6 w_{Foot} k_{Pad}, \end{aligned} \tag{13}$$

the coefficients of which are given in Table 2. In Fig. 5 a comparison between the rail sound power calculated with the implemented vibroacoustic tool and the

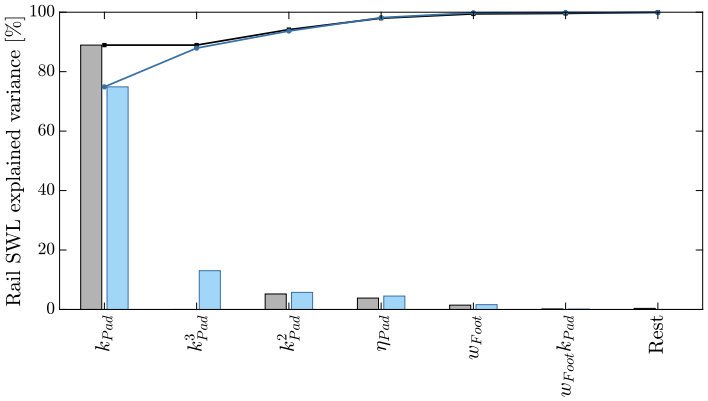

Fig. 4: Effect importance (bar) and cummulative value (line) on rail radiation: initial study (black) and refined study (blue).

Table 2: Coefficients* of rail sound power regression model presented in Eq. (13).

a_0	a_1	a_2	a_3	a_4	a_5	a_6
99.5	$-2.3 \cdot 10^{-2}$	$2 \cdot 10^{-5}$	$-5.7 \cdot 10^{-9}$	-10.7	$8 \cdot 10^{-2}$	$-3.7 \cdot 10^{-5}$

* Stiffness in MN/m, geometric parameters in mm and sound power in dB(A) re 1 pW.

prediction with the regression model is shown. The good approximation provided by the model makes it possible to analyse the coefficients of the regression and establish trends of the contributing variables on the rail sound radiation. It should be noted that the sound radiation calculation of the 8^3 design of experiments takes approximately 20 hours (140 seconds per combination) while the time associated with the prediction from Eq. (13) is negligible; the numerical simulations are carried out in a PC running with an ®Intel i7-9700 processor with 64 GB RAM.

The rail pad stiffness has a non-linear influence on the rail radiation. Although quadratic and cubic terms involving this parameter appear in the polynomial regression, this fact does not affect the importance of the other effects due to the independence obtained through the design of experiments. Thus, the rail pad stiffness is the most important parameter; as it increases, the vibrational field of the rail extends over a shorter length and, consequently, its radiation is reduced. The same happens when increasing the pad damping loss factor, although its range of realistic values is smaller. Also, reducing the rail foot width results in lower sound emission as it reduces the radiation ratio and the radiation area

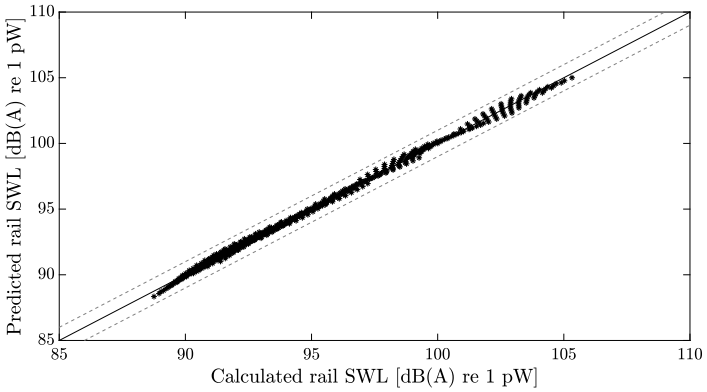

Fig. 5: Predicted vs calculated rail SWL. ——: reference line; - - -: 1 dB(A) deviation; ∗: each track design.

which, as mentioned above, is where the higher velocities of vibration appear. The interaction effect $w_{Foot}k_{Pad}$ represents the loss of importance of the rail foot width as the rail pad stiffness is increased due to the lower noise levels radiated; this phenomenon can be appreciated by modifying the regression model and introducing the influence of k_{Pad} implicitly:

$$SWL_{\sum,Rail} = b_0(k_{Pad}) + b_1(k_{Pad})w_{Foot} + b_2\eta_{Pad}, \tag{14}$$

where the influence of w_{Foot} is defined by means of the coefficient b_1, dependence of which on k_{Pad} is shown in Fig. 6. This coefficient is always positive, that is, reducing the rail foot width leads to lower rail radiation; however, its influence is reduced as the pad stiffness is increased. Note that a narrower rail foot would imply a greater pressure level on the rail pad and, given the non-linear nature of this material, its stiffness would increase [41]. This phenomenon would have, on the interaction effect $w_{Foot}k_{Pad}$, an influence of opposite sign to that previously attributed, so that it would increase the value of the coefficient a_6 in Eq. (13) and Table 2. Consequently, this would yield an increase of the slope in Fig. 6. However, this effect has not been considered in the present study.

Finally, the great variability in the rail sound power results should be noted, with a difference between the best and the worst combination of 16.6 dB(A). The optimal solution according to the regression model corresponds to the maximum value of k_{Pad}, 1300 MN/m in vertical direction and 100 MN/m in lateral direction, the maximum value of η_{Pad}, 0.5, and the minimum value of w_{Foot}, 120 mm, which implies a rail sound power of 88.8 dB(A).

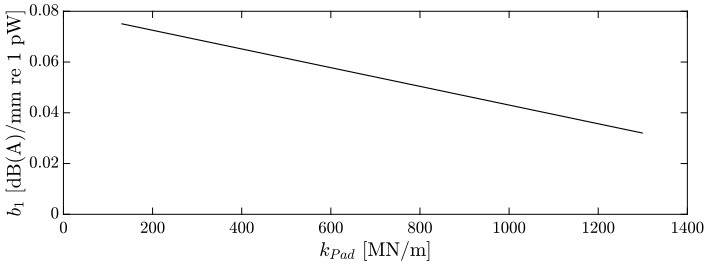

Fig. 6: Coefficient b_1 value from Eq. (14) as a function of k_{Pad}.

4.2 Influence on sleeper radiation

The same procedure is carried out with the sleeper sound radiation being the response variable. Firstly, the importance of each effect from the initial study is determined, which is shown in Fig. 7 (colour black); the more relevant parameters are determined: k_{Pad}, η_{Pad}, $k_{Ballast}$ and $\eta_{Ballast}$. In the frequency range in which the sleeper radiation is important (below 750 Hz), track dynamics and particularly sleeper dynamics are governed by the rail pad and ballast, whereas the rail cross-section geometry has a negligible influence. Considering these four contributing variables, a design of experiments with 5^4 combinations is proposed. Again, the Pratt methodology is applied on the simulation results, determining the importance of each significant effect, which is shown in Fig. 7 (colour blue). In this case, the regression model has $R^2 = 99.3\%$, k_{Pad} being the most important design variable again. The regression is given as

$$\begin{aligned} SWL_{\sum,Sleeper} =& a_0 + a_1 k_{Pad} + a_2 k_{Pad}^2 + a_3 k_{Pad}^3 + a_4 \eta_{Ballast} + a_5 k_{Ballast} \\ &+ a_6 \eta_{Pad} + a_7 k_{Pad} k_{Ballast} + a_8 k_{Pad} \eta_{Ballast} + a_9 k_{Pad} \eta_{Pad}, \end{aligned} \tag{15}$$

and the values of the corresponding coefficients are provided in Table 3. From the 5^4 design of experiments, the calculated sleeper sound power and its prediction by Eq. (15) are compared in Fig. 8.

Unlike the rail radiation, the higher the pad stiffness is, the more sound the sleeper radiates since the rail vibration is transmitted to a greater extent to the sleeper. On the contrary, the higher the ballast stiffness, the less the sleeper vibrates and, consequently, the less the sleeper radiates. Regarding the damping loss factors of pad and ballast, increasing them leads to a reduction in the sleeper sound power. Note that the rail pad stiffness not only dominates the sleeper radiation, but also takes part in the influence of the other parameters through the interaction effects.

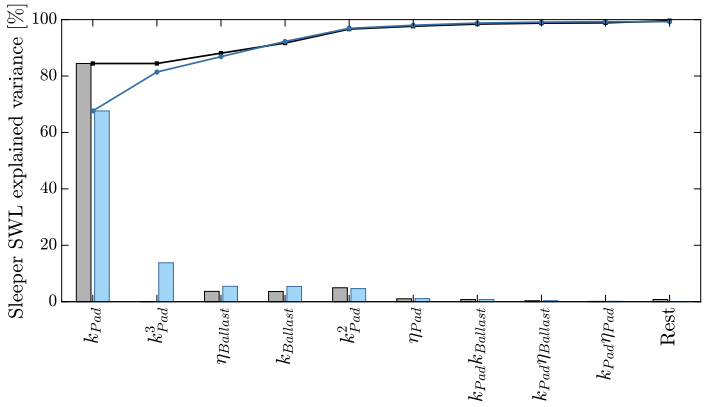

Fig. 7: Effect importance (bar) and cummulative value (line) on sleeper radiation: initial study (black) and refined study (blue).

Table 3: Coefficients* of sleeper sound power regression model presented in Eq. (15).

a_0	a_1	a_2	a_3	a_4
92.8	$1.8 \cdot 10^{-2}$	$-1.1 \cdot 10^{-5}$	$3.3 \cdot 10^{-9}$	-0.99

a_5	a_6	a_7	a_8	a_9
$-1 \cdot 10^{-2}$	-5	$-2.7 \cdot 10^{-5}$	$-1.1 \cdot 10^{-3}$	$2.6 \cdot 10^{-3}$

* Stiffness in MN/m and sound power in dB(A) re 1 pW.

In order to analyse this dependence, a polynomial fit is proposed in which the simple effect of k_{Pad} disappears, including it in the coefficients:

$$\begin{aligned} SWL_{\sum,Sleeper} =& b_0(k_{Pad}) + b_1(k_{Pad})k_{Ballast} + b_2(k_{Pad})\eta_{Ballast} \\ &+ b_3(k_{Pad})\eta_{Pad}. \end{aligned} \tag{16}$$

Fig. 9 shows the dependence of the coefficients in Eq. (16) with the rail pad stiffness. All of them are negative for any value of k_{Pad}, so that, independently of it, increasing the ballast stiffness or the damping loss factors leads to a reduction in the sleeper sound radiation. However, a higher value of k_{Pad} increases the influence of $k_{Ballast}$ and $\eta_{Ballast}$ and reduces the influence of η_{Pad}; this phenomenon

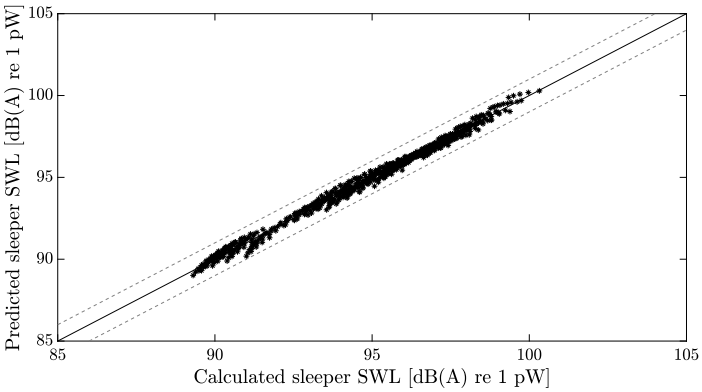

Fig. 8: Predicted vs calculated sleeper SWL. ——: reference line; - - -: 1 dB(A) deviation; ∗: each track design.

represents the loss of influence of the rail pad as its stiffness increases above that of the ballast.

On balance, the sleeper radiation shows a variation between the best and the worst combination of 11 dB(A). The optimal case corresponds to the minimum value of k_{Pad}, 130 MN/m in vertical direction and 10 MN/m in lateral direction, the maximum value of $k_{Ballast}$, 100 MN/m in vertical direction and 50 MN/m in lateral direction, the maximum value of $\eta_{Ballast}$, 2, and the maximum value of η_{Pad}, 0.5, with a sleeper sound power of 89.3 dB(A).

4.3 Influence on wheel radiation

Since the wheel properties are fixed in this work, its vibration depends exclusively on the contact forces, which have an inverse dependence on the combined receptance of the system at the contact point, the sum of the rail, wheel and contact receptances, as indicated in Eq. (7). Thus, the track parameters that influence the wheel radiation are those which give a notable modification of the rail contact point receptances in the frequency range in which the wheel radiation is important ($>$ 1.5 kHz). The railway wheel, being a finite structure, has a high number of natural frequencies and vibration modes (i.e. resonances) in that frequency range. Changes in the contact force influence the wheel vibration to a lesser or greater extent depending on the distribution of these resonances. For this reason, the influence of the track parameters on the wheel radiation might depend on

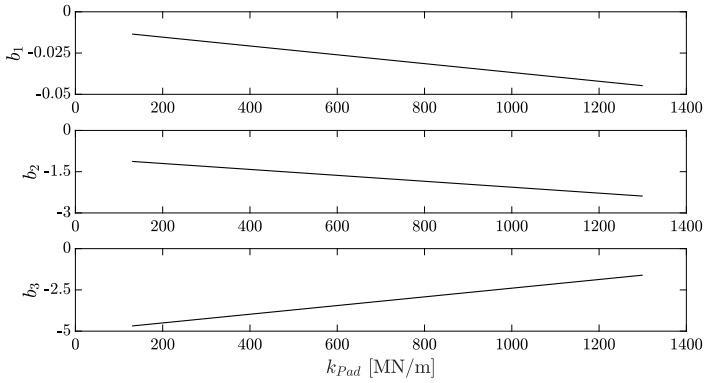

Fig. 9: Coefficient values from Eq. (16) as a function of k_{Pad}. b_1 has units of dB(A)/(MN/m) and b_2 and b_3 of dB(A).

the studied wheel. This section looks for trends applicable to any railway wheel, indicating which results are sensitive to the properties of the wheel.

The important parameters identified that influence the wheel radiation are the rail pad stiffness and all the rail cross-section geometric factors. Changes in the rail pad stiffness might modify the rail contact point receptances up to 3 kHz, whereas the pad damping loss factor, ballast stiffness and ballast damping loss factor do not influence significatively the rail receptances above 1.5 kHz. Therefore, these three parameters (η_{Pad}, $k_{Ballast}$ and $\eta_{Ballast}$) have a negligible effect on the wheel sound power. Although the wheel radiation generally occurs at frequencies above 1.5 kHz, these variables might influence the sound radiation of highly flexible railway wheels with acoustically predominant vibration modes in the low and medium frequency range. However, the trend to optimize the railway wheel in terms of noise is to stiffen it, increasing its natural frequencies and shifting the radiation to high frequencies [10].

In contrast to what it might appear, an increase in the rail pad stiffness reduces the wheel radiation. By stiffening the pad while keeping the mass of the track constant, its associated resonance frequency is increased and, as a result, the contact force magnitude decreases in the frequency range in which the wheel radiation is important. Regarding the rail geometric parameters, their influence might depend on the railway wheel considered. Generally, if the rail cross-section dimensions are reduced this will give a lower section stiffness and consequently lead to an increase in the magnitude of the rail contact point receptances. This reduces the contact force magnitude and wheel sound power.

In any case, since wheel properties are not modified, less variance is found in its sound radiation compared to the rail and sleeper. Specifically, the difference between the best and the worst combination is 3.3 dB(A), in contrast to 16.6 dB(A) for the rail and 11 dB(A) for the sleeper. The optimal combination for the wheel radiation is obtained generally with the maximum value of k_{Pad} and the minimum values of the rail geometric parameters. For the studied wheel, this combination implies a wheel sound power of 94.3 dB(A).

4.4 Influence on total radiation

From the initial design of experiments for the total sound radiation, the proportion of variance explained by each significant effect is determined, which is shown in Fig. 10 (colour black); in the context of the current investigation, the total sound radiation is influenced by the following design variables: w_{Foot}, k_{Pad}, η_{Pad}, $k_{Ballast}$ and $\eta_{Ballast}$. The rail pad properties influence the noise of all components, therefore being important in the total radiation. The ballast properties, which play an important role in the sleeper radiation, also appear as contributing variables. The rail foot width affects the radiation of the rail and, the rail power being the one that presents the highest variability, it is an important parameter in the total noise. Lastly, the remaining geometric parameters only influence the wheel radiation, variability of which, much less than that of the rail and sleeper, is mainly explained by the rail pad stiffness; therefore, they do not appear as important contributing variables in the total radiation.

With these five important parameters, a design of experiments with 5^5 combinations is carried out. The importance of the design variables in terms of explaining variability is determined and shown in Fig. 10 (colour blue). The regression model is given by

$$\begin{aligned} SWL_{\sum,Total} =& a_0 + a_1 k_{Pad} + a_2 k_{Pad}^2 + a_3 k_{Pad}^3 + a_4 \eta_{Pad} + a_5 w_{Foot} \\ &+ a_6 k_{Ballast} + a_7 \eta_{Ballast} + a_8 w_{Foot} k_{Pad} + a_9 k_{Pad} k_{Ballast} \\ &+ a_{10} k_{Pad} \eta_{Pad} + a_{11} k_{Pad} \eta_{Ballast}, \end{aligned} \tag{17}$$

and the values of the corresponding coefficients are provided in Table 4; it has $R^2 = 99.4\%$. The prediction carried out with this model is compared with the calculated results in Fig. 11. Given the good approximation provided by the regression model, the analysis of its coefficients allows the influence of the design variables on the total noise to be determined.

The rail pad stiffness is shown to be the most important parameter, explaining 83.6% of the noise variance (without considering the interaction effects). Increas-

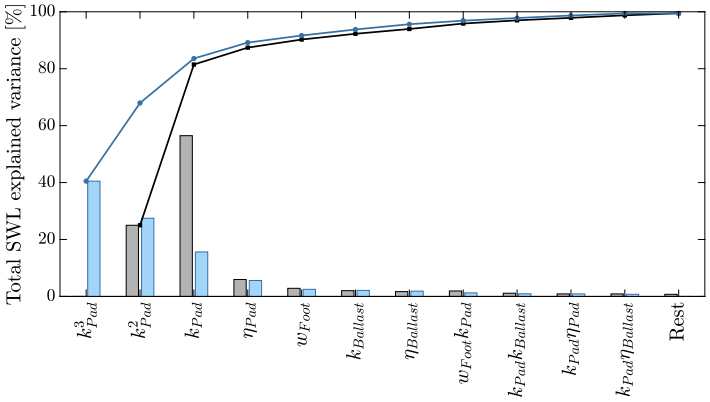

Fig. 10: Effect importance (bar) and cummulative value (line) on total radiation: initial study (black) and refined study (blue).

ing it leads to a reduction in the rail and wheel noise and an increase in the sleeper noise; for the total noise, at low rail pad stiffnesses the reduction in the rail by increasing it predominates over the increase in the sleeper noise, but at high stiffnesses there is a balance between the three components. This phenomenon is shown in Fig. 12, where it is observed that the highest sound mitigation occurs for intermediate/high values of the rail pad stiffness. Increasing the rail pad damping loss factor leads to a reduction of the rail and sleeper sound radiation and thus of the total acoustic power. Regarding the ballast, increasing its stiffness and damping reduces the sleeper radiation as seen previously and, although coefficients a_6 and a_7 in Eq. (17) are positive, it also reduces the total radiation due to the contribution of the interaction effects $k_{Pad}k_{Ballast}$ and $k_{Pad}\eta_{Ballast}$, which together with the term $k_{Pad}\eta_{Pad}$ have the same behaviour explained for the sleeper radiation; this was previously analysed through coefficients b_1, b_2 and b_3 of Eq. (16) in Fig. 9. Finally, increasing the rail foot width implies greater rail and total noise levels and the interaction effect $w_{\text{Foot}}k_{Pad}$ represents the same phenomenon that was explained for the rail radiation. In summary and for the sake of better understanding, the total sound power is represented as a function of the important design variables in Fig. 13.

Table 4: Coefficients* of total sound power regression model presented in Eq. (17).

a_0	a_1	a_2	a_3	a_4	a_5
101.2	$-1.4 \cdot 10^{-2}$	$2.2 \cdot 10^{-5}$	$-7.2 \cdot 10^{-9}$	-7.6	$5.6 \cdot 10^{-2}$

a_6	a_7	a_8	a_9	a_{10}	a_{11}
$1.7 \cdot 10^{-3}$	$6.3 \cdot 10^{-2}$	$-4.3 \cdot 10^{-5}$	$-1.9 \cdot 10^{-5}$	$4.3 \cdot 10^{-3}$	$-1 \cdot 10^{-3}$

* Stiffness in MN/m, geometric parameters in mm and sound power in dB(A) re 1 pW.

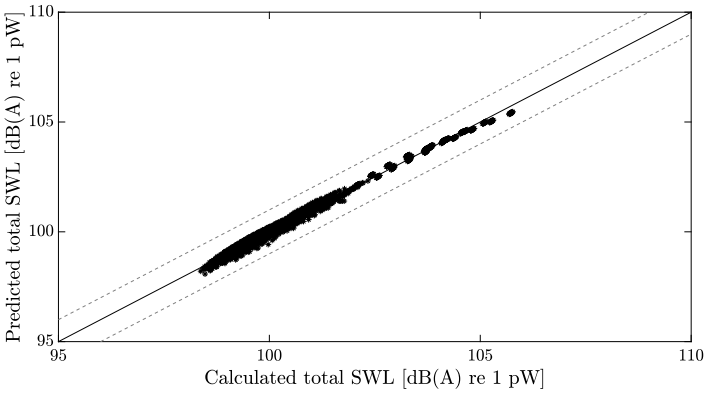

Fig. 11: Predicted vs calculated total SWL. ——: reference line; - - -: 1 dB(A) deviation; ∗: each track design.

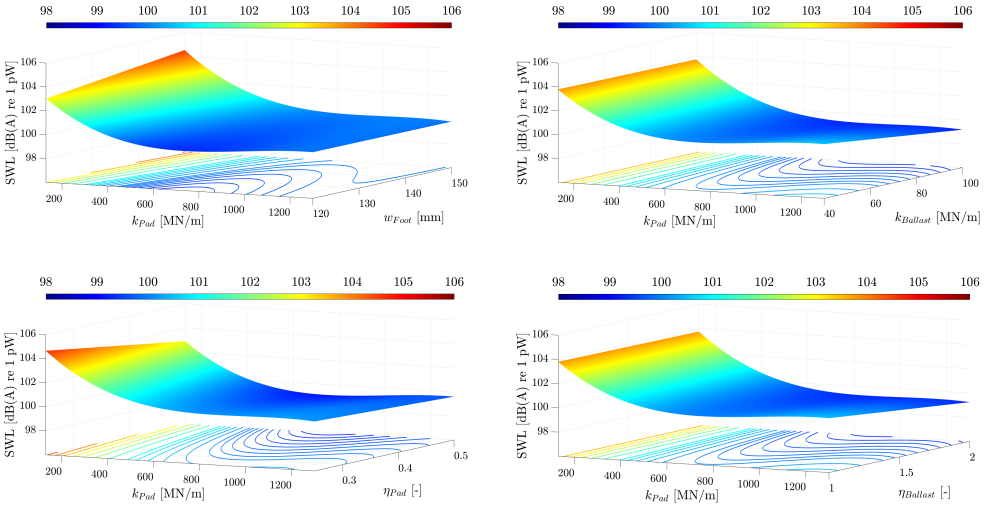

Fig. 13: Response surfaces of total sound power level for each important interaction of design variables. Parameters not represented take medium values in their ranges.

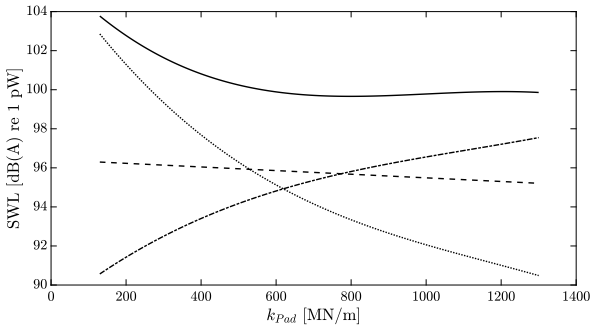

Fig. 12: Influence of rail pad stiffness on sound power level. ——: total; - - -: wheel component; ·····: rail component; -·-·-: sleeper component. The other contributing variables take medium values in their ranges.

The regression model predicts that the optimal track design is reached with the following parameters: $w_{Foot} = 120$ mm, $k_{Pad} = 780$ MN/m, $\eta_{Pad} = 0.5$, $k_{Ballast} = 100$ MN/m and $\eta_{Ballast} = 2$, with a total sound power of 98.4 dB(A). In contrast, the worst design corresponds to the following parameters: $w_{Foot} = 150$ mm, $k_{Pad} = 130$ MN/m, $\eta_{Pad} = 0.25$, $k_{Ballast} = 40$ MN/m and $\eta_{Ballast} = 1$, with a sound power of 105.8 dB(A). Therefore, there is a difference between the best and the worst combination of 7.4 dB(A). Fig. 14 shows the TDR in vertical direction and the total sound power levels, both evaluated for the track design with the worst combination of parameters and with the optimal one. The TDR has been computed in accordance with the standard EN15461 [31] using the track dynamic model of Section 2.2 and the acoustic radiation using the implemented tool of Section 2. Below about 2 kHz, in the frequency range in which the track contribution to the total noise is important, an inverse correlation between both variables can be appreciated. However, above about 2 kHz, the wheel contribution to the total noise makes it more difficult to correlate the TDR and total sound power radiation.

5 Conclusions

A vibroacoustic model of the railway wheel and track has been implemented which allows the sound power radiated by the wheel, rail and sleeper to be calculated as a consequence of the wheel/rail interaction. Then, the Pratt methodology has been used to analyse in detail the influence of the track design on the railway acoustic radiation.

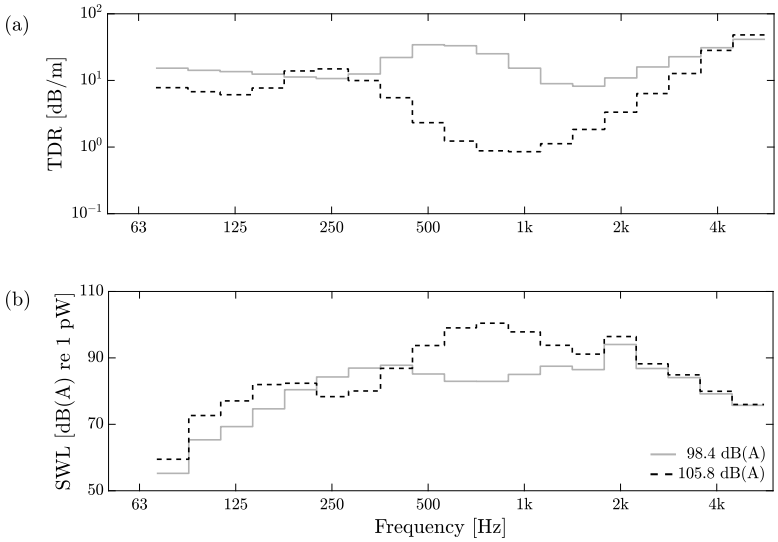

Fig. 14: Track Decay Rate in vertical direction (a) and total sound power level (b). ——: Optimal track design; - - -: Worst track design.

To do this, a geometric parameterization of the rail cross-section has been carried out according to the European rails specified by the standard EN13674-1. Considering six geometric parameters of the rail as well as the stiffness and damping of the rail pad and ballast (in total ten variables), a design of experiments has been carried out that allows the influence of these variables on the sound radiation of the different railway components to be determined.

The analysis of the results shows that the railway sound radiation is governed mainly by the viscoelastic properties of the rail pad and ballast; the only influencing geometric parameter is the rail foot width. For the total radiation, a regression model has been developed which allows explaining 99.4% of its variance. By far the most influential parameter is the rail pad stiffness, followed by, in descending order, the rail pad damping, rail foot width, ballast stiffness and ballast damping.

The minimum sound power levels are found with: intermediate/high values of the rail pad stiffness, having a compromise between the rail, sleeper and wheel radiation (a similar conclusion was found in [20]); maximum values of the rail pad damping, reducing the rail and sleeper radiation; minimum values of the rail foot width, giving a lower radiation of the rail, and maximum values of the

ballast stiffness and damping, reducing the sleeper radiation. Within the ranges of these five parameters, there is a difference between the best and the worst combination of 7.4 dB(A). However, this noise reduction is subject to the following considerations: (1) the calculations are for one speed and one roughness spectrum, (2) the range of rail pad stiffnesses in particular may not be acceptable to the track engineers for reasons other than noise pollution and (3) the narrower rail foot would require a modified rail fastening as it would be in greater danger of rail roll-over and would increase the mechanical stresses in that region of the rail putting its integrity at risk of fatigue.

Acknowledgements

This paper is part of the project PID2020-112886RA-I00 funded by MCIN/AEI /10.13039/501100011033 and grant FPU18/03999 funded by MCIN/AEI/10.130 39/501100011033 as well as by "ESF Investing in your future". The authors also acknowledge Programa PROMETEO/2021/046 of Generalitat Valenciana.

References

[1] T. Münzel, S. Kröller-Schön, M. Oelze, T. Gori, F. P. Schmidt, S. Steven, O. Hahad, M. Röösli, J. M. Wunderli, A. Daiber, M. Sørensen, Adverse cardiovascular effects of traffic noise with a focus on nighttime noise and the new WHO noise guidelines, Annual Review of Public Health 41 (1) (2020) 309–328, doi: http://dx.doi.org/10.1146/annurev-publhealth-081519-062400.

[2] D. J. Thompson, Railway Noise and Vibration. Mechanisms, Modelling and Means of Control, Elsevier, 2009, ISBN: 978-0-08-045147-3.

[3] X. Zhang, D. J. Thompson, E. Quaranta, G. Squicciarini, An engineering model for the prediction of the sound radiation from a railway track, Journal of Sound and Vibration 461 (2019) 114921, doi: http://dx.doi.org/10.1016/j.jsv.2019.114921.

[4] D. J. Thompson, N. Vincent, Track dynamic behaviour at high frequencies. Part 1: Theoretical models and laboratory measurements, Vehicle System Dynamics 24 (sup1) (1995) 86–99, doi: http://dx.doi.org/10.1080/00423119508969617.

[5] P. J. Remington, Wheel/rail noise, part IV: Rolling noise, Journal of Sound and Vibration 46 (3) (1976) 419–436, doi: http://dx.doi.org/10.1016/0022-460X(76)90864-6.

[6] D. J. Thompson, G. Squicciarini, J. Zhang, I. Lopez Arteaga, E. Zea, M. Dittrich, E. Jansen, K. Arcas, E. Cierco, F. X. Magrans, A. Malkoun, E. Iturritxa, A. Guiral, M. Stangl, G. Schleinzer, B. Martin Lopez, C. Chaufour, J. Wändell, Assessment of measurement-based methods for separating wheel and track contributions to railway rolling noise, Applied Acoustics 140 (2018) 48–62, doi: http://dx.doi.org/10.1016/j.apacoust.2018.05.012.

[7] J. C. O. Nielsen, Acoustic optimization of railway sleepers, Journal of Sound and Vibration 231 (3) (2000) 753–764, doi: http://dx.doi.org/10.1006/jsvi.1999.2560.

[8] D. J. Thompson, P-E. Gautier, Review of research into wheel/rail rolling noise reduction, Proceedings of the Institution of Mechanical Engineers, Part F: Journal of Rail and Rapid Transit 220 (4) (2006) 385–408, doi: http://dx.doi.org/10.1243/0954409JRRT79.

[9] J. C. O. Nielsen, C. R. Fredö, Multi-disciplinary optimization of railway wheels, Journal of Sound and Vibration 293 (2006) 510–521, doi: http://dx.doi.org/10.1016/j.jsv.2005.08.063.

[10] X. Garcia-Andrés, J. Gutiérrez-Gil, J. Martínez-Casas, F. D. Denia, Wheel shape optimization approaches to reduce railway rolling noise, Structural and Multidisciplinary Optimization 62 (2020) 2555–2570, doi: http://dx.doi.org/10.1007/s00158-020-02700-6.

[11] C. J. C. Jones, D. J. Thompson, Rolling noise generated by railway wheels with visco-elastic layers, Journal of Sound and Vibration 231 (3) (2000) 779–790, doi: http://dx.doi.org/10.1006/jsvi.1999.2562.

[12] J. Färm, Evaluation of wheel dampers on an intercity train, Journal of Sound and Vibration 267 (3) (2003) 739–747, doi: http://dx.doi.org/10.1016/S0022-460X(03)00737-5.

[13] C. Gramowski, T. Gerlach, Entering the real operation phase: design, construction and benefit verification of freight wheel noise absorber, Proceedings of 13th International Workshop on Railway Noise, Ghent, September 2019, pp. 16–20.

[14] F. Létourneaux, J. F. Cordier, F. Poisson, N. Douarche, High speed railway noise: assessment of mitigation measures, in: B. Schulte-Werning, *et al.* (Eds.), Proceedings of 9th International Workshop on Railway Noise, Munich, Germany, 4–8 September 2007, Notes on Numerical Fluid Mechanics & Multidisciplinary Design 99, 2008, pp. 56–62.

[15] D. J. Thompson, C. J. C. Jones, T. P. Waters, D. Farrington, A tuned damping device for reducing noise from railway track, Applied Acoustics 68 (1) (2007) 43–57, doi: http://dx.doi.org/10.1016/j.apacoust.2006.05.001.

[16] B. Asmussen, D. Stiebel, P. Kitson, D. Farrington, D. Benton, Reducing the noise emission by increasing the damping of the rail: results of a field test, in: B. Schulte-Werning, *et al.* (Eds.), Proceedings of 9th International Workshop on Railway Noise, Munich, Germany, 4–8 September 2007, Notes on Numerical Fluid Mechanics & Multidisciplinary Design 99, 2008, pp. 229–235.

[17] W. Sun, D. J. Thompson, M. Toward, M. Wiseman, E. Ntotsios, S. Byrne, The influence of track design on the rolling noise from trams, Applied Acoustics 170 (2020) 107536, doi: http://dx.doi.org/10.1016/j.apacoust.2020.107536.

[18] C. Gramowski, P. Suppin, Impact of rail dampers on the mainline rail roughness development, in: B. Schulte-Werning, *et al.* (Eds.), Proceedings of 12th International Workshop on Railway Noise, Terrigal, Australia, 12–16 September 2016, Notes on Numerical Fluid Mechanics & Multidisciplinary Design 139, 2018, pp. 367–374.

[19] C. J. C. Jones, D. J. Thompson, Means of controlling rolling noise at source, in: V. V. Krylov (Ed.), Noise and vibration from high-speed trains, Thomas Telford Ltd, London, 2001, Ch. 6, pp. 163–183, doi: http://dx.doi.org/10.1680/navfht.29637.0006.

[20] N. Vincent, P. Bouvet, D. J. Thompson, P-E. Gautier, Theoretical optimization of track components to reduce rolling noise, Journal of Sound and Vibration 193 (1) (1996) 161–171, doi: http://dx.doi.org/10.1006/jsvi.1996.0255.

[21] D. J. Thompson, B. Hemsworth, N. Vincent, Experimental validation of the TWINS prediction program for rolling noise, part 1: description of the model and method, Journal of Sound and Vibration 193 (1) (1996) 123–135, doi: http://dx.doi.org/10.1006/jsvi.1996.0252.

[22] D. J. Thompson, P. Fodiman, H. Mahé, Experimental validation of the TWINS prediction program for rolling noise, part 2: results, Journal of Sound and Vibration 193 (1) (1996) 137–147, doi: http://dx.doi.org/10.1006/jsvi.1996.0253.

[23] D. J. Thompson, Wheel-rail noise generation, part II: Wheel vibration, Journal of Sound and Vibration 161 (3) (1993) 401–419, doi: http://dx.doi.org/10.1006/jsvi.1993.1083.

[24] D. J. Thompson, Wheel-rail noise generation, part III: Rail vibration, Journal of Sound and Vibration 161 (3) (1993) 421–446, doi: http://dx.doi.org/10.1006/jsvi.1993.1084.

[25] Railway applications – Track – Rail – Part 1: Vignole railway rails 46 kg/m and above. EN 13674-1:2011+A1:2017, European Committee for Standardization (2017).

[26] D. C. Montgomery, Design and Analysis of Experiments, 10th Edition, John Wiley & Sons, Inc., 2019, ISBN: 978-1-119-49244-3.

[27] J. W. Pratt, Dividing the indivisible: Using simple symmetry to partition variance explained, Proceedings of the Second International Conference in Statistics, University of Tampere, Tampere, Finland, 1987, pp. 245–260.

[28] D. J. Thompson, C. J. C. Jones, Sound radiation from a vibrating railway wheel, Journal of Sound and Vibration 253 (2) (2002) 401–419, doi: http://dx.doi.org/10.1006/jsvi.2001.4061.

[29] D. J. Thompson, M. H. A. Janssens, F. G. de Beer, Track Wheel Interaction Noise Software (TWINS) Theoretical Manual (version 3.4), TNO report, TNO Institute of Applied Physics, 2019.

[30] D. J. Mead, A general theory of harmonic wave propagation in linear periodic systems with multiple coupling, Journal of Sound and Vibration 27 (2) (1973) 235–260, doi: http://dx.doi.org/10.1016/0022-460X(73)90064-3.

[31] Railway applications – Noise emission – Characterisation of the dynamic properties of track sections for pass by noise measurements. EN 15461:2008+A1:2010, European Committee for Standardization (2010).

[32] E. Salomons, Computational Atmospheric Acoustics, Kluwer, 2001, ISBN: 978-1-4020-0390-5.

[33] D. J. Thompson, C. J. C. Jones, N. Turner, Investigation into the validity of two-dimensional models for sound radiation from waves in rails, The Journal of the Acoustical Society of America 113 (2003) 1965–1974, doi: http://dx.doi.org/10.1121/1.1555612.

[34] Railway applications – Wheelsets and bogies – Monobloc wheels – Technical approval procedure – Part 1: Forged and rolled wheels. EN 13979-1:2020, European Committee for Standardization (2020).

[35] D. J. Thompson, Wheel-rail noise generation, part I: Introduction and interaction model, Journal of Sound and Vibration 161 (3) (1993) 387–400, doi: http://dx.doi.org/10.1006/jsvi.1993.1082.

[36] A. Johansson, J. C. O. Nielsen, R. Bolmsvik, A. Karlström, R. Lundén, Under sleeper pads—influence on dynamic train–track interaction, Wear 265 (2008) 1479–1487, doi: http://dx.doi.org/10.1016/j.wear.2008.02.032.

[37] N. Vincent, D. J. Thompson, Track dynamic behaviour at high frequencies. part 2: Experimental results and comparisons with theory, Vehicle System Dynamics 24 (sup1) (1995) 100–114, doi: http://dx.doi.org/10.1080/00423119508969618.

[38] Electroacoustics – Sound level meters – Part 1: Specifications. IEC 61672-1:2013, International Electrotechnical Commission (2013).

[39] D. R. Thomas, E. Hughes, B. D. Zumbo, On variable importance in linear regression, Social Indicators Research 45 (1/3) (1998) 253–275, doi: http://dx.doi.org/10.1023/A:1006954016433.

[40] D. R. Thomas, P. C. Zhu, Y. J. Decady, Point estimates and confidence intervals for variable importance in multiple linear regression, Educational and Behavioral Statistics 32 (1) (2007) 61–91, doi: http://dx.doi.org/10.3102/1076998606298037.

[41] D. J. Thompson, C. J. C. Jones, T. X. Wu, A. de France, The influence of the non-linear stiffness behaviour of rail pads on the track component of rolling noise, Proceedings of the Institution of Mechanical Engineers, Part F: Journal of Rail and Rapid Transit 213 (4) (1999) 233–241, doi: http://dx.doi.org/10.1243/0954409991531173.

PAPER 2

A model of a rotating railway wheel for the prediction of sound radiation

V. T. Andrés[a], J. Martínez-Casas[a], F. D. Denia[a], and D. J. Thompson[b]

[a] Instituto de Ingeniería Mecánica y Biomecánica, Universitat Politècnica de València, Valencia, Spain
[b] Institute of Sound and Vibration Research, University of Southampton, Southampton, UK

Journal of Sound and Vibration
Volume 553, Article number 117667, 2023
DOI: 10.1016/j.jsv.2023.117667

Abstract

The axial symmetry of a railway wheel is taken into account to expand its vibrational response around the circumferential direction using Fourier series. This allows the vibroacoustic problem of the wheel to be formulated in a two-dimensional frame, solving for the dynamic and acoustic variables analytically in the circumferential direction. By adopting an Eulerian approach, the inertial effects associated with the rotation of the wheelset are included in the model, assuming a constant angular speed of rotation. To represent a railway wheelset, the wheel is constrained at the inner edge of the hub and the contribution of the rigid body motion of the wheelset is superimposed on its response. The latter is evaluated analytically under the assumption of small rigid body displacements. The computational efficiency of the proposed methodology is found to be three orders of magnitude greater than a full three-dimensional methodology, without compromising the accuracy. The results are compared in terms of acoustic radiation with the commercial package Ansys, showing similar sound power levels in almost all the frequency range apart from some differences at low frequencies due to the use of an acoustic model based on radiation ratios.

Keywords

Wheel vibroacoustic model; railway wheelset; rigid body motion; rotation; axisymmetry; rolling noise.

Contents

1 Introduction

Noise pollution from railways can cause discomfort and even risk to people's health. For this reason, in recent decades, the development of quieter railway components through different techniques has proliferated; among these, is the implementation of damper elements, such as the use of viscoelastic layers on the wheel [1] and dynamic absorbers on the wheel and rail [2, 3], as well as the search for optimal designs of the wheel [4, 5], the study of perforation schemes for the wheel [6] and the analysis of the influence of track design on the radiated noise [7]. Generally, in the preliminary design phase of such treatments, numerous simulations are required to reach the optimal configuration in terms of noise mitigation. In situations with multiple design variables, the number of simulations that can be carried out is limited by the computational cost associated with the vibroacoustic calculation. Consequently, it is convenient to have efficient vibroacoustic models of the railway components. The present study focuses on the wheelset.

To evaluate the sound radiation from the wheel, it is first necessary to determine the vibrational field on its surface. The wheel vibration occurs in response to the excitation forces at the wheel–rail contact; on straight track, the main reason for this excitation is the existence of surface roughness on the wheel and rail running surfaces. The response of the wheelset to these interaction forces can be determined numerically using the Finite Element Method (FEM) [8]. In running conditions, the wheelset is rotating about its main axis, which changes the dynamics of this component compared with the stationary case. In Ref. [9], Thompson proposed to include the wheel rotation by means of a moving load problem, excluding the gyroscopic and inertial effects associated with the rotation. Other authors have proposed models based on Lagrangian coordinates to include the convective effects in flexible rotors. Geradin and Kill [10] developed the equations of motion (EoM) in both rotating and inertial frames by defining a reference system associated with local deformations and assuming small angles of rotation about the axis; in their work, the axial and flexural dynamic behaviour of the rotor was analysed, while the torsional one was neglected. Genta and Tonoli [11] developed a formulation that includes the axial, flexural and torsional dynamic behaviour of thin rotating discs. More recently, Sheng *et al.* [12] proposed a FE model of a rotating railway wheel using an axisymmetric approach, which includes the vertical vibration of the wheel axis by taking into account the momentum law; this was used to solve the response of the wheel to a vertical harmonic wheel–rail force and it was shown that the displacement of the wheel contact point, formulated in an inertial frame, is also harmonic at the same frequency as the interaction force. When the rotating body interacts with other

non-rotating structures, models based on Eulerian coordinates present a clear advantage over those based on Lagrangian coordinates, since the location of the interaction usually has a constant spatial position with respect to the inertial reference system. Fayos *et al.* [13] proposed a model based on Eulerian coordinates applied to the railway wheelset to give an efficient solution to the interaction with the track; to do this, they developed the EoM of the rotating body initially in Lagrangian coordinates and, then, a conversion to Eulerian coordinates was carried out. Later, Martínez-Casas *et al.* [14] developed the EoM of the rotating 3D wheelset directly in Eulerian coordinates, in a cartesian reference system. With a view to reducing the computational cost associated with the resolution of the dynamic problem, Baeza *et al.* [15] performed an expansion of the response around the circumferential direction using Fourier series, after transforming the EoM from a cartesian to a cylindrical reference system.

Once the vibrational field of the wheel has been computed, it is possible to evaluate its sound radiation. The most precise way to do this is by solving the air pressure field through a Fluid Structure Interaction (FSI) approach. In the literature, however, acoustic models can be found based on the use of radiation ratios, which have a lower computational cost. These are based on post-processing the vibrational field of the wheel surface, as proposed in Ref. [16]. In this reference, the wheel is constrained at the inner edge of the hub and the modelling of the axle is omitted, which gives a good approximation for the contribution to the radiation of the vibration modes with 2 or more nodal diameters; it is worth noting that, according to Ref. [8], these are the most important for rolling noise generation. However, the vibroacoustic behaviour of the wheelset in the low frequency range is influenced by the axle motion. To include this, the contribution of the rigid body modes of the wheelset can be added to the constrained wheel vibration [17].

In this work, a model of a rotating railway wheel which takes advantage of its axial symmetry is proposed. The wheel flexibility is considered and the wheelset rigid body motion (RBM) is superimposed on the wheel vibration. To do this, an analytical model of a rigid rotating wheelset is developed. Both the flexible wheel and rigid wheelset models can be applied to other rotating systems as long as there is axial symmetry. Regarding the former, the axisymmetric approach with Eulerian coordinates proposed by Baeza *et al.* [15] is extended through the direct formulation of the EoM in a cylindrical reference system. Subsequently, the acoustic model of Thompson [16] is considered to evaluate the acoustic radiation of the wheel, taking advantage of the periodicity of the response to formulate the sound field also in a two-dimensional frame. The wheel is constrained at the inner edge of the hub and the contribution of the wheelset RBM is included through the RB model developed. The accuracy of the results is studied by a comparison

with the solution of the FSI problem computed with the commercial FE software Ansys [18]. Likewise, the computational efficiency of the proposed methodology is evaluated by benchmarking against a full three-dimensional methodology.

Following this introduction, Section 2 presents the dynamic model of the rotating rigid wheelset. Then, the three-dimensional vibroacoustic model of the rotating wheel is presented in Section 3. In Section 4, the expansion of the wheel response around the circumferential direction is introduced and the EoM and sound radiation are obtained in a two-dimensional frame. Some results are presented in Section 5 and the main conclusions are summarized in Section 6.

2 Rigid body motion of the wheelset

This section describes the methodology used to determine the equations of the RBM including rotation at a constant speed Ω about its axis. There are six degrees of freedom associated with the RBM, three translations $\boldsymbol{\tau} = \begin{pmatrix} \tau_1 & \tau_2 & \tau_3 \end{pmatrix}^{\mathrm{T}}$ parallel to the cartesian axes in Fig. 1 and three rotations $\boldsymbol{\psi} = \begin{pmatrix} \psi_1 & \psi_2 & \psi_3 \end{pmatrix}^{\mathrm{T}}$ about them. Although the RBM is associated with the cartesian axes, the EoM are developed in a cylindrical reference frame with radial r, circumferential θ and axial z components. Considering only the RBM, the position $\mathbf{q}$ of any particle of the wheelset during the motion can be expressed as follows:

$$\mathbf{q} = \mathbf{u} + \mathbf{s}(\mathbf{u}, t), \tag{1}$$

where $\mathbf{u} = \begin{pmatrix} r & 0 & z \end{pmatrix}^{\mathrm{T}}$ is the spatial position, expressed in an inertial frame, corresponding to that particle without the motion and $\mathbf{s} = \begin{pmatrix} s_r & s_\theta & s_z \end{pmatrix}^{\mathrm{T}}$ contains the displacements of the particle in the position $\mathbf{u}$ at instant t due to the RBM in the radial, circumferential and axial directions, respectively. These displacements can be divided into the contribution of the translational $\mathbf{s}_\tau$ and rotational $\mathbf{s}_\psi$ motions, which yields the following vectorial sum:

$$\mathbf{s} = \mathbf{s}_\tau + \mathbf{s}_\psi. \tag{2}$$

On the one hand, the vector $\mathbf{s}_\tau$ is related to the translational motion $\boldsymbol{\tau}$ by means of the transformation matrix between the cartesian and cylindrical frame $\boldsymbol{\Theta}_\tau$, which, according to the definition of the coordinate θ in Fig. 1, is given by:

$$\mathbf{s}_\tau = \begin{bmatrix} \sin(\theta) & 0 & \cos(\theta) \\ \cos(\theta) & 0 & -\sin(\theta) \\ 0 & 1 & 0 \end{bmatrix} \boldsymbol{\tau} = \boldsymbol{\Theta}_\tau \boldsymbol{\tau}. \tag{3}$$

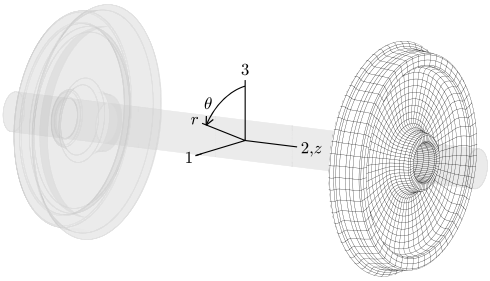

Fig. 1: Definition of the cartesian and cylindrical reference systems. The motion of the flexible wheel is evaluated through the FEM. The RBM of the wheelset, described analytically, is superimposed on it.

On the other hand, the vector $\mathbf{s}_\psi$ can be expressed as follows:

$$\mathbf{s}_\psi = \boldsymbol{\Theta}_\tau(\mathbf{R} - \mathbf{I}_{3\times3})\boldsymbol{\Theta}_\tau^{\mathrm{T}}\mathbf{u}, \tag{4}$$

where $\mathbf{I}_{3\times3}$ is the identity matrix of order 3×3 and the matrix $\mathbf{R}$ defines the position of a particle after the rigid body rotation expressed in an inertial frame and formulated in cartesian coordinates. Assuming small angles, this is given by:

$$\mathbf{R} = \begin{bmatrix} 1 & -\psi_3 & \psi_2 \\ \psi_3 & 1 & -\psi_1 \\ -\psi_2 & \psi_1 & 1 \end{bmatrix}. \tag{5}$$

After manipulating Eq. (4), the following relation between $\mathbf{s}_\psi$ and $\boldsymbol{\psi}$ is found:

$$\mathbf{s}_\psi = \begin{bmatrix} z\cos(\theta) & 0 & -z\sin(\theta) \\ -z\sin(\theta) & r & -z\cos(\theta) \\ -r\cos(\theta) & 0 & r\sin(\theta) \end{bmatrix} \boldsymbol{\psi} = \boldsymbol{\Theta}_\psi \boldsymbol{\psi}. \tag{6}$$

As the axis of rotation is coincident with the axial direction, i.e. $\boldsymbol{\Omega} = \begin{pmatrix} 0 & 0 & \Omega \end{pmatrix}^{\mathrm{T}}$ in the cylindrical frame, the velocity $\mathbf{v}_s$ due to the rigid body spinning is given by:

$$\mathbf{v}_s = \boldsymbol{\Omega} \times \mathbf{u} = r\Omega\widehat{\mathbf{e}_2}, \tag{7}$$

with $\widehat{\mathbf{e}_2} = \begin{pmatrix} 0 & 1 & 0 \end{pmatrix}^{\mathrm{T}}$. In an Eulerian approach, the velocity of any particle of the wheel can be evaluated as follows [19, 20]:

$$\frac{\mathrm{D}\mathbf{q}}{\mathrm{D}t} = \mathbf{v}_s + \boldsymbol{\Theta}_\tau \dot{\boldsymbol{\tau}} + \boldsymbol{\Theta}_\psi \dot{\boldsymbol{\psi}} + \Omega \mathbf{Y} \boldsymbol{\psi}, \tag{8}$$

where the matrix $\mathbf{Y}$ is given by:

$$\mathbf{Y} = \begin{bmatrix} 0 & -r & 0 \\ 0 & 0 & 0 \\ r\sin(\theta) & 0 & r\cos(\theta) \end{bmatrix}. \tag{9}$$

The kinetic energy of the rotating wheelset due to its RBM is given by:

$$\begin{aligned} K =& \frac{1}{2}\int_{V_S} \rho \frac{\mathrm{D}\mathbf{q}^{\mathrm{T}}}{\mathrm{D}t}\frac{\mathrm{D}\mathbf{q}}{\mathrm{D}t}\mathrm{d}V = \frac{1}{2}M\dot{\boldsymbol{\tau}}^{\mathrm{T}}\dot{\boldsymbol{\tau}} + \frac{1}{2}\dot{\boldsymbol{\psi}}^{\mathrm{T}}\boldsymbol{\mathcal{J}}\dot{\boldsymbol{\psi}} + \frac{1}{2}\Omega\mathcal{J}_z\dot{\boldsymbol{\psi}}^{\mathrm{T}}\mathbf{K}_1\boldsymbol{\psi} \\ &+ \frac{1}{2}\Omega^2\mathcal{J}_z\boldsymbol{\psi}^{\mathrm{T}}\mathbf{K}_2\boldsymbol{\psi} + \Omega\mathcal{J}_z\dot{\boldsymbol{\psi}}^{\mathrm{T}}\widehat{\mathbf{e}_2} + \frac{1}{2}\Omega^2\mathcal{J}_z, \end{aligned} \tag{10}$$

where ρ is the density of the material, V_S is the volume of the wheelset, M is its mass, $\mathcal{J}_z = \int_{V_S} \rho r^2 \mathrm{d}V$ is the moment of inertia about the axis of rotation, the matrices $\mathbf{K}_1$ and $\mathbf{K}_2$ are shown in the Appendix A and $\boldsymbol{\mathcal{J}}$ is the inertia tensor of the wheelset that, given the cartesian reference system defined (see Fig. 1), can be expressed as:

$$\boldsymbol{\mathcal{J}} = \begin{bmatrix} \mathcal{J}_r & 0 & 0 \\ 0 & \mathcal{J}_z & 0 \\ 0 & 0 & \mathcal{J}_r \end{bmatrix}, \tag{11}$$

with $\mathcal{J}_r = \frac{\mathcal{J}_z}{2} + \int_{V_S} \rho z^2 \mathrm{d}V$ being the moment of inertia about the radial axis. From the energy equation, Eq. (10), it follows that the translational and rotational motions are decoupled. The Lagrange equations for the translational motion are given by:

$$\frac{\mathrm{D}}{\mathrm{D}t}\left(\frac{\partial K}{\partial \dot{\boldsymbol{\tau}}}\right)^{\mathrm{T}} - \left(\frac{\partial K}{\partial \boldsymbol{\tau}}\right)^{\mathrm{T}} = M\ddot{\boldsymbol{\tau}}, \tag{12}$$

while for the rotation movement it is verified that:

$$\frac{\mathrm{D}}{\mathrm{D}t}\left(\frac{\partial K}{\partial \dot{\boldsymbol{\psi}}}\right)^{\mathrm{T}} - \left(\frac{\partial K}{\partial \boldsymbol{\psi}}\right)^{\mathrm{T}} = \boldsymbol{\mathcal{J}}\ddot{\boldsymbol{\psi}} + \Omega\mathcal{J}_z\mathbf{K}_1\dot{\boldsymbol{\psi}} - \Omega^2\mathcal{J}_z\mathbf{K}_2\boldsymbol{\psi}. \tag{13}$$

In this work, it is considered that the external forces come from the wheel–rail interaction. Also, for simplicity, the contact is assumed to occur at the angular

coordinate $\theta_c = 0$. Given the interaction forces $\mathbf{F} = \begin{pmatrix} F_r & F_\theta & F_z \end{pmatrix}^{\mathrm{T}}$ applied at the contact point, the six equations of the RBM are given by:

$$\begin{aligned} M\ddot{\boldsymbol{\tau}}(t) &= \begin{bmatrix} 0 & 1 & 0 \\ 0 & 0 & 1 \\ 1 & 0 & 0 \end{bmatrix} \mathbf{F}(t), \\ \boldsymbol{\mathcal{J}}\ddot{\boldsymbol{\psi}}(t) + \Omega \mathcal{J}_z \mathbf{K}_1 \dot{\boldsymbol{\psi}}(t) - \Omega^2 \mathcal{J}_z \mathbf{K}_2 \boldsymbol{\psi}(t) &= \begin{bmatrix} z_c & 0 & -r_c \\ 0 & r_c & 0 \\ 0 & -z_c & 0 \end{bmatrix} \mathbf{F}(t), \end{aligned} \tag{14}$$

where r_c and z_c are, respectively, the radial and axial coordinates of the contact point. For convenience, the EoM are transformed to the frequency domain. Considering a harmonic excitation of frequency ω and constant amplitude $\mathbf{F}(\omega)$, the steady state RBM is obtained by solving the following expressions:

$$\begin{aligned} -\omega^2 M\boldsymbol{\tau}(\omega) &= \begin{bmatrix} 0 & 1 & 0 \\ 0 & 0 & 1 \\ 1 & 0 & 0 \end{bmatrix} \mathbf{F}(\omega), \\ \boldsymbol{\Lambda}\boldsymbol{\psi}(\omega) &= \begin{bmatrix} z_c & 0 & -r_c \\ 0 & r_c & 0 \\ 0 & -z_c & 0 \end{bmatrix} \mathbf{F}(\omega), \end{aligned} \tag{15}$$

with the matrix $\boldsymbol{\Lambda}$ being defined as follows:

$$\boldsymbol{\Lambda} = \begin{bmatrix} -\omega^2 \mathcal{J}_r - \frac{1}{2}\Omega^2 \mathcal{J}_z & 0 & -\mathrm{i}\omega\Omega\mathcal{J}_z \\ 0 & -\mathcal{J}_z(\omega^2 + \Omega^2) & 0 \\ \mathrm{i}\omega\Omega\mathcal{J}_z & 0 & -\omega^2 \mathcal{J}_r - \frac{1}{2}\Omega^2 \mathcal{J}_z \end{bmatrix},$$

where i is the imaginary unit. The three translational motions and the rotation about the axial axis ψ_2 are decoupled from the other motions, while the rotations about the longitudinal ψ_1 and vertical ψ_3 axes are coupled to each other.

3 Three-dimensional vibroacoustic model of the wheel

In this section, the three-dimensional dynamic model developed by Martínez-Casas *et al.* [14] is formulated in a cylindrical reference system. This allows the axisymmetric approach to be developed in the next section. The models can be used to describe the dynamic behaviour of any rotating body with axial symmetry considering its flexibility and small RBM displacements. In this work, however, it is employed to evaluate the motion of a flexible railway wheel which is constrained

at the inner edge of the hub and is rotating at a constant speed Ω about its main axis. After solving its vibroacoustic behaviour, the contribution of the RBM of the wheelset is included according to the developments of Section 2.

3.1 Kinetic energy

Given the rotating wheel subjected to an external dynamic force, the position $\mathbf{p}$ of any particle in the deformed shape can be expressed as the following vector sum:

$$\mathbf{p} = \mathbf{u} + \mathbf{w}(\mathbf{u}, t), \tag{16}$$

where $\mathbf{w} = \begin{pmatrix} w_r & w_\theta & w_z \end{pmatrix}^{\mathrm{T}}$ contains the displacements of the particle at the position $\mathbf{u}$ and instant t due to flexibility in the radial, circumferential and axial directions. The velocity of any particle of the wheel can be evaluated as follows [19, 20]:

$$\frac{\mathrm{D}\mathbf{p}}{\mathrm{D}t} = \mathbf{v}_s + \dot{\mathbf{w}} + \Omega \frac{\partial \mathbf{w}}{\partial \theta} + \Omega \mathbf{J}\mathbf{w}, \tag{17}$$

where $\dot{\mathbf{w}} = \begin{pmatrix} \dot{w}_r & \dot{w}_\theta & \dot{w}_z \end{pmatrix}^{\mathrm{T}}$ contains the time derivatives of the displacements, $\frac{\partial \mathbf{w}}{\partial \theta} = \begin{pmatrix} \frac{\partial w_r}{\partial \theta} & \frac{\partial w_\theta}{\partial \theta} & \frac{\partial w_z}{\partial \theta} \end{pmatrix}^{\mathrm{T}}$ considers the derivatives with respect to the circumferential direction and the matrix $\mathbf{J}$ is specified in Appendix A. The kinetic energy E_k of the railway wheel is given by:

$$\begin{aligned} E_k =& \frac{1}{2}\int_V \rho \frac{\mathrm{D}\mathbf{p}^{\mathrm{T}}}{\mathrm{D}t}\frac{\mathrm{D}\mathbf{p}}{\mathrm{D}t}\mathrm{d}V = \frac{1}{2}\Omega^2 \int_V \rho r^2 \mathrm{d}V + \frac{1}{2}\int_V \rho \dot{\mathbf{w}}^{\mathrm{T}}\dot{\mathbf{w}}\mathrm{d}V \\ &+ \frac{1}{2}\Omega^2 \int_V \rho \frac{\partial \mathbf{w}^{\mathrm{T}}}{\partial \theta}\frac{\partial \mathbf{w}}{\partial \theta}\mathrm{d}V + \Omega^2 \int_V \rho \frac{\partial \mathbf{w}^{\mathrm{T}}}{\partial \theta}\mathbf{J}\mathbf{w}\mathrm{d}V + \Omega \int_V \rho r \widehat{\mathbf{e}}_2^{\,\mathrm{T}} \dot{\mathbf{w}}\mathrm{d}V \\ &+ \Omega^2 \int_V \rho r \widehat{\mathbf{e}}_2^{\,\mathrm{T}} \frac{\partial \mathbf{w}}{\partial \theta}\mathrm{d}V + \Omega^2 \int_V \rho r \widehat{\mathbf{e}}_2^{\,\mathrm{T}} \mathbf{J}\mathbf{w}\mathrm{d}V + \Omega \int_V \rho \dot{\mathbf{w}}^{\mathrm{T}} \frac{\partial \mathbf{w}}{\partial \theta}\mathrm{d}V \\ &+ \Omega \int_V \rho \dot{\mathbf{w}}^{\mathrm{T}} \mathbf{J}\mathbf{w}\mathrm{d}V + \frac{1}{2}\Omega^2 \int_V \rho \mathbf{w}^{\mathrm{T}} \mathbf{E}\mathbf{w}\mathrm{d}V, \end{aligned} \tag{18}$$

where V is the volume of the wheel, $\mathrm{d}V = r\mathrm{d}\theta\mathrm{d}r\mathrm{d}z$ and the matrix $\mathbf{E} = \mathbf{J}^{\mathrm{T}}\mathbf{J}$ can be found in Appendix A. Since the wheel is constrained at the inner edge of the hub, all the terms in the right hand side of Eq. (18) except the first one are associated with the wheel flexibility, while the first one is due to steady rolling.

3.2 Strain energy

The elastic potential energy E_p can be expressed as follows:

$$E_p = \frac{1}{2}\int_V \boldsymbol{\varepsilon}^{\mathrm{T}}\boldsymbol{\sigma}\mathrm{d}V = \frac{1}{2}\int_V \boldsymbol{\varepsilon}^{\mathrm{T}}\mathbf{D}\boldsymbol{\varepsilon}\mathrm{d}V, \tag{19}$$

where $\mathbf{D}$ is the material stiffness matrix obtained from Hooke's Law (see Appendix A). The strain vector satisfies $\boldsymbol{\varepsilon} = \mathbf{L}\mathbf{w} = \begin{pmatrix}\varepsilon_r & \varepsilon_\theta & \varepsilon_z & \gamma_{zr} & \gamma_{r\theta} & \gamma_{\theta z}\end{pmatrix}^{\mathrm{T}}$, with $\mathbf{L}$ being a matrix operator defined in Appendix A.

3.3 Virtual work

The roughness present on the wheel and rail running surfaces generates dynamic forces when the vehicle is travelling along the track. These forces are introduced in the wheel model as external loads applied at its contact point. The virtual work of the interaction forces $\mathbf{F} = \begin{pmatrix}F_r & F_\theta & F_z\end{pmatrix}^{\mathrm{T}}$ is given by:

$$\delta W = \delta\mathbf{w}^{\mathrm{T}}\mathbf{F}. \tag{20}$$

3.4 Equation of motion

A FE model is adopted, so that the displacement field in the eth element of the FE mesh is computed from the nodal solution by the following interpolation:

$$\mathbf{w}(r,\theta,z,t) = \mathbf{N}(r,\theta,z)\boldsymbol{w}^e(t), \tag{21}$$

$\mathbf{N}$ being the shape function matrix [21], which can be expressed as follows:

$$\begin{aligned}\mathbf{N} &= \begin{bmatrix}\mathbf{N}_1 & \cdots & \mathbf{N}_j & \cdots & \mathbf{N}_m\end{bmatrix};\\ \mathbf{N}_j &= N_j\begin{bmatrix}\cos(\theta-\theta_j) & \sin(\theta-\theta_j) & 0\\ -\sin(\theta-\theta_j) & \cos(\theta-\theta_j) & 0\\ 0 & 0 & 1\end{bmatrix},\end{aligned} \tag{22}$$

where subscript j refers to the jth node, m is the number of nodes in the eth element and N_j, which is dependent on the r, θ and z coordinates, is the shape function associated with the jth node. The vector $\boldsymbol{w}^e$ contains the displacements of the three Degrees of Freedom (DoF) of each node in the eth element, that is:

$$\boldsymbol{w}^e = \begin{pmatrix}\boldsymbol{w}_1^e & \cdots & \boldsymbol{w}_j^e & \cdots & \boldsymbol{w}_m^e\end{pmatrix}^{\mathrm{T}}; \qquad \boldsymbol{w}_j^e = \begin{pmatrix}w_{r,j}^e & w_{\theta,j}^e & w_{z,j}^e\end{pmatrix}. \tag{23}$$

By applying the expressions for the kinetic and strain energies in Eqs. (18) and (19) to the eth element and considering the FE approach of Eq. (21), the non-zero terms of the Lagrange equations are:

$$\begin{aligned}\frac{\mathrm{D}}{\mathrm{D}t}\left(\frac{\partial E_k}{\partial \dot{\boldsymbol{w}}^e}\right)^{\mathrm{T}} - \left(\frac{\partial E_k}{\partial \boldsymbol{w}^e}\right)^{\mathrm{T}} + \left(\frac{\partial E_p}{\partial \boldsymbol{w}^e}\right)^{\mathrm{T}} &= \mathbf{M}^e\ddot{\boldsymbol{w}}^e + 2\Omega\mathbf{V}^e\dot{\boldsymbol{w}}^e \\ &\quad + \left(\mathbf{K}^e + \Omega^2\mathbf{A}^e\right)\boldsymbol{w}^e - \Omega^2\mathbf{c}^e.\end{aligned} \tag{24}$$

The element matrices in Eq. (24) correspond to the following expressions:

$$\begin{aligned}\mathbf{M}^e &= \int_{V^e}\rho\mathbf{N}^{\mathrm{T}}\mathbf{N}\mathrm{d}V, \\ \mathbf{V}^e &= \int_{V^e}\rho\mathbf{N}^{\mathrm{T}}\frac{\partial\mathbf{N}}{\partial\theta}\mathrm{d}V + \int_{V^e}\rho\mathbf{N}^{\mathrm{T}}\mathbf{J}\mathbf{N}\mathrm{d}V, \\ \mathbf{K}^e &= \int_{V^e}\mathbf{B}^{\mathrm{T}}\mathbf{D}\mathbf{B}\mathrm{d}V, \\ \mathbf{A}^e &= \int_{V^e}\rho\mathbf{N}^{\mathrm{T}}\frac{\partial^2\mathbf{N}}{\partial\theta^2}\mathrm{d}V + 2\int_{V^e}\rho\mathbf{N}^{\mathrm{T}}\mathbf{J}\frac{\partial\mathbf{N}}{\partial\theta}\mathrm{d}V - \int_{V^e}\rho\mathbf{N}^{\mathrm{T}}\mathbf{E}\mathbf{N}\mathrm{d}V, \\ \mathbf{c}^e &= \int_{V^e}\rho\mathbf{N}^{\mathrm{T}}\widehat{\mathbf{e}_1}\mathrm{d}V,\end{aligned} \tag{25}$$

where V^e is the volume of the eth element, $\widehat{\mathbf{e}_1} = \begin{pmatrix}1 & 0 & 0\end{pmatrix}^{\mathrm{T}}$ and $\mathbf{B} = \mathbf{L}\mathbf{N}$. As stated in [14], the second derivative in the matrix $\mathbf{A}^e$ can be reduced to a first derivative by integrating its first term by parts and therefore the convergence of the integral is guaranteed when C^0 shape functions are taken into account.

Following the FEM approach, the element matrices are assembled to obtain the global matrices of the equation of motion. The DoF (displacements of nodes) of the wheel are also assembled into the vector $\boldsymbol{w}$. Similarly, the interaction forces $\mathbf{F}$ applied on the wheel contact point are considered in the FE assembly of the forces (applied on all nodes and directions) into the vector $\boldsymbol{\mathcal{F}}$. Thus, the EoM are given by:

$$\mathbf{M}\ddot{\boldsymbol{w}}(t) + 2\Omega\mathbf{V}\dot{\boldsymbol{w}}(t) + \left(\mathbf{K} + \Omega^2\mathbf{A}\right)\boldsymbol{w}(t) = \Omega^2\mathbf{c} + \boldsymbol{\mathcal{F}}(t). \tag{26}$$

In order to evaluate the rolling noise radiated by the wheel, the model is transformed to the frequency domain, in which the EoM can be expressed for $\omega > 0$ as follows:

$$\left(-\omega^2\mathbf{M} + 2\mathrm{i}\omega\Omega\mathbf{V} + \mathbf{K} + \Omega^2\mathbf{A}\right)\boldsymbol{w}(\omega) = \boldsymbol{\mathcal{F}}(\omega), \tag{27}$$

where $\boldsymbol{w}(\omega)$ represents the steady state response to a harmonic excitation of frequency ω and constant amplitude $\boldsymbol{\mathcal{F}}(\omega)$.

3.5 Sound radiation

After solving the railway wheel dynamics, its acoustic radiation is computed by postprocessing the vibrational field on its surface. The radiation model employed in this work was developed by Thompson [16] and it establishes that the wheel sound power is obtained as the sum of the power associated with each set of modes with the same number of nodal diameters n. The wheel acoustic power W for a given frequency ω is evaluated as follows:

$$W(\omega) = \rho_f c \sum_{n\geq 0} \left(\sigma_{z,n}(\omega) S_z \langle \widetilde{v}^2_{z,n}(\omega) \rangle + \sigma_{r,n}(\omega) S_r \langle \widetilde{v}^2_{r,n}(\omega) \rangle \right), \tag{28}$$

where ρ_f is the density of air (fluid surrounding the wheel) and c is the speed of sound in air. The participation of each set of modes with n nodal diameters is in turn divided into its axial (subscript z) and radial (subscript r) contribution. Functions σ are the radiation ratios, which are numerically assessed in Ref. [16]. The wheel surface is projected normal to the axial and radial directions, which yields the areas S_z and S_r, respectively. Similarly, the squared velocity of the wheel surface is projected into the axial and radial directions and the corresponding values are averaged over time ($\widetilde{\ }$) and space ($\langle \quad \rangle$); these are given by:

$$\langle \widetilde{v}^2_{i,n} \rangle = \frac{1}{2S_i} \int_S |v_{i,n}|^2 \mathrm{d}S_i, \quad i = z, r, \quad n \geq 0, \tag{29}$$

S being the wheel surface. In this work, the wheelset RBM is superimposed on the vibration of the wheel constrained at the inner edge of the hub. To do this, on the one hand, the EoM of the wheel given in Eq. (27) are solved and the vibrational velocity of any particle of the wheel $\dot{\mathbf{w}}(r, \theta, z, \omega)$ associated with its flexibility is obtained. On the other hand, the EoM of the rigid wheelset given in Eq. (15) are solved and the RB motions $\dot{\boldsymbol{\tau}}(\omega)$ and $\dot{\boldsymbol{\psi}}(\omega)$ are obtained; from these the vibrational velocity of any particle of the wheel $\dot{\mathbf{s}}(r, \theta, z, \omega)$ associated with the wheelset RBM can be found through the expressions in Eqs. (2), (3) and (6). Finally, both flexible and RB motions are superimposed. The wheelset RBM contributes to the response only for $n \leq 1$. Defining $\dot{w}|_n$ as the contribution to the velocity of the flexible wheel modes with n nodal diameters, then for $n = 0$ the total velocities of a wheel particle in the axial and radial directions are given by:

$$\begin{aligned} v_{z,0}(r,z,\omega) &= \dot{w}_z(r,z,\omega)|_{n=0} + \dot{\tau}_2(\omega), \\ v_{r,0}(r,z,\omega) &= \dot{w}_r(r,z,\omega)|_{n=0}, \end{aligned} \tag{30}$$

with $\dot{w}_z|_{n=0}$ and $\dot{w}_r|_{n=0}$ being associated with the wheel flexibility and $\dot{\tau}_2$ with the wheelset RBM. Likewise, the contribution of modes with $n = 1$ to the velocities is as follows:

$$\begin{aligned} v_{z,1}(r,\theta,z,\omega) &= \dot{w}_z(r,\theta,z,\omega)|_{n=1} - r\dot{\psi}_1(\omega)\cos(\theta) + r\dot{\psi}_3(\omega)\sin(\theta), \\ v_{r,1}(r,\theta,z,\omega) &= \dot{w}_r(r,\theta,z,\omega)|_{n=1} + (\dot{\tau}_3(\omega) + z\dot{\psi}_1(\omega))\cos(\theta) \\ &\quad + (\dot{\tau}_1(\omega) - z\dot{\psi}_3(\omega))\sin(\theta), \end{aligned} \tag{31}$$

with $\dot{w}_z|_{n=1}$ and $\dot{w}_r|_{n=1}$ being associated with the wheel flexibility and the remaining terms with the wheelset RBM. Finally, for $n \geq 2$ the velocities are given by:

$$v_{i,n}(r,\theta,z,\omega) = \dot{w}_i(r,\theta,z,\omega)|_n, \quad i = z,r, \quad n \geq 2, \tag{32}$$

where there is no contribution from the wheelset RBM.

4 Vibroacoustic model: Axisymmetric approach

Given the axial symmetry of the wheel geometry, the displacement field can be expressed by means of an expansion as a Fourier series given by [22]:

$$\begin{aligned} w_r &= w_{r,0} + \sum_{n>0} \left(w_{r,n}\cos(n\theta) - \overline{w}_{r,n}\sin(n\theta) \right), \\ w_\theta &= -\overline{w}_{\theta,0} + \sum_{n>0} \left(w_{\theta,n}\sin(n\theta) - \overline{w}_{\theta,n}\cos(n\theta) \right), \\ w_z &= w_{z,0} + \sum_{n>0} \left(w_{z,n}\cos(n\theta) - \overline{w}_{z,n}\sin(n\theta) \right), \end{aligned} \tag{33}$$

n being an integer number representing each Fourier term, corresponding to the set of modes with n nodal diameters. In Eq. (33), the harmonic amplitudes without a bar represent symmetric motions about $\theta = 0$ and those with a bar represent antisymmetric motions about $\theta = 0$. It should be noted that the harmonic amplitudes $w_{r,0}$, $w_{z,0}$ and $\overline{w}_{\theta,0}$ (for $n = 0$) as well as $w_{r,n}$, $w_{\theta,n}$, $w_{z,n}$, $\overline{w}_{r,n}$, $\overline{w}_{\theta,n}$ and $\overline{w}_{z,n}$ (for $n > 0$) are dependent on the r, z and t coordinates but are independent of the θ coordinate.

4.1 Kinetic energy

Due to the harmonic description of the displacement field in the circumferential direction, the kinetic energy of the system described in Eq. (18) can be integrated analytically over this direction; details of the procedure are given in Appendix B. As a result, the kinetic energy can be divided into the contribution of each Fourier term and is therefore given by:

$$E_k = E_{k,0} + \sum_{n>0} E_{k,n}. \tag{34}$$

When considering a stationary body with axial symmetry, for each Fourier term the energy associated with the symmetric harmonic motion about $\theta = 0$ is also decoupled from the antisymmetric harmonic motion about $\theta = 0$. However, if the axisymmetric body is rotating, there is a coupling between these motions due to the 8th and 9th terms of the kinetic energy in the right hand side of Eq. (18). As a consequence, for each Fourier term both motions are simultaneously solved. The harmonic amplitudes in Eq. (33) are grouped for each Fourier term as follows:

$$\begin{aligned} \mathbf{w}_0 &= \begin{pmatrix} w_{r,0} & w_{z,0} & \overline{w}_{\theta,0} \end{pmatrix}^{\mathrm{T}}, && n = 0, \\ \mathbf{w}_n &= \begin{pmatrix} w_{r,n} & w_{\theta,n} & w_{z,n} & \overline{w}_{r,n} & \overline{w}_{\theta,n} & \overline{w}_{z,n} \end{pmatrix}^{\mathrm{T}}, && n > 0. \end{aligned} \tag{35}$$

The kinetic energy for $n = 0$ is given by:

$$\begin{aligned} E_{k,0} =& \pi\Omega^2 \int_A \rho r^3 \mathrm{d}A + \pi \int_A \rho r \dot{\mathbf{w}}_0^{\mathrm{T}} \dot{\mathbf{w}}_0 \mathrm{d}A - 2\pi\Omega \int_A \rho r^2 \widehat{\mathbf{e}_3}^{\mathrm{T}} \dot{\mathbf{w}}_0 \mathrm{d}A \\ &+ 2\pi\Omega^2 \int_A \rho r^2 \widehat{\mathbf{e}_1}^{\mathrm{T}} \mathbf{w}_0 \mathrm{d}A + 2\pi\Omega \int_A \rho r \dot{\mathbf{w}}_0^{\mathrm{T}} \mathbf{J}_0 \mathbf{w}_0 \mathrm{d}A \\ &+ \pi\Omega^2 \int_A \rho r \mathbf{w}_0^{\mathrm{T}} \mathbf{E}_0 \mathbf{w}_0 \mathrm{d}A, \end{aligned} \tag{36}$$

where A is the area of the wheel cross-section, $\mathrm{d}A = \mathrm{d}r\mathrm{d}z$, $\widehat{\mathbf{e}_3} = \begin{pmatrix} 0 & 0 & 1 \end{pmatrix}^{\mathrm{T}}$ and the matrices $\mathbf{J}_0$ and $\mathbf{E}_0$ are presented in Appendix A. The kinetic energy due to steady rolling, first term in the right hand side of Eq. (36), is not associated with vibration for $n = 0$ but is also included in the kinetic energy for $n = 0$, although it will not appear in the EoM. The kinetic energy $E_{k,n}$ for each $n > 0$ is expressed as follows:

$$
\begin{aligned}
E_{k,n} =& \frac{\pi}{2}\int_A \rho r \dot{\mathbf{w}}_n^{\mathrm{T}}\dot{\mathbf{w}}_n \mathrm{d}A + \frac{\pi}{2}\Omega^2 \int_A \rho r n^2 \mathbf{w}_n^{\mathrm{T}}\mathbf{w}_n \mathrm{d}A \\
&+2\pi\Omega^2 \int_A \rho r n \mathbf{w}_n^{\mathrm{T}}\mathbf{J}_1\mathbf{w}_n \mathrm{d}A + \pi\Omega \int_A \rho r n \dot{\mathbf{w}}_n^{\mathrm{T}}\mathbf{J}_2\mathbf{w}_n \mathrm{d}A \\
&+\pi\Omega \int_A \rho r \dot{\mathbf{w}}_n^{\mathrm{T}}\mathbf{J}_3\mathbf{w}_n \mathrm{d}A + \frac{\pi}{2}\Omega^2 \int_A \rho r \mathbf{w}_n^{\mathrm{T}}\mathbf{E}_3\mathbf{w}_n \mathrm{d}A,
\end{aligned} \tag{37}
$$

with the matrices $\mathbf{J}_1$, $\mathbf{J}_2$, $\mathbf{J}_3$ and $\mathbf{E}_3$ being defined in Appendix A.

4.2 Strain energy

The strain energy in Eq. (19) can be integrated analytically over the circumferential direction according to the expansion of Eq. (33). Details of this are given in Appendix B. Similarly to the kinetic energy, the strain energy can be expressed as a sum of the contributions of each Fourier term, yielding the following expression:

$$
E_p = E_{p,0} + \sum_{n>0} E_{p,n}. \tag{38}
$$

Unlike the kinetic energy, for each Fourier term the contribution in the strain energy of the symmetric motion about $\theta = 0$ is decoupled from the antisymmetric motion about $\theta = 0$. Nevertheless, since the kinetic energy equation couples both motions, they are also considered simultaneously in the strain energy equation.

The strain energy $E_{p,0}$ for $n = 0$ is given by:

$$
E_{p,0} = \pi \int_A r \boldsymbol{\varepsilon}_0^{\mathrm{T}}\mathbf{D}\boldsymbol{\varepsilon}_0 \mathrm{d}A, \tag{39}
$$

where $\boldsymbol{\varepsilon}_0$ is defined as follows:

$$
\boldsymbol{\varepsilon}_0 = \mathbf{L}_0\mathbf{w}_0, \tag{40}
$$

with $\mathbf{L}_0$ being a matrix derivative operator specified in Appendix A. The strain energy $E_{p,n}$ for $n > 0$ is given by:

$$
E_{p,n} = \frac{\pi}{2}\int_A r \boldsymbol{\varepsilon}_n^{\mathrm{T}}\mathbf{D}\boldsymbol{\varepsilon}_n \mathrm{d}A + \frac{\pi}{2}\int_A r \overline{\boldsymbol{\varepsilon}}_n^{\mathrm{T}}\mathbf{D}\overline{\boldsymbol{\varepsilon}}_n \mathrm{d}A, \tag{41}
$$

where $\boldsymbol{\varepsilon}_n$ and $\overline{\boldsymbol{\varepsilon}}_n$ are defined as follows:

$$\begin{aligned}\boldsymbol{\varepsilon}_n &= (\mathbf{L}_a + n\mathbf{L}_b)\mathbf{w}_n,\\ \overline{\boldsymbol{\varepsilon}}_n &= (\overline{\mathbf{L}}_a + n\overline{\mathbf{L}}_b)\mathbf{w}_n.\end{aligned} \tag{42}$$

The matrix operators $\mathbf{L}_a$, $\mathbf{L}_b$, $\overline{\mathbf{L}}_a$ and $\overline{\mathbf{L}}_b$ are specified in Appendix A.

4.3 Virtual work

Although the interaction forces $\mathbf{F}$ are modelled as point loads at the wheel contact, they can be expressed as a function of the circumferential coordinate θ. Therefore, they are defined in terms of the external force distribution $\mathbf{f}$, which is equivalent to $\mathbf{F}$, applied along the locus of points with the same radial and axial coordinates as the contact point. This can be written as:

$$\mathbf{f}(\theta) = \mathbf{F}\frac{\delta(\theta-\theta_c)}{r_c}, \tag{43}$$

with $\delta(\theta-\theta_c)$ being the Dirac delta function. The force distribution $\mathbf{f} = \begin{pmatrix} f_r & f_\theta & f_z \end{pmatrix}^{\mathrm{T}}$ can also be decomposed as a Fourier series with respect to the circumferential direction, which yields the following expressions:

$$\begin{aligned} f_r &= f_{r,0} + \sum_{n>0} \left(f_{r,n}\cos(n\theta) - \overline{f}_{r,n}\sin(n\theta) \right),\\ f_\theta &= -\overline{f}_{\theta,0} + \sum_{n>0} \left(f_{\theta,n}\sin(n\theta) - \overline{f}_{\theta,n}\cos(n\theta) \right),\\ f_z &= f_{z,0} + \sum_{n>0} \left(f_{z,n}\cos(n\theta) - \overline{f}_{z,n}\sin(n\theta) \right), \end{aligned} \tag{44}$$

where the harmonic force coefficients $f_{r,0}$, $f_{z,0}$, $\overline{f}_{\theta,0}$, $f_{r,n}$, $f_{\theta,n}$, $f_{z,n}$, $\overline{f}_{r,n}$, $\overline{f}_{\theta,n}$ and $\overline{f}_{z,n}$ are independent of θ and, considering the expression in Eq. (43), can be evaluated as follows:

$$\begin{aligned}
\begin{pmatrix} f_{r,0} \\ \overline{f}_{\theta,0} \\ f_{z,0} \end{pmatrix} &= \frac{1}{2\pi}\int_{-\pi}^{\pi} \begin{pmatrix} f_r \\ -f_\theta \\ f_z \end{pmatrix} \mathrm{d}\theta = \frac{1}{2\pi r_c}\begin{pmatrix} F_r \\ -F_\theta \\ F_z \end{pmatrix}, && n = 0,\\
\begin{pmatrix} f_{r,n} \\ \overline{f}_{\theta,n} \\ f_{z,n} \end{pmatrix} &= \frac{1}{\pi}\int_{-\pi}^{\pi} \begin{pmatrix} f_r \\ -f_\theta \\ f_z \end{pmatrix} \cos(n\theta)\mathrm{d}\theta = \frac{1}{\pi r_c}\begin{pmatrix} F_r \\ -F_\theta \\ F_z \end{pmatrix}, && n > 0,\\
\begin{pmatrix} \overline{f}_{r,n} \\ f_{\theta,n} \\ \overline{f}_{z,n} \end{pmatrix} &= \frac{1}{\pi}\int_{-\pi}^{\pi} \begin{pmatrix} -f_r \\ f_\theta \\ -f_z \end{pmatrix} \sin(n\theta)\mathrm{d}\theta = \begin{pmatrix} 0 \\ 0 \\ 0 \end{pmatrix}, && n > 0.
\end{aligned} \tag{45}$$

As in Section 2, it is assumed for simplicity that $\theta_c = 0$. The virtual work of the load $\mathbf{f}$ is given by:

$$\delta W = \int_{-\pi}^{\pi} \delta \mathbf{w}^{\mathrm{T}} \mathbf{f} r_c \mathrm{d}\theta. \tag{46}$$

Introducing the expansion of Eqs. (33) and (44) in Eq. (46) along with the relations in Eq. (45), the virtual work can also be decomposed into the contribution associated with each Fourier term as follows:

$$\delta W = \delta W_0 + \sum_{n>0} \delta W_n. \tag{47}$$

The virtual work for $n \geq 0$ is given by:

$$\delta W_n = \delta \mathbf{w}_n^{\mathrm{T}} \mathbf{F}_n, \quad n \geq 0, \tag{48}$$

where the force vector is defined as follows:

$$\begin{aligned} \mathbf{F}_0 &= \begin{pmatrix} F_r & F_z & -F_\theta \end{pmatrix}^{\mathrm{T}}, & n = 0, \\ \mathbf{F}_n &= \begin{pmatrix} F_r & 0 & F_z & 0 & -F_\theta & 0 \end{pmatrix}^{\mathrm{T}}, & n > 0. \end{aligned} \tag{49}$$

4.4 Equation of motion

The harmonic amplitudes in Eq. (35) are the unknown DoF to be determined. Considering a FE model of the wheel cross-section, the following interpolation is proposed in the eth element for $n = 0$:

$$\mathbf{w}_0(r, z, t) = \mathbf{N}_0(r, z) \boldsymbol{w}_0^e(t), \tag{50}$$

where $\mathbf{N}_0$ is the shape function matrix defined for $n = 0$. When p nodes are considered in the wheel cross-section, this matrix is given by:

$$\mathbf{N}_0 = \begin{bmatrix} \mathbf{N}_{1,n=0} & \cdots & \mathbf{N}_{j,n=0} & \cdots & \mathbf{N}_{p,n=0} \end{bmatrix}; \qquad \mathbf{N}_{j,n=0} = N_j \mathbf{I}_{3\times 3}, \tag{51}$$

The vector of harmonic amplitudes of the eth element $\boldsymbol{w}_0^e$ can be expressed as follows:

$$\begin{aligned} \boldsymbol{w}_0^e &= \begin{pmatrix} \boldsymbol{w}_{1,n=0}^e & \cdots & \boldsymbol{w}_{j,n=0}^e & \cdots & \boldsymbol{w}_{p,n=0}^e \end{pmatrix}^{\mathrm{T}}; \\ \boldsymbol{w}_{j,n=0}^e &= \begin{pmatrix} w_{r,j,n=0}^e & w_{z,j,n=0}^e & \overline{w}_{\theta,j,n=0}^e \end{pmatrix}. \end{aligned} \tag{52}$$

Similar to the three-dimensional model, the Lagrange equations for motion with $n = 0$ are given by:

$$\begin{aligned}\frac{\mathrm{D}}{\mathrm{D}t}\left(\frac{\partial E_{k,0}}{\partial \dot{\boldsymbol{w}}_0^e}\right)^{\mathrm{T}} - \left(\frac{\partial E_{k,0}}{\partial \boldsymbol{w}_0^e}\right)^{\mathrm{T}} + \left(\frac{\partial E_{p,0}}{\partial \boldsymbol{w}_0^e}\right)^{\mathrm{T}} &= \mathbf{M}_0^e \ddot{\boldsymbol{w}}_0^e + 2\Omega \mathbf{V}_0^e \dot{\boldsymbol{w}}_0^e \\ &\quad + \left(\mathbf{K}_0^e + \Omega^2 \mathbf{A}_0^e\right) \boldsymbol{w}_0^e - \Omega^2 \mathbf{c}_0^e,\end{aligned} \tag{53}$$

from which the following element matrices are defined:

$$\begin{aligned}\mathbf{M}_0^e &= 2\pi \int_{A^e} \rho r \mathbf{N}_0^{\mathrm{T}} \mathbf{N}_0 \mathrm{d}A, \\ \mathbf{V}_0^e &= 2\pi \int_{A^e} \rho r \mathbf{N}_0^{\mathrm{T}} \mathbf{J}_0 \mathbf{N}_0 \mathrm{d}A, \\ \mathbf{K}_0^e &= 2\pi \int_{A^e} r \mathbf{B}_0^{\mathrm{T}} \mathbf{D} \mathbf{B}_0 \mathrm{d}A, \\ \mathbf{A}_0^e &= -2\pi \int_{A^e} \rho r \mathbf{N}_0^{\mathrm{T}} \mathbf{E}_0 \mathbf{N}_0 \mathrm{d}A, \\ \mathbf{c}_0^e &= 2\pi \int_{A^e} \rho r^2 \mathbf{N}_0^{\mathrm{T}} \widehat{\mathbf{e}}_1 \mathrm{d}A,\end{aligned} \tag{54}$$

where A^e is the area of the eth element and $\mathbf{B}_0 = \mathbf{L}_0 \mathbf{N}_0$. These element matrices can be assembled to obtain the global matrices of the EoM for $n = 0$. In the same way, the displacement DoF are assembled into the vector $\boldsymbol{w}_0$ and the forces applied at the contact point and defined by $\mathbf{F}_0$ in Eq. (49) are assembled into the vector $\boldsymbol{\mathcal{F}}_0$. Finally, the EoM are given by:

$$\mathbf{M}_0 \ddot{\boldsymbol{w}}_0(t) + 2\Omega \mathbf{V}_0 \dot{\boldsymbol{w}}_0(t) + \left(\mathbf{K}_0 + \Omega^2 \mathbf{A}_0\right) \boldsymbol{w}_0(t) = \Omega^2 \mathbf{c}_0 + \boldsymbol{\mathcal{F}}_0(t). \tag{55}$$

As in the 3D approach, the model can be transformed to the frequency domain, in which the EoM are given for $\omega > 0$ by:

$$\left(-\omega^2 \mathbf{M}_0 + 2\mathrm{i}\omega\Omega \mathbf{V}_0 + \mathbf{K}_0 + \Omega^2 \mathbf{A}_0\right) \boldsymbol{w}_0(\omega) = \boldsymbol{\mathcal{F}}_0(\omega). \tag{56}$$

The same procedure is carried out for each $n > 0$. In this case, the harmonic amplitudes in the eth element are interpolated by:

$$\mathbf{w}_n(r, z, t) = \mathbf{N}_\eta(r, z) \boldsymbol{w}_n^e(t), \tag{57}$$

where the shape function matrix for $n > 0$ $\mathbf{N}_\eta$ is independent of n and is defined as follows:

$$\mathbf{N}_\eta = \begin{bmatrix} \mathbf{N}_{1,\eta} & \cdots & \mathbf{N}_{j,\eta} & \cdots & \mathbf{N}_{p,\eta} \end{bmatrix}; \qquad \mathbf{N}_{j,\eta} = N_j \mathbf{I}_{6\times 6}, \tag{58}$$

with $\mathbf{I}_{6\times6}$ being the identity matrix of order 6×6. The harmonic amplitude vector in the eth element is given by:

$$\begin{aligned}\boldsymbol{w}_n^e &= \begin{pmatrix}\boldsymbol{w}_{1,n}^e & \cdots & \boldsymbol{w}_{j,n}^e & \cdots & \boldsymbol{w}_{p,n}^e\end{pmatrix}^{\mathrm{T}};\\ \boldsymbol{w}_{j,n}^e &= \begin{pmatrix}w_{r,j,n}^e & w_{\theta,j,n}^e & w_{z,j,n}^e & \overline{w}_{r,j,n}^e & \overline{w}_{\theta,j,n}^e & \overline{w}_{z,j,n}^e\end{pmatrix}.\end{aligned} \tag{59}$$

Thus, the Lagrange equations for each n greater than zero can be expressed as the following matrix system:

$$\begin{aligned}\frac{\mathrm{D}}{\mathrm{D}t}\left(\frac{\partial E_{k,n}}{\partial \dot{\boldsymbol{w}}_n^e}\right)^{\mathrm{T}} - \left(\frac{\partial E_{k,n}}{\partial \boldsymbol{w}_n^e}\right)^{\mathrm{T}} + \left(\frac{\partial E_{p,n}}{\partial \boldsymbol{w}_n^e}\right)^{\mathrm{T}} &= \mathbf{M}_\eta^e \ddot{\boldsymbol{w}}_n^e + 2\Omega\mathbf{V}_n^e \dot{\boldsymbol{w}}_n^e\\ &\quad + \left(\mathbf{K}_n^e + \Omega^2\mathbf{A}_n^e\right)\boldsymbol{w}_n^e,\end{aligned} \tag{60}$$

the element matrices being as follows:

$$\begin{aligned}\mathbf{M}_\eta^e =& \pi\int_{A^e} \rho r \mathbf{N}_\eta^{\mathrm{T}}\mathbf{N}_\eta \mathrm{d}A,\\ \mathbf{V}_n^e =& \pi\int_{A^e} \rho r \mathbf{N}_\eta^{\mathrm{T}}\mathbf{J}_3\mathbf{N}_\eta \mathrm{d}A + n\pi\int_{A^e} \rho r \mathbf{N}_\eta^{\mathrm{T}}\mathbf{J}_2\mathbf{N}_\eta \mathrm{d}A,\\ \mathbf{K}_n^e =& \pi\int_{A^e} r\left(\mathbf{B}_a^{\mathrm{T}} + n\mathbf{B}_b^{\mathrm{T}}\right)\mathbf{D}\left(\mathbf{B}_a + n\mathbf{B}_b\right)\mathrm{d}A\\ &+\pi\int_{A^e} r\left(\overline{\mathbf{B}}_a^{\mathrm{T}} + n\overline{\mathbf{B}}_b^{\mathrm{T}}\right)\mathbf{D}\left(\overline{\mathbf{B}}_a + n\overline{\mathbf{B}}_b\right)\mathrm{d}A,\\ \mathbf{A}_n^e =& -\pi\int_{A^e} \rho r \mathbf{N}_\eta^{\mathrm{T}}\mathbf{E}_3\mathbf{N}_\eta \mathrm{d}A - n2\pi\int_{A^e} \rho r \mathbf{N}_\eta^{\mathrm{T}}(\mathbf{J}_1^{\mathrm{T}} + \mathbf{J}_1)\mathbf{N}_\eta \mathrm{d}A\\ &-n^2\pi\int_{A^e} \rho r \mathbf{N}_\eta^{\mathrm{T}}\mathbf{N}_\eta \mathrm{d}A,\end{aligned} \tag{61}$$

where $\mathbf{B}_a = \mathbf{L}_a\mathbf{N}_\eta$, $\mathbf{B}_b = \mathbf{L}_b\mathbf{N}_\eta$, $\overline{\mathbf{B}}_a = \overline{\mathbf{L}}_a\mathbf{N}_\eta$ and $\overline{\mathbf{B}}_b = \overline{\mathbf{L}}_b\mathbf{N}_\eta$. Note that $\mathbf{M}_\eta^e$ is not dependent on n while $\mathbf{V}_n^e$, $\mathbf{K}_n^e$ and $\mathbf{A}_n^e$ are functions of n, which means that they are evaluated for each n. Nevertheless, matrices $\mathbf{V}_n^e$ and $\mathbf{A}_n^e$ are expressed as polynomials with constant (matrix) coefficients multiplying a power of n and it is straightforward to express $\mathbf{K}_n^e$ in the same way. Finally, after assembling the element matrices into global matrices, the displacement harmonic amplitudes into $\boldsymbol{w}_n$ and the contact forces $\mathbf{F}_n$ of Eq. (49) into $\boldsymbol{\mathcal{F}}_n$, the EoM for each n greater than zero are given by:

$$\mathbf{M}_\eta\ddot{\boldsymbol{w}}_n(t) + 2\Omega\mathbf{V}_n\dot{\boldsymbol{w}}_n(t) + \left(\mathbf{K}_n + \Omega^2\mathbf{A}_n\right)\boldsymbol{w}_n(t) = \boldsymbol{\mathcal{F}}_n(t). \tag{62}$$

If the model is transformed to the frequency domain, the EoM can be expressed for $\omega > 0$ as follows:

$$\left(-\omega^2\mathbf{M}_\eta + 2\mathrm{i}\omega\Omega\mathbf{V}_n + \mathbf{K}_n + \Omega^2\mathbf{A}_n\right)\boldsymbol{w}_n(\omega) = \boldsymbol{\mathcal{F}}_n(\omega). \tag{63}$$

4.5 Sound radiation

Considering the expression for the projected squared velocities in Eq. (29), the surface differentials $\mathrm{d}S_z$ and $\mathrm{d}S_r$ can be expressed as follows:

$$\begin{aligned} \mathrm{d}S_z &= r\mathrm{d}\theta\mathrm{d}r, \\ \mathrm{d}S_r &= r\mathrm{d}\theta\mathrm{d}z. \end{aligned} \tag{64}$$

The solution of the EoM for a given n results in the contribution of the set of vibration modes with n nodal diameters to the wheel response. Thus, for $n = 0$, considering the expressions of Eq. (30), the following relations are established:

$$\begin{aligned} v_{z,0}(r,z,\omega) &= \dot{w}_{z,0}(r,z,\omega) + \dot{\tau}_2(\omega), \\ v_{r,0}(r,z,\omega) &= \dot{w}_{r,0}(r,z,\omega), \end{aligned} \tag{65}$$

where the terms $\dot{w}_{z,0}$ and $\dot{w}_{r,0}$ are associated with the wheel flexibility and the term $\dot{\tau}_2$ with the wheelset RBM. Therefore, the integral in Eq. (29) can be evaluated analytically over the circumferential direction, yielding the following expressions:

$$\begin{aligned} S_z\langle\widetilde{v}_{z,0}^2\rangle &= \pi\int_\Gamma |\dot{w}_{z,0} + \dot{\tau}_2|^2 r\mathrm{d}r, \\ S_r\langle\widetilde{v}_{r,0}^2\rangle &= \pi\int_\Gamma |\dot{w}_{r,0}|^2 r\mathrm{d}z, \end{aligned} \tag{66}$$

where Γ is the wheel cross-section boundary. Similarly, for $n = 1$, according to Eq. (31), the following relations are satisfied:

$$\begin{aligned} v_{z,1}(r,\theta,z,\omega) &= \left(\dot{w}_{z,1}(r,z,\omega) - r\dot{\psi}_1(\omega)\right)\cos(\theta) \\ &\quad - \left(\dot{\overline{w}}_{z,1}(r,z,\omega) - r\dot{\psi}_3(\omega)\right)\sin(\theta), \\ v_{r,1}(r,\theta,z,\omega) &= \left(\dot{w}_{r,1}(r,z,\omega) + \dot{\tau}_3(\omega) + z\dot{\psi}_1(\omega)\right)\cos(\theta) \\ &\quad - \left(\dot{\overline{w}}_{r,1}(r,z,\omega) - \dot{\tau}_1(\omega) + z\dot{\psi}_3(\omega)\right)\sin(\theta), \end{aligned} \tag{67}$$

where the terms $\dot{w}_{z,1}$ and $\dot{w}_{r,1}$ are associated with the wheel flexibility and the rest with the wheelset RBM. Thus, the spatial average in Eq. (29) can be expressed as follows:

$$\begin{aligned} S_z\langle\widetilde{v}_{z,1}^2\rangle &= \frac{\pi}{2}\int_\Gamma \left(|\dot{w}_{z,1} - r\dot{\psi}_1|^2 + |\dot{\overline{w}}_{z,1} - r\dot{\psi}_3|^2\right) r\mathrm{d}r, \\ S_r\langle\widetilde{v}_{r,1}^2\rangle &= \frac{\pi}{2}\int_\Gamma \left(|\dot{w}_{r,1} + \dot{\tau}_3 + z\dot{\psi}_1|^2 + |\dot{\overline{w}}_{r,1} - \dot{\tau}_1 + z\dot{\psi}_3|^2\right) r\mathrm{d}z. \end{aligned} \tag{68}$$

Finally, for $n \geq 2$, the expression for the velocities in Eq. (32) can be written as:

$$v_{i,n}(r,\theta,z,\omega) = \dot{w}_{i,n}(r,z,\omega)\cos(n\theta) - \dot{\overline{w}}_{i,n}(r,z,\omega)\sin(n\theta), \quad i = z,r, \tag{69}$$

where the only contributions are from the wheel flexibility. The spatial average in Eq. (29) leads to the following expressions:

$$\begin{aligned} S_z\langle\widetilde{v}_{z,n}^2\rangle &= \frac{\pi}{2}\int_\Gamma \left(|\dot{w}_{z,n}|^2 + |\dot{\overline{w}}_{z,n}|^2\right) r\mathrm{d}r, \quad n \geq 2, \\ S_r\langle\widetilde{v}_{r,n}^2\rangle &= \frac{\pi}{2}\int_\Gamma \left(|\dot{w}_{r,n}|^2 + |\dot{\overline{w}}_{r,n}|^2\right) r\mathrm{d}z, \quad n \geq 2. \end{aligned} \tag{70}$$

Introducing Eqs. (66), (68) and (70) into Eq. (28), the sound radiation of a rotating wheel can be evaluated numerically in a two-dimensional frame.

5 Results

The model proposed in Section 4 is compared with the three-dimensional formulation presented in Section 3. Results are shown in terms of modal properties, frequency response functions (FRF), contact forces due to the wheel–rail interaction and sound power levels (SWL). For comparison, the FRF and SWL are also computed with the commercial package Ansys [18]; in this, the one-way FSI problem is solved (it is assumed that the air acoustic pressure does not to influence the wheel dynamics). Finally, the computational performance of the presented model, in terms of efficiency, is evaluated and benchmarked against the three-dimensional approach.

In this work, a railway wheel with straight web, a diameter of 900 mm and a mass of 345 kg is employed. Three-dimensional and cross-section two-dimensional FE meshes of this wheel are shown in Fig. 2, which are employed in the subsequent calculations. Quadratic elements are used in both approaches, considering 683 nodes in the two-dimensional FE discretization and 122628 nodes in the three-

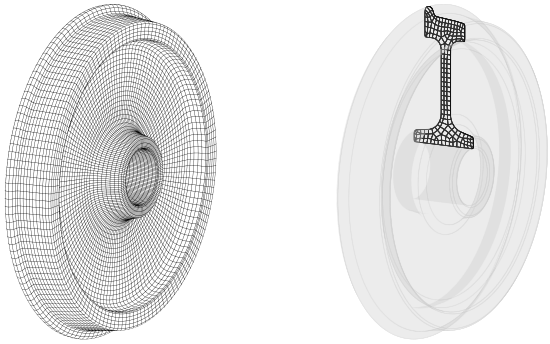

Fig. 2: Three-dimensional (left) and cross-section two-dimensional (right) FE meshes of the railway wheel.

dimensional one, the latter having 132 elements around the circumferential direction. Note that, out of the 683 nodes in the 2D discretization, 246 are placed at the corners of the quadratic elements, so the number of nodes in the 3D FE model can be obtained as $132 \cdot (683 + 246) = 122628$. The wheel is constrained at the inner edge of the hub and, additionally, the wheelset RBM is superimposed on the response of the wheel according to the developments in Section 2. The wheelset has a mass of 1005 kg and moments of inertia of 88 kg m^2 and 580 kg m^2 about the axial and radial axes, respectively.

5.1 Modal properties

Natural frequencies of the rotating wheel in the non-rotating frame are evaluated for different vehicle speeds. The results of the three-dimensional and axisymmetric models are presented for some modes in a Campbell diagram in Fig. 3. The maximum difference found between the two approaches is 0.44 Hz for a natural frequency of 6580 Hz, which represents a relative difference of 0.007%. Using the notation of Thompson [17], for the axial modes both the number of nodal diameters n and nodal circles m of each modeshape are given in the format (n,m) at the left of the lines. Regarding the radial and circumferential modes, since all the modeshapes presented in the Campbell diagram have $m = 0$, they are defined as (n,R) and (n,C), respectively.

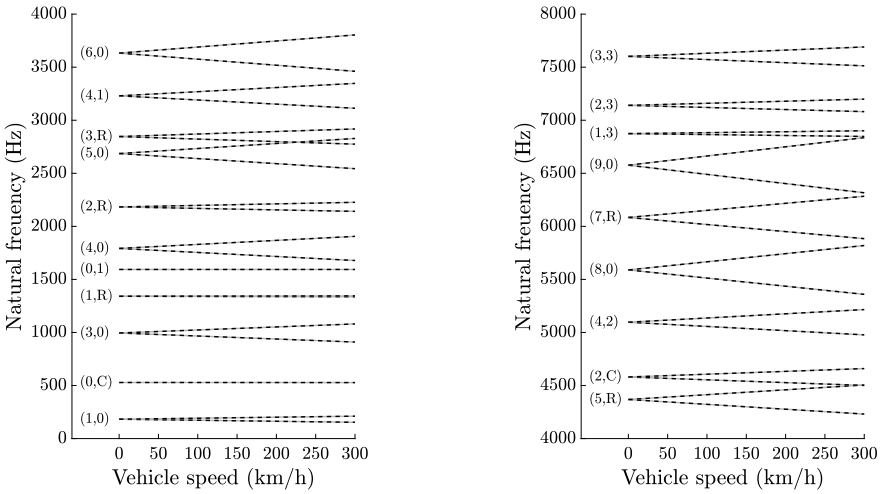

Fig. 3: Campbell diagram of the rotating wheel. Axial modeshapes are denoted as (n,m) while radial and circumferential modeshapes as (n,R) and (n,C), respectively. ——: Three-dimensional model; - - -: Axisymmetric approach.

5.2 Vibroacoustics

The wheel FRF at the contact point is evaluated through the three-dimensional and axisymmetric models for a vehicle speed of 80 km/h and the results are depicted in Fig. 4. As can be seen, there is no noticeable difference between the curves associated with the approaches presented in this work. A modal base formed by the vibration modes up to 12 kHz of the non-rotating wheel is considered for solving the EoM. Damping is included in the models using the empirical relation proposed by Thompson [17], in which the modal damping ratio ξ is related to the number of nodal diameters of the vibration mode, namely, $\xi = 10^{-3}$ for $n = 0$, $\xi = 10^{-2}$ for $n = 1$ and $\xi = 10^{-4}$ for $n \geq 2$. Also, the wheelset RBM contribution to the FRF is included in both methodologies. An adaptative frequency spacing is adopted based on the gradient of the contact receptances; the minimum resolution is 0.2 Hz and about 4000 different frequencies are evaluated.

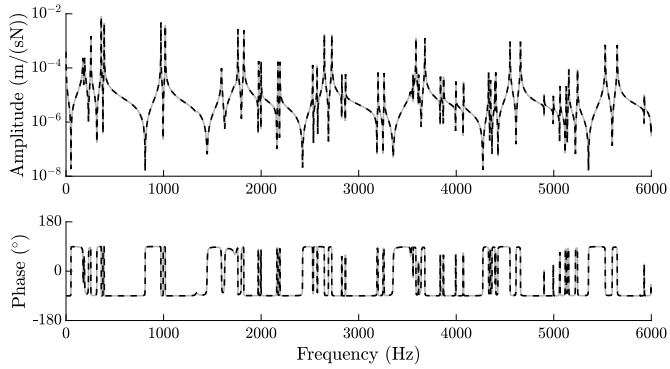

(a)

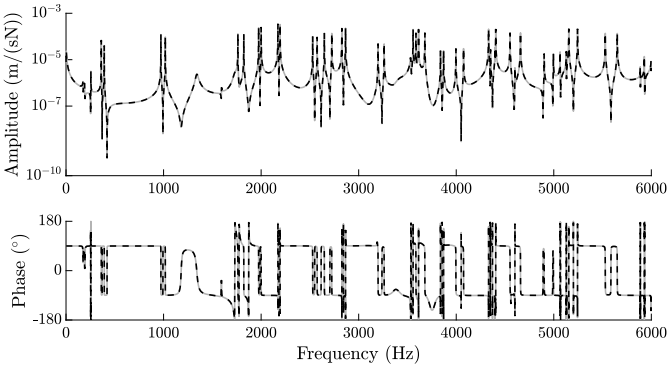

(b)

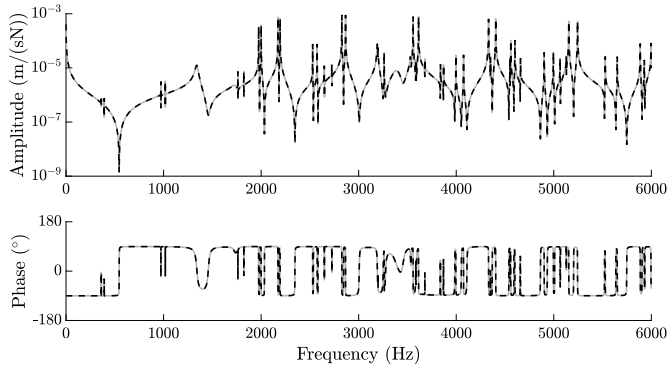

(c)

Fig. 4: Mobilities at the wheel contact point for a vehicle speed of 80 km/h. (a): direct axial/axial; (b): cross axial/radial; (c): direct radial/radial. ——: Three-dimensional model; - - -: Axisymmetric approach.

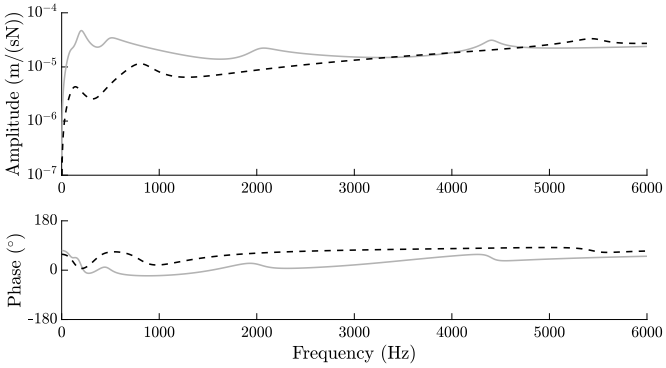

Fig. 5: Mobilities at the rail contact point. ——: direct lateral/lateral; - - -: direct vertical/vertical.

The interaction forces due to the roughness present on the wheel and rail running surfaces are also evaluated for the radial and axial directions. In this work, the contact model proposed by Thompson [17, 23] is used, in which the interaction forces are computed from the wheel and rail combined roughness by means of an operation involving the wheel and rail point receptances as well as the contact receptances. To do this, a continuous track model formed by a UIC60 rail profile supported by a spring–mass–spring system representing the rail pad, sleeper and ballast set is considered. The rail is modelled using periodic structure theory [24], the properties of the track are given in Table 1 and the FRF at the rail contact point are presented in Fig 5; the cross lateral/vertical mobility is considered to be null. For the interaction problem, a vertical static load of 50 kN per wheel is considered, which has influence on the contact receptances. The wheel–rail interaction forces for a vehicle speed of 80 km/h and a unit roughness input at each frequency are presented in Fig. 6. As can be noted, both approaches predict practically the same forces at the contact.

Finally, the sound power radiated by the rotating wheel at a vehicle speed of 80 km/h is calculated. To do this, the roughness spectrum for cast iron brake blocks defined by the standard EN13979-1 [25] is introduced in the model through the procedure described by the aforementioned standard. Also, the contact filter proposed by Thompson [17] is included in the SWL computation. This is dependent on the vehicle velocity and the size of the contact area; in the contact model employed, the latter is a function of the vertical static load (50 kN) as well as the wheel and rail material properties and curvature radii in the contact points. The sound power levels, presented in one-third octave bands as A-weighted spec-

Table 1: Properties of the track model used in the wheel–rail interaction.

Rail pad stiffness* (MN/m^2)	1200 | 90
Rail pad damping loss factor (-)	0.375
Sleeper mass** (kg/m)	205
Ballast stiffness* (MN/m^2)	120 | 60
Ballast damping loss factor (-)	1.5

* Per unit length. Format: Vertical direction | Lateral direction.
** Per unit length. Corresponding to half sleeper.

tra [26], are shown in Fig. 7. Results without and with the wheelset RBM contribution to the wheel vibration are given. This contribution mainly increases the sound radiation below about 1 kHz, while in the high frequency range there is no significant influence. Considering the wheelset RBM, the maximum difference found in one-third octave band level between the three-dimensional and axisymmetric approaches is 0.05 dB(A). Note that the proposed methodology does not consider the flexible motion of the axle, which might influence the wheel SWL in the low and medium frequency range, where the acoustic energy radiated by the wheel is lower than in higher frequencies. Modelling this flexible motion could increase the complexity and computational effort of the models presented here and therefore it is not considered in this work.

For comparison purposes, the flexible wheel is also modelled in the commercial package Ansys [18]. This software implements the dynamic rotation model proposed by Geradin and Kill [10] for an inertial frame, in which a system of reference associated with local deformations is employed to describe the displacements and to formulate the equation of motion of a flexible rotating body. The rotation axis (axial direction) is the out-of-plane axis and the other two (longitudinal and vertical directions) are the in-plane axes. The local reference system is related to the inertial one by rotations about the two in-plane axes of the rotating body whereas the rotation in the out-of-plane axis is only due to the rigid body spinning, so the torsional behaviour is not described by the model. The two rotations of the inertial system are assumed to be infinitesimal and so they are approximated by the first two terms of the Taylor expansion. This leads to the Eulerian and Lagrangian descriptions of in-plane coordinates being equivalent.

The 3D railway wheel is modelled in Ansys using the FEM (same mesh as in Fig. 2); then the rotation is included in the model and the receptances of the wheel at the contact point are evaluated for a given set of frequencies. These

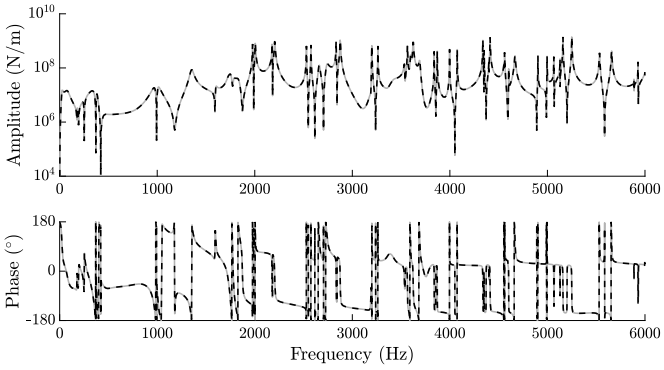

(a)

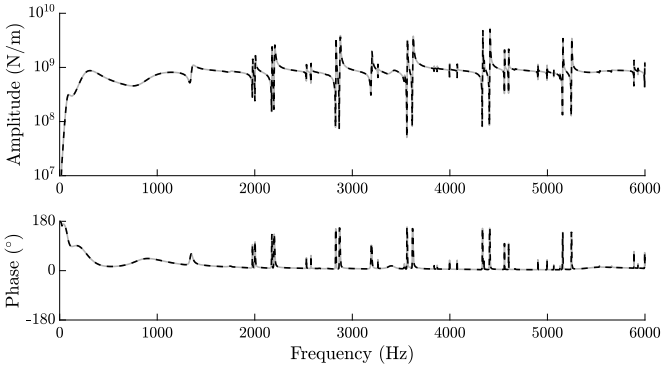

(b)

Fig. 6: Contact forces for a vehicle speed of 80 km/h and a unit roughness input. (a): axial; (b): radial. ——: Three-dimensional model; - - -: Axisymmetric approach.

receptances are exported and used to solve the interaction forces through an in-house code. Subsequently, the computed forces are imported into Ansys and applied to the wheel contact point, allowing the wheel response to be calculated. Once the dynamics of the rotating wheel is solved, the wave equation for the surrounding air within a sphere of radius 1.55 m [18] is also modelled with the FEM considering the acoustic pressure as DoF; the FE model has 891317 nodes in the fluid region. The velocity on the wheel surface is prescribed as an acoustic boundary condition and, at the external surface of the fluid sphere, the Ansys *Radiation Boundary* condition is applied, which approximates the volume under consideration to infinity [18]. A comparison of the FRF and SWL delivered by this software with results from the vibroacoustic models proposed in this work is

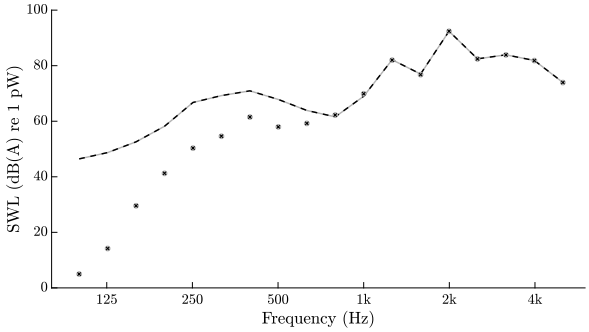

Fig. 7: SWL of the rotating wheel for a vehicle speed of 80 km/h. Lines include the wheelset RBM contribution while markers do not. —— and ●: Three-dimensional model; - - - and ×: Axisymmetric approach.

shown in Fig. 8 and Fig. 9, respectively. For this comparison, the wheelset RBM is not included in the models. Regarding the mobilities, the discrepancies are mainly found in the position of the two resonance peaks associated with natural frequencies of the wheel for $n > 0$, while the amplitudes are similar. In relation to the SWL, which is presented in one-third octave bands, there is a good agreement in most of the frequency range considered, the discrepancies being higher for lower frequencies. The main differences in the results between the proposed models and Ansys can be due to:

- The inclusion of the wheel rotation: Ansys implements the model developed by Geradin and Kill [10], briefly explained above.
- The methodology to solve the sound radiation: Ansys solves the one-way FSI problem whereas the proposed methodologies implement the acoustic model developed by Thompson [16]. This makes use of approximate expressions for radiation ratios, which are mostly influential in the low and medium frequency range, where the highest discrepancies are found in Fig. 9. Nevertheless, the energy contained in this frequency range is negligible compared with higher frequencies.

By adding the energy in each one-third octave frequency band, an overall SWL of 91.2 dB(A) is obtained by both the three-dimensional and axisymmetric approaches while 91.4 dB(A) is predicted by Ansys. It is also worth noting that the SWL given by the proposed models in Fig. 7 and 9 contain certain differences. The following reasons can be highlighted for this:

- As mentioned above, for simplicity, the wheelset RBM contribution to the flexible wheel motion is not included in the comparison with Ansys (Fig. 9), which introduces some differences in the low frequency range (see Fig. 7).
- Given the high computational cost associated with the acoustic calculation in Ansys, about 2250 different frequencies are evaluated in producing Fig. 9 with a minimum resolution of 1 Hz. As explained at the beginning of this Section, about 4000 frequencies with a minimum resolution of 0.2 Hz are considered in Fig. 7.
- When including rotation in Ansys, it is not possible to solve the wheel dynamics using a modal approach and the direct method is employed by inverting the EoM formulated in physical coordinates. Thus, the modal damping defined at the beginning of this Section, and considered in Fig. 7, cannot be included in the model in Ansys. Instead, a proportional damping with a mass multiplier of 19.9 and a stiffness multiplier of $1.24 \cdot 10^{-8}$ is considered to compute the three curves in Fig. 9. The matrix multipliers have been tuned to produce modal damping values as similar as possible to those used in Fig. 7.
- As stated in the previous paragraph, the solution of the EoM in Ansys is performed by the direct method. In the proposed methodologies, a modal approach is adopted, considering as modal basis the vibration modes with natural frequencies below 12 kHz. The difference between the proposed methodologies and Ansys corresponds to the contribution of higher order modes, which can be assumed constant in the frequency range studied (up to 6 kHz) [27]. Therefore, this contribution can be evaluated as the difference between the direct static solution (inversion of the stiffness matrix) and the solution for zero frequency using the modal approach. In Fig. 9, in order to minimize the differences with Ansys, the aforementioned contribution is added to the dynamic solution of the modal approach, but it has not been included in Fig. 7.

The previous four reasons also explain the differences between Fig. 4 and 8 regarding the results given by the proposed models. It is worth noting that the methodology proposed in this work, which leads to Fig. 4 and 7, is the more physically correct.

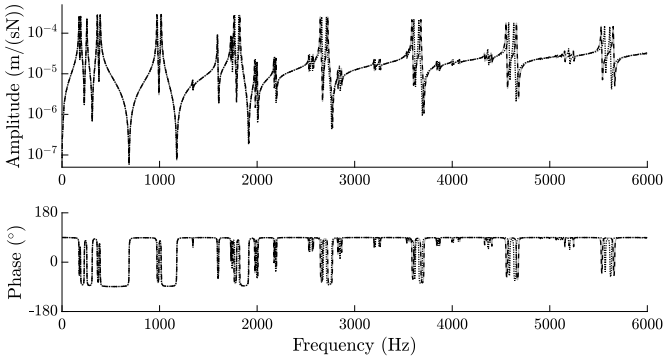

(a)

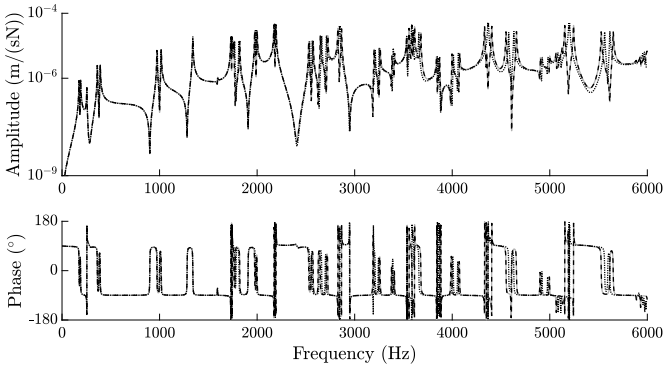

(b)

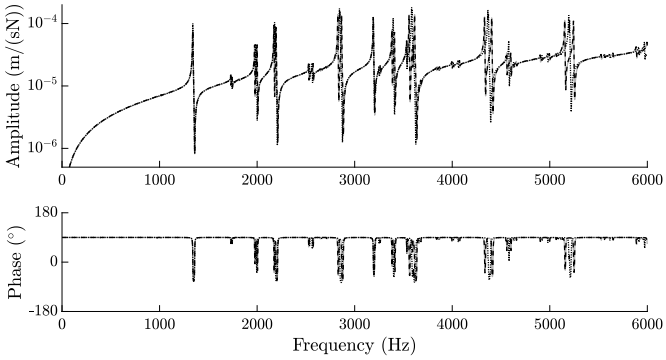

(c)

Fig. 8: Comparison of the mobilities at the wheel contact point for a vehicle speed of 80 km/h. (a): direct axial/axial; (b): cross axial/radial; (c): direct radial/radial. ——: Three-dimensional model; - - -: Axisymmetric approach; ·····: Ansys.

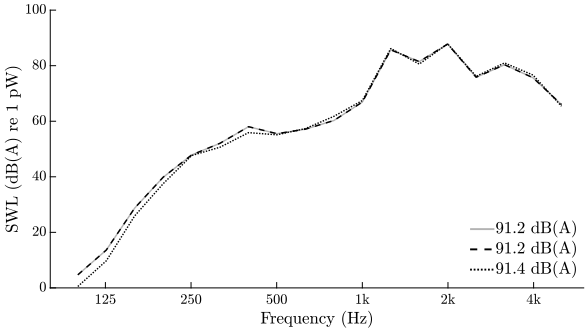

Fig. 9: SWL comparison of the rotating wheel for a vehicle speed of 80 km/h. ——: Three-dimensional model; - - -: Axisymmetric approach; ·····: Ansys.

5.3 Computational performance

The methodology used in the axisymmetric approach presented consists of solving the circumferential direction analytically and the other two dimensions numerically. This procedure, as opposed to the full three-dimensional methodology, suppresses the discretization error associated with the FEM in the circumferential direction. When using FE meshes with a sufficiently large number of nodes, the results obtained from the two models are indistinguishable. Nevertheless, the performance of the axisymmetric approach model is far superior in terms of computational effort.

To evaluate the computational performance, the SWL results from different FE meshes are compared with those from a highly refined three-dimensional FE mesh with 358592 nodes, which is consider as the reference case. Both the computational time required for the calculation of each FE mesh and the discrepancy with respect to the reference case are determined. The discrepancy for the ith FE mesh is defined as the average of the absolute difference in decibels for each one-third octave frequency band between the SWL for the ith case and the reference one. The same frequency resolution technique as explained in Section 5.2 is used in this analysis. In Fig. 10(a) the relation between the discrepancy and computational calculation time from both models is shown for each FE mesh (circle markers) and, in particular, for the meshes employed in the previous results (cross markers). Also, a regression line which fits the results is proposed. This allows the ratio to be evaluated between the computational time of the three-dimensional and axisymmetric approaches for a given discrepancy, which is shown in Fig. 10(b). The axisymmetric approach is, for small discrepancies, approximately three or-

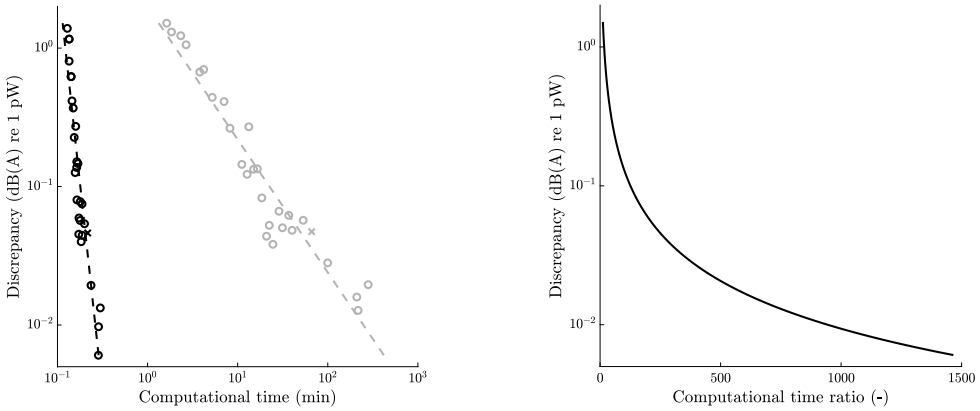

Fig. 10: (a): Discrepancy in the SWL results for the different FE meshes (markers), including the two used in the previous results (cross markers), and regression (dashed lines) for the three-dimensional (grey) and axisymmetric (black) models; (b): Discrepancy as a function of the ratio between the computational time from the three-dimensional and axisymmetric models.

ders of magnitude more efficient than the three-dimensional one, which makes the former suitable for implementation in optimization algorithms or SWL minimization routines. The numerical simulations are carried out in a PC running with an ®Intel i7-9700 processor with 64 GB RAM. Regarding the calculations performed in Ansys, for 2250 different frequencies a total time of approximately 11.5 days is required, which represents a computational cost five orders of magnitude higher than that of the axisymmetric approach.

6 Conclusions

A model of an axisymmetric rotating and flexible railway wheel is proposed which allows a solution in a two-dimensional frame for both the dynamic response and the sound radiation of the wheel due to its interaction with the rail. The wheelset RBM is described through an analytical model and it is superimposed on the wheel vibration, which is constrained at the inner edge of the hub. The proposed models are specifically aimed at describing the vibroacoustic behaviour of a railway wheel, but in general they are valid for any rotating system provided that axisymmetry exists.

First, a three-dimensional vibroacoustic model of the rotating flexible wheel, numerically addressed through the FEM, is presented. The response of the wheel around the circumferential direction is then expanded using Fourier series, which allows the dynamic and acoustic fields to be solved analytically in that direction. The other two directions, associated with the wheel cross-section, are solved numerically. Finally, the rigid wheelset motion, which is solved analytically, is superimposed on the flexible wheel motion; this mainly modifies the wheel response in the low frequency range. Further development of this model could consider the flexible motion of the axle which is subject for future study.

The results from the proposed axisymmetric model are compared with the three-dimensional methodology in terms of modal, dynamic and acoustic behaviour, obtaining virtually identical solutions. In addition, the SWL predicted from both aforementioned methodologies are compared with those from the commercial package Ansys and similar results are obtained although some discrepancies, mainly in the low frequency range, are noted. However, in overall terms, a difference of only 0.2 dB(A) is found.

The axisymmetric approach presented suppresses the discretization error associated with the FEM in the circumferential direction, therefore leading to similar results to the three-dimensional model when considering highly refined FE meshes. However, for these meshes, the computational time required by the proposed axisymmetric model to solve the sound radiation of the wheel is approximately 1000 times less than with the three-dimensional methodology.

Acknowledgements

This paper is part of the project PID2020-112886RA-I00, grant FPU18/03999 and grant EST21/00213 funded by MCIN/AEI/10.13039/501100011033 as well as by "ESF Investing in your future". The authors also acknowledge Programa PROMETEO/2021/046 of Generalitat Valenciana.

Appendix A. Matrices and matrix operators

A.1 Matrices

$$\mathbf{K}_1 = \begin{bmatrix} 0 & 0 & -1 \\ 0 & 0 & 0 \\ 1 & 0 & 0 \end{bmatrix}, \qquad \mathbf{K}_2 = \begin{bmatrix} \frac{1}{2} & 0 & 0 \\ 0 & 1 & 0 \\ 0 & 0 & \frac{1}{2} \end{bmatrix}. \tag{A.1}$$

$$\mathbf{J} = \begin{bmatrix} 0 & -1 & 0 \\ 1 & 0 & 0 \\ 0 & 0 & 0 \end{bmatrix}, \qquad \mathbf{E} = \mathbf{J}^{\mathrm{T}}\mathbf{J} = \begin{bmatrix} 1 & 0 & 0 \\ 0 & 1 & 0 \\ 0 & 0 & 0 \end{bmatrix}. \tag{A.2}$$

$$\mathbf{D} = \frac{\lambda}{(1+\nu)(1-2\nu)} \begin{bmatrix} 1-\nu & \nu & \nu & 0 & 0 & 0 \\ \nu & 1-\nu & \nu & 0 & 0 & 0 \\ \nu & \nu & 1-\nu & 0 & 0 & 0 \\ 0 & 0 & 0 & \frac{1-2\nu}{2} & 0 & 0 \\ 0 & 0 & 0 & 0 & \frac{1-2\nu}{2} & 0 \\ 0 & 0 & 0 & 0 & 0 & \frac{1-2\nu}{2} \end{bmatrix}, \tag{A.3}$$

with λ being the Young's modulus and ν the Poisson's ratio.

$$\mathbf{J}_0 = \begin{bmatrix} 0 & 0 & 1 \\ 0 & 0 & 0 \\ -1 & 0 & 0 \end{bmatrix}, \qquad \mathbf{E}_0 = \mathbf{J}_0^{\mathrm{T}}\mathbf{J}_0 = \begin{bmatrix} 1 & 0 & 0 \\ 0 & 0 & 0 \\ 0 & 0 & 1 \end{bmatrix}. \tag{A.4}$$

$$\mathbf{J}_1 = \begin{bmatrix} 0 & 1 & 0 & 0 & 0 & 0 \\ 0 & 0 & 0 & 0 & 0 & 0 \\ 0 & 0 & 0 & 0 & 0 & 0 \\ 0 & 0 & 0 & 0 & -1 & 0 \\ 0 & 0 & 0 & 0 & 0 & 0 \\ 0 & 0 & 0 & 0 & 0 & 0 \end{bmatrix}, \qquad \mathbf{J}_2 = \begin{bmatrix} 0 & 0 & 0 & -1 & 0 & 0 \\ 0 & 0 & 0 & 0 & 1 & 0 \\ 0 & 0 & 0 & 0 & 0 & -1 \\ 1 & 0 & 0 & 0 & 0 & 0 \\ 0 & -1 & 0 & 0 & 0 & 0 \\ 0 & 0 & 1 & 0 & 0 & 0 \end{bmatrix},$$
$$\mathbf{J}_3 = \begin{bmatrix} 0 & 0 & 0 & 0 & 1 & 0 \\ 0 & 0 & 0 & -1 & 0 & 0 \\ 0 & 0 & 0 & 0 & 0 & 0 \\ 0 & 1 & 0 & 0 & 0 & 0 \\ -1 & 0 & 0 & 0 & 0 & 0 \\ 0 & 0 & 0 & 0 & 0 & 0 \end{bmatrix}, \qquad \mathbf{E}_3 = \mathbf{J}_3^{\mathrm{T}}\mathbf{J}_3 = \begin{bmatrix} 1 & 0 & 0 & 0 & 0 & 0 \\ 0 & 1 & 0 & 0 & 0 & 0 \\ 0 & 0 & 0 & 0 & 0 & 0 \\ 0 & 0 & 0 & 1 & 0 & 0 \\ 0 & 0 & 0 & 0 & 1 & 0 \\ 0 & 0 & 0 & 0 & 0 & 0 \end{bmatrix}. \tag{A.5}$$

A.2 Matrix operators

$$\mathbf{L} = \begin{bmatrix} \frac{\partial}{\partial r} & 0 & 0 \\ \frac{1}{r} & \frac{1}{r}\frac{\partial}{\partial \theta} & 0 \\ 0 & 0 & \frac{\partial}{\partial z} \\ \frac{\partial}{\partial z} & 0 & \frac{\partial}{\partial r} \\ \frac{1}{r}\frac{\partial}{\partial \theta} & \frac{\partial}{\partial r} - \frac{1}{r} & 0 \\ 0 & \frac{\partial}{\partial z} & \frac{1}{r}\frac{\partial}{\partial \theta} \end{bmatrix}. \tag{A.6}$$

$$\mathbf{L}_0 = \begin{bmatrix} \frac{\partial}{\partial r} & 0 & 0 \\ \frac{1}{r} & 0 & 0 \\ 0 & \frac{\partial}{\partial z} & 0 \\ \frac{\partial}{\partial z} & \frac{\partial}{\partial r} & 0 \\ 0 & 0 & \frac{\partial}{\partial r} - \frac{1}{r} \\ 0 & 0 & \frac{\partial}{\partial z} \end{bmatrix}. \tag{A.7}$$

$$\mathbf{L}_a = \begin{bmatrix} \frac{\partial}{\partial r} & 0 & 0 & 0 & 0 & 0 \\ \frac{1}{r} & 0 & 0 & 0 & 0 & 0 \\ 0 & 0 & \frac{\partial}{\partial z} & 0 & 0 & 0 \\ \frac{\partial}{\partial z} & 0 & \frac{\partial}{\partial r} & 0 & 0 & 0 \\ 0 & \frac{\partial}{\partial r} - \frac{1}{r} & 0 & 0 & 0 & 0 \\ 0 & \frac{\partial}{\partial z} & 0 & 0 & 0 & 0 \end{bmatrix}, \qquad \mathbf{L}_b = \begin{bmatrix} 0 & 0 & 0 & 0 & 0 & 0 \\ 0 & \frac{1}{r} & 0 & 0 & 0 & 0 \\ 0 & 0 & 0 & 0 & 0 & 0 \\ 0 & 0 & 0 & 0 & 0 & 0 \\ -\frac{1}{r} & 0 & 0 & 0 & 0 & 0 \\ 0 & 0 & -\frac{1}{r} & 0 & 0 & 0 \end{bmatrix},$$

$$\overline{\mathbf{L}}_a = \begin{bmatrix} 0 & 0 & 0 & \frac{\partial}{\partial r} & 0 & 0 \\ 0 & 0 & 0 & \frac{1}{r} & 0 & 0 \\ 0 & 0 & 0 & 0 & 0 & \frac{\partial}{\partial z} \\ 0 & 0 & 0 & \frac{\partial}{\partial z} & 0 & \frac{\partial}{\partial r} \\ 0 & 0 & 0 & 0 & \frac{\partial}{\partial r} - \frac{1}{r} & 0 \\ 0 & 0 & 0 & 0 & \frac{\partial}{\partial z} & 0 \end{bmatrix}, \qquad \overline{\mathbf{L}}_b = \begin{bmatrix} 0 & 0 & 0 & 0 & 0 & 0 \\ 0 & 0 & 0 & 0 & -\frac{1}{r} & 0 \\ 0 & 0 & 0 & 0 & 0 & 0 \\ 0 & 0 & 0 & 0 & 0 & 0 \\ 0 & 0 & 0 & \frac{1}{r} & 0 & 0 \\ 0 & 0 & 0 & 0 & 0 & \frac{1}{r} \end{bmatrix}. \tag{A.8}$$

Appendix B. Kinetic and strain energy integration

In this appendix the analytical integration in the circumferential direction of the kinetic energy in Eq. (18) and strain energy in Eq. (19) is detailed. To compute the integrals, considering $n, l \in \mathbb{Z}$, the following relations are used:

$$\begin{aligned}
\int_{-\pi}^{\pi} \sin(n\theta)\sin(l\theta)\mathrm{d}\theta &= \begin{cases} \pi, & \text{if} \quad n = l \neq 0. \\ 0, & \text{if} \quad n \neq l \ \text{ or } \ n = l = 0. \end{cases} \\
\int_{-\pi}^{\pi} \cos(n\theta)\cos(l\theta)\mathrm{d}\theta &= \begin{cases} \pi, & \text{if} \quad n = l \neq 0. \\ 0, & \text{if} \quad n \neq l. \\ 2\pi, & \text{if} \quad n = l = 0. \end{cases} \\
\int_{-\pi}^{\pi} \sin(n\theta)\cos(l\theta)\mathrm{d}\theta &= 0, \quad \forall n, l.
\end{aligned} \tag{B.1}$$

Bearing in mind that $\mathrm{d}V = r\mathrm{d}\theta\mathrm{d}A$ and decomposing the kinetic energy into its ten terms, the result of the aforementioned integration is given by:

$$E_k^{(1)} = \frac{1}{2}\Omega^2 \int_V \rho r^2 \mathrm{d}V = \pi\Omega^2 \int_A \rho r^3 \mathrm{d}A, \tag{B.2a}$$

$$E_k^{(2)} = \frac{1}{2}\int_V \rho \dot{\mathbf{w}}^{\mathrm{T}}\dot{\mathbf{w}}\mathrm{d}V = \pi \int_A \rho r \dot{\mathbf{w}}_0^{\mathrm{T}}\dot{\mathbf{w}}_0 \mathrm{d}A + \sum_{n>0}\left(\frac{\pi}{2}\int_A \rho r \dot{\mathbf{w}}_n^{\mathrm{T}}\dot{\mathbf{w}}_n \mathrm{d}A\right), \tag{B.2b}$$

$$E_k^{(3)} = \frac{1}{2}\Omega^2 \int_V \rho \frac{\partial \mathbf{w}^{\mathrm{T}}}{\partial\theta}\frac{\partial \mathbf{w}}{\partial\theta}\mathrm{d}V = \sum_{n>0}\left(\frac{\pi}{2}\Omega^2 \int_A \rho r n^2 \mathbf{w}_n^{\mathrm{T}}\mathbf{w}_n \mathrm{d}A\right), \tag{B.2c}$$

$$E_k^{(4)} = \Omega^2 \int_V \rho \frac{\partial \mathbf{w}^{\mathrm{T}}}{\partial\theta}\mathbf{J}\mathbf{w}\mathrm{d}V = \sum_{n>0}\left(2\pi\Omega^2 \int_A \rho r n \mathbf{w}_n^{\mathrm{T}}\mathbf{J}_1\mathbf{w}_n \mathrm{d}A\right), \tag{B.2d}$$

$$E_k^{(5)} = \Omega \int_V \rho r \widehat{\mathbf{e}}_2^{\,\mathrm{T}}\dot{\mathbf{w}}\mathrm{d}V = -2\pi\Omega \int_A \rho r^2 \widehat{\mathbf{e}}_3^{\,\mathrm{T}}\dot{\mathbf{w}}_0 \mathrm{d}A, \tag{B.2e}$$

$$E_k^{(6)} = \Omega^2 \int_V \rho r \widehat{\mathbf{e}}_2^{\,\mathrm{T}}\frac{\partial \mathbf{w}}{\partial\theta}\mathrm{d}V = 0, \tag{B.2f}$$

$$E_k^{(7)} = \Omega^2 \int_V \rho r \widehat{\mathbf{e}}_2^{\,\mathrm{T}}\mathbf{J}\mathbf{w}\mathrm{d}V = 2\pi\Omega^2 \int_A \rho r^2 \widehat{\mathbf{e}}_1^{\,\mathrm{T}}\mathbf{w}_0 \mathrm{d}A, \tag{B.2g}$$

$$E_k^{(8)} = \Omega \int_V \rho \dot{\mathbf{w}}^{\mathrm{T}}\frac{\partial \mathbf{w}}{\partial\theta}\mathrm{d}V = \sum_{n>0}\left(\pi\Omega \int_A \rho r n \dot{\mathbf{w}}_n^{\mathrm{T}}\mathbf{J}_2\mathbf{w}_n \mathrm{d}A\right), \tag{B.2h}$$

$$E_k^{(9)} = \Omega \int_V \rho \dot{\mathbf{w}}^{\mathrm{T}} \mathbf{J} \mathbf{w} \mathrm{d}V$$
$$= 2\pi\Omega \int_A \rho r \dot{\mathbf{w}}_0^{\mathrm{T}} \mathbf{J}_0 \mathbf{w}_0 \mathrm{d}A + \sum_{n>0} \left(\pi\Omega \int_A \rho r \dot{\mathbf{w}}_n^{\mathrm{T}} \mathbf{J}_3 \mathbf{w}_n \mathrm{d}A \right), \tag{B.2i}$$

$$E_k^{(10)} = \frac{1}{2}\Omega^2 \int_V \rho \mathbf{w}^{\mathrm{T}} \mathbf{E} \mathbf{w} \mathrm{d}V$$
$$= \pi\Omega^2 \int_A \rho r \mathbf{w}_0^{\mathrm{T}} \mathbf{E}_0 \mathbf{w}_0 \mathrm{d}A + \sum_{n>0} \left(\frac{\pi}{2}\Omega^2 \int_A \rho r \mathbf{w}_n^{\mathrm{T}} \mathbf{E}_3 \mathbf{w}_n \mathrm{d}A \right). \tag{B.2j}$$

Similarly, considering the strain energy, the following expression is computed:

$$E_p = \frac{1}{2} \int_V \boldsymbol{\varepsilon}^{\mathrm{T}} \mathbf{D} \boldsymbol{\varepsilon} \mathrm{d}V$$
$$= \pi \int_A r \boldsymbol{\varepsilon}_0^{\mathrm{T}} \mathbf{D} \boldsymbol{\varepsilon}_0 \mathrm{d}A + \sum_{n>0} \left(\frac{\pi}{2} \int_A r \boldsymbol{\varepsilon}_n^{\mathrm{T}} \mathbf{D} \boldsymbol{\varepsilon}_n \mathrm{d}A + \frac{\pi}{2} \int_A r \bar{\boldsymbol{\varepsilon}}_n^{\mathrm{T}} \mathbf{D} \bar{\boldsymbol{\varepsilon}}_n \mathrm{d}A \right). \tag{B.3}$$

References

[1] C. J. C. Jones, D. J. Thompson, Rolling noise generated by railway wheels with visco-elastic layers, Journal of Sound and Vibration 231 (3) (2000) 779–790, http://dx.doi.org/10.1006/jsvi.1999.2562.

[2] F. Létourneaux, J. F. Cordier, F. Poisson, N. Douarche, High speed railway noise: assessment of mitigation measures, in: B. Schulte-Werning, *et al.* (Eds.), Proceedings of 9th International Workshop on Railway Noise, Munich, Germany, 4–8 September 2007, Notes on Numerical Fluid Mechanics & Multidisciplinary Design 99, 2008, pp. 56–62, http://dx.doi.org/10.1007/978-3-540-74893-9_8.

[3] D. J. Thompson, C. J. C. Jones, T. P. Waters, D. Farrington, A tuned damping device for reducing noise from railway track, Applied Acoustics 68 (1) (2007) 43–57, http://dx.doi.org/10.1016/j.apacoust.2006.05.001.

[4] J. C. O. Nielsen, C. R. Fredö, Multi-disciplinary optimization of railway wheels, Journal of Sound and Vibration 293 (3) (2006) 510–521, http://dx.doi.org/10.1016/j.jsv.2005.08.063.

[5] X. Garcia-Andrés, J. Gutiérrez-Gil, J. Martínez-Casas, F. D. Denia, Wheel shape optimization approaches to reduce railway rolling noise, Structural and

Multidisciplinary Optimization 62 (2020) 2555–2570, http://dx.doi.org/10.1007/s00158-020-02700-6.

[6] J. Gutiérrez-Gil, X. Garcia-Andrés, J. Martínez-Casas, E. Nadal, F. D. Denia, Optimized Perforation Schemes in Railway Wheels Toward Acoustic Radiation Mitigation, Journal of Vibration and Acoustics 142 (4) (2020) 041009, http://dx.doi.org/10.1115/1.4046681.

[7] V. T. Andrés, J. Martínez-Casas, F. D. Denia, D. J. Thompson, Influence study of rail geometry and track properties on railway rolling noise, Journal of Sound and Vibration 525 (2022) 116701, http://dx.doi.org/10.1016/j.jsv.2021.116701.

[8] D. J. Thompson, Wheel-rail noise generation, part II: Wheel vibration, Journal of Sound and Vibration 161 (3) (1993) 401–419, http://dx.doi.org/10.1006/jsvi.1993.1083.

[9] D. J. Thompson, Wheel-rail noise generation, part V: Inclusion of wheel rotation, Journal of Sound and Vibration 161 (3) (1993) 467–482, http://dx.doi.org/10.1006/jsvi.1993.1086.

[10] M. Geradin, N. Kill, A new approach to finite element modelling of flexible rotors, Engineering Computations 1 (1) (1984) 52–64, http://dx.doi.org/10.1108/eb023560.

[11] G. Genta, A. Tonoli, A harmonic finite element for the analysis of flexural, torsional and axial rotordynamic behaviour of discs, Journal of Sound and Vibration 196 (1) (1996) 19–43, http://dx.doi.org/10.1006/jsvi.1996.0465.

[12] X. Sheng, Y. Liu, X. Zhou, The response of a high-speed train wheel to a harmonic wheel–rail force, Journal of Physics: Conference Series 744 (2016) 012145, http://dx.doi.org/10.1088/1742-6596/744/1/012145.

[13] J. Fayos, L. Baeza, F. D. Denia, J. E. Tarancón, An Eulerian coordinate-based method for analysing the structural vibrations of a solid of revolution rotating about its main axis, Journal of Sound and Vibration 306 (3) (2007) 618–635, http://dx.doi.org/10.1016/j.jsv.2007.05.051.

[14] J. Martínez-Casas, L. Mazzola, L. Baeza, S. Bruni, Numerical estimation of stresses in railway axles using a train–track interaction model, International Journal of Fatigue 47 (2013) 18–30, http://dx.doi.org/10.1016/j.ijfatigue.2012.07.006.

[15] L. Baeza, J. Giner-Navarro, D. J. Thompson, J. Monterde, Eulerian models of the rotating flexible wheelset for high frequency railway dynamics, Journal of Sound and Vibration 449 (2019) 300–314, http://dx.doi.org/10.1016/j.jsv.2019.03.002.

[16] D. J. Thompson, C. J. C. Jones, Sound radiation from a vibrating railway wheel, Journal of Sound and Vibration 253 (2) (2002) 401–419, http://dx.doi.org/10.1006/jsvi.2001.4061.

[17] D. J. Thompson, Railway Noise and Vibration. Mechanisms, Modelling and Means of Control, Elsevier, 2009, ISBN: 978-0-08-045147-3, http://dx.doi.org/10.1016/B978-0-08-045147-3.X0023-0.

[18] Ansys® Academic Research Mechanical, Release 19.2, Help System, ANSYS, Inc.

[19] G. K. Batchelor, An Introduction to Fluid Dynamics, Cambridge University Press, 2000, ISBN: 9780511800955, http://dx.doi.org/10.1017/CBO9780511800955.

[20] R. B. Bird, W. E. Stewart, E. N. Lightfoot, Transport Phenomena, Revised 2nd Edition, John Wiley & Sons, 2006, ISBN: 978-0-470-11539-8.

[21] O. C. Zienkiewicz, R. L. Taylor, J. Z. Zhu, The Finite Element Method: Its Basis and Fundamentals, 7th Edition, Butterworth-Heinemann, 2013, ISBN: 978-1-85617-633-0, http://dx.doi.org/10.1016/C2009-0-24909-9.

[22] M. Petyt, Introduction to Finite Element Vibration Analysis, 2nd Edition, Cambridge University Press, 2010, ISBN: 9780521191609, http://dx.doi.org/10.1017/CBO9780511761195.

[23] D. J. Thompson, Wheel-rail noise generation, part I: Introduction and interaction model, Journal of Sound and Vibration 161 (3) (1993) 387–400, http://dx.doi.org/10.1006/jsvi.1993.1082.

[24] D. J. Thompson, Wheel-rail noise generation, part III: Rail vibration, Journal of Sound and Vibration 161 (3) (1993) 421–446, http://dx.doi.org/10.1006/jsvi.1993.1084.

[25] Railway applications – Wheelsets and bogies – Monobloc wheels – Technical approval procedure – Part 1: Forged and rolled wheels. EN 13979-1:2020, European Committee for Standardization (2020).

[26] Electroacoustics – Sound level meters – Part 1: Specifications. IEC 61672-1:2013, International Electrotechnical Commission (2013).

[27] O. E. Hansteen, K. Bell, On the accuracy of mode superposition analysis in structural dynamics, Earthquake Engineering & Structural Dynamics 7 (5) (1979) 405–411, http://dx.doi.org/10.1002/eqe.4290070502.

PAPER 3

Railway rolling noise in curved tracks: Dynamic modelling of the wheelset and influence of the curve

V. T. Andrés[a], J. Martínez-Casas[a], F. D. Denia[a], D. J. Thompson[b], and S. Bruni[c]

[a] Instituto de Ingeniería Mecánica y Biomecánica, Universitat Politècnica de València, Valencia, Spain

[b] Institute of Sound and Vibration Research, University of Southampton, Southampton, UK

[c] Departament of Mechanical Engineering, Politecnico di Milano, Milan, Italy

Submitted for publication to *Journal of Sound and Vibration*

Preprint version available. DOI: 10.2139/ssrn.4683502

Abstract

Railway wheelsets operating on curved tracks experience complex dynamic behaviour which can affect the generation of rolling noise. This paper presents a comprehensive study on the dynamic response of wheelsets on curved tracks and the associated rolling noise radiation from the wheel and track. A dynamic model is developed to accurately compute the vibrational response of the flexible wheelset, considering the inertial effects associated with its rotation and trajectory along the curved track. An axisymmetric approach is proposed, which reduces significantly the computational effort in comparison to a three-dimensional numerical model. Considering a railway vehicle and its interaction with the track, the rolling noise generated in curved conditions is evaluated. A parametric analysis is then carried out to investigate the impact of curve radius, non-compensated acceleration, and superelevation on noise generation. The results show that rolling noise from the wheel and rail in a curve can be higher than in a tangent track for curve radii smaller than about 500 m, whereas it is generally lower for larger radii. Also, it is observed that certain wheels within a vehicle exhibit significantly higher noise levels in a curve. In addition, the track curvature is found to be the most important variable in terms of rolling noise radiation, being influential even for curves of radius up to 5 km.

Keywords

Curved railway track; rotating wheelset; dynamic model; axisymmetry;railway rolling noise; curve influence

Contents

1 Introduction

Railways are a significant contributor to sustainable mobility, offering an environmentally friendly and efficient mode of transportation for both passengers and freight. However, noise emission from railway lines remains a major environmental issue that has been increasingly recognized as a significant challenge. Among the sources of sound radiation from railway vehicles, curve squeal and rolling noise are two of the most important [1]. The former is characterised by a high-pitched tonal sound, often arising in sharp curves due to a number of complex phenomena, such as self-excited vibration of a wheel caused by unsteady lateral forces [2, 3]. The latter, on the other hand, is generated by the interaction between the wheels and track in the presence of roughness on the wheel and rail rolling surfaces inducing vertical excitation [4]. Due to its nature, squeal noise is strongly linked to running on curved track (according to [4], it is less likely to occur in curves of radius greater than 200 m). Most studies of rolling noise, however, have focused on tangent track, although it is present on curved tracks as well. Furthermore, curved segments often exhibit rail corrugation, which can lead to higher rolling noise levels [5, 6]. Hence, the investigation of rolling noise for curved tracks takes on significance. Wang *et al.* [7] used a time-domain model for the vehicle/track interaction to simulate the vehicle curving behaviour and to study rolling noise on curved tracks. Their analysis involved assessing noise emissions from the inner side of the wheelset/track interaction on curves with varying radii. Their findings revealed that as track curvature increased, higher sound pressure levels were observed, primarily because of increased lateral rail vibrations as a consequence of higher lateral forces. While the previous work provides valuable insights into rolling noise on curved tracks, additional research and mathematical modelling is needed to understand this phenomenon and to support the identification of mitigation measurements.

When a railway vehicle negotiates a curve, the lateral displacement and angle of attack of the wheelset cause a change in the position, size, and shape of the wheel/rail contact patch as well as slip velocities within the contact area [8–11]. This affects the wheel/rail interaction forces and thus influences the levels of noise radiation compared with circulation on a tangent track. To accurately assess rolling noise emission in curve conditions, an advanced model of the railway vehicle is needed. In such conditions, the vehicle behaviour can be characterized as a superposition of the steady-state regime and the dynamic oscillations [12]. The former is commonly described with a multibody model which accounts for the centrifugal effects induced by the curved trajectory, while a high frequency model of the wheelsets is necessary for the latter. To this end, Martínez-Casas *et al.* [13] initially proposed an Eulerian approach to model the wheelset on a tangent track,

which was subsequently extended to consider its motion along a curved track through the incorporation of a trajectory coordinate set [14]. Later, Andrés *et al.* [15] adopted an axisymmetric approach for the aforementioned wheelset model in a tangent track, thereby reducing significantly the computational calculation time by three orders of magnitude. However, this efficient model does not account for the inertial effects of the curved trajectory and, to the authors' knowledge, no axisymmetric wheelset model considering these inertial effects has been presented so far.

In this work, the wheelset model for a curved trajectory presented in reference [14] is formulated first in a cylindrical reference system and, subsequently, an axisymmetric approach is proposed by expanding the displacements of the flexible body around the circumferential direction, yielding a much more efficient model. Using the above wheelset model, rolling noise radiated by a single wheelset or a complete vehicle while running through a curve is evaluated. To do this, the steady-state conditions during curving are simulated using the VI-Rail software [16] and then the dynamic behaviour around these conditions is studied. The wheelset dynamics are described through the aforementioned model, while the track is characterised using wave propagation theory [17, 18]. A frequency-domain model of the vehicle/track interaction is then proposed, which allows the wheel/rail contact forces to be solved. Later, the wheelset sound radiation is determined by applying an acoustic model based on the use of radiation ratios [19], whereas the track radiation is computed using a methodology based on equivalent acoustic sources [20]. A design of experiments (DoE) with parameters of the curved track is conducted to determine the influence of the curve on the rolling noise. While, as previously mentioned, corrugation might alter rail roughness on different curves, the present study is concerned with the effect of curved tracks for the same assumed roughness.

Following this introduction, Section 2 presents a three-dimensional model of the railway wheelset which incorporates the inertial effects associated with running on curved tracks. In Section 3, an axisymmetric approach is introduced as an alternative method to investigate the wheelset behaviour on curved tracks, offering faster computational performance without sacrificing accuracy. Section 4 focuses on the dynamic model of the vehicle, track, and wheel/rail interaction. Section 5 presents the results of the numerical simulations and analyses, revealing valuable insights into the influence of the curve on noise generation. Finally, Section 6 summarizes the conclusions and suggests potential avenues for future research.

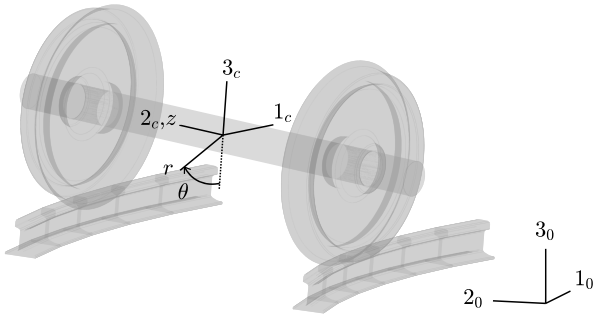

Fig. 1: Definition of the reference systems.

2 Three-dimensional dynamic model of the wheelset

In this section, the three-dimensional dynamic model developed in [14] is formulated in a cylindrical reference system. To do this, three different reference systems are defined: an inertial (fixed) Cartesian frame $\mathbf{u}_{0,1}\mathbf{u}_{0,2}\mathbf{u}_{0,3}$, a trajectory coordinate Cartesian frame $\mathbf{u}_{c,1}\mathbf{u}_{c,2}\mathbf{u}_{c,3}$ travelling with the wheelset and a cylindrical frame also travelling with the wheelset with coordinates (r,θ,z), as defined in Fig. 1; the last two frames are centred in the undeformed configuration of the wheelset and will be referred to as track frames. To denote a variable in different frames of reference, the subscript 0 indicates the inertial frame, the subscript c represents the travelling Cartesian frame, and no subscript is used for the travelling cylindrical frame. Thus, for an arbitrary variable $\mathbf{\Phi}$, the following relationships hold:

$$\begin{aligned} \mathbf{\Phi}_0 &= \mathbf{T}\mathbf{\Phi}_c, \\ \mathbf{\Phi}_c &= \mathbf{\Theta}\mathbf{\Phi}, \end{aligned} \tag{1}$$

where the matrices $\mathbf{T}$ and $\mathbf{\Theta}$ are defined as follows:

$$\mathbf{T} = \begin{bmatrix} \cos(\beta) & -\sin(\beta)\cos(\gamma) & \sin(\beta)\sin(\gamma) \\ \sin(\beta) & \cos(\beta)\cos(\gamma) & -\cos(\beta)\sin(\gamma) \\ 0 & \sin(\gamma) & \cos(\gamma) \end{bmatrix}, \tag{2}$$

$$\mathbf{\Theta} = \begin{bmatrix} -\sin(\theta) & -\cos(\theta) & 0 \\ 0 & 0 & 1 \\ -\cos(\theta) & \sin(\theta) & 0 \end{bmatrix}, \tag{3}$$

with β being the track angle, defined as a rotation around the $\mathbf{u}_{0,3}$ vector, and γ being the cant angle, defined as a rotation around the $\mathbf{u}_{c,1}$ vector. Note that, in the case of a right-hand curve, β is negative while γ is positive.

Considering the motion of the flexible wheelset, the position $\mathbf{q}_0$ of any particle of this in the deformed shape formulated in the inertial frame can be expressed as follows:

$$\mathbf{q}_0 = \mathbf{p}_0 + \mathbf{T}\boldsymbol{\Theta}\left(\mathbf{u} + \mathbf{w}(\mathbf{u}, t)\right), \tag{4}$$

where $\mathbf{p}_0$ defines the position of the travelling frames, $\mathbf{u} = \begin{pmatrix} r & 0 & z \end{pmatrix}^{\mathrm{T}}$ is the spatial position corresponding to that particle in the undeformed configuration and $\mathbf{w} = \begin{pmatrix} w_r & w_\theta & w_z \end{pmatrix}^{\mathrm{T}}$ contains the displacements of the particle at the position $\mathbf{u}$ and instant t due to the body flexibility and small rigid body motion (RBM) in the radial, circumferential, and axial directions, respectively. The velocity of that particle of the wheelset expressed in the inertial frame can be written as [21, 22]:

$$\frac{\mathrm{D}\mathbf{q}_0}{\mathrm{D}t} = \dot{\mathbf{p}}_0 + \dot{\mathbf{T}}\boldsymbol{\Theta}\left(\mathbf{u} + \mathbf{w}\right) + \mathbf{T}\boldsymbol{\Theta}\frac{\mathrm{D}(\mathbf{u} + \mathbf{w})}{\mathrm{D}t}, \tag{5}$$

where $\frac{\mathrm{D}(\mathbf{u}+\mathbf{w})}{\mathrm{D}t}$ represents the velocity of the wheelset particle expressed in the cylindrical frame when running on a tangent track which is given by Eq. (17) of [15]. For convenience, the velocity of the particle is now formulated in the Cartesian frame using the relation in Eq. (1), yielding:

$$\frac{\mathrm{D}\mathbf{q}_c}{\mathrm{D}t} = \dot{\mathbf{p}}_c + \tilde{\boldsymbol{\omega}}_c\boldsymbol{\Theta}\left(\mathbf{u} + \mathbf{w}\right) + \boldsymbol{\Theta}\frac{\mathrm{D}(\mathbf{u} + \mathbf{w})}{\mathrm{D}t}, \tag{6}$$

where $\tilde{\boldsymbol{\omega}}_c = \mathbf{T}^{\mathrm{T}}\dot{\mathbf{T}}$ is the angular velocity matrix of the track frames expressed in the Cartesian travelling frame. The kinetic energy K of the railway wheelset is thus given by:

$$\begin{aligned} K = \frac{1}{2}\int_V \rho\frac{\mathrm{D}\mathbf{q}_c^{\mathrm{T}}}{\mathrm{D}t}\frac{\mathrm{D}\mathbf{q}_c}{\mathrm{D}t}\mathrm{d}V = \frac{1}{2}\dot{\mathbf{p}}_c^{\mathrm{T}}\dot{\mathbf{p}}_c M + \dot{\mathbf{p}}_c^{\mathrm{T}}\tilde{\boldsymbol{\omega}}_c\int_V \rho\boldsymbol{\Theta}\left(\mathbf{u} + \mathbf{w}\right)\mathrm{d}V \\ + \dot{\mathbf{p}}_c^{\mathrm{T}}\int_V \rho\boldsymbol{\Theta}\frac{\mathrm{D}(\mathbf{u} + \mathbf{w})}{\mathrm{D}t}\mathrm{d}V + \frac{1}{2}\int_V \rho(\mathbf{u} + \mathbf{w})^{\mathrm{T}}\boldsymbol{\Theta}^{\mathrm{T}}\tilde{\boldsymbol{\omega}}_c^{\mathrm{T}}\tilde{\boldsymbol{\omega}}_c\boldsymbol{\Theta}(\mathbf{u} + \mathbf{w})\mathrm{d}V \\ + \int_V \rho(\mathbf{u} + \mathbf{w})^{\mathrm{T}}\boldsymbol{\Theta}^{\mathrm{T}}\tilde{\boldsymbol{\omega}}_c^{\mathrm{T}}\boldsymbol{\Theta}\frac{\mathrm{D}(\mathbf{u} + \mathbf{w})}{\mathrm{D}t}\mathrm{d}V + K_t, \end{aligned} \tag{7}$$

where ρ and V are, respectively, the density and volume of the wheelset, $\mathrm{d}V = r\mathrm{d}\theta\mathrm{d}r\mathrm{d}z$, and K_t is the kinetic energy of the wheelset when running on a tangent track (further details are given in Eq. (18) of reference [15]).

In this work, a model based on the Finite Element Method (FEM) is utilised, wherein the computation of the displacement field in the eth element of the FE mesh is accomplished through interpolation of the nodal solution using the following approach:

$$\mathbf{w}(r,\theta,z,t) = \mathbf{N}(r,\theta,z)\boldsymbol{w}^e(t), \tag{8}$$

where the shape function matrix $\mathbf{N}$ and the vector $\boldsymbol{w}^e$ with the displacements or degrees of freedom (DoF) can be expressed as indicated in Eqs. (22) and (23) of [15], respectively. The terms of the Lagrange equations associated with the wheelset kinetic energy in Eq. (7), when this is applied to the eth element of the FE mesh, can be evaluated as follows:

$$\begin{aligned}\frac{\mathrm{D}}{\mathrm{D}t}\left(\frac{\partial K}{\partial \dot{\boldsymbol{w}}^e}\right)^{\mathrm{T}} - \left(\frac{\partial K}{\partial \boldsymbol{w}^e}\right)^{\mathrm{T}} &= 2\mathbf{P}^e\dot{\boldsymbol{w}}^e + \left(2\Omega\mathbf{S}^e + \mathbf{R}^e + \mathbf{B}^e\right)\boldsymbol{w}^e - 2\Omega\mathbf{U}^e \\ &-\mathbf{H}^e - \mathbf{L}^e - \mathbf{G}^e\mathbf{T}^{\mathrm{T}}\ddot{\mathbf{p}}_0 + \left(\frac{\mathrm{D}}{\mathrm{D}t}\left(\frac{\partial K_t}{\partial \dot{\boldsymbol{w}}^e}\right)^{\mathrm{T}} - \left(\frac{\partial K_t}{\partial \boldsymbol{w}^e}\right)^{\mathrm{T}}\right).\end{aligned} \tag{9}$$

where a constant rotational speed Ω of the wheelset about its main axis is assumed. The last term in Eq. (9) considers the contribution to the Lagrange equations of the kinetic energy of the wheelset during its motion along a tangent track. This contribution is explicitly detailed in Eq. (24) of [15]. Considering the new terms due to the curve, the element matrices in Eq. (9) are given by the following expressions:

$$\begin{aligned}\mathbf{P}^e &= \int_{V^e} \rho\mathbf{N}^{\mathrm{T}}\tilde{\boldsymbol{\omega}}\mathbf{N}\mathrm{d}V, \\ \mathbf{S}^e &= \int_{V^e} \rho\mathbf{N}^{\mathrm{T}}\tilde{\boldsymbol{\omega}}\left(\frac{\partial\mathbf{N}}{\partial\theta} + \mathbf{J}\mathbf{N}\right)\mathrm{d}V, \\ \mathbf{R}^e &= \int_{V^e} \rho\mathbf{N}^{\mathrm{T}}\dot{\tilde{\boldsymbol{\omega}}}\mathbf{N}\mathrm{d}V, \\ \mathbf{B}^e &= -\int_{V^e} \rho\mathbf{N}^{\mathrm{T}}\tilde{\boldsymbol{\omega}}^{\mathrm{T}}\tilde{\boldsymbol{\omega}}\mathbf{N}\mathrm{d}V, \\ \mathbf{U}^e &= -\int_{V^e} \rho\mathbf{N}^{\mathrm{T}}\tilde{\boldsymbol{\omega}}\widehat{\mathbf{e}}_2 r\mathrm{d}V, \\ \mathbf{H}^e &= -\int_{V^e} \rho\mathbf{N}^{\mathrm{T}}\dot{\tilde{\boldsymbol{\omega}}}\mathbf{u}\mathrm{d}V, \\ \mathbf{L}^e &= \int_{V^e} \rho\mathbf{N}^{\mathrm{T}}\tilde{\boldsymbol{\omega}}^{\mathrm{T}}\tilde{\boldsymbol{\omega}}\mathbf{u}\mathrm{d}V,\end{aligned} \tag{10}$$

$$\mathbf{G}^e = -\int_{V^e} \rho \mathbf{N}^{\mathrm{T}} \boldsymbol{\Theta}^{\mathrm{T}} \mathrm{d}V, \tag{10}$$

where V^e is the volume of the eth element, $\tilde{\boldsymbol{\omega}} = \boldsymbol{\Theta}^{\mathrm{T}} \tilde{\boldsymbol{\omega}}_c \boldsymbol{\Theta}$ represents the angular velocity matrix of the track frames formulated in the cylindrical reference system, the matrix $\mathbf{J}$ is given in Appendix A and $\widehat{\mathbf{e}_2} = \begin{pmatrix} 0 & 1 & 0 \end{pmatrix}^{\mathrm{T}}$. Assembling the element matrices into the global ones according to the FEM approach [23] and considering the contribution of the last term in Eq. (9), the equation of motion (EoM) of the wheelset when running on a curved track are given by:

$$\begin{aligned} \mathbf{M}\ddot{\boldsymbol{w}}(t) + (2\Omega\mathbf{V} + 2\mathbf{P})\,\dot{\boldsymbol{w}}(t) + \left(\mathbf{K} + \Omega^2\mathbf{A} + 2\Omega\mathbf{S} + \mathbf{R} + \mathbf{B}\right)\boldsymbol{w}(t) \\ = \Omega^2\mathbf{c} + 2\Omega\mathbf{U} + \mathbf{H} + \mathbf{L} + \mathbf{G}\mathbf{T}^{\mathrm{T}}\ddot{\mathbf{p}}_0 + \boldsymbol{\mathcal{F}}(t), \end{aligned} \tag{11}$$

where the matrices $\mathbf{M}$, $\mathbf{V}$, $\mathbf{K}$, $\mathbf{A}$, and $\mathbf{c}$ describe the behaviour of the wheelset on a tangent track, the expressions for which can be found in Eq. (25) of [15]. The force vector $\boldsymbol{\mathcal{F}}$ accounts for the external forces applied to the system due to the wheel/rail interaction. In order to evaluate the rolling noise radiated by the wheels in the wheelset, the model is transformed to the frequency domain, in which the EoM can be expressed for $\omega > 0$ as:

$$\left(-\omega^2\mathbf{M} + \mathrm{i}\omega\,(2\Omega\mathbf{V} + 2\mathbf{P}) + \mathbf{K} + \Omega^2\mathbf{A} + 2\Omega\mathbf{S} + \mathbf{R} + \mathbf{B}\right)\boldsymbol{w}(\omega) = \boldsymbol{\mathcal{F}}(\omega). \tag{12}$$

Regarding the sound radiation from the wheelset, the acoustic model developed by Thompson [19] is applied on the surface vibrational field of both wheels, while the axle radiation is considered to be insignificant compared with that of the wheels.

3 Axisymmetric dynamic model of the wheelset

Due to the axial symmetry of the wheelset geometry, the displacement field can be represented using a Fourier series expansion around the circumferential direction as follows [24]:

$$\begin{aligned} w_r &= w_{r,0} + \sum_{n>0} \left(w_{r,n}\cos(n\theta) - \overline{w}_{r,n}\sin(n\theta)\right), \\ w_\theta &= -\overline{w}_{\theta,0} + \sum_{n>0} \left(w_{\theta,n}\sin(n\theta) - \overline{w}_{\theta,n}\cos(n\theta)\right), \\ w_z &= w_{z,0} + \sum_{n>0} \left(w_{z,n}\cos(n\theta) - \overline{w}_{z,n}\sin(n\theta)\right), \end{aligned} \tag{13}$$

with n being an integer number representing each Fourier term. For convenience, the harmonic amplitudes can be assembled in a vector $\mathbf{w}_h$, defined by:

$$\begin{aligned}
\mathbf{w}_h &= \begin{pmatrix} \mathbf{w}_0 & \mathbf{w}_1 & \cdots & \mathbf{w}_n & \cdots & \mathbf{w}_m \end{pmatrix}^{\mathrm{T}}, \\
\mathbf{w}_0 &= \begin{pmatrix} w_{r,0} & w_{z,0} & \overline{w}_{\theta,0} \end{pmatrix}, \\
\mathbf{w}_n &= \begin{pmatrix} w_{r,n} & w_{\theta,n} & w_{z,n} & \overline{w}_{r,n} & \overline{w}_{\theta,n} & \overline{w}_{z,n} \end{pmatrix}, \quad n = 1, \cdots, m,
\end{aligned} \tag{14}$$

where a truncation up to the Fourier term m is assumed on the expansion of the wheelset response. When considering this expansion, the kinetic energy of the wheelset described in Eq. (7) can be integrated analytically over the θ coordinate, as detailed in Appendix B. Unlike the tangent track case [15], the harmonics from different Fourier terms are now coupled. The integration mentioned above yields the following expression for the kinetic energy:

$$\begin{aligned}
K = {} & \frac{1}{2}\dot{\mathbf{p}}_c^{\mathrm{T}}\dot{\mathbf{p}}_c M + \pi\dot{\mathbf{p}}_c^{\mathrm{T}}\tilde{\boldsymbol{\omega}}_c \int_A \rho\left(\mathbf{J}_1\mathbf{w}_h + \mathbf{J}_2\right) r\mathrm{d}A + \pi\dot{\mathbf{p}}_c^{\mathrm{T}} \int_A \rho\mathbf{J}_1\dot{\mathbf{w}}_h r\mathrm{d}A \\
& + \frac{\pi}{2}\int_A \rho\left((\omega_{11}^2 + \omega_{33}^2)r^2 + 2\omega_{22}^2 z^2\right) r\mathrm{d}A + \pi\int_A \rho\mathbf{J}_3^{\mathrm{T}}\mathbf{w}_h r\mathrm{d}A \\
& + \frac{\pi}{2}\int_A \rho\mathbf{w}_h^{\mathrm{T}}\mathbf{J}_4\mathbf{w}_h r\mathrm{d}A + \Omega 2\pi\omega_2 \int_A \rho r^3\mathrm{d}A + \pi\int_A \rho\left(\mathbf{J}_5^{\mathrm{T}} + \mathbf{w}_h^{\mathrm{T}}\mathbf{J}_7\right)\dot{\mathbf{w}}_h r\mathrm{d}A \\
& + \Omega\pi\int_A \rho\left(\mathbf{J}_6^{\mathrm{T}} + \mathbf{w}_h^{\mathrm{T}}\mathbf{J}_8\right)\mathbf{w}_h r\mathrm{d}A + K_t,
\end{aligned} \tag{15}$$

where A is the area of the wheelset cross-section, $\mathrm{d}A = \mathrm{d}r\mathrm{d}z$, and the matrices $\mathbf{J}_i$ are given in Appendix A. The kinetic energy of the wheelset associated with a tangent track, K_t, is given in Eqs. (36) and (37) of reference [15]; equivalently, it can be expressed as a function of the assembled vector $\mathbf{w}_h$ as indicated in Appendix B. Regarding the angular velocities of the track frame ω_i as well as the squared angular velocities ω_{ij}^2, these can be identified from the following terms in $\tilde{\boldsymbol{\omega}}_c$ and $\tilde{\boldsymbol{\omega}}_c^{\mathrm{T}}\tilde{\boldsymbol{\omega}}_c$:

$$\tilde{\boldsymbol{\omega}}_c = \begin{bmatrix} 0 & -\omega_3 & \omega_2 \\ \omega_3 & 0 & -\omega_1 \\ -\omega_2 & \omega_1 & 0 \end{bmatrix}, \qquad \tilde{\boldsymbol{\omega}}_c^{\mathrm{T}}\tilde{\boldsymbol{\omega}}_c = \begin{bmatrix} \omega_{11}^2 & \omega_{12}^2 & \omega_{13}^2 \\ \omega_{12}^2 & \omega_{22}^2 & \omega_{23}^2 \\ \omega_{13}^2 & \omega_{23}^2 & \omega_{33}^2 \end{bmatrix}. \tag{16}$$

A FE model is proposed for the wheelset cross-section (see Fig. 2), which allows the evaluation of the unknown harmonic amplitudes by means of the following interpolation in the eth element of the mesh:

$$\mathbf{w}_h(r, z, t) = \mathbf{N}_h(r, z)\boldsymbol{w}_h^e(t), \tag{17}$$

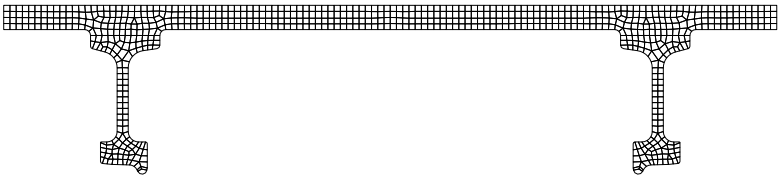

Fig. 2: FE mesh of the wheelset cross-section.

$\mathbf{N}_h$ being the shape function matrix defined for the axisymmetric model. When p nodes are considered in the eth element, this matrix is given by:

$$\mathbf{N}_h = \begin{bmatrix} \mathbf{N}_{h,1} & \cdots & \mathbf{N}_{h,j} & \cdots & \mathbf{N}_{h,p} \end{bmatrix}, \qquad \mathbf{N}_{h,j} = N_j \mathbf{I}_{(3+6m)\times(3+6m)}, \tag{18}$$

where N_j is the shape function associated with the jth node and $\mathbf{I}_{k\times k}$ is the identity matrix of order k. The vector of harmonic amplitudes of the eth element $\boldsymbol{w}_h^e$ can be expressed as follows:

$$\begin{aligned} \boldsymbol{w}_h^e &= \begin{pmatrix} \boldsymbol{w}_{h,1}^e & \cdots & \boldsymbol{w}_{h,j}^e & \cdots & \boldsymbol{w}_{h,p}^e \end{pmatrix}^{\mathrm{T}}, \\ \boldsymbol{w}_{h,j}^e &= \begin{pmatrix} \boldsymbol{w}_{0,j}^e & \boldsymbol{w}_{1,j}^e & \cdots & \boldsymbol{w}_{n,j}^e & \cdots & \boldsymbol{w}_{m,j}^e \end{pmatrix}, \end{aligned} \tag{19}$$

where $\boldsymbol{w}_{0,j}^e$ contains the three harmonic amplitudes in the jth node defined for $n = 0$ and $\boldsymbol{w}_{n,j}^e$ the six harmonic amplitudes in the same node defined for $n > 0$, sorted as expressed in Eq. (14).

When considering the kinetic energy in Eq. (15) for the eth element and evaluating the Lagrange equations, the result is given by:

$$\begin{aligned} \frac{\mathrm{D}}{\mathrm{D}t}\left(\frac{\partial K}{\partial \dot{\boldsymbol{w}}_h^e}\right)^{\mathrm{T}} - \left(\frac{\partial K}{\partial \boldsymbol{w}_h^e}\right)^{\mathrm{T}} &= 2\mathbf{P}_h^e \dot{\boldsymbol{w}}_h^e + \left(2\Omega \mathbf{S}_h^e + \mathbf{R}_h^e + \mathbf{B}_h^e\right) \boldsymbol{w}_h^e - 2\Omega \mathbf{U}_h^e \\ &\quad - \mathbf{H}_h^e - \mathbf{L}_h^e - \mathbf{G}_h^e \mathbf{T}^{\mathrm{T}} \ddot{\mathbf{p}}_0 + \left(\frac{\mathrm{D}}{\mathrm{D}t}\left(\frac{\partial K_t}{\partial \dot{\boldsymbol{w}}_h^e}\right)^{\mathrm{T}} - \left(\frac{\partial K_t}{\partial \boldsymbol{w}_h^e}\right)^{\mathrm{T}}\right), \end{aligned} \tag{20}$$

where, as in the 3D model, the last term considers the contribution of the wheelset kinetic energy during its motion along a tangent track. The development of this term can be found in Eqs. (53) and (60) of reference [15], wherein the harmonics are uncoupled, allowing the matrices to be expressed independently for each Fourier term. Later these matrices will be reformulated for the assembled vector of harmonic amplitudes. The element matrices for the new terms arising from Eq. (20) are obtained using the following expressions:

$$
\begin{aligned}
\mathbf{P}_h^e &= \sum_{i=1}^{3} \omega_i \mathbf{P}_{h,i}^e, & \mathbf{P}_{h,i}^e &= \pi \int_{A^e} \rho \mathbf{N}_h^{\mathrm{T}} \frac{\partial \mathbf{J}_7^{\mathrm{T}}}{\partial \omega_i} \mathbf{N}_h r \mathrm{d}A, \\
\mathbf{S}_h^e &= \sum_{i=1}^{3} \omega_i \mathbf{S}_{h,i}^e, & \mathbf{S}_{h,i}^e &= -\frac{\pi}{2} \int_{A^e} \rho \mathbf{N}_h^{\mathrm{T}} \left(\frac{\partial \mathbf{J}_8^{\mathrm{T}}}{\partial \omega_i} + \frac{\partial \mathbf{J}_8}{\partial \omega_i} \right) \mathbf{N}_h r \mathrm{d}A, \\
\mathbf{R}_h^e &= \sum_{i=1}^{3} \dot{\omega}_i \mathbf{R}_{h,i}^e, & \mathbf{R}_{h,i}^e &= \mathbf{P}_{h,i}^e, \\
\mathbf{B}_h^e &= \sum_{i=1}^{3} \sum_{j=i}^{3} \omega_{ij}^2 \mathbf{B}_{h,ij}^e, & \mathbf{B}_{h,ij}^e &= -\frac{\pi}{2} \int_{A^e} \rho \mathbf{N}_h^{\mathrm{T}} \left(\frac{\partial \mathbf{J}_4^{\mathrm{T}}}{\partial \omega_{ij}^2} + \frac{\partial \mathbf{J}_4}{\partial \omega_{ij}^2} \right) \mathbf{N}_h r \mathrm{d}A, \\
\mathbf{U}_h^e &= \sum_{i=1}^{3} \omega_i \mathbf{U}_{h,i}^e, & \mathbf{U}_{h,i}^e &= \frac{\pi}{2} \int_{A^e} \rho \mathbf{N}_h^{\mathrm{T}} \frac{\partial \mathbf{J}_6}{\partial \omega_i} r \mathrm{d}A, \\
\mathbf{H}_h^e &= \sum_{i=1}^{3} \dot{\omega}_i \mathbf{H}_{h,i}^e, & \mathbf{H}_{h,i}^e &= -\pi \int_{A^e} \rho \mathbf{N}_h^{\mathrm{T}} \frac{\partial \mathbf{J}_5}{\partial \omega_i} r \mathrm{d}A, \\
\mathbf{L}_h^e &= \sum_{i=1}^{3} \sum_{j=i}^{3} \omega_{ij}^2 \mathbf{L}_{h,ij}^e, & \mathbf{L}_{h,ij}^e &= \pi \int_{A^e} \rho \mathbf{N}_h^{\mathrm{T}} \frac{\partial \mathbf{J}_3}{\partial \omega_{ij}^2} r \mathrm{d}A, \\
\mathbf{G}_h^e &= -\pi \int_{A^e} \rho \mathbf{N}_h^{\mathrm{T}} \mathbf{J}_1^{\mathrm{T}} r \mathrm{d}A,
\end{aligned}
\tag{21}
$$

where A^e is the area of the eth element. Following the FEM approach, the element matrices in Eq. (21) are assembled into the global ones and, together with the contribution from the last term in Eq. (20), the EoM of the wheelset using an axisymmetric approach are given by:

$$
\begin{aligned}
&\mathbf{M}_h \ddot{\boldsymbol{w}}_h(t) + \left(2\Omega \mathbf{V}_h + 2 \sum_{i=1}^{3} \omega_i \mathbf{P}_{h,i} \right) \dot{\boldsymbol{w}}_h(t) \\
&+ \left(\mathbf{K}_h + \Omega^2 \mathbf{A}_h + 2\Omega \sum_{i=1}^{3} \omega_i \mathbf{S}_{h,i} + \sum_{i=1}^{3} \dot{\omega}_i \mathbf{R}_{h,i} + \sum_{i=1}^{3} \sum_{j=i}^{3} \omega_{ij}^2 \mathbf{B}_{h,ij} \right) \boldsymbol{w}_h(t) \\
&= \Omega^2 \mathbf{c}_h + 2\Omega \sum_{i=1}^{3} \omega_i \mathbf{U}_{h,i} + \sum_{i=1}^{3} \dot{\omega}_i \mathbf{H}_{h,i} + \sum_{i=1}^{3} \sum_{j=i}^{3} \omega_{ij}^2 \mathbf{L}_{h,ij} + \mathbf{G}_h \mathbf{T}^{\mathrm{T}} \ddot{\mathbf{p}}_0 + \boldsymbol{\mathcal{F}}_h(t).
\end{aligned}
\tag{22}
$$

It is worth noting that, in the proposed approach, the angular velocities appear explicitly in the EoM, while the matrices are functions only of the coordinates r

and z. This does not happen for the 3D model, associated with Eq. (11), in which the angular velocities are included implicitly in the EoM through the definition of the matrices involved; however, these matrices could as well be formulated to be independent of those variables if the matrix multiplications in the integrals of Eq. (10) are developed. By doing this, it is not necessary to evaluate the matrices of the wheelset at every time step of a curving simulation even if the curve radius, vehicle velocity or superelevation (cant) are not constant (note that these three quantities define the aforementioned angular velocities).

Regarding the force vector $\boldsymbol{\mathscr{F}}_h$ in Eq. (22), it considers the wheel/rail interaction forces after expanding them in Fourier series; a detailed methodology to evaluate the harmonic amplitudes of the forces for each Fourier term is exposed in Section 4.3 of [15]. The vector $\boldsymbol{\mathscr{F}}_h$ is then obtained by assembling the amplitudes from each Fourier term in accordance with the order of the vector of unknowns $\mathbf{w}_h$, defined in Eq. (14). The matrices $\mathbf{M}_h$, $\mathbf{V}_h$, $\mathbf{K}_h$, $\mathbf{A}_h$, and $\mathbf{c}_h$ describe the dynamics of the wheelset when running on a tangent track and their expressions can be found in Eqs. (54) and (61) of reference [15], formulated independently for each Fourier term. Due to the coupling between harmonics introduced by the new matrices in a curved track, the matrices from [15] could be assembled according to $\mathbf{w}_h$. Alternatively, the assembled element matrices can be evaluated as follows:

$$\begin{aligned}
\mathbf{M}_h^e &= \pi \int_{A^e} \rho \mathbf{N}_h^{\mathrm{T}} \mathbf{J}_9 \mathbf{N}_h r \mathrm{d}A, \\
\mathbf{V}_h^e &= \pi \int_{A^e} \rho \mathbf{N}_h^{\mathrm{T}} \mathbf{J}_{11}^{\mathrm{T}} \mathbf{N}_h r \mathrm{d}A, \\
\mathbf{K}_h^e &= \pi \int_{A^e} \tilde{\mathbf{B}}^{\mathrm{T}} \tilde{\mathbf{D}} \tilde{\mathbf{B}} r \mathrm{d}A, \\
\mathbf{A}_h^e &= -\pi \int_{A^e} \rho \mathbf{N}_h^{\mathrm{T}} \left(\mathbf{J}_{13}^{\mathrm{T}} + \mathbf{J}_{13} \right) \mathbf{N}_h r \mathrm{d}A, \\
\mathbf{c}_h^e &= \pi \int_{A^e} \rho \mathbf{N}_h^{\mathrm{T}} \mathbf{J}_{10} r \mathrm{d}A,
\end{aligned} \tag{23}$$

where $\tilde{\mathbf{B}} = \tilde{\mathbf{L}} \mathbf{N}_h$, with $\tilde{\mathbf{L}}$ being a matrix operator given in Appendix A together with the matrix $\tilde{\mathbf{D}}$. As in the 3D model, to allow the subsequent sound radiation evaluation, the EoM is transformed to the frequency domain for $\omega > 0$, yielding:

$$\begin{aligned}
\Bigg(-\omega^2 \mathbf{M}_h + \mathrm{i}\omega \left(2\Omega \mathbf{V}_h + 2 \sum_{i=1}^{3} \omega_i \mathbf{P}_{h,i} \right) + \mathbf{K}_h + \Omega^2 \mathbf{A}_h + 2\Omega \sum_{i=1}^{3} \omega_i \mathbf{S}_{h,i} \\
+ \sum_{i=1}^{3} \dot{\omega}_i \mathbf{R}_{h,i} + \sum_{i=1}^{3} \sum_{j=i}^{3} \omega_{ij}^2 \mathbf{B}_{h,ij} \Bigg) \boldsymbol{w}_h(\omega) = \boldsymbol{\mathscr{F}}_h(\omega).
\end{aligned} \tag{24}$$

In line with the dynamic behaviour of the wheelset, the sound radiation can be formulated in a two-dimensional frame, taking advantage of the expansion of the response around the circumferential direction. To this end, the methodology described in Section 4.5 of reference [15] is performed over the surface of the wheels. However, the RBM contribution mentioned in the previous reference is explicitly excluded in this work since the wheelset FE model proposed already includes it. As stated in Section 2, the axle contribution to the acoustic radiation is neglected.

4 Vehicle/track interaction model

In this work, the Manchester Benchmark vehicle [25] is considered to be running on a curved track with constant curvature. The behaviour of the wheelset and track in a curve is characterized as a superposition of the steady-state regime and the dynamic oscillations around it. For simplicity, the former is obtained using the VI-Rail software [16]. The steady-state variables on the curve, together with the wheel and rail combined roughness spectrum, are used as an input for the calculation of rolling noise radiated by the wheelset and track. This is done through the procedure described below.

4.1 Wheelset

The models developed previously are employed to describe the vibroacoustic behaviour of the wheelset. Due to its higher computational performance, the axisymmetric approach is preferred over the 3D methodology. Additionally, the primary suspension of the vehicle and the axlebox are included, the latter being modelled as a point mass. If the primary suspension were added on the surface of the axle, then different Fourier harmonics would be coupled in the axisymmetric model. Therefore, for simplicity, both elements are considered to be attached to the wheelset at its axis of rotation. As the axial coordinate is $z = 0$ in the centre of the wheelset, two nodes of the FE model with opposite coordinate z are chosen to attach the primary suspension and axlebox. Due to the symmetry of these nodes, the incorporation of the primary suspension and axlebox is illustrated below for just one side of the model, at a node denoted as p, and the same terms shall be incorporated for the other node in the model symmetric to p. For convenience, the radial coordinate of the node p is assumed not to be zero but tending to it ($r_p \to 0$). Considering this, the kinetic energy of the axlebox mass K_b and the potential and dissipating energies associated with the primary suspension (U_p and C_p, respectively) are given by:

$$
\begin{aligned}
K_b &= \frac{m_b}{2}\left(\dot{w}_{c,1}^2(r_p,\theta,z_p) + \dot{w}_{c,2}^2(r_p,z_p) + \dot{w}_{c,3}^2(r_p,\theta,z_p)\right),\\
U_p &= \frac{1}{2}\left(k_1 w_{c,1}^2(r_p,\theta,z_p) + k_2 w_{c,2}^2(r_p,z_p) + k_3 w_{c,3}^2(r_p,\theta,z_p)\right),\\
C_p &= \frac{1}{2}\left(c_1 \dot{w}_{c,1}^2(r_p,\theta,z_p) + c_2 \dot{w}_{c,2}^2(r_p,z_p) + c_3 \dot{w}_{c,3}^2(r_p,\theta,z_p)\right),
\end{aligned}
\tag{25}
$$

with m_b being the axlebox mass, k_i and c_i the stiffness and damping, respectively, of the primary suspension in the ith direction, and $w_{c,i}(r_p,\theta,z_p)$ the Cartesian displacement in the ith direction for a point with axial and radial coordinates corresponding to those of the point p. Regarding the angular coordinate θ, which determines the position on the circumference of radius $r_p \to 0$ where the elements are attached, it is arbitrary since any position is equivalent to the node p. When considering the transformation from Cartesian to cylindrical coordinates as defined in Eq. (1), the energies can be expressed as follows:

$$
\begin{aligned}
K_b &= \frac{1}{2}\dot{\mathbf{w}}^{\mathrm{T}}(r_p,\theta,z_p)\begin{bmatrix} m_b & 0 & 0\\ 0 & m_b & 0\\ 0 & 0 & m_b\end{bmatrix}\dot{\mathbf{w}}(r_p,\theta,z_p),\\
U_p &= \frac{1}{2}\mathbf{w}^{\mathrm{T}}(r_p,\theta,z_p)\begin{bmatrix} k_1\sin^2(\theta)+k_3\cos^2(\theta) & (k_1-k_3)\cos(\theta)\sin(\theta) & 0\\ (k_1-k_3)\cos(\theta)\sin(\theta) & k_1\cos^2(\theta)+k_3\sin^2(\theta) & 0\\ 0 & 0 & k_2\end{bmatrix}\mathbf{w}(r_p,\theta,z_p),\\
C_p &= \frac{1}{2}\dot{\mathbf{w}}^{\mathrm{T}}(r_p,\theta,z_p)\begin{bmatrix} c_1\sin^2(\theta)+c_3\cos^2(\theta) & (c_1-c_3)\cos(\theta)\sin(\theta) & 0\\ (c_1-c_3)\cos(\theta)\sin(\theta) & c_1\cos^2(\theta)+c_3\sin^2(\theta) & 0\\ 0 & 0 & c_2\end{bmatrix}\dot{\mathbf{w}}(r_p,\theta,z_p),
\end{aligned}
\tag{26}
$$

where the vector $\mathbf{w}$ is defined after Eq. (4). As mentioned before, any angular coordinate θ leads to the same point p. For simplicity, it is set to zero, so that the energies result in the following expressions:

$$
\begin{aligned}
K_b &= \frac{1}{2}\dot{\mathbf{w}}^{\mathrm{T}}(r_p,0,z_p)\begin{bmatrix} m_b & 0 & 0\\ 0 & m_b & 0\\ 0 & 0 & m_b\end{bmatrix}\dot{\mathbf{w}}(r_p,0,z_p),\\
U_p &= \frac{1}{2}\mathbf{w}^{\mathrm{T}}(r_p,0,z_p)\begin{bmatrix} k_3 & 0 & 0\\ 0 & k_1 & 0\\ 0 & 0 & k_2\end{bmatrix}\mathbf{w}(r_p,0,z_p),\\
C_p &= \frac{1}{2}\dot{\mathbf{w}}^{\mathrm{T}}(r_p,0,z_p)\begin{bmatrix} c_3 & 0 & 0\\ 0 & c_1 & 0\\ 0 & 0 & c_2\end{bmatrix}\dot{\mathbf{w}}(r_p,0,z_p).
\end{aligned}
\tag{27}
$$

Applying the Lagrange equations to Eq. (27), the axlebox is included by adding m_b in the diagonal terms of the mass matrix in Eq. (12) associated with the three DoF of the node p. The stiffness of the primary suspension is taken into account by adding k_3, k_1, and k_2 to the diagonal terms of the stiffness matrix associated with the DoF w_r, w_θ, and w_z, respectively, of the node p. Similarly, the damping of the primary suspension is included in the damping matrix. As previously mentioned, the same needs to be done for the node symmetric to p (opposite z coordinate). It is worth indicating that there is no damping matrix in Eq. (12), so it needs to be generated to add the dissipative properties of the primary suspension. Also, a modal damping ratio ξ is included in the wheelset model using the empirical relation proposed by Thompson [4], relating the modal damping ratio and the number of nodal diameters of a modeshape. When the angular coordinate is set to a different value, the terms associated with the radial and circumferential DoF are modified, although the FE model is equivalent. This is a consequence of evaluating any variable expressed in the cylindrical frame at a zero radial coordinate, which results in the radial and circumferential axes having arbitrary direction (always keeping a right handed reference system).

Regarding the axisymmetric model, keeping the treatment given to the node p as this being a circumference of radius $r_p \to 0$, the response expansion of such node is given by:

$$\mathbf{w}(r_p,\theta,z_p) = \begin{pmatrix} w_r(r_p,\theta,z_p) \\ w_\theta(r_p,\theta,z_p) \\ w_z(r_p,z_p) \end{pmatrix} = \begin{pmatrix} w_{r,1}(r_p,z_p)\cos(\theta) - \overline{w}_{r,1}(r_p,z_p)\sin(\theta) \\ w_{\theta,1}(r_p,z_p)\cos(\theta) - \overline{w}_{\theta,1}(r_p,z_p)\sin(\theta) \\ w_{z,0}(r_p,z_p) \end{pmatrix}, \tag{28}$$

where only the harmonic $n = 1$ contributes for the radial and circumferential coordinates and $n = 0$ for the axial, as a result of p being a point. Another consequence of this fact is that different harmonic amplitudes can be related as follows:

$$\begin{aligned} w_r(r_p,\theta=0,z_p) = -w_\theta(r_p,\theta=\frac{\pi}{2},z_p) \quad &\Longrightarrow \quad w_{\theta,1}(r_p,z_p) = -w_{r,1}(r_p,z_p), \\ w_r(r_p,\theta=\frac{\pi}{2},z_p) = w_\theta(r_p,\theta=0,z_p) \quad &\Longrightarrow \quad \overline{w}_{\theta,1}(r_p,z_p) = \overline{w}_{r,1}(r_p,z_p). \end{aligned} \tag{29}$$

By introducing into Eq. (25) the Cartesian-cylindrical coordinate transformation of Eq. (1) together with the expansion in Eq. (28) and the relation between harmonic amplitudes in Eq. (29), the energies can be expressed as follows:

$$
\begin{aligned}
K_b &= \frac{m_b}{2}\left(\dot{w}_{z,0}^2(r_p,z_p) + \dot{w}_{r,1}^2(r_p,z_p) + \dot{\overline{w}}_{r,1}^2(r_p,z_p)\right),\\
U_p &= \frac{1}{2}\left(k_2 w_{z,0}^2(r_p,z_p) + k_3 w_{r,1}^2(r_p,z_p) + k_1 \overline{w}_{r,1}^2(r_p,z_p)\right),\\
C_p &= \frac{1}{2}\left(c_2 \dot{w}_{z,0}^2(r_p,z_p) + c_3 \dot{w}_{r,1}^2(r_p,z_p) + c_1 \dot{\overline{w}}_{r,1}^2(r_p,z_p)\right),
\end{aligned}
\tag{30}
$$

where there is no need to set the angular coordinate since it has been implicitly fixed in Eq. (29). Again, applying the Lagrange equations to Eq. (30), the axlebox mass is included in the model by adding m_b in the diagonal terms of the mass matrix from Eq. (24) associated with the DoF $w_{z,0}$, $w_{r,1}$, and $\overline{w}_{r,1}$ of the pth node. Regarding the primary suspension, its stiffness is considered in the model by adding k_2, k_3, and k_1 in the diagonal terms of the stiffness matrix associated with, respectively, the DoF $w_{z,0}$, $w_{r,1}$, and $\overline{w}_{r,1}$ of the pth node. Similarly, the damping of the primary suspension is included in a generated damping matrix, considering the corresponding values of c_i. As in the three-dimensional model, the modal damping ratio ξ proposed by Thompson [4] is included in the wheelset model. Also, the same procedure needs to be repeated for the node symmetric to p.

4.2 Track

The two-layer continuous track model described in [26] is adapted for the current investigation by including both rails, which are dynamically coupled through the sleepers. This allows both the dynamic and acoustic behaviour of the rails and sleepers to be evaluated. The sound radiation calculation requires the assumption that the different waves in the track can be considered to radiate independently [20], and a condition for this to be true is that different waves have different wavenumbers. Due to the symmetry of the track, for each wavenumber there are two independent waves (symmetric and antisymmetric relative to the track centre) and so the previous assumption does not hold. To apply the acoustic model, these pairs of waves are combined and thus their contribution to the track response $\mathbf{w}_T$ can be expressed as follows:

$$
\begin{aligned}
\mathbf{w}_T &= \sum_r \left(A_r \boldsymbol{\Psi}_r + \overline{A}_r \overline{\boldsymbol{\Psi}}_r\right) \mathrm{e}^{-\mathrm{i}k_r|x|} = \sum_r \widetilde{A}_r \widetilde{\boldsymbol{\Psi}}_r \mathrm{e}^{-\mathrm{i}k_r|x|},\\
\widetilde{A}_r &= A_r,\\
\widetilde{\boldsymbol{\Psi}}_r &= \boldsymbol{\Psi}_r + \frac{\overline{A}_r}{A_r}\overline{\boldsymbol{\Psi}}_r,
\end{aligned}
\tag{31}
$$

where subscript r represents each pair of waves with the same wavenumber, x is the longitudinal coordinate of the track coordinate system (running direction), and A_r, $\mathbf{\Psi}_r$, and k_r represent, respectively, the generalised coordinate, waveshape and wavenumber of the corresponding wave. The generalised coordinates and waveshapes with and without a bar are associated with the two independent waves, while the ones with a tilde represent the combined wave properties. In references [17,18], a detailed explanation on how to evaluate the waveshapes and wavenumbers is given. Regarding the generalised coordinates, they depend on the external forces applied to the track, and given these forces, the coordinates can be evaluated as described in [20]. These wave properties are subsequently used in the acoustic model, which predicts both rail and sleeper sound power radiation. In this work, due to the existence of significant lateral forces coming from the curving behaviour, the sleeper is assumed to radiate from top, bottom and both lateral faces, and it is modelled as a rigid body with 4 degrees of freedom (DoF): three Cartesian translations and a rotation with respect to the longitudinal axis.

Note that, according to reference [27], the curvature of the track does not notably affect its dynamic response when the curve radius is greater than 30 m, a value lower than the minimum radius used in the simulations conducted in this work. Therefore, the curvature is not considered in the track dynamic model described above.

4.3 Wheel/rail interaction

Rolling noise occurs as a consequence of the wheel/rail interaction when roughness is present on their rolling surfaces. The forces resulting from this interaction are evaluated using the model developed by Thompson [4,28], which is here extended to consider non-zero mean values of the creepages, the dynamic fluctuation of the normal contact force and the effect of the contact angle, leading to a coupling of vertical and lateral vibration of the wheels and rails. The wheel/rail interaction module is defined in the form of a linearised input-output relationship between the relative motion of the wheel and rail surfaces at the contact point and the contact forces. This relationship is initially derived for the case of a wheelset running centred over the track so that the small contact angle can be neglected. Then, the model is extended to the case of a wheelset running through a curve, considering the effect of the contact angle, i.e. the inclination of the plane tangent to the contacting surfaces with respect to the top-of-rail plane.

Considering the three directions of the space, a diagram of the interaction model showing the sign convention used in this work is depicted in Fig. 3. The Roman Numerals I and II make reference to the left and right sides, respectively. The text

I/II indicates that the same diagram applies to both sides. Roughness is assumed to exist only in the vertical direction, in which the wheel and rail are connected through a contact stiffness (see Fig. 3(c)). In the other two directions, the relation between velocity and force in the contact area will be explored later. Due to continuity in the contact, the following relation between velocities is found [4]:

$$\begin{pmatrix} v_{W,\mathrm{I1}} \\ v_{W,\mathrm{I2}} \\ v_{W,\mathrm{I3}} \\ v_{W,\mathrm{II1}} \\ v_{W,\mathrm{II2}} \\ v_{W,\mathrm{II3}} \end{pmatrix} - \begin{pmatrix} v_{R,\mathrm{I1}} \\ v_{R,\mathrm{I2}} \\ v_{R,\mathrm{I3}} \\ v_{R,\mathrm{II1}} \\ v_{R,\mathrm{II2}} \\ v_{R,\mathrm{II3}} \end{pmatrix} - \begin{pmatrix} v_{C,\mathrm{I1}} \\ v_{C,\mathrm{I2}} \\ v_{C,\mathrm{I3}} \\ v_{C,\mathrm{II1}} \\ v_{C,\mathrm{II2}} \\ v_{C,\mathrm{II3}} \end{pmatrix} = \begin{pmatrix} 0 \\ 0 \\ r_{S,\mathrm{I}} \\ 0 \\ 0 \\ r_{S,\mathrm{II}} \end{pmatrix} \mathrm{i}\omega \quad \Longrightarrow \quad \mathbf{v}_W - \mathbf{v}_R - \mathbf{v}_C = \mathbf{r}\mathrm{i}\omega, \tag{32}$$

where, in the velocities, the first subscript refers to the component (W for wheelset, R for rail, and C for contact) and the second to the element side and direction (for example, $v_{R,\mathrm{I2}}$ is the lateral velocity of the left rail contact point). A wheel/rail combined (system) roughness with angular frequency ω is considered in the vertical direction of the left and right sides with amplitude $r_{S,\mathrm{I}}$ and $r_{S,\mathrm{II}}$, respectively, which are assumed to be randomly uncorrelated. Note that, while the subscript c is used in Sections 2, 3, and 4.1 to denote the travelling Cartesian frame, the subscript C (capital letter) is employed in this section to denote a contact variable. For convenience, the first vector in the left hand of Eq. (32) is defined as $\mathbf{v}_W$, the second as $\mathbf{v}_R$, and the third as $\mathbf{v}_C$, while the vector in the right hand is defined as $\mathbf{r}$. Assembling the interaction forces accordingly, that is $\mathbf{F} = \begin{pmatrix} F_{\mathrm{I1}} & F_{\mathrm{I2}} & F_{\mathrm{I3}} & F_{\mathrm{II1}} & F_{\mathrm{II2}} & F_{\mathrm{II3}} \end{pmatrix}^{\mathrm{T}}$, and taking into account the sign convention shown in Fig. 3, the wheelset velocities can be related to the forces as follows:

$$\begin{aligned} \mathbf{v}_W &= -\begin{bmatrix} Y_{W,\mathrm{I1\text{-}I1}} & Y_{W,\mathrm{I1\text{-}I2}} & Y_{W,\mathrm{I1\text{-}I3}} & Y_{W,\mathrm{I1\text{-}II1}} & Y_{W,\mathrm{I1\text{-}II2}} & Y_{W,\mathrm{I1\text{-}II3}} \\ Y_{W,\mathrm{I2\text{-}I1}} & Y_{W,\mathrm{I2\text{-}I2}} & Y_{W,\mathrm{I2\text{-}I3}} & Y_{W,\mathrm{I2\text{-}II1}} & Y_{W,\mathrm{I2\text{-}II2}} & Y_{W,\mathrm{I2\text{-}II3}} \\ Y_{W,\mathrm{I3\text{-}I1}} & Y_{W,\mathrm{I3\text{-}I2}} & Y_{W,\mathrm{I3\text{-}I3}} & Y_{W,\mathrm{I3\text{-}II1}} & Y_{W,\mathrm{I3\text{-}II2}} & Y_{W,\mathrm{I3\text{-}II3}} \\ Y_{W,\mathrm{II1\text{-}I1}} & Y_{W,\mathrm{II1\text{-}I2}} & Y_{W,\mathrm{II1\text{-}I3}} & Y_{W,\mathrm{II1\text{-}II1}} & Y_{W,\mathrm{II1\text{-}II2}} & Y_{W,\mathrm{II1\text{-}II3}} \\ Y_{W,\mathrm{II2\text{-}I1}} & Y_{W,\mathrm{II2\text{-}I2}} & Y_{W,\mathrm{II2\text{-}I3}} & Y_{W,\mathrm{II2\text{-}II1}} & Y_{W,\mathrm{II2\text{-}II2}} & Y_{W,\mathrm{II2\text{-}II3}} \\ Y_{W,\mathrm{II3\text{-}I1}} & Y_{W,\mathrm{II3\text{-}I2}} & Y_{W,\mathrm{II3\text{-}I3}} & Y_{W,\mathrm{II3\text{-}II1}} & Y_{W,\mathrm{II3\text{-}II2}} & Y_{W,\mathrm{II3\text{-}II3}} \end{bmatrix} \mathbf{F} \\ &= -\mathbf{Y}_W \mathbf{F}, \end{aligned} \tag{33}$$

with $\mathbf{Y}_W$ being a mobility matrix associated with the wheelset contact points. As for the velocities, the first subscript of the mobilities refers to the element while the second subscript denotes where the response is measured and the unit force applied. For example, the mobility $Y_{W,\mathrm{II3\text{-}I2}}$ represents the vertical (3) velocity

of the wheelset right side contact point (II) when only a unit lateral (2) force is applied on the wheelset left side contact point (I). These mobilities, as explained in Section 4.1, are determined using either the three-dimensional or axisymmetric wheelset model proposed in this work. Equivalently, the rail velocities are given by:

$$\mathbf{v}_R = \mathbf{Y}_R \mathbf{F}, \tag{34}$$

where the rail mobility matrix is defined analogously as the one for the wheel. Using the model discussed in Section 4.2, the components of $\mathbf{Y}_R$ are determined by applying a unit force and solving the generalized coordinates [20], and then evaluating Eq. (31) and its time derivative. Regarding the contact velocities, the following relation with the interaction forces is found:

$$\mathbf{v}_C = \begin{bmatrix} Y_{C,\text{I1-I1}} & 0 & Y_{C,\text{I1-I3}} & 0 & 0 & 0 \\ 0 & Y_{C,\text{I2-I2}} & Y_{C,\text{I2-I3}} & 0 & 0 & 0 \\ 0 & 0 & Y_{C,\text{I3-I3}} & 0 & 0 & 0 \\ 0 & 0 & 0 & Y_{C,\text{II1-II1}} & 0 & Y_{C,\text{II1-II3}} \\ 0 & 0 & 0 & 0 & Y_{C,\text{II2-II2}} & Y_{C,\text{II2-II3}} \\ 0 & 0 & 0 & 0 & 0 & Y_{C,\text{II3-II3}} \end{bmatrix} \mathbf{F} = \mathbf{Y}_C \mathbf{F}, \tag{35}$$

where the left and right contact zones are not coupled. Thus, hereafter the side subscripts I and II are omitted for simplicity. A Hertz contact spring is considered for the normal direction, in which the (linearised) mobility is given by [4, 28]:

$$Y_{C,3\text{-}3} = \mathrm{i}\omega \frac{\xi}{2} \left(\frac{2}{3E' F_3^0 r_e} \right)^{\frac{1}{3}}, \tag{36}$$

with $E' = \frac{E}{1-\nu^2}$ being the plane strain elastic modulus, E and ν the Young's modulus and Poisson's ratio, respectively, F_3^0 the steady-state (superscript 0) force normal to the contact, r_e the effective radius of curvature of the wheel/rail surfaces in contact, and ξ a parameter depending on the aspect ratio of the assumed contact patch ellipse. Further details on the last two parameters can be found in [4]. It is worth indicating that the mobility in Eq. (36) is linearised about the steady-state normal load obtained from the curve simulations conducted in the VI-Rail software [16]. In relation to the tangential directions, the model developed by Gross-Thebing [29] is utilised, which considers non-zero steady-state values of longitudinal, lateral, and spin creepages to evaluate the dynamic tangent forces at the contact. In the aforementioned work, the creepages are described as a superposition of a mean value (steady-state value) and a fluctuation around it:

$$\begin{aligned}\gamma_1 &= \gamma_1^0 + \Delta\gamma_1 = \frac{1}{V_v}\left(v_{C,1}^0 + \Delta v_{C,1}\right),\\ \gamma_2 &= \gamma_2^0 + \Delta\gamma_2 = \frac{1}{V_v}\left(v_{C,2}^0 + \Delta v_{C,2}\right),\\ w_3 &= w_3^0 + \Delta w_3 = \frac{1}{V_v}\left(\omega_{C,3}^0 + \Delta\omega_{C,3}\right),\end{aligned} \tag{37}$$

where γ_1, γ_2, and w_3 are the longitudinal, lateral, and spin creepages, respectively, V_v is the vehicle speed, $\omega_{C,3}$ is the relative rotational speed between the wheel and rail contact points around the normal axis to the contact patch, subscript 0 represents the mean value and Δ denotes the increment around the previous value. Considering only linearised effects, the creep forces are related to the creepages as follows [29]:

$$\begin{aligned}F_1 &= F_1^0 + Gab\widehat{C}_{11}\Delta\gamma_1,\\ F_2 &= F_2^0 + Gab\left(\widehat{C}_{22}\Delta\gamma_2 + \sqrt{ab}\widehat{C}_{23}\Delta w_3\right),\\ M_3 &= M_3^0 + Gab\left(\sqrt{ab}\widehat{C}_{32}\Delta\gamma_2 + ab\widehat{C}_{33}\Delta w_3\right),\end{aligned} \tag{38}$$

with G being the shear modulus, a and b the longitudinal (running direction) and lateral semi-axis lengths of the assumed contact patch ellipse, respectively, $\widehat{C}_{jk}$ the complex creep coefficients developed by Gross-Thebing [29], which depend on the frequency and steady-state values of the creepages, and M_3 the creep torque around the normal direction. As proposed by Thompson [30,31], the normal load F_3 influences the contact patch size and, in this case, also the complex creep coefficients and steady-state creep forces. Taking increments in Eq. (38) and neglecting the products of small quantities, the following equations are obtained:

$$\begin{aligned}\Delta F_1 &= \Delta F_1^0 + \frac{G}{V_v}a^0b^0\widehat{C}_{11}^0\Delta v_{C,1},\\ \Delta F_2 &= \Delta F_2^0 + \frac{G}{V_v}a^0b^0\left(\widehat{C}_{22}^0\Delta v_{C,2} + \sqrt{a^0b^0}\widehat{C}_{23}^0\Delta\omega_{C,3}\right),\\ \Delta M_3 &= \Delta M_3^0 + \frac{G}{V_v}a^0b^0\left(\sqrt{a^0b^0}\widehat{C}_{32}^0\Delta v_{C,2} + a^0b^0\widehat{C}_{33}^0\Delta\omega_{C,3}\right).\end{aligned} \tag{39}$$

Since the steady-state creep forces are dependent on the contact patch semi-axis lengths as well as the normal load [32], their increments can be expressed as follows:

$$\Delta F_k^0 = \frac{\partial F_k^0}{\partial a}\Delta a + \frac{\partial F_k^0}{\partial b}\Delta b + \frac{\partial F_k^0}{\partial F_3}\Delta F_3, \quad k = 1,2,6, \quad F_6^0 = M_3^0, \tag{40}$$

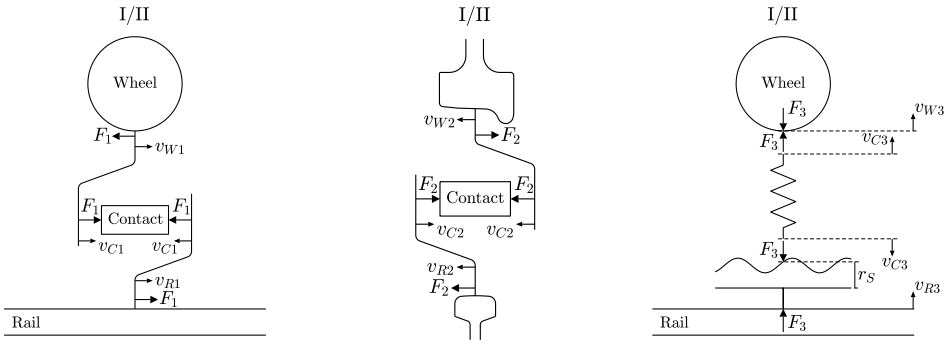

Fig. 3: Diagram of the wheel/rail interaction model. (a) Longitudinal direction. (b) Lateral direction. (c) Vertical direction.

in which subscript 6 makes reference to the rotational speed and torque around the direction 3 (normal to the contact patch, i.e. spin). The semi-axis lengths of the contact patch are given by [4]:

$$\begin{aligned} a &= \sigma_1 \left(\frac{3F_3 r_e}{2E'} \right)^{\frac{1}{3}}, \\ b &= \sigma_2 \left(\frac{3F_3 r_e}{2E'} \right)^{\frac{1}{3}}, \end{aligned} \tag{41}$$

where σ_1 and σ_2 are parameters depending on the aspect ratio of the contact patch ellipse (the corresponding expressions can be found in [4]). Therefore, the increments of these lengths can be evaluated as follows:

$$\begin{aligned} \Delta a &= \frac{\partial a}{\partial F_3} \Delta F_3 = \frac{a}{3F_3} \Delta F_3, \\ \Delta b &= \frac{\partial b}{\partial F_3} \Delta F_3 = \frac{b}{3F_3} \Delta F_3. \end{aligned} \tag{42}$$

Introducing Eqs. (42) and (40) into Eq. (39), the increments of the contact relative velocities are related to those of the creep forces by:

$$\begin{aligned}
\frac{G}{V_v}a^0b^0\widehat{C}^0_{11}\Delta v_{C,1} &= \Delta F_1 - T_1\Delta F_3,\\
\frac{G}{V_v}a^0b^0\widehat{C}^0_{22}\Delta v_{C,2} + \frac{G}{V_v}(a^0b^0)^{\frac{3}{2}}\widehat{C}^0_{23}\Delta\omega_{C,3} &= \Delta F_2 - T_2\Delta F_3,\\
\frac{G}{V_v}(a^0b^0)^{\frac{3}{2}}\widehat{C}^0_{32}\Delta v_{C,2} + \frac{G}{V_v}(a^0b^0)^{2}\widehat{C}^0_{33}\Delta\omega_{C,3} &= \Delta M_3 - T_6\Delta F_3,
\end{aligned} \tag{43}$$

where the variables T_k are given by:

$$T_k = \frac{\partial F^0_k}{\partial a}\frac{a}{3F_3} + \frac{\partial F^0_k}{\partial b}\frac{b}{3F_3} + \frac{\partial F^0_k}{\partial F_3}, \quad k = 1, 2, 6, \quad F^0_6 = M^0_3, \tag{44}$$

with the partial derivatives of the steady-state forces being, in this work, evaluated numerically using the FASTSIM algorithm developed by Kalker [33] and linearised around the steady-state values. Solving the system in Eq. (43), the contact relative velocities can be expressed as follows:

$$\begin{aligned}
\begin{pmatrix}\Delta v_{C,1}\\ \Delta v_{C,2}\\ \Delta\omega_{C,3}\end{pmatrix} &= \begin{bmatrix}
\frac{V_v}{Ga^0b^0\widehat{C}^0_{11}} & 0 & -\frac{V_vT_1}{Ga^0b^0\widehat{C}^0_{11}} & 0\\
0 & \frac{V_v\widehat{C}^0_{33}}{Ga^0b^0S_1} & \frac{V_v\left(\widehat{C}^0_{23}T_6 - \sqrt{a^0b^0}\widehat{C}^0_{33}T_2\right)}{G\left(a^0b^0\right)^{\frac{3}{2}}S_1} & -\frac{V_v\widehat{C}^0_{23}}{G\left(a^0b^0\right)^{\frac{3}{2}}S_1}\\
0 & -\frac{V_v\widehat{C}^0_{32}}{G\left(a^0b^0\right)^{\frac{3}{2}}S_1} & -\frac{V_v\left(\widehat{C}^0_{22}T_6 - \sqrt{a^0b^0}\widehat{C}^0_{32}T_2\right)}{G\left(a^0b^0\right)^{2}S_1} & \frac{V_v\widehat{C}^0_{22}}{G\left(a^0b^0\right)^{2}S_1}
\end{bmatrix}\begin{pmatrix}\Delta F_1\\ \Delta F_2\\ \Delta F_3\\ \Delta M_3\end{pmatrix}\\
&= \begin{bmatrix}
Y_{C,1\text{-}1} & 0 & Y_{C,1\text{-}3} & 0\\
0 & Y_{C,2\text{-}2} & Y_{C,2\text{-}3} & Y_{C,2\text{-}6}\\
0 & Y_{C,6\text{-}2} & Y_{C,6\text{-}3} & Y_{C,6\text{-}6}
\end{bmatrix}\begin{pmatrix}\Delta F_1\\ \Delta F_2\\ \Delta F_3\\ \Delta M_3\end{pmatrix},
\end{aligned} \tag{45}$$

where $S_1 = \widehat{C}^0_{22}\widehat{C}^0_{33} - \widehat{C}^0_{23}\widehat{C}^0_{32}$. Eq. (45) defines the mobilities $Y_{C,1\text{-}1}$, $Y_{C,1\text{-}3}$, $Y_{C,2\text{-}2}$, and $Y_{C,2\text{-}3}$ used in Eq. (35). The mobilities $Y_{C,2\text{-}6}$, $Y_{C,6\text{-}2}$, $Y_{C,6\text{-}3}$, and $Y_{C,6\text{-}6}$ are also defined in Eq. (45) although they are not used in this work as the coupling between the wheel and rail dynamic spin motion is not considered. Note that, as described by Thompson [30,31], the presence of steady-state creepage (or, equivalently, steady-state creep forces) induces a coupling between the normal and tangential directions, in which a harmonic normal load generates harmonic tangential vibration. The contact mobilities in the previous equation are linearised about the steady-state variables (subscript 0) obtained from the VI-Rail software curve simulations [16]. Finally, by introducing Eqs. (33), (34), and (35) into Eq. (32), the interaction forces are evaluated by solving the resultant system of equations, given by:

$$-\left(\mathbf{Y}_W + \mathbf{Y}_R + \mathbf{Y}_C\right)\mathbf{F} = \mathbf{r}\mathrm{i}\omega, \tag{46}$$

where the wheel and rail combined roughness is considered as an input.

So far, as it is represented in Fig. 3, the components of the wheelset, rail, and contact coordinate systems are considered to be parallel. When the vehicle runs on a curved track, the position of the wheel and rail contact point is displaced, often leading to a non-negligible contact angle. With this consideration, Fig. 4 shows the reference systems of the aforementioned three elements. In this work, the roll angle of the wheelset due to its lateral displacement is assumed to be negligible, so that the wheelset and track frame components are considered to be parallel. The contact reference system is defined rotating the track reference by the contact angle α. The angle γ has already been defined in Section 2 as the cant angle. As the components of the three reference systems are not parallel, Eq. (46) cannot be directly applied. Previously, the mobilities needed to be formulated in the same frame. In this work, the interaction is solved in the contact reference system. Therefore, both wheelset and rail mobilities need to be rotated by the contact angle as follows:

$$\begin{aligned}\mathbf{Y}_W^C &= \boldsymbol{\Xi}^{\mathrm{T}}\mathbf{Y}_W^W\boldsymbol{\Xi},\\ \mathbf{Y}_R^C &= \boldsymbol{\Xi}^{\mathrm{T}}\mathbf{Y}_R^R\boldsymbol{\Xi},\end{aligned} \tag{47}$$

where the notation for the mobilities has changed by adding a superscript that indicates the frame in which the variable is expressed. Note that $\mathbf{Y}_W^W$ and $\mathbf{Y}_R^R$ are the wheelset and rail mobilities as defined in Eqs. (33) and (34). The matrix $\boldsymbol{\Xi}$ is given by:

$$\boldsymbol{\Xi} = \begin{bmatrix} 1 & 0 & 0 & 0 & 0 & 0 \\ 0 & \cos(\alpha_{\mathrm{I}}) & -\sin(\alpha_{\mathrm{I}}) & 0 & 0 & 0 \\ 0 & \sin(\alpha_{\mathrm{I}}) & \cos(\alpha_{\mathrm{I}}) & 0 & 0 & 0 \\ 0 & 0 & 0 & 1 & 0 & 0 \\ 0 & 0 & 0 & 0 & \cos(\alpha_{\mathrm{II}}) & -\sin(\alpha_{\mathrm{II}}) \\ 0 & 0 & 0 & 0 & \sin(\alpha_{\mathrm{II}}) & \cos(\alpha_{\mathrm{II}}) \end{bmatrix}, \tag{48}$$

with α_{I} and α_{II} being the contact angle of the left and right sides, respectively. In order to determine the interaction forces, the matrices $\mathbf{Y}_W$ and $\mathbf{Y}_R$ in Eq. (46) are substituted by $\mathbf{Y}_W^C$ and $\mathbf{Y}_R^C$, respectively, and the resultant system is solved. Note that the contact mobilities do not need any rotation. The roughness vector $\mathbf{r}$ is also assumed to be expressed in the contact reference system, which means that roughness is only considered in the direction normal to the contact patch.

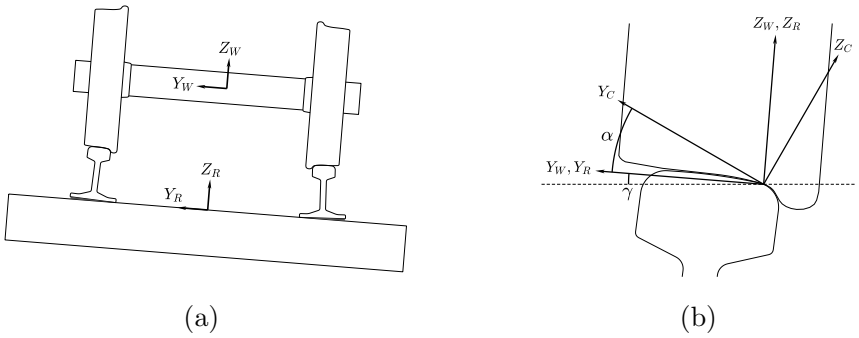

Fig. 4: (a) Diagram of wheelset and rails when running on a curved track along with their reference systems. (b) Zoom around one contact point and angles between the different reference systems.

As a result of this methodology, the interaction forces are also expressed in the contact frame.

The combined roughness acting at each wheel/rail contact is considered to be incoherent and so, given a wheelset running on the rails, the methodology to calculate the rolling noise is as follows:

1. The roughness on the right side is set to zero ($r_{S,\mathrm{II}} = 0$) and the interaction forces are obtained by solving Eq. (46). Then, the vibrational response to these is evaluated on the surfaces of both wheels, both rails, and sleepers. Subsequently, the rolling noise radiated by these elements is calculated.

2. The same procedure is repeated setting the left side roughness to zero ($r_{S,\mathrm{I}} = 0$), resulting in the noise radiated by the same elements as in the previous step, but with roughness being present on the other side.

3. The sound power radiated in both cases is added up, resulting in the noise emitted by the wheelset and track as a consequence of the roughness on both sides.

When considering a bogie instead of a single wheelset, two wheelsets are taken into account. In this case, the previous three points are independently applied to both wheelsets. The incoherence of the combined roughness, particularly that of the wheel surfaces, allows the radiated power from the elements to be added. In this work, the same approach is applied to the Manchester Benchmark vehicle [25], which consists of four wheelsets.

5 Results

Regarding the different dynamic simulations performed in this work, the following properties are considered:

- A track consisting of rails with UIC60 rail profile, with a gauge of 1435 mm, a rail inclination of 1:40, and a damping loss factor of 0.02 for the rails. The latter are supported by a spring–mass–spring system formed by the rail pad, sleeper, and ballast, the properties of which are converted to represent an equivalent continuously supported track assuming a sleeper span of 0.6 m. The rail pad has a stiffness of 715 MN/m in the vertical direction and 55 MN/m in the other two directions as well as a damping loss factor of 0.375. The sleeper has a mass of 244 kg, a length of 2500 mm in the lateral direction, a width of 250 mm in the longitudinal direction (running direction), and a height of 220 mm. The ballast has a stiffness of 70 MN/m in the vertical direction and 35 MN/m in the other two directions and a damping loss factor of 1.5.

- A wheelset with straight web wheels (see Fig. 2) and an approximate mass of 1050 kg. The wheels have a nominal diameter of 920 mm and a S1002 profile.

- A primary suspension connected to both ends of each wheelset with the same stiffness and damping as for the Manchester Benchmark vehicle [25]. Also, an axle box at each end of the wheelsets with a mass of 150 kg is included in the model.

- A wheel/rail combined roughness spectrum according to the standard EN13979-1 [34] for cast iron brake blocks (see Fig. 5(a)), which is assumed to exist only in the normal direction to the contact plane, as indicated in Section 4.3. Also, the contact filter proposed by Thompson [4], which corrects the effect of the roughness due to contact patch size (see Fig. 5(b)), is considered. In addition, a friction coefficient of 0.4 is taken into account for the wheel/rail interaction.

- The Manchester Benchmark vehicle running on a curved track. As a result, one car body with two bogies, and thus four wheelsets, is analysed.

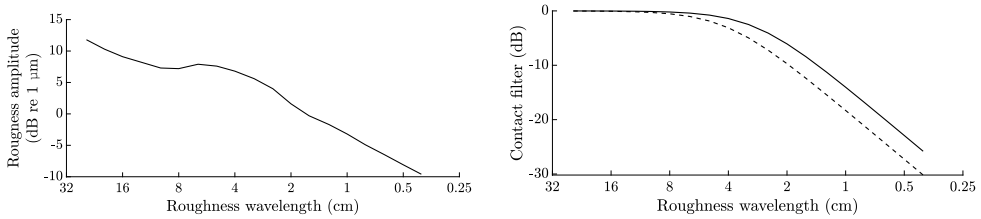

Fig. 5: (a) Roughness spectrum. (b) Contact filter for $a = 5$ mm (solid line) and $a = 7$ mm (dashed line).

5.1 Comparison of methodologies

The three-dimensional model presented in Section 2 is compared with the axisymmetric approach developed in Section 3. To do this, the Manchester Benchmark vehicle [25] is considered, running on a 300 m radius curve with 100 mm of superelevation and a speed of 75 km/h. The comparison concerns the frequency response function (FRF) in the radial-radial direction for the contact point of the outer wheel in the leading wheelset of the vehicle, as well as the sound power levels (SWL) of that wheelset due to the interaction of its wheels with the rails, evaluating it according to the method described in Section 4.3. As can be observed in the corresponding results depicted in Fig. 6, no significant differences are found between both approaches, whereas the computational performance of the axisymmetric approach is two orders of magnitude higher.

5.2 Influence of the curve on rolling noise

With the purpose of carrying out an analysis of the curve influence on the rolling noise, three curve circulation parameters are considered. These are the curve radius R_c, the non-compensated acceleration a_{nc}, and the superelevation h. The latter is related to the cant angle γ as $h = \sin(\gamma)(g_T + b_R)$, where g_T is the track gauge and b_R the rail head width. The influence of the aforementioned three variables on the noise is studied by means of a DoE, varying them within the bounds shown in Table 1. Since higher variability is expected around small values of the curve radius, and with the aim of developing a uniform DoE, the variable describing the radius is replaced by $l_R = \log_{10}(R_c)$.

For the DoE, a factorial design based on 10 values of each design parameter is performed, first simulating the steady-state contact variables in the VI-Rail

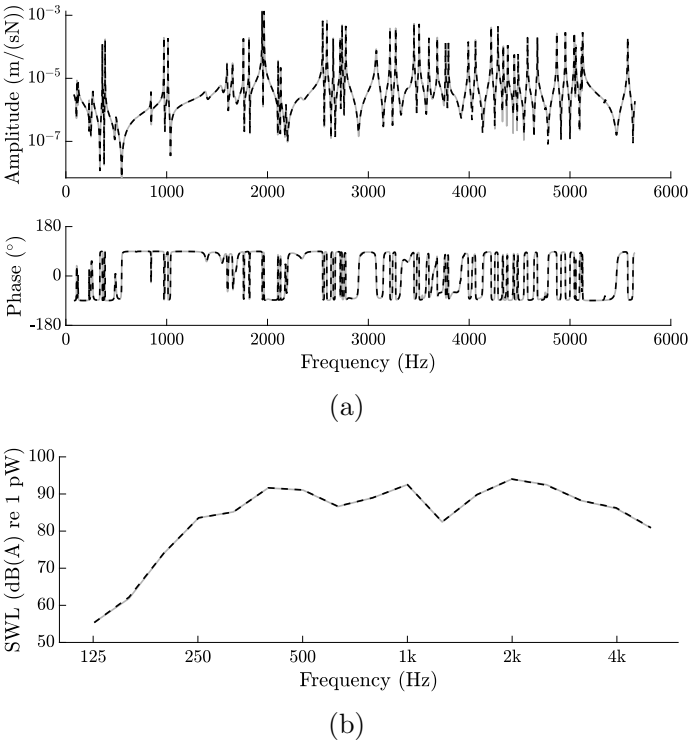

Fig. 6: Comparison of the three-dimensional (——) and axisymmetric (- - -) models for a vehicle speed of 75 km/h. (a) Radial-radial mobility at the contact point for the outer wheel of the leading wheelset. (b) Rolling noise radiated from this wheelset.

software [16] and subsequently evaluating the noise radiated by the wheelset, rail, and sleeper for each combination through the calculation methodology described in Section 4.3.

Note that the vehicle speed V_v is derived from the three curve design variables through the relation $V_v^2 \cos(\gamma) = R_c \left(a_{nc} + g \sin(\gamma)\right)$. This speed, in turn, determines the frequency content of the roughness. In order to reduce the influence of this factor on the results, the SWL in a curve is compared with that radiated if the vehicle were running on a tangent track at the same speed. Furthermore, to perform a detailed analysis, the radiation from each element (wheels, rails, and sleepers) is studied individually, as well as the total noise obtained by adding the three contributions. Therefore, the dependent variables are defined as follows:

$$\Delta L_{\Sigma,i} = L^c_{\Sigma,i} - L^t_{\Sigma,i}, \qquad i = W, R, S, T, \tag{49}$$

Table 1: Bounds of the curve circulation variables.

Design variable	Lower bound	Upper bound
R_c (m)	300	5500
a_{nc} (m/s^2)	0	1
h (mm)	30	120

where $L^c_{\Sigma,i}$ and $L^t_{\Sigma,i}$ are the overall SWL in a curved and tangent track, respectively, for the ith element. The subscripts W, R, S, and T stand for wheel, rail, sleeper, and total, respectively. The overall SWL is determined by adding the power in each one-third octave frequency band of the SWL after including the contact filter proposed by Thompson [4] as well as the A-weighting filter [35], therefore expressed in dB(A) respect to 1 pW. As indicated in Section 4.3, the sound levels correspond to the interaction of the four wheelsets of the Manchester Benchmark vehicle [25] with the track.

The dependent variable in terms of total noise $\Delta L_{\Sigma,T}$ is represented in Fig. 7 in a contour plot as a function of two of the design variables, while the third one is fixed at a constant value. The results correspond to an interpolation of the levels evaluated for the 10^3 simulations from the DoE within the ranges of the design variables. Higher variability is found with respect to the track curvature, whereas the non-compensated acceleration and, particularly, the superelevation explain much less variability of the total noise. The same is observed for the radiation of the individual elements. Interestingly, the position of the contact point of the leading wheelsets is mostly affected by the curve radius and not so much by the other two variables. As analysed later, the position of the contact point explains very well the variability of the SWL. Simplifying, the influence of the less important two variables (a_{nc} and h) can be summarised based on how they affect the vehicle speed. For this reason, it is more convenient to analyse the results of the DoE in terms of the influence on rolling noise of track curvature and vehicle speed.

The left column of Fig 8 shows the dependent variables as a function of the track curvature and vehicle speed for each element (wheel, rail, and sleeper) as well as the total component. Again, an interpolation of the noise calculated for the DoE cases is performed within the ranges of the variables. Although the SWL in a curve is compared with the corresponding one in a tangent track to reduce the influence of the roughness spectrum, this spectrum may actually be affecting

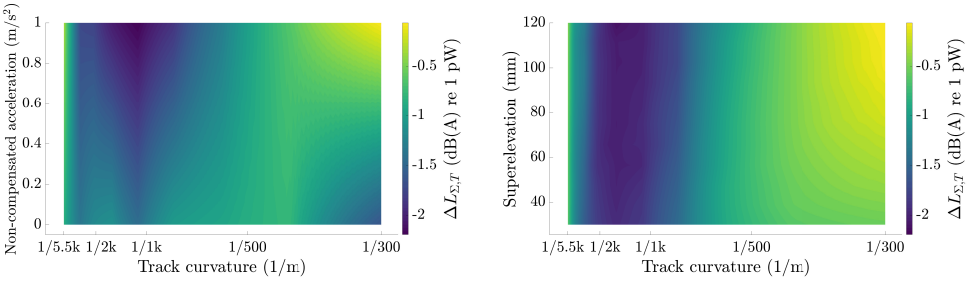

Fig. 7: Influence of the design variables on $\Delta L_{\Sigma,T}$. (a) Variations of l_R and a_{nc} with $h = 70$ mm. (b) Variations of l_R and h with $a_{nc} = 0.56$ m/s^2.

the interpretation of the results since it varies with frequency and its content is shifted to higher frequencies for increasing velocities, which may have a different effect on the SWL in a curve and in a tangent track. Additionally, the contact filter may also be influencing the analysis of the results since it also has a non-constant frequency distribution which depends on the vehicle speed and contact patch length along the running direction a. The latter is generally greater in a curve (for all the curve simulations, it is always higher for the high side interaction and almost always higher for the low side). As a consequence, for a given speed, the contact filter has more impact and reduces the SWL more in a curve than in a tangent track (see Fig. 5(b)). Thus, a raw analysis of the SWL without including the contact filter and assuming a constant roughness spectrum of 1 µm in each frequency band is performed and depicted in the right column of Fig. 8. This analysis, while not realistic, facilitates the understanding of the results.

The wheel noise component for the raw case, Fig. 8(b), generally increases with the track curvature. In the frequency range where the wheel radiation is the highest (above 1.5 kHz), the lateral component of the interaction forces (unit roughness and no contact filter) is found to increase significantly with the curvature when compared with the tangent case. The same curve-tangent comparison for the vertical component shows a parabolic trend, having positive differences around the extremes (low and high curvature) and negative values in between, although with much lower differences than for the lateral component. Nevertheless, the vertical-lateral coupling of the wheel increases when the contact point moves away from the centre of the tread; then, even for the same vertical force, the axial vibration (and noise radiation) is higher in a high curvature track than in a tangent one. Therefore, both lateral and vertical components of the interaction forces describe the behaviour of the variable $\Delta L_{\Sigma,W}$. When the contact

filter is included, the SWL for all cases decreases, the simulation cases with high track curvature and low vehicle speed being more penalised (these conditions lead to higher contact patch length along the running direction); however, when the roughness spectrum is considered, its effect on the SWL is not as evident as the contact filter. For the wheel case, the combined effect of these two elements, Fig. 8(a), yields a reduction of the levels for all cases, with slightly higher reductions for low curvatures.

Regarding the rail, when a constant spectrum of the roughness is assumed, its highest radiation appears in the same frequency range as the wheel. However, in contrast to the wheel, when considering a roughness spectrum with decreasing frequency content (see Fig. 5(a)), the rail highest radiation is shifted to lower frequencies (in the range of 500 Hz to 2 kHz). The rail noise component for the raw analysis, Fig. 8(d), follows a parabolic trend with the curvature explained by the vertical force component (described previously), since above 1.5 kHz the vertical vibration of the rail is, in acoustic radiation terms, more important than the lateral. When both the contact filter and standard roughness are considered, Fig. 8(c), the highest radiation from the rail is shifted to lower frequencies (as mentioned above). Within this frequency range, the differences in the interaction forces between curve and tangent track remain similar to the variations observed at higher frequencies. However, in this frequency range, the lateral vibration of the rail becomes influential. This lateral vibration is due, in general, to the lateral component of the force, which increases with the curvature, so the rail noise component $\Delta L_{\Sigma,R}$ also increases. Additionally, as the track curvature increases and the contact point moves away from the centre of the rail, the vertical-lateral coupling becomes larger and the vertical component of the force also contributes to the lateral vibration of the rail, similarly to the wheel case. Therefore, the combined effect of the contact filter and standard roughness, compared to the raw case, is mostly increasing the levels for medium and high curvatures, although it also decreases slightly the levels for low curvatures.

The sleeper noise component is governed by the vertical vibration of this element due to its higher radiation surface in such direction. Also, the vertical vibration is, for all the curve simulations, significantly higher than the lateral vibration since (1) the vertical forces are higher and (2) the rail pad stiffness is lower in the lateral direction. Therefore, the sleeper noise is mainly determined by the vertical forces. When attending to the raw analysis, Fig. 8(f), the sleeper noise component decreases with the track curvature. In the frequency range where the sleeper radiation is the highest (below 750 Hz), the vertical component of the interaction forces decreases with the curvature, explaining the trend in the acoustic levels. When including the contact filter and roughness spectrum, Fig.

8(e), all levels decrease, especially the ones associated with high curvatures and low velocities.

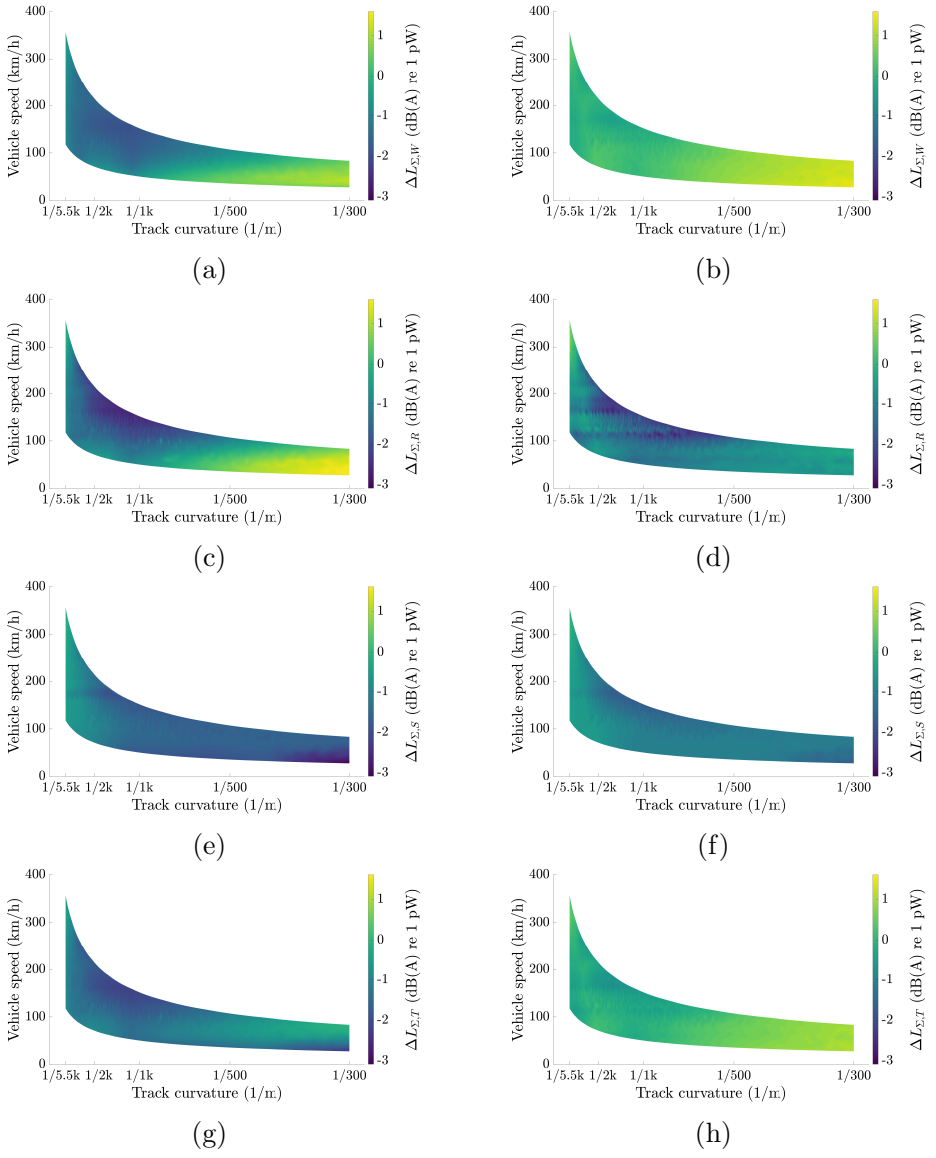

Fig. 8: Influence of the track curvature and vehicle speed on ΔL_Σ. Left column: considering standard roughness and contact filter. Right column: considering unit roughness and without contact filter. First row: wheel. Second row: rail. Third row: sleeper. Fourth row: total.

With respect to the total component, this is the combination of the three railway elements. Since the sleeper component has an opposite trend to the wheel and rail components, the total noise follows a parabolic trend with the curvature. While for the raw analysis, Fig. 8(h), approximately half of the cases have a positive $\Delta L_{\Sigma,T}$, mainly distributed around high and low curvatures, for the analysis including the contact filter and roughness spectrum, Fig. 8(g), the total noise radiation in a curve is always smaller than in a tangent track. This is due to the fact that for high curvatures, associated with low velocities, the roughness spectrum is concentrated in the frequency range where the sleeper dominates the noise emission. Since the sleeper radiates less in a curve than in a tangent track, a similar behaviour is found for the total component. However, this might differ when considering a different roughness spectrum or properties of the track (and wheelset), which can reduce the contribution of the sleeper to the total noise and increase that from the rail (as, for example, lower rail pad stiffness). The investigation into the combined effect of these properties and the curving behaviour on rolling noise is highlighted as a potential area for future research.

Regarding the analyses presented in Fig. 8, the SWL corresponds to the full vehicle (four wheelsets and their interaction with the track). However, due to the different steady-state lateral displacement and angle of attack of each wheelset, different behaviours are observed among them. To study this, the dependent variable ΔL_{Σ} is evaluated for each single wheelset and its interaction with the track. With the purpose of showing a clearer picture of the influence of the track curvature, the results corresponding to simulations with the same curve radius but different values of the other two design variables are averaged and depicted in Fig. 9. Therefore, each marker represents the average of the results from 100 curve simulations, although the variability among them is known to be small in comparison with the variability with respect to the curvature. The wheelsets are arranged in order from the front to the back, with the leading wheelset of the first bogie identified as 1 and the trailing wheelset of the second bogie as 4. Also, the sound levels associated with the full vehicle are shown in the figure. These are obtained by averaging the results shown in Fig. 8 over the vehicle speed. In general terms, the leading wheelsets exhibit similar behaviour, as do the trailing wheelsets. The former experience higher lateral displacement when running on a curve, therefore the curve-tangent differences being greater for them. The full vehicle curve generally follows the trends found for the leading wheelsets but with lower differences due to the smaller levels of the trailing wheelsets. It is noticeable that, even for large radius (up to 5 km), the curve is still influential on the rolling noise radiation, especially in the the case with standard roughness spectrum and contact filter.

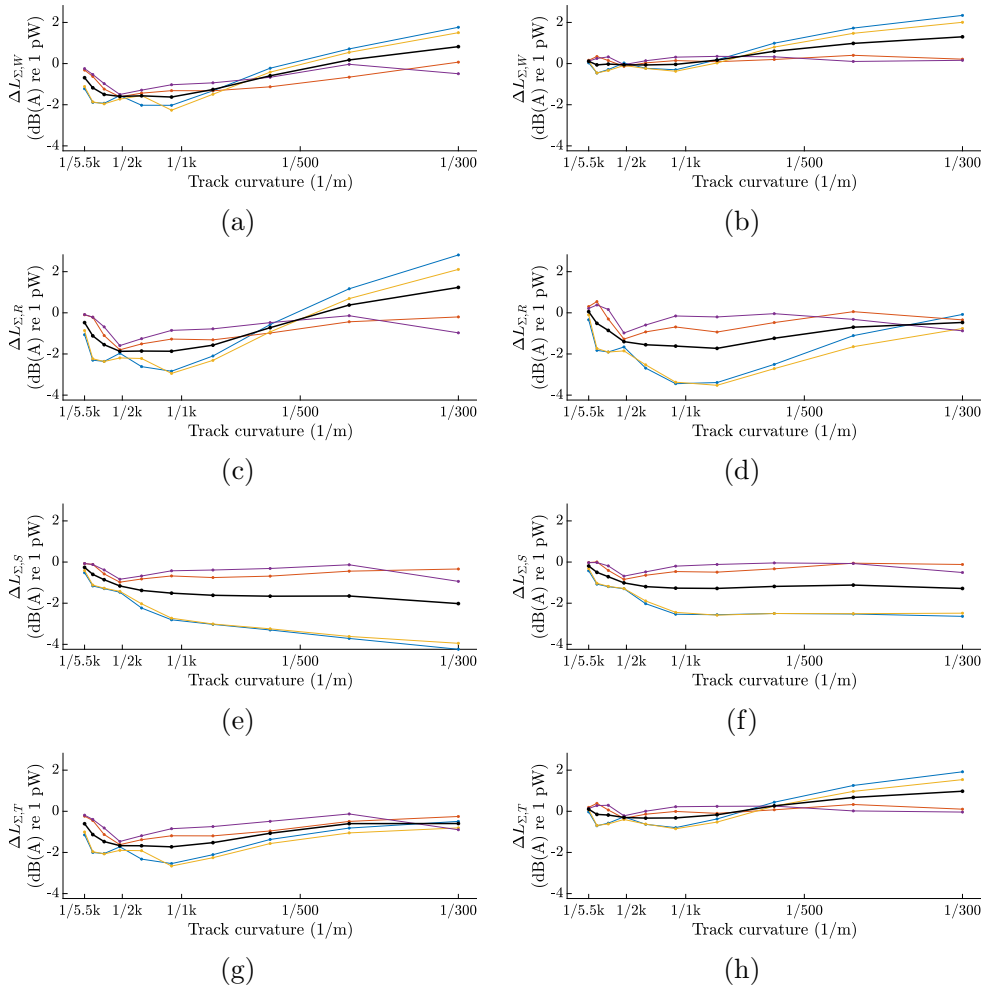

Fig. 9: Influence of the track curvature on ΔL_Σ evaluated for the first (blue), second (orange), third (yellow), and fourth (purple) wheelset and its interaction with the track, as well as the full vehicle (black). Left column: considering standard roughness and contact filter. Right column: considering unit roughness and without contact filter. First row: wheel. Second row: rail. Third row: sleeper. Fourth row: total.

The explanations given above about the trends found in Fig. 8 can be applied as well to the individual wheelsets, Fig. 9, bearing in mind that they have different lateral displacement for the same curve radius. Actually, the radiated noise in a curve, compared with the one in a tangent track, is mainly dependent on the

displacement of the contact point with respect to the nominal position. Fig. 10 depicts the dependent variables ΔL_Σ evaluated for each single wheelset and its interaction with the track as a function of the lateral displacement of the contact point of the wheel with respect to its nominal position. A positive lateral displacement is defined as a movement away from the wheel flange. The results are divided into two groups: levels corresponding to the case with roughness applied on the high rail and those corresponding to the case with roughness applied on the low rail (see the calculation methodology described in Section 4.3). The levels in the first group are represented by black markers and the ones in the second by grey markers. For each group, the independent variable is the lateral displacement of the contact point of the wheel in the side with roughness applied. Although there are interaction forces in the side without roughness, those are significantly less important for the vibration of the railway elements. As in previous analyses, the raw case and the case with standard roughness and contact filter are considered. In both studies, the observed behaviours in the noise of the different railway elements align with the explanations relating to Fig. 8. For the raw case, right column of Fig. 10, the markers follow a smoother trend. When the standard roughness and contact filter are considered, left column of Fig. 10, there is a higher dispersion due to their effect. In particular, they affect differently the groups with roughness applied in the left and right sides, due to differences between them in the vehicle speed. Around the value -8.5 mm for the lateral displacement of the wheel contact point, there is an abrupt change in the dependent variables. Such displacement for the wheel contact corresponds to a displacement of approximately -10 mm for the rail contact point (see Fig. 11), where the UIC60 rail profile changes from a transverse radius of 300 mm to 80 mm. This affects the contact normal mobility, Eq. (36), and thus the interaction forces. Regarding the dependent values, a drop in that area of, approximately, 2 dB(A), 2.5 dB(A), 1.5 dB(A), and 2 dB(A) is observed for the wheel, rail, sleeper, and total component, respectively.

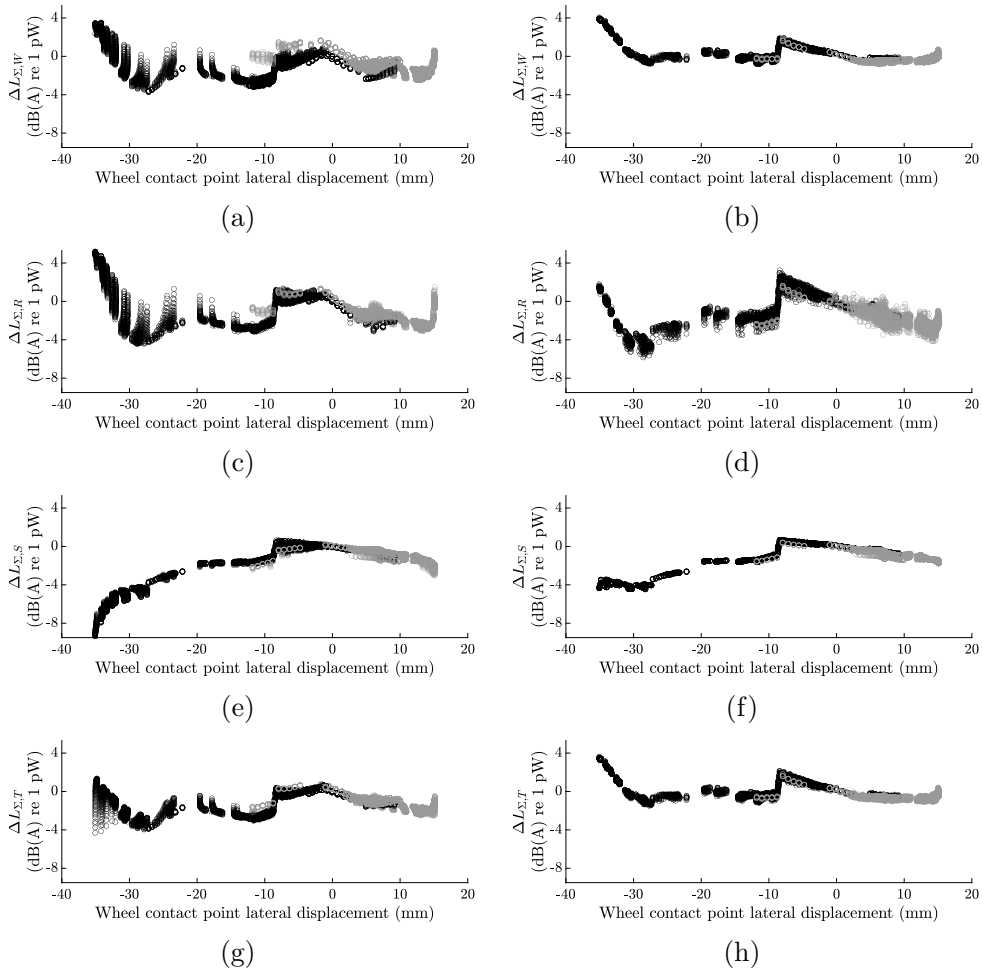

Fig. 10: Influence of the lateral displacement of the wheel contact point on ΔL_Σ evaluated for each wheelset in the vehicle and its interaction with the track. Black markers indicate roughness only in the high side and grey markers roughness only in the low side. Left column: considering standard roughness and contact filter. Right column: considering unit roughness and without contact filter. First row: wheel. Second row: rail. Third row: sleeper. Fourth row: total.

Even though the representations in Fig. 10 only consider the contact point displacement of the wheel, this is uniquely related to the contact point displacement of the rail, as shown in Fig. 11, where the relation is evaluated for each wheel/rail pair. For the rail, as for the wheel, a positive displacement of the contact point is

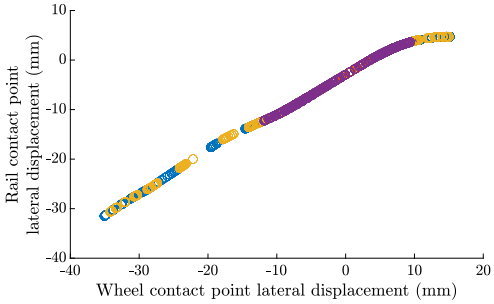

Fig. 11: Lateral displacement of the rail and wheel contact points for the interaction of the first (blue), second (orange), third (yellow), and fourth (purple) wheelset of the vehicle with the track.

defined as a movement outwards from the track centre line. Here, pairs on both the high and low side are represented without any colour distinction. Nevertheless, different colours are used for different wheelsets. In the trailing wheelsets of both bogies, the contact points experience smaller displacements, resulting in generally less variation in the noise between curve and tangent track (see Fig. 10), as also illustrated in Fig. 9. The opposite happens with the leading wheelsets, which exhibit higher noise differences and thus govern the trends found for the full vehicle. Since the curve radius is the variable that most influences the position of the contact point of the wheel/rail pairs in the leading wheelsets, this variable is also the most important one in noise radiation terms.

In the same way that each wheelset contributes differently to the rolling noise in a curved track, so does each wheel of the same wheelset (and associated track). The dependent value for the wheel $\Delta L_{\Sigma,W}$ is evaluated for particular wheels and represented against the track curvature in Fig. 12. As before, the results for different values of non-compensated acceleration and superelevation but the same curve radius are averaged. Here, for simplicity, only the case with standard roughness and contact filter is studied, since their effect is already known. The outer wheels of the leading wheelsets exhibit higher sound levels for low radius curves (about 2 dB(A) more than the other wheels). This is coherent with the previous analyses, as the contact point of these wheels is the one that exhibits larger lateral displacement when running on a curve (see Figs. 11 and 10). The difference in the radiation among the wheels may impact acoustic pressure measurements depending on the position of the microphones.

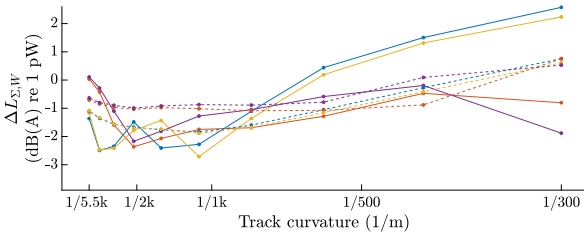

Fig. 12: Influence of track curvature on $\Delta L_{\Sigma,W}$ evaluated for individual wheels in the first (blue), second (orange), third (yellow), and fourth (purple) wheelset of the vehicle. Solid line indicates outer wheels and dashed line inner wheels.

6 Conclusions

In this study, a dynamic model of a flexible wheelset is proposed to evaluate the rolling noise radiation when operating on curved tracks. Two formulations are considered, both of them valid for any rotating structure with axial symmetry describing a generic trajectory (in particular, a curve of constant radius). On the one hand, a full three-dimensional numerical approach based on the FEM and, on the other, an axisymmetric model combining a FE approach for the wheelset cross-section and an analytical expansion of the response along the circumferential direction. In both cases, an Eulerian formulation is adopted to consider the inertial effects associated with the rotation and curved trajectory. It is shown that the results of both approaches present an excellent agreement, the axisymmetric one exhibiting significantly better computational performance.

To evaluate the rolling noise generation in curves, the dynamic behaviour of the track and wheelset is assessed relative to the vehicle steady-state position in the curve. The latter is determined through the commercial software VI-Rail, considering the Manchester Benchmark vehicle. The wheelset is then dynamically coupled with the track through the wheel/rail interaction of both sides. The contact is modelled in the frequency domain considering a linearised Hertz contact spring for the normal direction, while the creep forces in the tangential directions are calculated considering their dynamic nature as well as non-zero steady-state values of the longitudinal, lateral, and spin creepages. Once the interaction forces are solved, the vibroacoustic behaviour of the wheelsets, rails, and sleepers is determined.

Additionally, the study investigates the effect of the curve on rolling noise radiation. A parametric analysis is conducted by considering three design variables: curve radius, non-compensated acceleration, and superelevation. A DoE is proposed, which varies these variables within predefined ranges simulating several curve conditions. On these, the noise calculation methodology is performed to evaluate the radiated noise in a curve. This is compared with the results associated with a tangent track, assuming the same vehicle speed.

The analysis reveals that the curve radius is the most influential parameter on the dependent variable (noise difference between a curved and tangent track), due to its influence on the position of the wheel/rail contact point. In general terms, the wheels and rails radiate more noise in a curve than on a tangent track for high curvatures (curve radius below 500 m), but the opposite is found for lower curvatures. Regarding the sleeper, this radiates less noise in a curve. Then, the trend observed for the total noise (sum of wheel, rail, and sleeper contributions) is a combination of different behaviours for the elements, resulting in less radiation in a curve than in a tangent track. However, this might depend on the roughness spectrum considered for the wheel and rail surfaces as well as the properties of the wheelset and track. Another influential factor is the contact filter, which normally affects more the noise in a curve due to the greater length of the contact patch in the running direction in curve conditions. To provide a deeper physical insight, computations without contact filter have been carried out for a constant roughness spectrum, showing that the rolling noise radiation in a curved track is generally higher. Although this is not a realistic scenario, it helps to understand the results.

Differences among the four wheelsets of the vehicle, and their interaction with the track, are found in terms of rolling noise radiation in a curve. However, the analysis is simplified when looking at the steady-state contact point position of the wheel (and rail). A strong relation between this and the radiated noise is found, which explains the general trends of the noise from the vehicle running on a curve compared with a tangent track. Moreover, among the wheels in the vehicle, some of them exhibit significantly higher noise levels on curves than others, which may have implications for the location of microphones when acoustic pressure measurements are conducted in curved track segments.

Acknowledgements

This paper is part of the project PID2020-112886RA-I00, project PID2023-148483OB-I00, grant FPU18/03999, and grant EST22/00353 funded by MCIN/AEI/10.13039/501100011033 as well as by "ESF Investing in your future". The authors also acknowledge Programa PROMETEO/2021/046 of Generalitat Valenciana.

Appendix A. Matrices and matrix operators

From Eq. (10), the matrix $\mathbf{J}$ is given by:

$$\mathbf{J} = \begin{bmatrix} 0 & -1 & 0 \\ 1 & 0 & 0 \\ 0 & 0 & 0 \end{bmatrix}. \tag{A.1}$$

The matrices $\mathbf{J}_i$ in Eqs. (15), (21), (23) and (B.2–B.6) are sparse and thus they are defined in this appendix through their non-zero elements as follows:

$$\begin{aligned} &\mathbf{J}_1 \ \{\text{size } 3 \times (3+6m)\}: \\ &(1,7) = 1, \ \ (1,8) = 1, \ \ (2,2) = 2, \ \ (3,4) = -1, \ \ (3,5) = 1, \end{aligned} \tag{A.2}$$

$$\begin{aligned} &\mathbf{J}_2 \ \{\text{size } 3 \times 1\}: \\ &(2,1) = 2z, \end{aligned} \tag{A.3}$$

$$\begin{aligned} &\mathbf{J}_3 = \sum_{i=1}^{3}\sum_{j=i}^{3} \omega_{ij}^2 \frac{\partial \mathbf{J}_3}{\partial \omega_{ij}^2} \ \{\text{size } (3+6m) \times 1\}: \\ &\frac{\partial \mathbf{J}_3}{\partial \omega_{11}^2}: \ \ (1,1) = r, \ \ (10,1) = -\frac{r}{2}, \ \ (11,1) = \frac{r}{2}, \\ &\frac{\partial \mathbf{J}_3}{\partial \omega_{22}^2}: \ \ (2,1) = 2z, \\ &\frac{\partial \mathbf{J}_3}{\partial \omega_{33}^2}: \ \ (1,1) = r, \ \ (10,1) = \frac{r}{2}, \ \ (11,1) = -\frac{r}{2}, \\ &\frac{\partial \mathbf{J}_3}{\partial \omega_{12}^2}: \ \ (7,1) = z, \ \ (8,1) = z, \ \ (9,1) = r, \\ &\frac{\partial \mathbf{J}_3}{\partial \omega_{23}^2}: \ \ (4,1) = -z, \ \ (5,1) = z, \ \ (6,1) = -r, \\ &\frac{\partial \mathbf{J}_3}{\partial \omega_{13}^2}: \ \ (13,1) = -r, \ \ (14,1) = -r, \end{aligned} \tag{A.4}$$

$$
\begin{aligned}
&\mathbf{J}_4 = \sum_{i=1}^{3}\sum_{j=i}^{3} \omega_{ij}^2 \frac{\partial \mathbf{J}_4}{\partial \omega_{ij}^2} \ \{\text{size } (3+6m)\times(3+6m)\}: \\
&\frac{\partial \mathbf{J}_4}{\partial \omega_{11}^2}: \ (1,)=1, \ \ (3,)=1, \ \ (4,)=\frac{1}{4}, \ \ (5,)=\frac{1}{4}, \ \ (7,)=\frac{3}{4}, \ \ (8,)=\frac{3}{4}, \\
&\qquad (1,10)=-1, \ \ (1,11)=1, \ \ (3,13)=1, \ \ (3,14)=1, \ \ (4,5)=\frac{1}{2}, \ \ (7,8)=\frac{1}{2}, \\
&\qquad \Big[\Big[(6n-3+k,)=\frac{1}{2}\Big]_{k=1,2,4,5}\Big]_{n=2}^{m}, \ \ \Big[\Big[\Big[(6n-j,6n+9+k)=\frac{(-1)^k}{2}, \\
&\qquad (6n+j,6n+12+k)=\frac{(-1)^j}{2}\Big]_{j=1,2}\Big]_{k=1,2}\Big]_{n=1}^{m-2} \\
&\frac{\partial \mathbf{J}_4}{\partial \omega_{22}^2}: \ \ (2,)=2, \ \ \Big[(6n,)=1, \ \ (6n+3,)=1\Big]_{n=1}^{m}, \\
&\frac{\partial \mathbf{J}_4}{\partial \omega_{33}^2}: \ (1,)=1, \ \ (3,)=1, \ \ (4,)=\frac{3}{4}, \ \ (5,)=\frac{3}{4}, \ \ (7,)=\frac{1}{4}, \ \ (8,)=\frac{1}{4}, \ \ (1,10)=1, \\
&\qquad (1,11)=-1, \ \ (3,13)=-1, \ \ (3,14)=-1, \ \ (4,5)=-\frac{1}{2}, \ \ (7,8)=-\frac{1}{2}, \\
&\qquad \Big[\Big[(6n-3+k,)=\frac{1}{2}\Big]_{k=1,2,4,5}\Big]_{n=2}^{m}, \ \ \Big[\Big[\Big[(6n-j,6n+9+k)=-\frac{(-1)^k}{2}, \\
&\qquad (6n+j,6n+12+k)=-\frac{(-1)^j}{2}\Big]_{j=1,2}\Big]_{k=1,2}\Big]_{n=1}^{m-2}, \\
&\frac{\partial \mathbf{J}_4}{\partial \omega_{12}^2}: \ (1,9)=2, \ \ (2,7)=2, \ \ (2,8)=2, \ \ (3,6)=2, \ \ \Big[(6n-2,6n+9)=1, \\
&\qquad (6n-1,6n+9)=1, \ \ (6n,6n+7)=1, \ \ (6n,6n+8)=1, \\
&\qquad (6n+1,6n+6)=-1, \ \ (6n+2,6n+6)=1, \ \ (6n+3,6n+4)=-1, \\
&\qquad (6n+3,6n+5)=1\Big]_{n=1}^{m-1}, \\
&\frac{\partial \mathbf{J}_4}{\partial \omega_{23}^2}: \ (1,6)=-2, \ \ (2,4)=-2, \ \ (2,5)=2, \ \ (3,9)=2, \\
&\qquad \Big[(6n-2,6n+6)=-1, \ \ (6n-1,6n+6)=-1, \ \ (6n,6n+4)=-1, \\
&\qquad (6n,6n+5)=1, \ \ (6n+1,6n+9)=1, \ \ (6n+2,6n+9)=1, \\
&\qquad (6n+3,6n+7)=-1, \ \ (6n+3,6n+8)=-1\Big]_{n=1}^{m-1}, \\
&\frac{\partial \mathbf{J}_4}{\partial \omega_{13}^2}: \ (1,13)=-2, \ \ (1,14)=-2, \ \ (3,10)=-2, \ \ (3,11)=2, \ \ (4,7)=-1, \\
&\qquad (4,8)=-1, \ \ (5,7)=1, \ \ (5,8)=1, \ \ \Big[(6n-2,6n+13)=-1, \\
&\qquad (6n-2,6n+14)=-1, \ \ (6n-1,6n+13)=-1, \ \ (6n-1,6n+14)=-1, \\
&\qquad (6n+1,6n+10)=1, \ \ (6n+1,6n+11)=-1, \ \ (6n+2,6n+10)=-1, \\
&\qquad (6n+2,6n+11)=1\Big]_{n=1}^{m-2},
\end{aligned}
\tag{A.5}
$$

$$
\begin{aligned}
&\mathbf{J}_5 = \sum_{i=1} \omega_i \frac{\partial \mathbf{J}_5}{\partial \omega_i} \ \{\text{size } (3+6m)\times 1\}: \\
&\frac{\partial \mathbf{J}_5}{\partial \omega_1}: \ (4,1) = -z, \ \ (5,1) = z, \ \ (6,1) = r, \\
&\frac{\partial \mathbf{J}_5}{\partial \omega_2}: \ (3,1) = -2r, \\
&\frac{\partial \mathbf{J}_5}{\partial \omega_3}: \ (7,1) = -z, \ \ (8,1) = -z, \ \ (9,1) = r,
\end{aligned}
\tag{A.6}
$$

$$
\begin{aligned}
&\mathbf{J}_6 = \sum_{i=1} \omega_i \frac{\partial \mathbf{J}_6}{\partial \omega_i} \ \{\text{size } (3+6m)\times 1\}: \\
&\frac{\partial \mathbf{J}_6}{\partial \omega_1}: \ (9,1) = -2r, \\
&\frac{\partial \mathbf{J}_6}{\partial \omega_2}: \ (1,1) = 4r, \\
&\frac{\partial \mathbf{J}_6}{\partial \omega_3}: \ (6,1) = 2r,
\end{aligned}
\tag{A.7}
$$

$$
\begin{aligned}
&\mathbf{J}_7 = \sum_{i=1} \omega_i \frac{\partial \mathbf{J}_7}{\partial \omega_i} \ \{\text{size } (3+6m)\times (3+6m)\}(\text{antisymmetric}): \\
&\frac{\partial \mathbf{J}_7}{\partial \omega_1}: \ (1,6) = 1, \ \ (2,4) = -1, \ \ (2,5) = 1, \ \ (3,9) = -1, \ \ \Big[(6n-2,6n+6) = \frac{1}{2}, \\
&\qquad (6n-1,6n+6) = \frac{1}{2}, \ \ (6n,6n+4) = -\frac{1}{2}, \ \ (6n,6n+5) = \frac{1}{2}, \\
&\qquad (6n+1,6n+9) = \frac{1}{2}, \ \ (6n+2,6n+9) = -\frac{1}{2}, \ \ (6n+3,6n+7) = -\frac{1}{2}, \\
&\qquad (6n+3,6n+8) = -\frac{1}{2}, \Big]_{n=1}^{m-1}, \\
&\frac{\partial \mathbf{J}_7}{\partial \omega_2}: \ (1,3) = -2, \ \ (4,8) = -1, \ \ (5,7) = 1, \\
&\qquad \Big[(6n-2,6n+2) = -1, \ \ (6n-1,6n+1) = 1\Big]_{n=2}^{m}, \\
&\frac{\partial \mathbf{J}_7}{\partial \omega_3}: \ (1,9) = 1, \ \ (2,7) = -1, \ \ (2,8) = -1, \ \ (3,6) = 1, \ \ \Big[(6n-2,6n+9) = \frac{1}{2}, \\
&\qquad (6n-1,6n+9) = \frac{1}{2}, \ \ (6n,6n+7) = -\frac{1}{2}, \ \ (6n,6n+8) = -\frac{1}{2}, \\
&\qquad (6n+1,6n+6) = -\frac{1}{2}, \ \ (6n+2,6n+6) = \frac{1}{2}, \ \ (6n+3,6n+4) = \frac{1}{2}, \\
&\qquad (6n+3,6n+5) = -\frac{1}{2}\Big]_{n=1}^{m-1},
\end{aligned}
\tag{A.8}
$$

$$
\begin{aligned}
&\mathbf{J}_8 = \sum_{i=1} \omega_i \frac{\partial \mathbf{J}_8}{\partial \omega_i} \ \{\text{size } (3+6m)\times(3+6m)\}: \\
&\frac{\partial \mathbf{J}_8}{\partial \omega_1}: \ (1,9) = -2, \ \ (3,6) = -2, \ \ \Big[(6n-2, 6n+9) = -(n+1), \\
&\qquad (6n-1, 6n+9) = -(n+1), \ \ (6n, 6n+7) = n, \ \ (6n, 6n+8) = n, \\
&\qquad (6n+1, 6n+6) = n+1, \ \ (6n+2, 6n+6) = -(n+1), \\
&\qquad (6n+3, 6n+4) = -n, \ \ (6n+3, 6n+5) = n\Big]_{n=1}^{m-1}, \\
&\frac{\partial \mathbf{J}_8}{\partial \omega_2}: \ (1,) = 2, \ \ (3,) = 2, \ \ (4,5) = 2, \ \ (7,8) = -2, \\
&\qquad \Big[\Big[(6n-3+k,) = 1\Big]_{k=1,2,4,5}\Big]_{n=1}^{m}, \ \ \Big[(6n-2, 6n-1) = 2n, \\
&\qquad (6n+1, 6n+2) = -2n,\Big]_{n=2}^{m}, \\
&\frac{\partial \mathbf{J}_8}{\partial \omega_3}: \ (1,6) = 2, \ \ (3,9) = -2, \ \ \Big[(6n-2, 6n+6) = n+1, \\
&\qquad (6n-1, 6n+6) = n+1, \ \ (6n, 6n+4) = -n, \ \ (6n, 6n+5) = n, \\
&\qquad (6n+1, 6n+9) = n+1, \ \ (6n+2, 6n+9) = -(n+1), \\
&\qquad (6n+3, 6n+7) = -n, \ \ (6n+3, 6n+8) = -n\Big]_{n=1}^{m-1},
\end{aligned}
\tag{A.9}
$$

$$
\begin{aligned}
&\mathbf{J}_9 \ \{\text{size } (3+6m)\times(3+6m)\}: \\
&\Big[(k,) = 2\Big]_{k=1,2,3}, \ \ \Big[\Big[(6n-3+k,) = 1\Big]_{k=1}^{6}\Big]_{n=1}^{m},
\end{aligned}
\tag{A.10}
$$

$$
\begin{aligned}
&\mathbf{J}_{10} \ \{\text{size } (3+6m)\times 1\}: \\
&(3,1) = -2r,
\end{aligned}
\tag{A.11}
$$

$$
\begin{aligned}
&\mathbf{J}_{11} \ \{\text{size } (3+6m)\times(3+6m)\}(\text{antisymmetric}): \\
&(1,3) = -2, \ \ \Big[(6n-2, 6n+2) = -1, \ \ (6n-2, 6n+1) = n, \\
&(6n-1, 6n+1) = 1, \ \ (6n-1, 6n+2) = -n, \ \ (6n, 6n+3) = n\Big]_{n=1}^{m},
\end{aligned}
\tag{A.12}
$$

$$
\begin{aligned}
&\mathbf{J}_{12} \ \{\text{size } (3+6m)\times 1\}: \\
&(1,1) = 2r,
\end{aligned}
\tag{A.13}
$$

$$
\begin{aligned}
&\mathbf{J}_{13}\ \{\text{size } (3+6m)\times(3+6m)\}: \\
&(1,)=1,\ \ (3,)=1,\ \ \left[\left[(6n-3+k,)=\frac{n^2+1}{2}\right]_{k=1,2,4,5}\right]_{n=1}^{m}, \\
&\left[(6n-3+k,)=\frac{n^2}{2}\right]_{k=3,6},\ \ (6n-2,6n-1)=2n, \\
&(6n+1,6n+2)=-2n\Big]_{n=1}^{m},
\end{aligned}
\tag{A.14}
$$

where, as indicated in Section 3, m indicates the truncation harmonic on the expansion of the response along the circumferential direction. Regarding the notation in the previous equations, it is worth indicating the following aspects:

- An element (k,k) in the diagonal of a matrix is denoted as $(k,)$.
- Matrices $\mathbf{J}_7$ and $\mathbf{J}_{11}$ are antisymmetric and therefore only the terms over the diagonal are given.
- The notation $\Big[f(n)\Big]_{n=j}^{m}$ indicates that f is evaluated for every integer n from j to m.
- The notation $\Big[f(k)\Big]_{k=r,s}$ indicates that f is evaluated for $k=r$ and $k=s$.
- The nested notation $\Big[\Big[f(k,n)\Big]_{k=r,s}\Big]_{n=j}^{m}$ indicates that f is evaluated for any combination of k and n.

Regarding the matrix $\tilde{\mathbf{D}}$ from Eq. (23), it is a square matrix of order $(6+12m)$, evaluated as follows:

$$
\tilde{\mathbf{D}}=\begin{bmatrix}
2\mathbf{D} & \mathbf{0} & \cdots & \mathbf{0} \\
\mathbf{0} & \mathbf{D} & \cdots & \mathbf{0} \\
\vdots & \vdots & \ddots & \vdots \\
\mathbf{0} & \mathbf{0} & \cdots & \mathbf{D}
\end{bmatrix},
\tag{A.15}
$$

where $\mathbf{0}$ is a square null matrix of order 6 and $\mathbf{D}$ is the material stiffness matrix obtained from Hooke's Law, given by [23]:

$$\mathbf{D} = \frac{E}{(1+\nu)(1-2\nu)} \begin{bmatrix} 1-\nu & \nu & \nu & 0 & 0 & 0 \\ \nu & 1-\nu & \nu & 0 & 0 & 0 \\ \nu & \nu & 1-\nu & 0 & 0 & 0 \\ 0 & 0 & 0 & \frac{1-2\nu}{2} & 0 & 0 \\ 0 & 0 & 0 & 0 & \frac{1-2\nu}{2} & 0 \\ 0 & 0 & 0 & 0 & 0 & \frac{1-2\nu}{2} \end{bmatrix}, \tag{A.16}$$

with E being the Young's modulus and ν the Poisson's ratio. In relation to the matrix operator $\tilde{\mathbf{L}}$, which allows the calculation of $\tilde{\mathbf{B}}$ in Eq. (23), it is a non-square matrix of dimensions $(6+12m) \times (3+6m)$, given by:

$$\tilde{\mathbf{L}} = \begin{bmatrix} \mathbf{L}_0 & \mathbf{0}_2 & \cdots & \mathbf{0}_2 \\ \mathbf{0}_1 & \mathbf{L}_1 & \cdots & \mathbf{0}_3 \\ \vdots & \vdots & \ddots & \vdots \\ \mathbf{0}_1 & \mathbf{0}_3 & \cdots & \mathbf{L}_n \end{bmatrix}, \tag{A.17}$$

where $\mathbf{0}_1$, $\mathbf{0}_2$, and $\mathbf{0}_3$ are null matrices of dimensions 12×3, 6×6, and 12×6, respectively, and the operators $\mathbf{L}_0$ and $\mathbf{L}_n$ (with $n > 0$) are defined as follows:

$$\mathbf{L}_0 = \begin{bmatrix} \frac{\partial}{\partial r} & 0 & 0 \\ \frac{1}{r} & 0 & 0 \\ 0 & \frac{\partial}{\partial z} & 0 \\ \frac{\partial}{\partial z} & \frac{\partial}{\partial r} & 0 \\ 0 & 0 & \frac{\partial}{\partial r} - \frac{1}{r} \\ 0 & 0 & \frac{\partial}{\partial z} \end{bmatrix}. \tag{A.18}$$

$$\mathbf{L}_n = \begin{bmatrix} \frac{\partial}{\partial r} & 0 & 0 & 0 & 0 & 0 \\ \frac{1}{r} & \frac{n}{r} & 0 & 0 & 0 & 0 \\ 0 & 0 & \frac{\partial}{\partial z} & 0 & 0 & 0 \\ \frac{\partial}{\partial z} & 0 & \frac{\partial}{\partial r} & 0 & 0 & 0 \\ -\frac{n}{r} & \frac{\partial}{\partial r} - \frac{1}{r} & 0 & 0 & 0 & 0 \\ 0 & \frac{\partial}{\partial z} & -\frac{n}{r} & 0 & 0 & 0 \\ 0 & 0 & 0 & \frac{\partial}{\partial r} & 0 & 0 \\ 0 & 0 & 0 & \frac{1}{r} & -\frac{n}{r} & 0 \\ 0 & 0 & 0 & 0 & 0 & \frac{\partial}{\partial z} \\ 0 & 0 & 0 & \frac{\partial}{\partial z} & 0 & \frac{\partial}{\partial r} \\ 0 & 0 & 0 & \frac{n}{r} & \frac{\partial}{\partial r} - \frac{1}{r} & 0 \\ 0 & 0 & 0 & 0 & \frac{\partial}{\partial z} & \frac{n}{r} \end{bmatrix}, \quad n = 1, \cdots, m. \tag{A.19}$$

Appendix B. Kinetic energy integration

In this appendix, a detailed term-by-term analytical integration of the kinetic energy in Eq. (7) around the circumferential direction is provided.

$$K_1 = \frac{1}{2}\dot{\mathbf{p}}_c^{\mathrm{T}}\dot{\mathbf{p}}_c M, \tag{B.1}$$

$$K_2 = \dot{\mathbf{p}}_c^{\mathrm{T}}\tilde{\boldsymbol{\omega}}_c \int_V \rho\boldsymbol{\Theta}\left(\mathbf{u}+\mathbf{w}\right)\mathrm{d}V = \pi\dot{\mathbf{p}}_c^{\mathrm{T}}\tilde{\boldsymbol{\omega}}_c \int_A \rho\left(\mathbf{J}_1\mathbf{w}_h + \mathbf{J}_2\right) r\mathrm{d}A, \tag{B.2}$$

$$K_3 = \dot{\mathbf{p}}_c^{\mathrm{T}} \int_V \rho\boldsymbol{\Theta}\frac{\mathrm{D}(\mathbf{u}+\mathbf{w})}{\mathrm{D}t}\mathrm{d}V = \pi\dot{\mathbf{p}}_c^{\mathrm{T}} \int_A \rho\mathbf{J}_1\dot{\mathbf{w}}_h r\mathrm{d}A, \tag{B.3}$$

$$\begin{aligned} K_4 =& \frac{1}{2}\int_V \rho(\mathbf{u}+\mathbf{w})^{\mathrm{T}}\boldsymbol{\Theta}^{\mathrm{T}}\tilde{\boldsymbol{\omega}}_c^{\mathrm{T}}\tilde{\boldsymbol{\omega}}_c\boldsymbol{\Theta}(\mathbf{u}+\mathbf{w})\mathrm{d}V \\ =& \frac{\pi}{2}\int_A \rho\left((\omega_{11}^2+\omega_{33}^2)r^2 + 2\omega_{22}^2 z^2\right) r\mathrm{d}A + \pi\int_A \rho\mathbf{J}_3^{\mathrm{T}}\mathbf{w}_h r\mathrm{d}A \\ &+ \frac{\pi}{2}\int_A \rho\mathbf{w}_h^{\mathrm{T}}\mathbf{J}_4\mathbf{w}_h r\mathrm{d}A, \end{aligned} \tag{B.4}$$

$$
\begin{aligned}
K_5 =& \frac{1}{2}\int_V \rho(\mathbf{u}+\mathbf{w})^{\mathrm{T}}\boldsymbol{\Theta}^{\mathrm{T}}\tilde{\boldsymbol{\omega}}_c^{\mathrm{T}}\tilde{\boldsymbol{\omega}}_c\boldsymbol{\Theta}\frac{\mathrm{D}(\mathbf{u}+\mathbf{w})}{\mathrm{D}t}\mathrm{d}V = \Omega 2\pi\omega_2\int_A \rho r^3\mathrm{d}A \\
&+\pi\int_A \rho\left(\mathbf{J}_5^{\mathrm{T}}+\mathbf{w}_h^{\mathrm{T}}\mathbf{J}_7\right)\dot{\mathbf{w}}_h r\mathrm{d}A + \Omega\pi\int_A \rho\left(\mathbf{J}_6^{\mathrm{T}}+\mathbf{w}_h^{\mathrm{T}}\mathbf{J}_8\right)\mathbf{w}_h r\mathrm{d}A,
\end{aligned}
\tag{B.5}
$$

$$
\begin{aligned}
K_t =& \frac{1}{2}\int_V \rho\frac{\mathrm{D}(\mathbf{u}+\mathbf{w})^{\mathrm{T}}}{\mathrm{D}t}\frac{\mathrm{D}(\mathbf{u}+\mathbf{w})}{\mathrm{D}t}\mathrm{d}V = \Omega^2\pi\omega_2\int_A \rho r^3\mathrm{d}A \\
&+\frac{\pi}{2}\int_A \rho\dot{\mathbf{w}}_h^{\mathrm{T}}\mathbf{J}_9\dot{\mathbf{w}}_h r\mathrm{d}A + \Omega\pi\int_A \rho\left(\mathbf{J}_{10}^{\mathrm{T}}+\mathbf{w}_h^{\mathrm{T}}\mathbf{J}_{11}\right)\dot{\mathbf{w}}_h r\mathrm{d}A \\
&+\Omega^2\pi\int_A \rho\left(\mathbf{J}_{12}^{\mathrm{T}}+\mathbf{w}_h^{\mathrm{T}}\mathbf{J}_{13}\right)\mathbf{w}_h r\mathrm{d}A,
\end{aligned}
\tag{B.6}
$$

where $\mathrm{d}V = r\mathrm{d}\theta\mathrm{d}A$ and the matrices $\mathbf{J}_i$ are defined in the Appendix A.

References

[1] D. J. Thompson, C. J. C. Jones, A review of the modelling of wheel/rail noise generation, Journal of Sound and Vibration 231 (3) (2000) 519–536, http://dx.doi.org/10.1006/jsvi.1999.2542.

[2] M. J. Rudd, Wheel/rail noise—part II: Wheel squeal, Journal of Sound and Vibration 46 (3) (1976) 381–394, http://dx.doi.org/10.1016/0022-460X(76)90862-2.

[3] I. Zenzerovic, W. Kropp, A. Pieringer, An engineering time-domain model for curve squeal: Tangential point-contact model and Green's functions approach, Journal of Sound and Vibration 376 (2016) 149–165, http://dx.doi.org/10.1016/j.jsv.2016.04.037.

[4] D. J. Thompson, Railway Noise and Vibration. Mechanisms, Modelling and Means of Control, Elsevier, 2009, ISBN: 978-0-08-045147-3, http://dx.doi.org/10.1016/B978-0-08-045147-3.X0023-0.

[5] S. L. Grassie, J. Kalousek, Rail corrugation: Characteristics, causes and treatments, Proceedings of the Institution of Mechanical Engineers, Part F: Journal of Rail and Rapid Transit 207 (1) (1993) 57–68, http://dx.doi.org/10.1243/PIME_PROC_1993_207_227_02.

[6] P. T. Torstensson, M. Schilke, Rail corrugation growth on small radius curves—measurements and validation of a numerical prediction model, Wear

303 (1) (2013) 381–396, http://dx.doi.org/10.1016/j.wear.2013.03.029.

[7] J. Wang, D. J. Thompson, G. Squicciarini, Rolling noise on curved track: an efficient time domain model including coupling between the two wheels and rails, in: Noise and Vibration Mitigation for Rail Transportation Systems, 2024, pp. 307–315, ISBN: 978-981-99-7852-6.

[8] A. Wickens, Fundamentals of Rail Vehicle Dynamics, CRC Press, 2003, ISBN: 9780429224652, http://dx.doi.org/10.1201/9780203970997.

[9] K. Knothe, S. Stichel, Rail Vehicle Dynamics, Springer International Publishing, 2017, ISBN: 978-3-319-45376-7, http://dx.doi.org/10.1007/978-3-319-45376-7.

[10] S. Iwnicki, M. Spiryagin, C. Cole, T. McSweeney (Eds.), Handbook of Railway Vehicle Dynamics, Second Edition (2nd ed.), CRC Press, 2019, ISBN: 9780429469398, http://dx.doi.org/10.1201/9780429469398.

[11] S. Bruni, J. P. Meijaard, G. Rill, A. L. Schwab, State-of-the-art and challenges of railway and road vehicle dynamics with multibody dynamics approaches, Multibody System Dynamics 49 (2020) 1–32, http://dx.doi.org/10.1007/s11044-020-09735-z.

[12] E. Di Gialleonardo, F. Braghin, S. Bruni, The influence of track modelling options on the simulation of rail vehicle dynamics, Journal of Sound and Vibration 331 (19) (2012) 4246–4258, http://dx.doi.org/10.1016/j.jsv.2012.04.024.

[13] J. Martínez-Casas, L. Mazzola, L. Baeza, S. Bruni, Numerical estimation of stresses in railway axles using a train–track interaction model, International Journal of Fatigue 47 (2013) 18–30, http://dx.doi.org/10.1016/j.ijfatigue.2012.07.006.

[14] J. Martínez-Casas, E. Di Gialleonardo, S. Bruni, L. Baeza, A comprehensive model of the railway wheelset–track interaction in curves, Journal of Sound and Vibration 333 (18) (2014) 4152–4169, http://dx.doi.org/10.1016/j.jsv.2014.03.032.

[15] V. T. Andrés, J. Martínez-Casas, F. D. Denia, D. J. Thompson, A model of a rotating railway wheel for the prediction of sound radiation, Journal of Sound and Vibration 553 (2023) 117667, http://dx.doi.org/10.1016/j.jsv.2023.117667.

[16] VI-Grade GmbH, VI-Rail 2022.1 Documentation, VI-Grade Engineering Software & Services, 2022.

[17] D. J. Thompson, Wheel-rail noise generation, part III: Rail vibration, Journal of Sound and Vibration 161 (3) (1993) 421–446, doi: http://dx.doi.org/10.1006/jsvi.1993.1084.

[18] D. J. Mead, A general theory of harmonic wave propagation in linear periodic systems with multiple coupling, Journal of Sound and Vibration 27 (2) (1973) 235–260, doi: http://dx.doi.org/10.1016/0022-460X(73)90064-3.

[19] D. J. Thompson, C. J. C. Jones, Sound radiation from a vibrating railway wheel, Journal of Sound and Vibration 253 (2) (2002) 401–419, http://dx.doi.org/10.1006/jsvi.2001.4061.

[20] D. J. Thompson, M. H. A. Janssens, F. G. de Beer, Track Wheel Interaction Noise Software (TWINS) Theoretical Manual (version 3.4), TNO report, TNO Institute of Applied Physics, 2019.

[21] G. K. Batchelor, An Introduction to Fluid Dynamics, Cambridge University Press, 2000, ISBN: 9780511800955, http://dx.doi.org/10.1017/CBO9780511800955.

[22] R. B. Bird, W. E. Stewart, E. N. Lightfoot, Transport Phenomena, Revised 2nd Edition, John Wiley & Sons, 2006, ISBN: 978-0-470-11539-8.

[23] O. C. Zienkiewicz, R. L. Taylor, J. Z. Zhu, The Finite Element Method: Its Basis and Fundamentals, 7th Edition, Butterworth-Heinemann, 2013, ISBN: 978-1-85617-633-0, http://dx.doi.org/10.1016/C2009-0-24909-9.

[24] M. Petyt, Introduction to Finite Element Vibration Analysis, 2nd Edition, Cambridge University Press, 2010, ISBN: 9780521191609, http://dx.doi.org/10.1017/CBO9780511761195.

[25] S. Iwnicki, Manchester benchmarks for rail vehicle simulation, Vehicle System Dynamics 30 (3-4) (1998) 295–313, http://dx.doi.org/10.1080/00423119808969454.

[26] V. T. Andrés, J. Martínez-Casas, F. D. Denia, D. J. Thompson, Influence study of rail geometry and track properties on railway rolling noise, Journal of Sound and Vibration 525 (2022) 116701, http://dx.doi.org/10.1016/j.jsv.2021.116701.

[27] W. Liu, L. Du, W. Liu, D. J. Thompson, Dynamic response of a curved railway track subjected to harmonic loads based on the periodic structure theory, Proceedings of the Institution of Mechanical Engineers, Part

F: Journal of Rail and Rapid Transit 232 (7) (2018) 1932–1950, http://dx.doi.org/10.1177/0954409718754470.

[28] D. J. Thompson, Wheel-rail noise generation, part I: Introduction and interaction model, Journal of Sound and Vibration 161 (3) (1993) 387–400, doi: http://dx.doi.org/10.1006/jsvi.1993.1082.

[29] A. Gross-Thebing, Frequency-dependent creep coefficients for three-dimensional rolling contact problems, Vehicle System Dynamics 18 (6) (1989) 359–374, doi: http://dx.doi.org/10.1080/00423118908968927.

[30] D. J. Thompson, Wheel-rail noise: theoretical modelling of the generation of vibrations, PhD Thesis, University of Southampton (1990).

[31] D. J. Thompson, Wheel-rail noise generation, part IV: Contact zone and results, Journal of Sound and Vibration 161 (3) (1993) 447–466, doi: http://dx.doi.org/10.1006/jsvi.1993.1085.

[32] J. J. Kalker, Wheel-rail rolling contact theory, Wear 144 (1) (1991) 243–261, doi: http://dx.doi.org/10.1016/0043-1648(91)90018-P.

[33] J. J. Kalker, A fast algorithm for the simplified theory of rolling contact, Vehicle System Dynamics 11 (1) (1982) 1–13, doi: http://dx.doi.org/10.1080/00423118208968684.

[34] Railway applications – Wheelsets and bogies – Monobloc wheels – Technical approval procedure – Part 1: Forged and rolled wheels. EN 13979-1:2020, European Committee for Standardization (2020).

[35] Electroacoustics – Sound level meters – Part 1: Specifications. IEC 61672-1:2013, International Electrotechnical Commission (2013).

CONFERENCE PAPERS

International conferences

I. J. Giner-Navarro, V. T. Andrés, J. Martínez-Casas, and F. D. Denia. Study of the influence falling friction on the wheel/rail contact in railway dynamics. In *Proceedings of Mathematical Modelling in Engineering & Human Behaviour*, pages 88-93, Valencia, Spain, 2019. http://imm.upv.es/jornadas/proceedings/Modelling2019.pdf.

II. J. Giner-Navarro, V. T. Andrés, J. Martínez-Casas, and F. D. Denia. Extension of the modal superposition method for general damping applied in railway dynamics. In *Proceedings of Mathematical Modelling in Engineering & Human Behaviour*, pages 94-98, Valencia, Spain, 2019. http://imm.upv.es/jornadas/proceedings/Modelling2019.pdf.

III. V. T. Andrés, J. Martínez-Casas, J. Carballeira, and F. D. Denia. Railway rolling noise mitigation through optimal track design. In *Proceedings of ECCOMAS Young Investigators Conference*, pages 313-319, Valencia, Spain, 2021. http://dx.doi.org/10.4995/YIC2021.2021.12583.

IV. V. T. Andrés, J. Martínez-Casas, J. Carballeira, and F. D. Denia. A vibroacoustic model of the stationary railway wheel for sound radiation prediction through an axisymmetric approach. In *Proceedings of ECCOMAS Young Investigators Conference*, pages 320-325, Valencia, Spain, 2021. http://dx.doi.org/10.4995/YIC2021.2021.12584.

V. X. Garcia-Andrés, J. Gutiérrez-Gil, V. T. Andrés, J. Martínez-Casas, and F. D. Denia. Rolling noise reduction through GA-based wheel shape optimization techniques. In *Proceedings of ECCOMAS Young Investigators Conference*, pages 304-312, Valencia, Spain, 2021. http://dx.doi.org/10.4995/YIC2021.2021.12577

VI. V. T. Andrés, J. Martínez-Casas, J. Carballeira, and F. D. Denia. Development of a dynamic model of the axisymmetric railway wheel for sound radiation prediction. In *Proceedings of Internoise*, pages 3362-3368(7), Washington, D.C., USA, 2021. http://dx.doi.org/10.3397/IN-2021-2385.

VII. V. T. Andrés, J. Martínez-Casas, F. D. Denia, G. Squicciarini, and D. J. Thompson. A model of the rotating rigid wheelset and its influence on the wheel and track rolling noise. In *Proceedings of Internoise*, pages 3959-3965(7), Glasgow, Scotland, 2022. http://dx.doi.org/10.3397/IN_2022_0564.

VIII. V. T. Andrés, J. Martínez-Casas, F. D. Denia, G. Squicciarini, and D. J. Thompson. Modelización de la influencia de los modos de sólido rígido del eje ferroviario montado en el ruido de rodadura de rueda y vía. In *Proceedings of Congreso Iberoamericano de Ingeniería Mecánica*, pages 478-483(1), Madrid, España, 2022. http://dx.doi.org/10.5944/bicim2022.215.

National conferences

I. V. T. Andrés, J. Martínez-Casas, J. Carballeira, and F. D. Denia. Desarrollo de un modelo vibroacústico integral rueda-vía para la predicción de ruido de rodadura ferroviario y estudio para su mitigación. In Proceedings of *Congreso Nacional de Ingeniería Mecánica*, Jaén, Spain, 2021. http:///www.asoc-aeim.es/Indices_anales/CNIM2020.pdf.